Source attribution of oxygenated volatile organic compounds in the remote tropical atmosphere

Analysis of a near-continuous 2-year (O)VOC data set recorded at the Maïdo observatory, La Réunion

Bert W. D. Verreyken

Doctoral examination committee:

J.-P. Cammas	LACy, OSU-R	Chair
H. Sodemann	UiB	Rapporteur
V. Gros	LSCE	Rapporteur
S. Evan	LACy	Examiner
M. De Mazière	BIRA-IASB, UGent	Examiner
F. Vanhaecke	UGent	Examiner
C. Amelynck	BIRA-IASB, UGent	Co-director
J. Brioude	LACy	Co-director

Mass spectrometry
Sources and sinks of atmospheric constituents
Royal Belgian Institute for Space Aeronomy,
Brussels, Belgium

Laboratoire de l'Atmosphère et des Cyclones,
UMR 8105 CNRS,
Université de La Réunion
Saint-Denis, La Réunion, France

Department of Chemistry
Faculty of Sciences
Ghent University
Ghent, Belgium

Doctoral thesis, submitted in partial fulfilment of the requirements for the degree of:
Doctor of Science: Chemistry (UGent), Docteur en Physique Atmosphérique (UR)

17 June 2021

LETTRE D'ENGAGEMENT DE NON-PLAGIAT

Je, Bert Verreyken, en ma qualité de doctorant de l'Université de La Réunion, déclare être conscient que le plagiat est un acte délictueux passible de sanctions disciplinaires. Aussi, dans le respect de la propriété intellectuelle et du droit d'auteur, je m'engage à systématiquement citer mes sources, quelle qu'en soit la forme (textes, images, audiovisuel, internet), dans le cadre de la rédaction de ma thèse et de toute autre production scientifique, sachant que l'établissement est susceptible de soumettre le texte de ma thèse à un logiciel anti-plagiat.

Fait à Sint-Niklaas, le 03/02/2021.

Acknowledgements

A thesis is not only the efforts of one person tirelessly contemplating on ways to move forward, plummeting to existential crises in an effort to move a small pebble in a sea of scientific knowledge. If one is lucky enough, they are accompanied by a vast community of family, friends, and colleagues to provide support, feedback, and advise on how to continue forward in order to attain the goal. I am thankful to say that I have been such a lucky person and would like to take some time here to thank the efforts of those around me.

First, my thanks goes out to Jérôme Brioude and Crist Amelynck, for supervising the thesis. Their guidance, creative input, and meticulous reviewing of all the work performed has been crucial for my development as a researcher, and consequentially, the work presented here. It has been an honor and a pleasure working with you both during these last four years. Similarly, I would like to thank Trissevgeni (Jenny) Stavrakou, and Jean-François Müller who have inspired me by leading by example and supplying feedback, motivation, and, maybe most importantly, perspective when I was in dire need. I am thankful to all four of you for providing the opportunity to work on a Ph.D. within the OCTAVE project, and allowing me to pursue a career in atmospheric research.

Furthermore, I would like to thank all the co-authors on the research that has been published or is in review. Their contributions to the work presented is invaluable. Without their input the thesis would not have been the success it is today.

Additionally, I thank all members of the doctoral examination committee for their careful review of the manuscript, the discussions during the internal defence, and their constructive comments to improve the work presented here.

A special thanks goes out to colleagues with whom I was in contact through their involvement with the PTR-MS measurements, either in a direct, or indirect way. Crist Amelynck and Niels Schoon, who were responsible for the routine observations, quality assurance, and data processing. I have learned a lot from both of you when we were performing intensive maintenance on the PTR-MS instrument and stayed at the Maïdo observatory for an extended period of time. For their more indirect contributions, I would like to thank colleagues at La Réunion with whom I have spent long hours in the car going back and forth to the observatory to perform maintenance on the instrument and secure the instrumentation when tropical cyclones approached the island. This has been mostly Jean-Marc Metzger[1], but also Olivier Magand, Jérôme Brioude, Jean-Pierre Cammas, and the technical staff performing routine observations using the lidar instrument (Eric Golbic, Patrick Hernandez, and Louis Mottet).

Next, I would like to thank the support provided at La Réunion by Sandrine Prunier. During my stay at LACy, her near-constant presence at the laboratory and readiness to provide assistance with the more administrative aspects of research provided a sense of stability and reliability at LACy. Her constant cheerfulness was infecting and has undeniably contributed to the amazing experience I had at La Réunion.

But not all gratitude is reserved for colleagues with whom I've worked on research. I would also like to thank colleagues that made the workplace a warming and welcoming environment. For this, I owe many thanks to Brice, Damien, Jean-Maurice and Alicia, without whom La Réunion would not have become the home it was during my 2 years abroad. They have not only been co-workers with whom I shared an office and lunch, but friends that have made the experience unforgettable. At BIRA, I would like to thank Beata, Maite, Catalina, Jenny and Jean-François, with whom I have shared many a meal and celebration. Thank you for making me feel welcome at the institute and helping to create the friendly working environments to which I looked forward returning to during the COVID-19 pandemic.

I would like to thank my friends and family for their continuing support throughout the years. My mother and father for pushing me forward in life and providing me with all the opportunities I needed in order to pursue

---

[1]With whom I risked my life more than once during car rides towards, and back from, the observatory

academics. My sister, for serving as an inspiration to leave home, in the most extreme of ways[2], and my brother for his unwavering belief in my capacities to bring this work to a successful conclusion.

Among my friends, special thanks goes out to Véronique Cremers and Kevin Louwagie. Véronique for the many uplifting brief 8-hour brunches. Sharing facts at these momentous occasions kept my spirits high. Kevin for the continued interest you showed in the progress on my Ph.D. and the friendship you offered when times were difficult.

And lastly, I would like to thank Matthias. Thank you for pushing me towards a job in research, suffering me during a 2-year stay at la Réunion and the continuing support you have provided me since way before I started this Ph.D. Without you I would never have started pursuing a Ph.D., let alone finish one successfully.

I know there have been a lot more people involved in the success of this work. My sincerest apologies to all the people that fall into this category but have not yet been thanked explicitly above.

---

[2]I think our mother will not share my gratitude here.

Abstracts

Source attribution of oxygenated volatile organic compounds in the remote tropical atmosphere

Volatile organic compounds (VOCs) have a significant impact on the oxidative capacity of the atmosphere and thus on air quality and climate. Among them, the oxygenated VOCs (OVOCs) represent the largest sink of OH in the remote marine atmosphere. Large uncertainties in the global budget of OVOCs still exist due to the incomplete representation of their chemistry in atmospheric models, and poor characterisation of the terrestrial emissions as well as the ocean-atmosphere exchanges for these compounds and their precursors. This is partly due to a paucity in data, especially in remote tropical regions. Analysis of a 2-year, near-continuous data set of (O)VOC concentrations, registered at the Maïdo observatory (21°S, 54°E, 2160 m altitude), located on La Réunion, is presented. The work presented consists of i) the development of a mesoscale Lagrangian particle dispersion model, FLEXPART-AROME, ii) the study of biomass burning (BB) signals recorded at the observatory, and iii) a source attribution study of (O)VOCs at La Réunion relying on a combination of a multivariate statistical model, and back-trajectory calculations generated with FLEXPART-AROME.

Bronbepaling van zuurstofhoudende vluchtige organische stoffen in de afgelegen, tropische atmosfeer

Vluchtige organische stoffen (VOS) hebben een grote impact op de oxiderende capaciteit van de atmosfeer en dus ook op de luchtkwaliteit en het klimaat. Van de vluchtige organische stoffen zijn de zuurstofhoudende VOS (ZH-VOS) de oorzaak van het grootste verlies van OH in de afgelegen marine atmosfeer. Grote onzekerheden op de globale abundantie van deze ZH-VOS bestaan door de onvolledige representatie van de relevante chemie in atmosfeermodellen, en beperkte karakterisatie van directe emissies van het oppervlak en de interactie tussen atmosfeer en oceaan. Dit is gedeeltelijk te wijten aan een gebrek aan data in dit type regio's. We presenteren hier de analyse van een 2-jaar durende dataset aan (ZH-)VOS concentraties geregistreerd aan het Maïdo observatorium (21°ZB, 54°OL, 2160 m hoogte), gelegen op La Réunion, een tropisch eiland in de zuidwestelijke Indische Oceaan. Het werk omvat i) de ontwikkeling van een atmosferisch transport model dat transport op mesoschaal in rekening brengt (FLEXPART-AROME), ii) de studie van pluimen afkomstig van brandhaarden in Afrika en Madagascar die geobserveerd werden op Maïdo, en iii) een analyse van de volledige 2-jaar lange dataset door een combinatie van een multivariaat statistisch model en de berekening van luchtmassatransport achterwaarts in de tijd bekomen met het FLEXPART-AROME model.

Attribution des sources de composés organiques volatils dans l'atmosphère tropicale isolée

Les composés organiques volatils (COV) ont un impact significatif sur la capacité oxydante de l'atmosphère et donc sur la qualité de l'air et le climat. Parmi eux, les COV oxygénés (COVO) représentent le plus grand puits des radicaux OH dans l'atmosphère marine isolée. De larges incertitudes existent toujours dans le bilan global des COVO, en raison d'une représentation incomplète de leur chimie, d'une mauvaise caractérisation de leurs émissions terrestres ainsi que des échanges océan-atmosphère associés à ces espèces chimiques et de leurs précurseurs. Ceci est en partie la conséquence d'un manque de données dans les régions tropicales isolées. L'objet de cette thèse porte sur la présentation et l'analyse d'une base de données quasi-continue de 2 ans de mesures in situ de COVO obtenue à l'observatoire du Maïdo (21°S, 54°E, 2160 m d'altitude), situé sur l'ile de la Réunion. Le travail présenté consiste en i) le développement d'un modèle dispersif Lagrangien mésoéchelle FLEXPART-AROME, ii) l'étude de cas de feux de biomasses mesurés à l'observatoire, et iii) l'attribution des sources de COVO à la Réunion en s'appuyant sur un modèle statistique multivariable et des calculs de rétro-trajectoires obtenus à l'aide de FLEXPART-AROME.

x

Table of contents

List of terms

AROME applications de la recherche à l'opérationnel à méso-echelle.

BB biomass burning.

BVOC biogenically emitted VOC.

$\mathbf{C_{10}H_{16}}$ monoterpenes.

$\mathbf{C_5H_8}$ isoprene.

$\mathbf{C_6H_6}$ benzene.

$\mathbf{C_7H_8}$ toluene.

$\mathbf{C_8H_{10}}$ C_8-aromatics.

CAMS Copernicus atmosphere monitoring service.

CCN cloud condenstation nuclei.

$\mathbf{CH_3CHO}$ acetaldehyde.

$\mathbf{CH_3CN}$ acetonitrile.

$\mathbf{CH_3COCH_3}$ acetone.

$\mathbf{CH_3COOH}$ acetic acid.

$\mathbf{CH_3OH}$ methanol.

$\mathbf{CH_4}$ methane.

CO carbon monoxide.

CO$_2$ carbon dioxide.

CTM chemical transport model.

DMS dimethyl sulfide.

EDGAR emissions database for global atmospheric research.

EnR enhancement ratio.

EPA Environmental Protection Agency.

ER emissions ratio.

EU European Union.

FLEXPART FLEXible PARTicle dispersion model.

FLEXPART-MNH FLEXPART limited area version driven by meteorological fields obtained from Meso-NH.

FLEXPART-WRF FLEXPART limited area version driven by meteorological data provided by WRF.

FLEXPART-AROME FLEXPART limited area version driven by meteorological fields obtained from AROME.

FT free troposphere.

FTIR Fourier-transform infrared spectroscopy.

GFAS global fire assimilation system.

GHG greenhouse gas.

H$_2$O water.

H$_3$O$^+$ hydronium ion.

HC hollow cathode.

HCHO formaldehyde.

HCOOH formic acid.

HNO$_3$ nitric acid.

HO$_x$ hydrogen oxide radical.

HO$_2$ hydrogen peroxy radical.

hs-PTR-Quad-MS high-sensitivity quadrupole-based PTR-MS VOC analyser.

Iox isoprene oxidation products.

ITCZ inter tropical convergence zone.

LPDM Lagrangian particle dispersion model.

MAX-DOAS multi-axis differential optical absorption spectroscopy.

MEGAN model for emissions of gases and aerosols from nature.

MEK methyl ethyl ketone.

Meso-NH mesoscale non-hydrostatic.

MVK methyl vinyl ketone.

NH Northern Hemisphere.

NMVOC non-methane VOC.

NO nitrogen oxide.

NO$_x$ nitrogen oxides (NO$_x$=NO+NO$_2$).

NO$_2$ nitrogen dioxide.

NO$_3$ nitrate.

NRT near-real-time.

NWP numerical weather prediction.

O$_2$ diatomic oxygen.

O$_3$ ozone.

OCTAVE oxygenated compounds in the tropical atmosphere: variability and exchanges.

OH hydroxyl radical.

OVOC oxygenated VOC.

PA proton affinity.

PBL planetary boundary layer.

PMF positive matrix factorisation.

PTR-MS proton-transfer-reaction mass-spectrometry.

R organic radical.

RO organic oxy radical.

RO_2 organic peroxy radical.

ROOH hydroperoxides.

RT residence time.

SH Southern Hemisphere.

SOA secondary organic aerosol.

SRR source-receptor relationship.

STILT stochastic time-inverted transport model.

TKE turbulent kinetic energy.

VOC volatile organic compound.

WHO World Health Organisation.

WRF weather research and forecasting.

WRF-Chem weather research and forecasting model coupled with chemistry.

Introduction

Volatile organic compounds (VOCs) are chemically reactive species that are present in trace amounts in the atmosphere. They are introduced into, transformed in, and removed from the atmosphere through numerous processes. The oxygenated VOCs (OVOCs), of which methanol (CH_3OH), acetaldehyde (CH_3CHO), and acetone (CH_3COCH_3) are among the most abundant, play an important role on the oxidative capacity in the atmosphere, especially in the remote marine atmosphere through their interaction with the hydroxyl radical (OH) (Travis et al., 2020). Large uncertainties are still related to the global budgets of these OVOC species due to incomplete representation of their chemistry, uncertainties in terrestrial emissions and ocean–atmosphere exchanges (e.g., Millet et al., 2010; Read et al., 2012; Wang et al., 2019, 2020). This is in part due to the paucity in OVOC data in remote and tropical regions. OVOC chemistry and ocean–atmosphere exchanges of OVOCs and their precursors in remote regions are crucial to correctly estimate the oxidative capacity of the atmosphere and quantify their impact on climate (Zhao et al., 2019; Thames et al., 2020).

In order to address this issue, a two-year near-continuous data set of in situ VOC concentrations was generated using a proton-transfer-reaction mass-spectrometry (PTR-MS) VOC analyser deployed at the high-altitude Maïdo observatory (21.1 °S, 55.4 °E, 2,150 m altitude). The observatory is located on La Réunion, a remote tropical french volcanic island about 700 km east of Madagascar in the south-west Indian Ocean. Due to the island's complex terrain, mesoscale transport processes are not well resolved in global numerical weather prediction models. During the day, air masses originating from the marine boundary layer are transported towards the Maïdo observatory along the sea-breeze coupled with upslope transport on the Maïdo mountain slope. During the night, the observatory is often located in the free troposphere. One of the challenges to analyse data

taken at the Maïdo observatory is the representation of the island's complex terrain and its impact on transport from local emission sources towards the observatory.

The work presented here is focused on the development of a Lagrangian transport model capable to represent mesoscale transport features induced by the island's orography, as well as on the generation and analysis of a 2-year VOC data set recorded at the Maïdo observatory.

Structure of the manuscript

The thesis manuscript is divided into three parts: scientific foundation, research, and general discussions.

The first part will serve as an introduction, discussing general concepts, measurement techniques, and analytical tools used in atmospheric sciences. Chapter 1 contains a discussion on VOCs, starting with their definition and detailing how they are emitted into, transformed in, and removed from the atmosphere. We will also discuss the importance of these trace compounds in the atmosphere. Chapter 2 will briefly discuss the different processes which impact VOC concentrations measured in the atmosphere and how this type of measurements can be analysed. Afterwards, we discuss some of the most popular in situ techniques used to quantify the atmospheric composition with a large focus on the PTR-MS technique which has been used to generate the core data set for this thesis. Towards the end of Chapter 3, the instrumental set-up at La Réunion is presented. At the end of this introductory part (Chapter 4), we discuss the motivation of the current work, the measurement site, and we lay out the objectives and roadmap for the thesis.

The second part (Chapters 5–7) will present the research performed in the framework of this thesis. Each chapter is based on a research paper that will briefly be introduced in order to frame it in the larger picture and discuss the methodology used to reach the specific objectives addressed in the paper.

In the third and last part we discuss the research performed, and summarise the conclusions (Chapter 8). Prospects on how to improve on the work presented and the natural continuation of the research will also be given in this part (Chapter 9).

Additional literature

The introductory chapters (Chapter 1–3) have been written by referring to peer reviewed literature and consulting standard textbooks in atmospheric sciences. The textbooks consulted for Chapter 1 are Seinfeld and Pandis (2016), Holloway and Wayne (2010), and Koppmann (2007). Chapter 2 leans on atmospheric transport and turbulence descriptions found in Wallace and Hobbs (2006) and chemical kinetics from Seinfeld and Pandis (2016). Chapter 3 relies on the review of PTR-MS from Ellis and Mayhew (2014).

Bibliography

Ellis, A. M. and Mayhew, C. A.: Proton Transfer Reaction Mass Spectrometry: Principles and Applications, John Wiley & Sons, Inc, Chichester, West Sussex, 2014.

Holloway, A. M. and Wayne, R. P.: Atmospheric Chemistry, RSC Pub, Cambridge, 2010.

Koppmann, R., ed.: Volatile Organic Compounds in the Atmosphere, Blackwell Publishing Ltd, Oxford, UK, https://doi.org/10.1002/9780470988657, 2007.

Millet, D. B., Guenther, A., Siegel, D. A., Nelson, N. B., Singh, H. B., de Gouw, J. A., Warneke, C., Williams, J., Eerdekens, G., Sinha, V., Karl, T., Flocke, F., Apel, E., Riemer, D. D., Palmer, P. I., and Barkley, M.: Global Atmospheric Budget of Acetaldehyde: 3-D Model Analysis and Constraints from in-Situ and Satellite Observations, Atmospheric Chemistry and Physics, 10, 3405–3425, https://doi.org/10.5194/acp-10-3405-2010, 2010.

Read, K. A., Carpenter, L. J., Arnold, S. R., Beale, R., Nightingale, P. D., Hopkins, J. R., Lewis, A. C., Lee, J. D., Mendes, L., and Pickering, S. J.: Multiannual Observations of Acetone, Methanol, and Acetaldehyde in Remote Tropical Atlantic Air: Implications for Atmospheric OVOC Budgets and Oxidative Capacity, Environmental Science & Technology, 46, 11 028–11 039, https://doi.org/10.1021/es302082p, 2012.

Seinfeld, J. H. and Pandis, S. N.: Atmospheric Chemistry and Physics: From Air Pollution to Climate Change, John Wiley & Sons, Hoboken, New Jersey, third edition edn., 2016.

Thames, A. B., Brune, W. H., Miller, D. O., Allen, H. M., Apel, E. C., Blake, D. R., Bui, T. P., Commane, R., Crounse, J. D., Daube, B. C., Diskin, G. S., DiGangi, J. P., Elkins, J. W., Hall, S. R., Hanisco, T. F., Hannun, R. A., Hintsa, E., Hornbrook, R. S., Kim, M. J., McKain, K., Moore, F. L., Nicely, J. M., Peischl, J., Ryerson, T. B., St. Clair, J. M., Sweeney, C., Teng, A., Thompson, C. R., Ullmann, K., Wennberg, P. O., and Wolfe, G. M.: Missing OH Reactivity in the Global Marine Boundary Layer, Atmospheric Chemistry and Physics, 20, 4013–4029, https://doi.org/10.5194/acp-20-4013-2020, 2020.

Travis, K. R., Heald, C. L., Allen, H. M., Apel, E. C., Arnold, S. R., Blake, D. R., Brune, W. H., Chen, X., Commane, R., Crounse, J. D., Daube, B. C., Diskin, G. S., Elkins, J. W., Evans, M. J., Hall, S. R., Hintsa, E. J., Hornbrook, R. S., Kasibhatla, P. S., Kim, M. J., Luo, G., McKain, K., Millet, D. B., Moore, F. L., Peischl, J., Ryerson, T. B., Sherwen, T., Thames, A. B., Ullmann, K., Wang, X., Wennberg, P. O., Wolfe, G. M., and Yu, F.: Constraining Remote Oxidation Capacity with ATom Observations, Atmospheric Chemistry and Physics, 20, 7753–7781, https://doi.org/10.5194/acp-20-7753-2020, 2020.

Wallace, J. M. and Hobbs, P. V.: Atmospheric Science: An Introductory Survey, no. v. 92 in International Geophysics Series, Elsevier Academic Press, Amsterdam ; Boston, 2nd ed edn., 2006.

Wang, S., Hornbrook, R. S., Hills, A., Emmons, L. K., Tilmes, S., Lamarque, J.-F., Jimenez, J. L., Campuzano-Jost, P., Nault, B. A., Crounse, J. D., Wennberg, P. O., Kim, M., Allen, H., Ryerson, T. B., Thompson, C. R., Peischl, J., Moore, F., Nance, D., Hall, B., Elkins, J., Tanner, D., Huey, L. G., Hall, S. R., Ullmann, K., Orlando, J. J., Tyndall, G. S., Flocke, F. M., Ray, E., Hanisco, T. F., Wolfe, G. M., St. Clair, J., Commane, R., Daube, B., Barletta, B., Blake, D. R., Weinzierl, B., Dollner, M., Conley, A., Vitt, F., Wofsy, S. C., Riemer, D. D., and Apel, E. C.: Atmospheric Acetaldehyde: Importance of Air-Sea Exchange and a Missing Source in the Remote Troposphere, Geophysical Research Letters, 46, 5601–5613, https://doi.org/10.1029/2019GL082034, 2019.

Wang, S., Apel, E. C., Schwantes, R. H., Bates, K. H., Jacob, D. J., Fischer, E. V., Hornbrook, R. S., Hills, A. J., Emmons, L. K., Pan, L. L.,

Honomichl, S., Tilmes, S., Lamarque, J.-F., Yang, M., Marandino, C. A., Saltzman, E. S., Bruyn, W., Kameyama, S., Tanimoto, H., Omori, Y., Hall, S. R., Ullmann, K., Ryerson, T. B., Thompson, C. R., Peischl, J., Daube, B. C., Commane, R., McKain, K., Sweeney, C., Thames, A. B., Miller, D. O., Brune, W. H., Diskin, G. S., DiGangi, J. P., and Wofsy, S. C.: Global Atmospheric Budget of Acetone: Air-Sea Exchange and the Contribution to Hydroxyl Radicals, Journal of Geophysical Research: Atmospheres, 125, https://doi.org/10.1029/2020JD032553, 2020.

Zhao, Y., Saunois, M., Bousquet, P., Lin, X., Berchet, A., Hegglin, M. I., Canadell, J. G., Jackson, R. B., Hauglustaine, D. A., Szopa, S., Stavert, A. R., Abraham, N. L., Archibald, A. T., Bekki, S., Deushi, M., Jöckel, P., Josse, B., Kinnison, D., Kirner, O., Marécal, V., O'Connor, F. M., Plummer, D. A., Revell, L. E., Rozanov, E., Stenke, A., Strode, S., Tilmes, S., Dlugokencky, E. J., and Zheng, B.: Inter-Model Comparison of Global Hydroxyl Radical (OH) Distributions and Their Impact on Atmospheric Methane over the 2000–2016 Period, Atmospheric Chemistry and Physics, 19, 13 701–13 723, https://doi.org/10.5194/acp-19-13701-2019, 2019.

PART I

Scientific foundation

Chapter 1

Volatile organic compounds

1.1 Definition

As volatile organic compounds play a central role in this thesis, it might be interesting to have a closer look at how they are defined. Whether a compound is considered as volatile or not depends on its volatility, which is a qualitative measure to describe how fast a material vaporises. It can be defined using either the vapor pressure[1] or the boiling point[2] for liquids. Compounds with high vapor pressure at a certain temperature are characterised as volatile at this temperature and thus likely found in the gaseous rather than the liquid state. Alternatively, one can use the boiling point, if this value is low, the liquid is considered to have a high volatility.

Organic chemistry is the chemistry involving carbon-containing compounds, excluding substances that are traditionally considered as inorganic, e.g. carbon monoxide (CO), and carbon dioxide (CO_2)[3]. Organic compounds are subdivided according to the level of saturation[4] and their functional groups

---

[1]The vapor pressure is defined as the pressure in a closed system where there is an equilibrium between the liquid and gaseous state of the chemical compound and is dependent on temperature.

[2]The temperature of a liquid at a certain pressure where the vapor pressure equals the surrounding pressure.

[3]The complete list of traditionally excluded classes of carbon containing compounds differs from author to author.

[4]Saturated organic compounds only contain single bonds between carbon atoms $(C-C)$ and are generally more stable than their unsaturated counterparts.

which determine largely how these compounds will react. The classes of organic compounds and the specific compounds of interest for this thesis are given in (Table 1.1).

Volatile organic compounds (VOCs) are organic compounds which have a high volatility. However, as 'high' volatility is ambiguous, several specific definitions of VOCs exist. They often depend on the context. For example, the U.S. Environmental Protection Agency (EPA) makes use of different definitions between indoor and outdoor VOCs. The European Union (EU) legislature also defines VOCs differently in directives pertaining anthropogenic emissions[5], chemical composition of organic solvents, or fugitive emissions from paints and varnishes. The World Health Organisation (WHO) further subdivides VOCs to very volatile, volatile, and semi-volatile organic compounds. As an illustration, differences in EU legislation are given in Appendix A.

In this thesis, the term VOCs refers to carbon-containing compounds with sufficient volatility to be present in gaseous form in the atmosphere. More specifically, we will focus on the VOCs whose atmospheric concentrations are sufficiently high for them to be quantified in measurements.

1.2   VOCs, from emission to deposition

Figure 1.1 shows the different processes affecting the presence of VOCs in the atmosphere. Organic carbon is emitted by multiple sources into the atmosphere where it can interact with solar radiation or react with the major atmospheric oxidants, i.e. the hydroxyl radical (OH), ozone (O_3), and nitrate (NO_3), to form other VOCs which are further oxidized and ultimately form CO_2 and water (H_2O). Alternatively, low vapor pressure organic compounds can nucleate to, or deposit on, secondary organic aerosol (SOA). Finally, organic matter will be removed from the atmosphere through wet or dry deposition. During the chemical processing of VOCs in the atmosphere, nitrogen oxide (NO) can interact with oxidation products of the VOCs to form nitrogen dioxide (NO_2), which is the main precursor of O_3 in the troposphere.

In the following section we will discuss the sources emitting VOCs directly

---

[5]Aside from setting a definition based on the volatility, these directives also consider the source for qualifying a compound as a VOC.

Class	Chemical formula	Examples
alcohols	R‑OH	Methanol
aldehydes	$\overset{\displaystyle O}{\underset{}{R\text{-}C\text{-}H}}$	formaldehyde (HCHO)
		acetaldehyde (CH_3CHO)
ketones	$\overset{\displaystyle O}{R\text{-}C\text{-}R'}$	acetone (CH_3COCH_3)
		methyl vinyl ketone (MVK)
		methyl ethyl ketone (MEK)
carboxylic acids	$\overset{\displaystyle O}{R\text{-}C\text{-}OH}$	formic acid (HCOOH)
		acetic acid (CH_3COOH)
terpenoids		isoprene (C_5H_8)
		monoterpenes ($C_{10}H_{16}$)
aromatics		benzene (C_6H_6)
		toluene (C_7H_8)
		C_8-aromatics (C_8H_{10})
sulfides	R−S‑R′	dimethyl sulfide (DMS)
nitriles	R‑C≡N	acetonitrile (CH_3CN),
		a.k.a. methyl cyanide

Table 1.1: Chemical formula of organic compound classes of interest in this thesis.
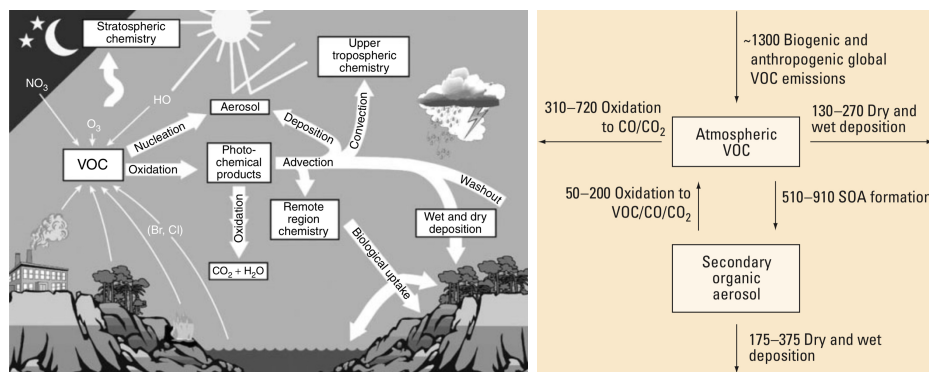
Figure 1.1: Overview of processes impacting VOC concentrations in the atmosphere (left). Mass-balance-based estimate of global budget of VOCs, estimates for rates of conversion in units in Tg C yr^{-1} (right). Figures taken from Williams and Koppmann (2007) (left) and Goldstein and Galbally (2007) (right).

into the atmosphere, the general mechanism behind the VOC oxidation process and the deposition of VOCs to the surface.

1.2.1 Emissions of VOCs

BVOCs are the dominant source of VOCs in the atmosphere. The emissions originate predominantly from terrestrial vegetation and account for an estimated global emission rate of about 1000 TgC yr^{-1}(Guenther et al., 2012). Although BVOCs are predominantly emitted by foliage (leaves and needles), other plant tissues (e.g. stems, flowers, fruit, roots) and ecosystem components (e.g. soil microbes, leaf litter) also contribute. BVOCs are involved in plant growth, reproduction, decay, and defence mechanisms of plants (Laothawornkitkul et al., 2009). Biosynthesis of BVOCs in leaves depends, among other things, on the supply of precursor species, leaf temperature, and solar irradiance (Guenther et al., 2012). After synthesis, they can either be emitted into the atmosphere through stomata[6] or stored in specific storage pools. Whether or not emission through the stomata immediately follows production depends on the physicochemical properties of the compounds and their tendency to dissolve in non-specific leaf stor-

---

[6]Stomata are pores in the surface of the leaf with the explicit function to exchanges gasses between the leaves and the environment.

age compartments, e.g. storage of methanol, CH_3OH, in the leaf aqueous phase (Niinemets et al., 2014). Emission through the stomata is controlled by stomatal conductance, which in turn strongly depends on environmental factors such as solar radiation, relative humidity and soil water potential. VOC emission from specific storage pools proceeds by temperature dependent diffusion through membranes. Terrestrial vegetation emit predominantly terpenoids, mainly isoprene (C_5H_8), which accounts for half of the biogenic emissions at the global scale, and monoterpenes ($C_{10}H_{16}$), but also oxygenated species such as alcohols, aldehydes, ketones and organic acids. The chemical composition and emission rates of VOCs emitted by vegetation is strongly plant-specific. Over the past decades, BVOC fluxes have therefore been measured in various ecosystems worldwide and in controlled laboratory settings by using leaf or branch enclosures (e.g., Bracho-Nunez et al., 2011; Mozaffar et al., 2018) and by performing eddy covariance flux measurements at ecosystem scale (e.g., Langford et al., 2010; Laffineur et al., 2011; Jardine et al., 2015; Millet et al., 2018).

In order to allow integration of BVOC emissions into chemical transport models (CTMs), the development of the model for emissions of gases and aerosols from nature (MEGAN) was initiated in the early ninetees and the most recent version (MEGAN v2.1) allows the estimation of emissions of $\sim$ 150 BVOCs (Guenther et al., 2012).

The second largest source of VOC in the global atmosphere is related to human activities. The emissions originate mostly from fossil fuel use and production, but also industrial processes, biofuel combustion and waste management. Biomass burning related to agricultural practices, especially in the tropics, can also be considered as an anthropogenic VOC source, but will be discussed separately. Anthropogenic activity is the dominant source of alkanes and alkenes in the atmosphere. Aromatics, such as benzene (C_6H_6), toluene (C_7H_8), and C_8-aromatics (C_8H_{10}), are important components of fossil fuels and originate predominantly from car exhaust and fuel evaporation. Some oxygenated VOC (OVOC) species, e.g. formaldehyde (HCHO), methanol (CH_3OH), acetaldehyde (CH_3CHO), and acetone (CH_3COCH_3), have been identified in anthropogenic emissions from incomplete fuel combustion (Kean et al., 2001) and residential wood burning (Bruns et al., 2017). Recent eddy-covariance flux measurements in an urban region in Europe (Innsbruck, Austria) showed that oxygenated compounds comprise a surprisingly large fraction of anthropogenic emissions (Karl et al., 2018). Karl et al. (2018) speculated that OVOC emissions are underrepresented

in current air quality models (Karl et al., 2018). Due to a strong increase in population and quality of living, volatile chemical products (e.g. paints, personal care products, cooking) have been identified as an emerging source of anthropogenic emissions (McDonald et al., 2018; Gkatzelis et al., 2020). Legislative restrictions on anthropogenic emissions have been imposed in order to mitigate their detrimental impact on air quality and human health (e.g. hole in the ozone layer, generation of photochemical smog, acid rain, and most recently climate change).

Anthropogenic emissions have been compiled in emission inventories to allow their incorporation into chemical transport models (CTMs) for air quality estimation. For example, the emissions database for global atmospheric research (EDGAR) provides an extensive list of sector- and country- specific anthropogenic tracers with high temporal resolution (Crippa et al., 2020).

Biomass burning (BB) is a relatively small source of VOCs in the atmosphere on the global scale[7]. However, due to its episodic nature, it has a large inter-annual variability (van der Werf et al., 2006) and can have a significant local impact on air quality. Following terrestrial biogenic emissions, BB is the second largest source of OVOC in the atmosphere (Reimann and Lewis, 2007). Typical BB emitted (classes of) compounds are carbon monoxide (CO), CO_2, alkanes, alkenes, alcohols, aldehydes, ketones and organic acids. An extensive list of emission factors[8] related to BB is compiled by Andreae (2019). A typical BB marker not related significantly to other sources is acetonitrile (CH_3CN) (de Gouw, 2003).

The ocean represents a large reservoir for several VOCs. Biotic synthesis of CH_3OH, CH_3CHO, CH_3COCH_3, and C_5H_8 by phytoplankton under impulse of light was shown in outdoor mesocosm (e.g., Sinha et al., 2007) and laboratory (e.g., Halsey et al., 2017) studies. Subsequent consumption of these VOC by bacterioplankton, however, may limit emissions of these compounds from the ocean into the atmosphere (Halsey et al., 2017). Biogenic production of dimethyl sulfide (DMS) in the ocean and subsequent

---

[7](Stavrakou et al., 2015) used inverse modelling to evaluate VOC emissions on a global scale using satellite measurements of formaldehyde. They found that the biomass burning source emits half the mass of VOCs emitted by anthropogenic activity. This method also accounts for emissions of methane, an important VOC which is often discussed separately in atmospheric sciences due to its long atmospheric lifetime and its importance as a greenhouse gas. However, biomass burning constitutes the second largest source of non-methane VOCs (NMVOCs) on the global scale.

[8]The mass of a VOC emitted by burning 1 kg of fuel.
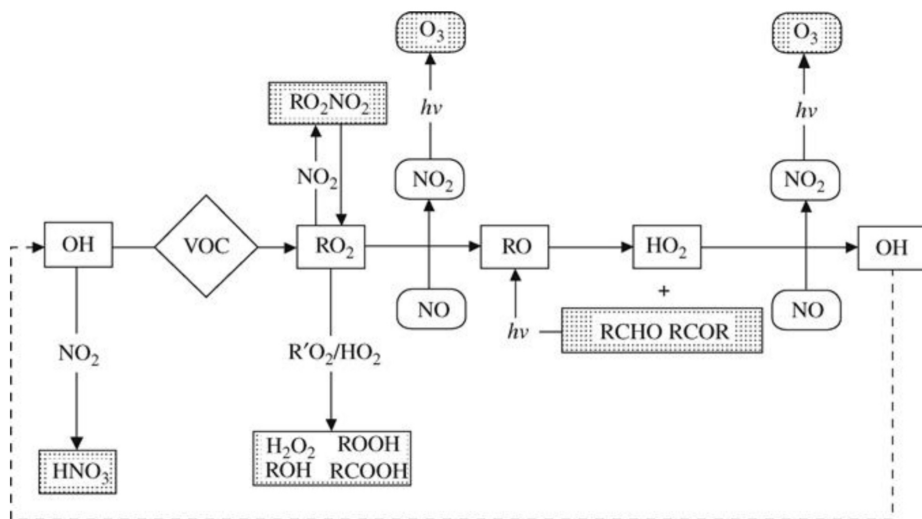
Figure 1.2: Oxidation cycle VOCs by OH. Figure from (Holloway and Wayne, 2010), adapted from (Bras, 1997).

emission to the atmosphere is a large source of atmospheric sulfur. Abiotic production of C_5H_8 has been suggested in the ocean surface micro layer (Brüggemann et al., 2018) as a missing source in atmospheric models. It has been estimated that this abiotic production of OVOC in the surface layer and subsequent emission into the atmosphere is negligible compared to observed fluxes (Yang et al., 2014; Brüggemann et al., 2018).

Despite numerous studies aiming to characterise VOC emission from the ocean, large uncertainties related to this source still exists. This is due to a large bi-directional interaction between the atmosphere and the ocean and a paucity in data from remote regions.

1.2.2 Tropospheric chemistry of VOCs

The atmosphere is an oxidizing medium with the oxidative capacity determined largely by OH. Other oxidizing agents in the atmosphere are O_3, NO_3, and, in the marine atmosphere, halogen radicals (Cl, Br, I, not discussed here). Oxidation by NO_3 only occurs at night as it readily dissociates in the presence of sunlight to NO_2 and atomic oxygen. Aside from oxidation, various VOCs dissociate under the influence of sunlight. Oxida-

Name	Description
Radical	Atom, molecule or ion with an unpaired valence electron which is highly reactive.
Carbonyl	Hydrocarbons where an oxygen atom is attached to a carbon atom by a double bond, e.g. aldehydes and ketones.
Alkyl	Functional group formed from the subtraction of a H-atom from alkanes.
Peroxide	Hydrocarbon containing the peroxide functional group ($R-O-O-R'$).
Alkoxy radical	Alkyl group bonded with a oxygen atom via a single bond ($R-O$).
Isomerization	Transformation of a molecule to an isomer (i.e. a molecule with the same exact mass) by internal rearrangement.

Table 1.2: Terminology from organic chemistry used here.

tion of VOCs results in other, generally less volatile, organic compounds which in turn are further oxidized (ultimately leading to CO_2 and H_2O, see overview in Figure 1.1) or contribute to the formation and growth of secondary organic aerosol (SOA). Here we briefly discuss the generalized oxidation mechanisms of VOCs in the atmosphere as described in atmospheric chemistry textbooks (e.g., Holloway and Wayne, 2010; Seinfeld and Pandis, 2016). Some chemical nomenclature, especially related to classes of hydrocarbons, used in this section is summarised in Table 1.2.

Oxidation by OH

The OH radical is the most important oxidant in the troposphere. Its main formation mechanism is the reaction of excited oxygen atoms, $O(^1D)$, formed by photolysis ($\lambda < 310nm$) of O_3, with water vapour.

$$O_3 + h\nu \longrightarrow O(^1D) + O_2 \tag{1.1}$$

$$O(^1D) + H_2O \longrightarrow 2OH \tag{1.2}$$
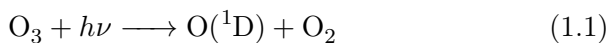
OH is highly reactive with most tropospheric compounds, resulting in a short lifetime ($\sim$ 1s) and very low concentrations[9].

The generalised oxidation mechanism of VOCs initiated by reaction with OH is visualised in Figure 1.2. It should be noticed, however, that the detailed reaction scheme can be extremely complicated and is not well known for many compounds. Even for isoprene, which is the biogenic compound with the highest emission rate, theoretical developments on reaction mechanisms (Peeters and Müller, 2010), supported by experimental data (Fuchs et al., 2013), have shown that the OH-initiated oxidation is more complex than previously thought.

The OH-initiated oxidation of VOCs starts either by H-atom abstraction (for saturated hydrocarbons such as alkanes) or by OH-addition to an unsaturated carbon-carbon bond (C=C). The former process results in the formation of an organic radical (R), which readily associates to O_2 to form an organic peroxy radical (RO_2), and H_2O. The latter process results in the formation of various isomeric hydroxyl substituted organic radicals which also readily form peroxides ($R(OH)O_2$).

$$RH + OH \xrightarrow{O_2} RO_2 + H_2O \qquad (1.3)$$
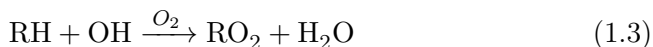
What happens with the RO_2 (or $R(OH)O_2$) radicals strongly depends on the availability of nitrogen oxides (NO_x=NO+NO_2).

VOC oxidation at high NO_x conditions   At high NO_x concentrations, RO_2 efficiently reacts with NO to an organic oxy radical (RO) and NO_2, which is the main precursor of tropospheric O_3 (see section 1.4).

$$RO_2 + NO \longrightarrow RO + NO_2 \qquad (1.4)$$

The RO radicals are mainly lost by reaction with O_2, unimolecular decomposition or isomerization. Reaction with O_2 is the preferential pathway for smaller radicals and results in the formation of hydrogen peroxy radicals (HO_2) and an aldehyde ($R'C(O)H$), or a ketone ($R'C(O)R''$). Regeneration of RO by photolysis of those carbonyl compounds and conversion of NO

---

[9]OH-concentrations are typically only a few 10^6 molecules cm^{-3}, at standard temperature and pressure, the atmosphere contains a few 10^{19} molecules cm^{-3}.

to NO_2 and OH by reaction with HO_2 are largely responsible for the HO_x-catalysed production of O_3 in the presence of NO_x during VOC oxidation (see Figure 1.2 and Section 1.4). Decomposition and isomerization become important for organic oxy radicals with a longer chain and result in the formation of carbonyls and alkyl (and hydroxy alkyl) peroxy radicals, allowing further radical propagation and conversion of NO to NO_2 by reaction 1.4. Besides reaction with NO, RO_2 radicals can also react with NO_2 to form alkyl nitrates (RO_2NO_2).

OH-initated VOC oxidation in remote regions   In remote regions, where NO_x concentrations are low, the major sink for RO_2 is reaction with HO_2 or other organic peroxy radicals to produce hydroperoxides (ROOH) and organic peroxides (ROOR′), respectively. The latter reaction can also lead to the production of carboxylic acids, alcohols and oxy radicals.

$$RO_2 + HO_2 \longrightarrow ROOH + O_2 \qquad (1.5)$$
$$RO_2 + R'O_2 \longrightarrow ROOR' + O_2 \qquad (1.6)$$
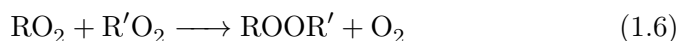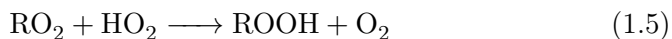
The predominant pathway is the reaction with HO_2 and the resulting hydroperoxides can photodissociate, regenerating RO and OH radicals, or react with OH, forming RO_2 and unstable R′CHOOH radicals which dissociate to OH and aldehydes.

$$ROOH + h\nu \longrightarrow RO + OH \qquad (1.7)$$
$$ROOH + OH \longrightarrow RO_2 + H_2O \qquad (1.8)$$
$$\longrightarrow R'CHOOH + H_2 \qquad (1.9)$$
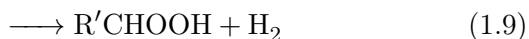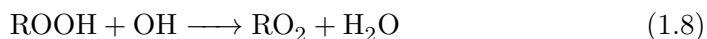
Oxidation by NO_3

Similar to oxidation by OH, the NO_3 radical will either proceed by H-atom abstraction from a C−H bond or by addition to a double carbon bond in unsaturated hydrocarbons. Further reactions of the hereby created organic radicals mainly proceed in a similar way as for the OH-initiated VOC oxidation. However, notable differences are i) the formation of nitric acid (HNO_3) instead of H_2O in the first oxidation step in the case of H-abstraction, and ii) the potential of formation of nitrogen-containing hydrocarbons resulting from NO_3 addition to unsaturated hydrocarbons.

Oxidation by O$_3$

Unlike oxidation by OH or NO$_3$, ozone does not react efficiently with saturated hydrocarbons. It will however add to a double carbon bond resulting in an unstable intermediate species, referred to as a primary ozonide, which rapidly decomposes in either a stable ketone or aldehyde in combination with a carbonyl oxide reactive intermediate. This intermediate is referred to as a Criegee intermediate but will not be further discussed here.

1.2.3 Deposition

The removal of matter from the atmosphere is organised by deposition processes[10]. They are categorised in two distinct types: dry deposition, i.e. deposition of matter directly to the surface in the absence of precipitation, and wet deposition, i.e. deposition of matter in hydrometeors (cloud droplets, mist droplets, rain or snow). Scavenging of aerosols and trace gases by rain is often referred to as 'wash out' (as in Figure 1.1).

The rate at which a species is lost from the atmosphere through dry deposition depends on i) turbulence (i.e. on how fast species in the atmosphere are delivered to the surface), ii) the chemical properties of the species (solubility and reactivity), and iii) the nature of the surface itself. Reactive surfaces such as vegetation generally promote dry deposition of species (biological uptake in Figure 1.1) whereas smooth surfaces may lead to particles bouncing off more easily.

We talk about wet deposition when VOCs are dissolved in hydrometeors and subsequently delivered to the surface. It depends on the presence of water in the atmosphere as well as the solubility of the VOC. Once the VOC is dissolved into hydrometeors is can undergo chemical transformations and/or evaporate back into the atmosphere.
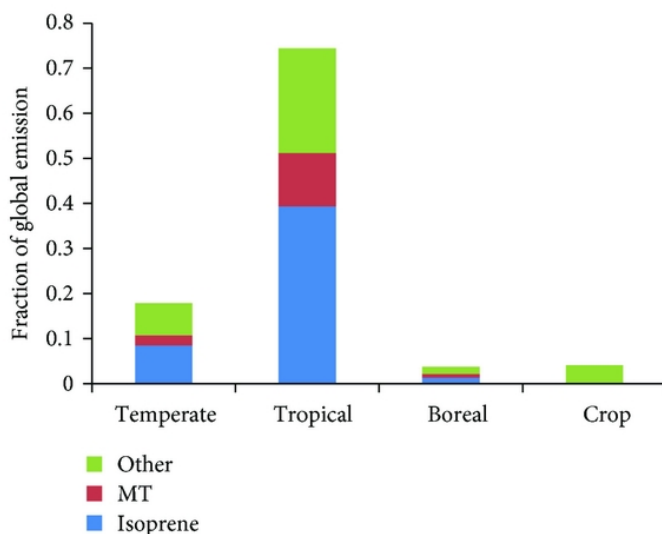
Figure 1.3: Estimated fraction of BVOC emissions for major biome types and compound categories. Image from Guenther (2013).

1.3 VOCs in remote and tropical regions

BVOCs account for the largest part of the global VOC budget. They are emitted predominantly by terrestrial foliage. BVOC fluxes in tropical forests account for the majority of the global biogenic emissions (Figure 1.3). However, due to difficult access to these regions, they are comparatively understudied compared to temperate forest regions (Guenther, 2013). While top-down emission estimates using satellite data found that emissions over tropical regions may be overestimated by the bottom-up inventories (e.g., Stavrakou et al., 2014; Bauwens et al., 2016), measurement campaigns performing eddy-covariance measurements show the bottom-up inventories are sufficient to represent emissions on a global scale (e.g., Karl et al., 2004; Gu et al., 2017; Sarkar et al., 2020). However, they highlight large local and regional differences (factor up to 3) between the bottom-up inventories

---

[10]In principle there is a second way for matter to leave the atmosphere which is emission from the exosphere to space. This however is only possible for species whose mass is small enough to escape Earth's gravity. This effect is only relevant for helium or hydrogen atoms. As we are concerned with processes near the surface this will not be of any importance.

and their measurements due the underrepresentation of the heterogeneity of the surface in the model (Gu et al., 2017; Sarkar et al., 2020).

In the remote marine boundary layer, the impact of terrestrial biogenic emissions is relatively low due to the typically short lifetimes of the primary biogenic emission species. As a result, over these regions VOC concentrations are typically lower than over land and are limited to ubiquitous long-lived species, compounds formed due to degradation of other VOCs, or species emitted directly from the ocean surface. Although the ocean covers most of the Earth's surface, its fluxes account only for a small part of the global VOCs budget. Air-sea exchanges are still prone to large uncertainties (e.g., Read et al., 2012; Wang et al., 2020). It has been shown that the ocean surface can serve both as a source and sink for different species. For example, while the ocean is expected to be a net source of CH_3COCH_3 in the tropics, at higher latitudes it serves as a net sink (Wang et al., 2020). These regional differences depend on VOC production mechanisms and concentrations in the ocean surface layer. Warm-water up-welling and pythoplankton blooming can also significantly enhance atmospheric concentrations of VOC in the remote marine boundary layer (e.g. Colomb et al., 2009).

Since the use of remote sensing instrument on board of satellites, global coverage of column densities are available for different VOCs (e.g. formaldehyde, methanol, formic acid, and acetone). However, this type of measurements is typically less sensitive to VOCs near the surface. As such, additional in-situ measurements of VOC concentrations, especially in remote tropical regions where few observations are available, provide valuable information to characterise the atmospheric composition.

1.4   Importance of VOCs in the atmosphere

Although they are only present in trace amounts in the atmosphere, VOCs have a significant impact on both human health and climate. Some VOCs such as benzene (C_6H_6) and formaldehyde (HCHO) are carcinogenic and thus affect human health in a direct manner (Cogliano et al., 2004; Loomis et al., 2017). VOCs also play a key role in formation of surface level O_3, and SOA, long-term exposure to both of which is associated with an increased risk of death due to cardiopulmonary diseases (Jerrett et al., 2009). Methane (CH_4) is the third most potent GHGs but is often excluded from
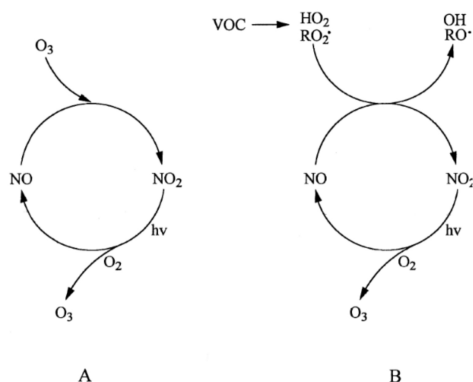
Figure 1.4: (A) Regular NO_x cycle in the troposphere. (B) NO_x cycle in the troposphere interrupted by VOC species leading to accumulation of O_3. Figure from (Atkinson, 2000).

discussions on VOCs. The non-methane VOCs (NMVOCs) however still have a significant impact on climate. Variations in NMVOC emission rates and chemistry in chemical transport models (CTMs) result in large variations in mixing ratio distributions of OH (Zhao et al., 2019). As OH is the major pathway for CH_4 to leave the atmosphere, NMVOCs have an indirect impact on climate. Moreover, the SOA formed by NMVOC oxidation also impact climate directly, through their interaction with solar radiation as illustrated in Figure 1.1, and indirectly, by serving as cloud condenstation nuclei (CCN) (IPCC, 2013). As tropospheric O_3 is a GHG itself, VOCs also affect climate through their involvement in the formation of O_3.

Ozone production

In the atmosphere NO and NO_2 are rapidly interconverted in the regular NO_x cycle in which O_3 acts as a catalyst (Figure 1.4 (A)). During the day, O_3 is produced in the troposphere by the photolysis of NO_2.

$$NO_2 + h\nu \longrightarrow NO + O \tag{1.10}$$

The free oxygen atom will react with O_2 to form O_3 in the presence of a

third body, M.

$$O + O_2 \xrightarrow{M} O_3 \tag{1.11}$$

This reaction is balanced by the reaction of NO with O_3 to produce NO_2.

$$NO + O_3 \longrightarrow NO_2 + O_2 \tag{1.12}$$
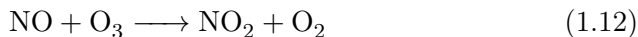
However, when VOCs are present in the atmosphere, their oxidation cycle will consume NO to form NO_2 (Reaction 1.4), resulting in the accumulation of O_3 in the troposphere (Figure 1.4). Moreover, HO_2 produced from VOC oxidation also interacts with NO to form NO_2 and OH, further disturbing the regular NO_x cycle (Figures 1.2 and 1.4).

Production of O_3 in the troposphere depends on the ratio between the concentration of VOCs and NO_x, $[VOC]/[NO_x]$. If the ratio is large, there is significant production of RO_2 to react with NO and the formation of O_3 is proportional to the concentration of NO_x. In this case, the O_3 production is said to be NO_x-limited. Alternatively, when the ratio is small, the OH-radical will preferentially react with NO_2 compared to VOCs.

$$NO_2 + OH \longrightarrow HNO_3 \tag{1.13}$$
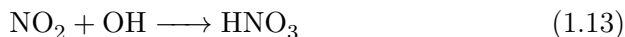
This reaction removes both NO_x and HO_x from the system. Increasing the concentration of VOCs in these conditions promotes conversion from NO to NO_2 and therefore the formation of O_3. These conditions are referred to as the VOC-limited regime.

Bibliography

Andreae, M. O.: Emission of Trace Gases and Aerosols from Biomass Burning – an Updated Assessment, Atmospheric Chemistry and Physics, 19, 8523–8546, https://doi.org/10.5194/acp-19-8523-2019, 2019.

Atkinson, R.: Atmospheric Chemistry of VOCs and NOx, Atmospheric Environment, 34, 2063–2101, https://doi.org/10.1016/S1352-2310(99)00460-4, 2000.

Bauwens, M., Stavrakou, T., Müller, J.-F., De Smedt, I., Van Roozendael, M., van der Werf, G. R., Wiedinmyer, C., Kaiser, J. W., Sindelarova, K., and Guenther, A.: Nine Years of Global Hydrocarbon Emissions Based on Source Inversion of OMI Formaldehyde Observations, Atmospheric Chemistry and Physics, 16, 10 133–10 158, https://doi.org/10.5194/acp-16-10133-2016, 2016.

Bracho-Nunez, A., Welter, S., Staudt, M., and Kesselmeier, J.: Plant-Specific Volatile Organic Compound Emission Rates from Young and Mature Leaves of Mediterranean Vegetation, Journal of Geophysical Research, 116, D16 304, https://doi.org/10.1029/2010JD015521, 2011.

Bras, G.: Chemical Processes in Atmospheric Oxidation: Laboratory Studies of Chemistry Related to Tropospheric Ozone, Springer Berlin Heidelberg, Berlin, Heidelberg, 1997.

Brüggemann, M., Hayeck, N., and George, C.: Interfacial Photochemistry at the Ocean Surface Is a Global Source of Organic Vapors and Aerosols, Nature Communications, 9, 2101, https://doi.org/10.1038/s41467-018-04528-7, 2018.

Bruns, E. A., Slowik, J. G., El Haddad, I., Kilic, D., Klein, F., Dommen, J., Temime-Roussel, B., Marchand, N., Baltensperger, U., and Prévôt, A. S. H.: Characterization of Gas-Phase Organics Using Proton Transfer Reaction Time-of-Flight Mass Spectrometry: Fresh and Aged Residential Wood Combustion Emissions, Atmospheric Chemistry and Physics, 17, 705–720, https://doi.org/10.5194/acp-17-705-2017, 2017.

Cogliano, V., Grosse, Y., Baan, R., Straif, K., Secretan, B., and Ghissassi, F. E.: Advice on Formaldehyde and Glycol Ethers, The Lancet Oncology, 5, 528, https://doi.org/10.1016/S1470-2045(04)01562-1, 2004.

Colomb, A., Gros, V., Alvain, S., Sarda-Esteve, R., Bonsang, B., Moulin, C., Klüpfel, T., and Williams, J.: Variation of Atmospheric Volatile Organic Compounds over the Southern Indian Ocean (30–49°S), Environmental Chemistry, 6, 70–82, https://doi.org/10.1071/EN08072, 2009.

Crippa, M., Solazzo, E., Huang, G., Guizzardi, D., Koffi, E., Muntean, M., Schieberle, C., Friedrich, R., and Janssens-Maenhout, G.: High Resolution Temporal Profiles in the Emissions Database for Global Atmospheric Research, Scientific Data, 7, 121, https://doi.org/10.1038/s41597-020-0462-2, 2020.

de Gouw, J. A.: Emission Sources and Ocean Uptake of Acetonitrile (CH$_3$CN) in the Atmosphere, Journal of Geophysical Research, 108, 4329, https://doi.org/10.1029/2002JD002897, 2003.

Fuchs, H., Hofzumahaus, A., Rohrer, F., Bohn, B., Brauers, T., Dorn, H.-P., Häseler, R., Holland, F., Kaminski, M., Li, X., Lu, K., Nehr, S., Tillmann, R., Wegener, R., and Wahner, A.: Experimental Evidence for Efficient Hydroxyl Radical Regeneration in Isoprene Oxidation, Nature Geoscience, 6, 1023–1026, https://doi.org/10.1038/ngeo1964, 2013.

Gkatzelis, G. I., Coggon, M. M., McDonald, B. C., Peischl, J., Aikin, K. C., Gilman, J. B., Trainer, M., and Warneke, C.: Identifying Volatile Chemical Product Tracer Compounds in U.S. Cities, Environmental Science & Technology, p. acs.est.0c05467, https://doi.org/10.1021/acs.est.0c05467, 2020.

Goldstein, A. H. and Galbally, I. E.: Known and Unexplored Organic Constituents in the Earth's Atmosphere, Environmental Science & Technology, 41, 1514–1521, https://doi.org/10.1021/es072476p, 2007.

Gu, D., Guenther, A. B., Shilling, J. E., Yu, H., Huang, M., Zhao, C., Yang, Q., Martin, S. T., Artaxo, P., Kim, S., Seco, R., Stavrakou, T., Longo, K. M., Tóta, J., de Souza, R. A. F., Vega, O., Liu, Y., Shrivastava, M., Alves, E. G., Santos, F. C., Leng, G., and Hu, Z.: Airborne Observations Reveal Elevational Gradient in Tropical Forest Isoprene Emissions, Nature Communications, 8, 15 541, https://doi.org/10.1038/ncomms15541, 2017.

Guenther, A.: Biological and Chemical Diversity of Biogenic Volatile Organic Emissions into the Atmosphere, ISRN Atmospheric Sciences, 2013, 1–27, https://doi.org/10.1155/2013/786290, 2013.

Guenther, A. B., Jiang, X., Heald, C. L., Sakulyanontvittaya, T., Duhl, T., Emmons, L. K., and Wang, X.: The Model of Emissions of Gases and Aerosols from Nature Version 2.1 (MEGAN2.1): An Extended and Updated Framework for Modeling Biogenic Emissions, Geoscientific Model Development, 5, 1471–1492, https://doi.org/10.5194/gmd-5-1471-2012, 2012.

Halsey, K. H., Giovannoni, S. J., Graus, M., Zhao, Y., Landry, Z., Thrash, J. C., Vergin, K. L., and de Gouw, J.: Biological Cycling of Volatile

Organic Carbon by Phytoplankton and Bacterioplankton: VOC Cycling by Marine Plankton, Limnology and Oceanography, 62, 2650–2661, https://doi.org/10.1002/lno.10596, 2017.

Holloway, A. M. and Wayne, R. P.: Atmospheric Chemistry, RSC Pub, Cambridge, 2010.

IPCC: Climate Change 2013: The Physical Science Basis. Contribution of Working Group I to the Fifth Assessment Report of the Intergovernmental Panel on Climate Change, Cambridge University Press, Cambridge, United Kingdom and New York, NY, USA, 2013.

Jardine, K., Yañez-Serrano, A. M., Williams, J., Kunert, N., Jardine, A., Taylor, T., Abrell, L., Artaxo, P., Guenther, A., Hewitt, C. N., House, E., Florentino, A. P., Manzi, A., Higuchi, N., Kesselmeier, J., Behrendt, T., Veres, P. R., Derstroff, B., Fuentes, J. D., Martin, S. T., and Andreae, M. O.: Dimethyl Sulfide in the Amazon Rain Forest: DMS in the Amazon, Global Biogeochemical Cycles, 29, 19–32, https://doi.org/10.1002/2014GB004969, 2015.

Jerrett, M., Burnett, R. T., Pope, C. A., Ito, K., Thurston, G., Krewski, D., Shi, Y., Calle, E., and Thun, M.: Long-Term Ozone Exposure and Mortality, New England Journal of Medicine, 360, 1085–1095, https://doi.org/10.1056/NEJMoa0803894, 2009.

Karl, T., Potosnak, M., Guenther, A., Clak, D., Walker, J., Herrick, J. D., and Geron, C.: Exchange Processes of Volatile Organic Compounds above a Tropical Rain Forest: Implications for Modeling Tropospheric Chemistry above Dense Vegetation, Journal of Geophysical Research, 109, D18 306, https://doi.org/10.1029/2004JD004738, 2004.

Karl, T., Striednig, M., Graus, M., Hammerle, A., and Wohlfahrt, G.: Urban Flux Measurements Reveal a Large Pool of Oxygenated Volatile Organic Compound Emissions, Proceedings of the National Academy of Sciences, 115, 1186–1191, https://doi.org/10.1073/pnas.1714715115, 2018.

Kean, A. J., Grosjean, E., Grosjean, D., and Harley, R. A.: On-Road Measurement of Carbonyls in California Light-Duty Vehicle Emissions, Environmental Science & Technology, 35, 4198–4204, https://doi.org/10.1021/es010814v, 2001.

Laffineur, Q., Aubinet, M., Schoon, N., Amelynck, C., Müller, J.-F., Dewulf, J., Van Langenhove, H., Steppe, K., Šimpraga, M., and Heinesch, B.: Isoprene and Monoterpene Emissions from a Mixed Temperate Forest, Atmospheric Environment, 45, 3157–3168, https://doi.org/10.1016/j.atmosenv.2011.02.054, 2011.

Langford, B., Misztal, P. K., Nemitz, E., Davison, B., Helfter, C., Pugh, T. A. M., MacKenzie, A. R., Lim, S. F., and Hewitt, C. N.: Fluxes and Concentrations of Volatile Organic Compounds from a South-East Asian Tropical Rainforest, Atmospheric Chemistry and Physics, 10, 8391–8412, https://doi.org/10.5194/acp-10-8391-2010, 2010.

Laothawornkitkul, J., Taylor, J. E., Paul, N. D., and Hewitt, C. N.: Biogenic Volatile Organic Compounds in the Earth System, New Phytologist, 183, 27–51, https://doi.org/10.1111/j.1469-8137.2009.02859.x, 2009.

Loomis, D., Guyton, K. Z., Grosse, Y., El Ghissassi, F., Bouvard, V., Benbrahim-Tallaa, L., Guha, N., Vilahur, N., Mattock, H., and Straif, K.: Carcinogenicity of Benzene, The Lancet Oncology, 18, 1574–1575, https://doi.org/10.1016/S1470-2045(17)30832-X, 2017.

McDonald, B. C., de Gouw, J. A., Gilman, J. B., Jathar, S. H., Akherati, A., Cappa, C. D., Jimenez, J. L., Lee-Taylor, J., Hayes, P. L., McKeen, S. A., Cui, Y. Y., Kim, S.-W., Gentner, D. R., Isaacman-VanWertz, G., Goldstein, A. H., Harley, R. A., Frost, G. J., Roberts, J. M., Ryerson, T. B., and Trainer, M.: Volatile Chemical Products Emerging as Largest Petrochemical Source of Urban Organic Emissions, Science, 359, 760–764, https://doi.org/10.1126/science.aaq0524, 2018.

Millet, D. B., Alwe, H. D., Chen, X., Deventer, M. J., Griffis, T. J., Holzinger, R., Bertman, S. B., Rickly, P. S., Stevens, P. S., Léonardis, T., Locoge, N., Dusanter, S., Tyndall, G. S., Alvarez, S. L., Erickson, M. H., and Flynn, J. H.: Bidirectional Ecosystem–Atmosphere Fluxes of Volatile Organic Compounds Across the Mass Spectrum: How Many Matter?, ACS Earth and Space Chemistry, 2, 764–777, https://doi.org/10.1021/acsearthspacechem.8b00061, 2018.

Mozaffar, A., Schoon, N., Bachy, A., Digrado, A., Heinesch, B., Aubinet, M., Fauconnier, M.-L., Delaplace, P., du Jardin, P., and Amelynck, C.: Biogenic Volatile Organic Compound Emissions from Senescent Maize

Leaves and a Comparison with Other Leaf Developmental Stages, Atmospheric Environment, 176, 71–81, https://doi.org/10.1016/j.atmosenv.2017.12.020, 2018.

Niinemets, Ü., Fares, S., Harley, P., and Jardine, K. J.: Bidirectional Exchange of Biogenic Volatiles with Vegetation: Emission Sources, Reactions, Breakdown and Deposition: Bidirectional BVOC Exchange, Plant, Cell & Environment, 37, 1790–1809, https://doi.org/10.1111/pce.12322, 2014.

Peeters, J. and Müller, J.-F.: HOx Radical Regeneration in Isoprene Oxidation via Peroxy Radical Isomerisations. II: Experimental Evidence and Global Impact, Physical Chemistry Chemical Physics, 12, 14 227, https://doi.org/10.1039/c0cp00811g, 2010.

Read, K. A., Carpenter, L. J., Arnold, S. R., Beale, R., Nightingale, P. D., Hopkins, J. R., Lewis, A. C., Lee, J. D., Mendes, L., and Pickering, S. J.: Multiannual Observations of Acetone, Methanol, and Acetaldehyde in Remote Tropical Atlantic Air: Implications for Atmospheric OVOC Budgets and Oxidative Capacity, Environmental Science & Technology, 46, 11 028–11 039, https://doi.org/10.1021/es302082p, 2012.

Reimann, S. and Lewis, A. C.: Anthropogenic VOCs, in: Volatile Organic Compounds in the Atmosphere, edited by Koppmann, R., pp. 33–81, Blackwell Publishing Ltd, Oxford, UK, https://doi.org/10.1002/9780470988657.ch2, 2007.

Sarkar, C., Guenther, A. B., Park, J.-H., Seco, R., Alves, E., Batalha, S., Santana, R., Kim, S., Smith, J., Tóta, J., and Vega, O.: PTR-TOF-MS Eddy Covariance Measurements of Isoprene and Monoterpene Fluxes from an Eastern Amazonian Rainforest, Atmospheric Chemistry and Physics, 20, 7179–7191, https://doi.org/10.5194/acp-20-7179-2020, 2020.

Seinfeld, J. H. and Pandis, S. N.: Atmospheric Chemistry and Physics: From Air Pollution to Climate Change, John Wiley & Sons, Hoboken, New Jersey, third edition edn., 2016.

Sinha, V., Williams, J., Meyerhöfer, M., Riebesell, U., Paulino, A. I., and Larsen, A.: Air-Sea Fluxes of Methanol, Acetone, Acetaldehyde, Isoprene and DMS from a Norwegian Fjord Following a Phytoplankton Bloom in a Mesocosm Experiment, Atmospheric Chemistry and Physics, 7, 739–755, https://doi.org/10.5194/acp-7-739-2007, 2007.

Stavrakou, T., Müller, J.-F., Bauwens, M., De Smedt, I., Van Roozen-
dael, M., Guenther, A., Wild, M., and Xia, X.: Isoprene Emissions
over Asia 1979–2012: Impact of Climate and Land-Use Changes, Atmo-
spheric Chemistry and Physics, 14, 4587–4605, https://doi.org/10.5194/
acp-14-4587-2014, 2014.

Stavrakou, T., Müller, J.-F., Bauwens, M., De Smedt, I., Van Roozendael,
M., De Mazière, M., Vigouroux, C., Hendrick, F., George, M., Clerbaux,
C., Coheur, P.-F., and Guenther, A.: How Consistent Are Top-down Hy-
drocarbon Emissions Based on Formaldehyde Observations from GOME-
2 and OMI?, 2015.

van der Werf, G. R., Randerson, J. T., Giglio, L., Collatz, G. J., Kasibhatla,
P. S., and Arellano, A. F.: Interannual Variability in Global Biomass
Burning Emissions from 1997 to 2004, Atmospheric Chemistry and
Physics, 6, 3423–3441, https://doi.org/10.5194/acp-6-3423-2006, 2006.

Wang, S., Apel, E. C., Schwantes, R. H., Bates, K. H., Jacob, D. J., Fis-
cher, E. V., Hornbrook, R. S., Hills, A. J., Emmons, L. K., Pan, L. L.,
Honomichl, S., Tilmes, S., Lamarque, J.-F., Yang, M., Marandino, C. A.,
Saltzman, E. S., Bruyn, W., Kameyama, S., Tanimoto, H., Omori, Y.,
Hall, S. R., Ullmann, K., Ryerson, T. B., Thompson, C. R., Peischl, J.,
Daube, B. C., Commane, R., McKain, K., Sweeney, C., Thames, A. B.,
Miller, D. O., Brune, W. H., Diskin, G. S., DiGangi, J. P., and Wofsy,
S. C.: Global Atmospheric Budget of Acetone: Air-Sea Exchange and
the Contribution to Hydroxyl Radicals, Journal of Geophysical Research:
Atmospheres, 125, https://doi.org/10.1029/2020JD032553, 2020.

Williams, J. and Koppmann, R.: Volatile Organic Compounds in the At-
mosphere: An Overview, in: Volatile Organic Compounds in the Atmo-
sphere, edited by Koppmann, R., pp. 1–32, Blackwell Publishing Ltd,
Oxford, UK, https://doi.org/10.1002/9780470988657.ch1, 2007.

Yang, M., Blomquist, B. W., and Nightingale, P. D.: Air-Sea Exchange of
Methanol and Acetone during HiWinGS: Estimation of Air Phase, Water
Phase Gas Transfer Velocities, Journal of Geophysical Research: Oceans,
119, 7308–7323, https://doi.org/10.1002/2014JC010227, 2014.

Zhao, Y., Saunois, M., Bousquet, P., Lin, X., Berchet, A., Hegglin,
M. I., Canadell, J. G., Jackson, R. B., Hauglustaine, D. A., Szopa,
S., Stavert, A. R., Abraham, N. L., Archibald, A. T., Bekki, S.,
Deushi, M., Jöckel, P., Josse, B., Kinnison, D., Kirner, O., Marécal, V.,

O'Connor, F. M., Plummer, D. A., Revell, L. E., Rozanov, E., Stenke, A., Strode, S., Tilmes, S., Dlugokencky, E. J., and Zheng, B.: Inter-Model Comparison of Global Hydroxyl Radical (OH) Distributions and Their Impact on Atmospheric Methane over the 2000–2016 Period, Atmospheric Chemistry and Physics, 19, 13 701–13 723, https://doi.org/10.5194/acp-19-13701-2019, 2019.

Chapter 2

VOCs: atmospheric transport, lifetime and analysis tools

In situ VOC measurements provide important information to identify emission sources, study atmospheric chemistry and validate chemical transport models (CTMs). Here we will briefly review some of the physical and chemical mechanisms that impact local air quality (Sections 2.2, and 2.1) and a non-exhaustive list of methods to analyse this type of data (Sections 2.3.1, 2.3.2, and 2.3.3).

2.1   Atmospheric transport

In Section 1.2, we have discussed VOCs, from emission to deposition, focusing on chemical transformation in the atmosphere. However, when we want to study atmospheric composition at a specific site, transport becomes an important factor that should not be neglected. Measurement of a compound at a location is only possible if the compound is transported from the point of entry[1] in the atmosphere, to the measurement site before being lost[2]. In this section, we will briefly discuss the vertical structure of the atmosphere, general circulation patterns, and transport in the planetary boundary layer.

---

[1] Entry either due to direct emission or secondary production in the atmosphere
[2] Lost either due to deposition or transformation to other atmospheric constituents.
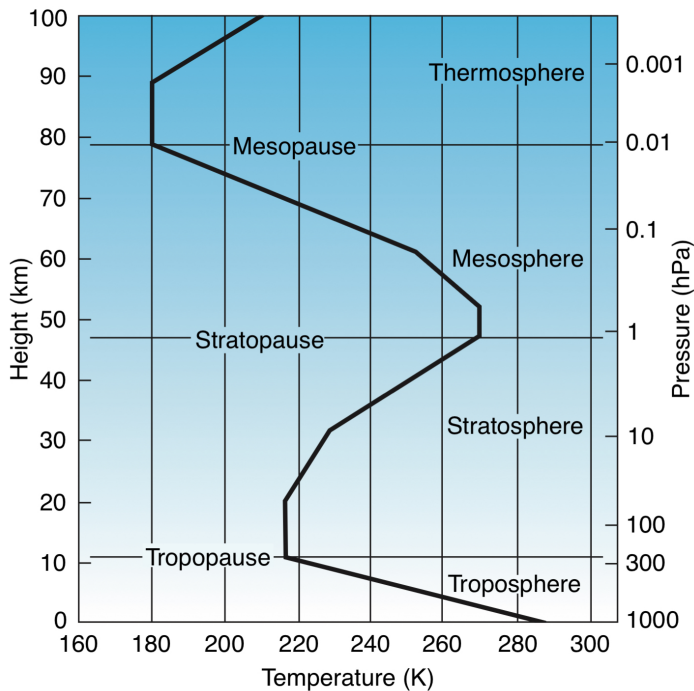
Figure 2.1: Representation of the U.S. standard atmosphere, temperature profile in the atmosphere at mid-latitudes. Figure from Wallace and Hobbs (2006).

2.1.1 Structure of the atmosphere

The atmosphere is divided in four vertical layers based on the average temperature profile shown in Figure 2.1. The lowest part of the atmosphere is called the troposphere. It accounts for $\sim$ 85 % of the atmospheric mass and is characterised in general by a monotonically decreasing temperature profile with an average temperature lapse rate ($-\frac{\mathrm{d}T}{\mathrm{d}z}$) of 6.5 K km^{-1} down to $\sim$ -50 °C (midlatitudes) and -80 °C (tropics) at the top. The vertical structure of the troposphere can be subdivided into the planetary boundary layer — near the surface — and the free troposphere — aloft — which will be discussed in more detail below. The top of the troposphere is called the tropopause and is located between 8 – 12 km altitude at the poles and up to 18 km at the equator. Above lies the stratosphere which is characterised by temperatures that increase with altitude and slow vertical mixing. The stratosphere extends to $\sim$ 50 km altitude. The temperature maximum at

the top of the stratosphere, i.e. the stratopause, is on average about -15 °C. The upper two layers of the atmosphere are the mesosphere and the thermosphere, separated by the mesopause (80 – 90 km altitude).

2.1.2   General circulation

The term general circulation is used to denote average wind patterns present on a global scale. At the equator, the planet emits less energy than it receives from the sun while at the poles the reverse is true. The energy received at the equator dissipates towards the poles through atmospheric transport and by oceanic circulations. Near the equator, hot air masses rise while at the poles cold and dense air masses subside. This transport is organised through three large circulation patterns in each hemisphere: the Hadley cells (equator – 30 ° latitude), the mid-latitude or Ferrel cells (30 ° latitude – 60 ° latitude), and the polar cells. The location where the surface winds of the Northern Hemisphere (NH) and the Southern Hemisphere (SH) Hadley cells converge is called the inter tropical convergence zone (ITCZ), a low-pressure belt[3] located near the equator. Its location varies according to the season and gives rise to the dry and wet seasons in tropical regions. During the boreal summer, i.e. summer in the NH, the ITCZ migrates northward. The inverse is true during austral summer, i.e. summer in the SH. The prevailing easterlies near the surface towards the ITCZ in the tropics are called trade winds (Figure 2.2). The trade winds are generally stronger during the winter season in the respective hemispheres.

Zonal transport at midlatitudes is relatively fast (1 – 2 weeks). Mixing of air within a hemisphere takes longer ($\sim$ 1 – 2 months). Interhemispheric mixing is organised through i) horizontal mixing in convective storm out-flows between the Hadley cells, the seasonal migration of the ITCZ and local breaking of the ITCZ caused by local circulations. As such, inter-hemispheric mixing is a slow process and takes about 1 year.

---

[3]Due the persistent rising of humid air masses at the equator, the ITCZ generally manifests itself as a cloud belt that wraps around the earth. This is also clear from the occurrence of rain at the location of the ITCZ in Figure 2.2.
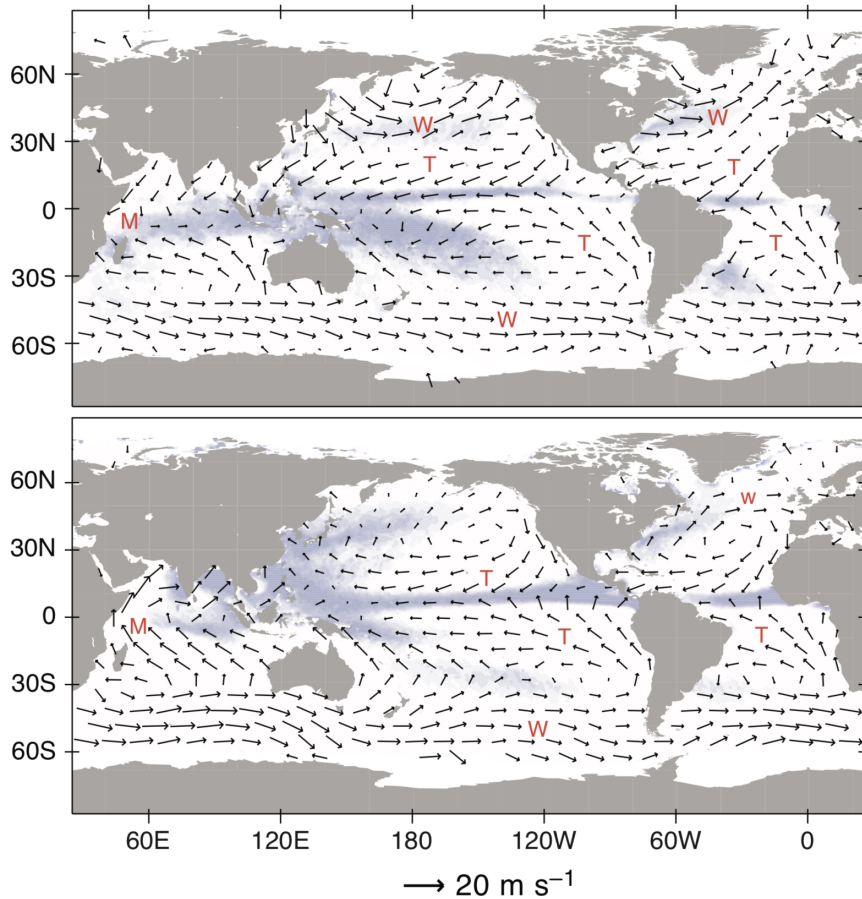
Figure 2.2: December-January-February (top) and June-July-August (bottom) average surface winds over the ocean based on satellite observations of capillary waves on the ocean surface. Major rain belts are shown as shaded areas. The letter 'W' denotes dominant westerly synoptic flows in the mid-latitude circulation, 'T' indicates regions with easterly trade winds at the surface associated with the Hadley cells. The letter 'M' shows regions where monsoon circulation patterns occur (not discussed). Figure from Wallace and Hobbs (2006).

2.1.3 The planetary boundary layer (PBL)

In this thesis, we are interested in observations in the lowest part of the atmosphere, i.e. the troposphere. The troposphere can be split up into two distinct layers. The lower part of the troposphere consists of a layer which is directly influenced by the surface and is called the planetary boundary layer (PBL). Above it lies the free troposphere (FT) which is free of direct perturbations by the surface. Winds in the FT may differ greatly from the winds in the PBL. Friction with the surface and mesoscale transport affects winds in the PBL which is characterised by high turbulence. Vertical mixing in the PBL is organised by turbulence at different scales and is by definition a fast process. Due to the discrete boundary between the PBL and the FT, exchange between both is generally slow. As such, pollutants, heat and humidity are trapped within the PBL. The vertical extent of the PBL thus directly affects the concentration of chemical species. Vertical mixing in the FT is, in general, also a slow process due to the low turbulence in the largely laminar wind flows. Typically, tracers released at the surface reach the top of the PBL within a few hours and only reach the tropopause after about 3 months. Notable exceptions on this slow vertical mixing in the FT are induced by strong convective activity in the tropics (e.g., Héron et al., 2020) and tropical cyclones which completely mix the boundary layer into the free troposphere. Other fast vertical transport may occur due to large heat sources at the surface by intensive biomass burning events (e.g., Khaykin et al., 2020), or by explosive volcanic eruptions (e.g., Vernier et al., 2011) where emissions from the surface have been observed to be mixed even into the stratosphere for extreme cases (e.g., Khaykin et al., 2020; Vernier et al., 2011).

Turbulence in the PBL

The PBL is characterised by turbulence which is generated either mechanically, thermally, or inertially. Mechanically induced turbulence originates from shear in the mean wind[4]. Thermally induced turbulence, also called convective turbulence or free convection, is caused by warm air that rises and which is balanced by sinking cold air. Inertial turbulence is generated

---

[4]Wind shear can be caused by frictional drag from the surface, or away from the surface which is referred to as free shear.

by wind-shear at the edges of turbulence[5] loops, also called eddies. As such, turbulent swirls in the atmosphere cause smaller scale eddies at their edge which cascades down to the millimeter scale before their energy dissipates into internal energy by molecular viscosity. The kinetic energy from turbulence is called turbulent kinetic energy (TKE) and is not a conserved quantity in the atmosphere due to its dissipation on the smallest scale. From the dissipation of energy following inertial turbulence, it is clear that, in order for turbulence to exists, there must be a continuous source of TKE either from free convection or wind shear.

PBL variability and impact on VOC measurements

Generation of TKE by buoyancy is proportional to the surface sensible heat flux. During clear sky conditions, shortwave solar radiation incident on the land surface[6] is partly absorbed causing it to heat up. Part of the absorbed radiation is emitted back into the atmosphere in the form of longwave radiation which heats up the atmosphere. During the day, the surface will serve as a source of heat providing energy to the atmosphere which manifests itself in free convection. In the morning, the PBL is shallow, free convection results in entrainment of overlying air masses and the PBL is growing. At night, this process halts, the surface cools down rapidly and turbulence is only generated by wind shear. As the PBL traps pollutants emitted by the surface, a shallow PBL will contain high concentrations of pollutants while a deep boundary layer will disperse the pollutants over a large volume resulting in low concentrations.

Diurnal circulation patterns in the PBL

Heterogeneous heating of the atmosphere due to changes in terrain may induce thermally driven diurnal circulation patterns. These occur along coastlines but also in mountainous terrain.

On a mountain slope in clear weather, heating of overlying air masses by the surface creates a layer with lower density than air masses at the same

---

[5]Note that turbulence is defined as random fluctuations on the mean winds. As such, the shear arising from turbulent swirls is not categorised as 'mechanically induced'.

[6]Over sea the heat capacity of the surface is much larger which can cause the surface to be cooler than the atmosphere during the day and vise versa during the night.
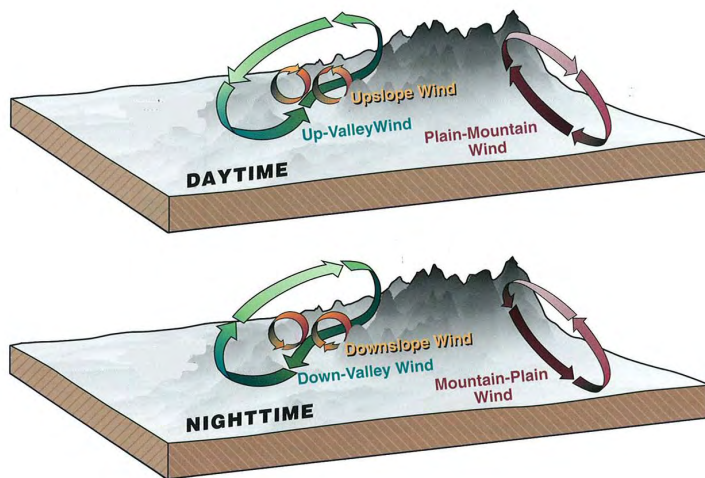
Figure 2.3: Schematic illustration of the mesoscale mountain circulation phenomena. During the daytime, winds flow along the pressure gradient, induced due heating from the surface, towards higher altitudes while at night, dense air cooled by the surface subsides to lower altitudes. Figure taken from Whiteman (2000).
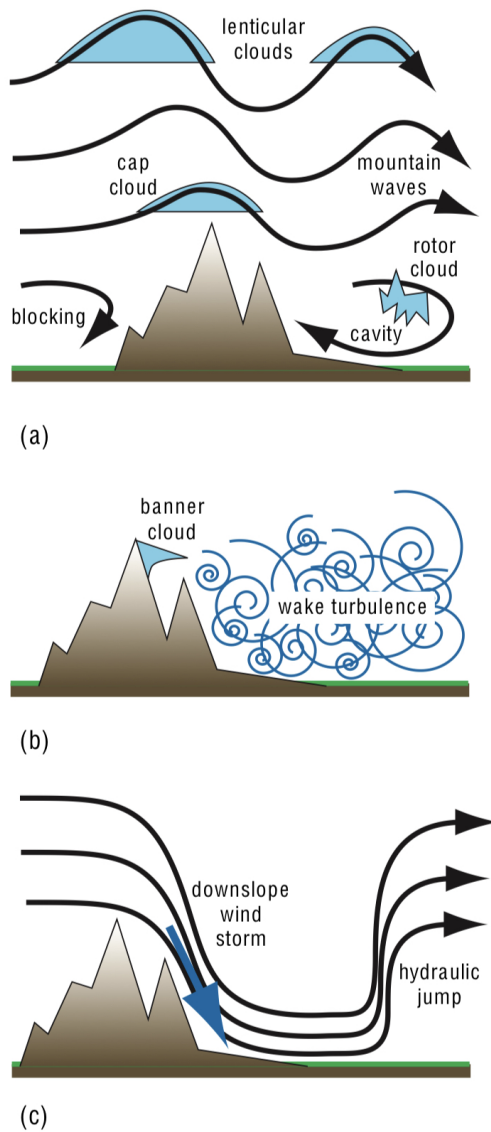
Figure 2.4: Schematic representation of the impact of complex terrain on a synoptic flow. The mountain can block low level winds or force strong winds over the mountian crest and give rise to mountain waves which may be accompanied by the formation of lenticular clouds. On the lee side, cavity circulation, wake turbulence, downslope wind storm and hydraulic jumps can be induced by the mountain. Figure taken from Wallace and Hobbs (2006).

altitude. This creates a pressure gradient normal to the surface which conducts the heated air masses along the mountainside to higher altitudes. This upslope or anabatic flow is closed by return circulations over the valley below. At night, the mountain side cools the overlying air which sinks to lower altitudes giving rise to downslope or katabatic winds. These winds are closed by rising air masses in the valley below which may diffuse horizontally at higher altitude. A schematic representation of these mountain phenomena is shown in Figure 2.3.

The coastline constitutes a discrete border between land and sea. During the day, landmass is heated faster than the ocean giving rise to low-density air masses near the surface which rise up leaving behind a low pressure system creating a pressure gradient parallel to the surface which makes cool air over the ocean flow land-inward. This is called the sea-breeze. At night, this process is inverted. Due to the fast cooling of the land surface and the relatively warmer ocean, air masses over the ocean are warmer compared to those over land. These mesoscale circulation patterns are often suppressed by stronger, synoptic scale flows. However, complex terrain can still exert a strong influence on synoptic scale transport by blocking the flow and give rise to a range of local weather phenomena which are visualised in Figure 2.4.

2.2   Chemical kinetics and atmospheric lifetime

We have seen that trace species are emitted into the atmosphere, VOC transform during transport to form other compounds (possible source and sink) or nucleate to form SOA, and ultimately they are removed from the atmosphere by deposition.

We can calculate the average atmospheric lifetime of a VOC using chemical kinetics. We will focus here on first-order (Reaction 2.1) and second-order (Reaction 2.2) chemical reactions.

$$A \longrightarrow B + C \qquad (2.1)$$
$$A + B \longrightarrow C + D \qquad (2.2)$$

Examples of first-order reactions in the atmosphere are photolysis of VOC (Reaction 2.3) or radioactive decay (not considered). In photolysis re-

actions, matter interacts with light, which leads to dissociation of the molecule. This reaction is represented by:

$$A + h\nu \longrightarrow B + C, \tag{2.3}$$

where $h\nu$[7] is the photon energy. In the presence of light, Reaction 2.3 will take place with rate:

$$\frac{\mathrm{d}[A]}{\mathrm{d}t} = -j[A], \tag{2.4}$$

where $[A]$ is the reactant concentration (expressed in molecules cm^{-3}) and j is the photolysis rate coefficient (in units s^{-1}). The average time that a molecule of A resides in the atmosphere before being lost from photolysis (τ) is calculated by:

$$\tau = \frac{[A]}{j[A]} = \frac{1}{j}. \tag{2.5}$$

For bimolecular reactions (Reaction 2.2), the loss rate and average atmospheric lifetime of compound A due to reaction with B (τ_B) is giving by:

$$\frac{\mathrm{d}[A]}{\mathrm{d}t} = -k[A][B], \tag{2.6}$$

$$\tau_B = \frac{1}{k[B]}, \tag{2.7}$$

where k is the reaction rate coefficient (in molecules $\mathrm{cm}^{-3}\ \mathrm{s}^{-1}$).

By applying this to the oxidation reactions from VOCs interacting with OH, NO_3, or O_3 (Section 1.2.2), we can calculate the lifetime of VOCs with respect to the different chemical sinks, given an average concentration of the respective reactants.

---

[7]Here, ν is the frequency of light while h is the Planck constant. The frequency is related to the wavelength (λ) by $\nu = \frac{c}{\lambda}$, where c is the speed of light. In general, the photodissociation of a molecule by light depends on the energy of the incident light.

$$\text{VOC} + \text{OH} \longrightarrow \dots,$$
$$\text{VOC} + \text{NO}_3 \longrightarrow \dots,$$
$$\text{VOC} + \text{O}_3 \longrightarrow \dots,$$
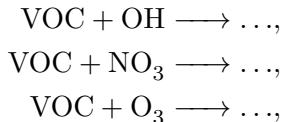
The average atmospheric lifetime is calculated by combining the different loss processes:

$$\frac{\mathrm{d}[\text{VOC}]}{\mathrm{d}t} = -[\text{VOC}] \times \left(k_{\text{OH}}[OH] + k_{\text{NO}_3}[NO_3] + k_{\text{O}_3}[O_3] \right), \quad (2.8)$$

and Equation 2.5, to obtain

$$\tau = \frac{[\text{VOC}]}{[\text{VOC}] \times \left(k_{\text{OH}}[OH] + k_{\text{NO}_3}[NO_3] + k_{\text{O}_3}[O_3] \right)}, \quad (2.9)$$

$$\tau^{-1} = k_{\text{OH}}[OH] + k_{\text{NO}_3}[NO_3] + k_{\text{O}_3}[O_3], \quad (2.10)$$

$$\tau^{-1} = \tau_{\text{OH}}^{-1} + \tau_{\text{NO}_3}^{-1} + \tau_{\text{O}_3}^{-1}. \quad (2.11)$$

As expected, the shortest lifetime will be the most important factor in determining the average atmospheric lifetime. The combination of atmospheric lifetime together with the average mixing in the atmosphere discussed in the previous section allows us to determine how far away from the source we can expect to measure atmospheric compounds. This is shown in Figure 2.5

2.3   Analysing atmospheric composition data

2.3.1   Positive matrix factorisation

Statistical models can be employed to search for co-varying signals in a data set in order to isolate chemical profiles of potential sources impacting the measured atmospheric composition. The positive matrix factorisation
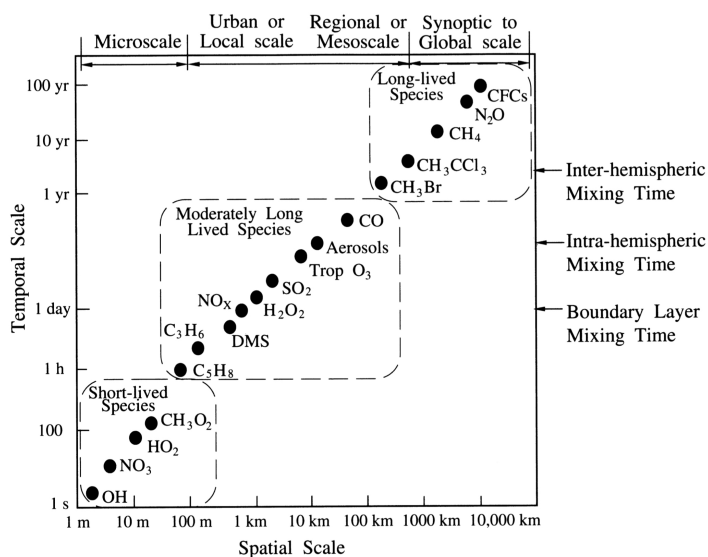
Figure 2.5: Relation between the average atmospheric lifetime of atmospheric constituents and the spatial scale to which they are mixed in the atmosphere. Short-lived species will be consumed in quickly in the atmosphere and are not able to traverse large distances. Long lived species on the other hand can get mixed on a global scale. Figure from Seinfeld and Pandis (2016).

(PMF) algorithm is a popular tool using this principle which has application for the analysis of the chemical composition of water (e.g., Jiang et al., 2019), aerosols (e.g., Petit et al., 2014), or the atmosphere (e.g., Rocco et al., 2020) in order to isolate chemical signatures of sources which impact the dataset. The general idea is that each source has its unique chemical profile which contributes partially to the chemical composition of the medium under study. In Chapter 1, Section 1.2.1, we have seen that biogenic emissions are the dominant source of C_5H_8 in the atmosphere but the biosphere also emits oxygenated species such as alcohols, aldehydes, etc. Anthropogenic emissions on the other hand are the primary source of aromatic compounds, e.g. C_6H_6, in the atmosphere but also include oxygenated species. The PMF algorithm tries to pick up on a correspondence between C_5H_8 and OVOCs as well as between C_6H_6 and OVOCs. As both sources have distinct emissions patterns, both in time and space, they will have a different temporal impact on the data. PMF will exploit these differences and attribute a fraction of OVOC mass to each source. PMF is a robust method to identify the chemical signature of different sources which impact on the data set. However, due to the robustness and simplicity of the method, some subtleties are lost in this analysis. As we have seen previously, VOCs are reactive compounds which are oxidized and deposited during transport. The ageing of a species depends strongly on the chemical and physical properties of the chemical compound. This distinction is not taken into account by the PMF algorithm. Instead, the transformation of air masses during transport is represented as a linear combination between different source factors. Another difficulty is the numerical nature of the PMF analysis. This kind of analysis can never stand on its own but rather serves to support a more elaborate study which checks the results of the PMF by either using alternative methods which support the outcome or by going back into the field to measure the chemical profile of specific sources in the atmosphere.

A description of the mathematical principle behind the PMF algorithm is detailed in Chapter 7.

2.3.2   Lagrangian transport models

Lagrangian transport modelling in the atmosphere refers to models which follow the motion of an air mass. The earliest Lagrangian models assumed isobaric or isentropic trajectories (Danielsen, 1961). The hypothesis that

the potential temperature is conserved along a Lagrangian trajectory is accurate at large scale, and outside the PBL. Hence, only 2-D isentropic wind fields were needed to calculate a Lagrangian trajectory starting at a given potential temperature. Owing to the computation capability of computers in the 60s and 70s, the adiabatic assumption was a necessity. Later, Haagenson et al. (1987) showed that kinematic trajectories with 3-D wind fields were needed to better represent the trajectories within the PBL. In particular, Stohl and Wotawa (1995) presented a new method to describe the Lagrangian transport in the PBL with a single trajectory, which was integrated in the FLEXTRA Lagrangian model (Stohl et al., 1995). This type of transport modelling considers air masses, also called air parcels, as a single trajectory which is not subject to turbulence. As such, they are not suited for simulating transport in the PBL, which is characterised by turbulence. A simple way to dilute the parcels due to turbulence is by using a Lagrangian puff model (e.g. CALPUFF, (Scire et al., 2000)), which considers Gaussian diffusion of the air parcel in 3-D space to represent turbulent diffusion. This type of models perform best when mean wind fields and turbulence are relatively constant throughout their trajectory and thus are not ideal to simulate transport in the lower troposphere. Lagrangian particle dispersion models (LPDMs), however, represent an air mass by an large number of infinitesimally small parcels or particles which are transported along average wind fields with a turbulent term added to it (e.g. FLEXPART (Stohl et al., 2005)).

LPDMs

Offline LPDMs are efficient tools to model atmospheric transport of aerosols or gases from a source (forward simulation) or towards a receptor site (backward simulation). They can be operated on global and regional scales and are used in hazard preparedness exercises, identification and evaluation of surface or point emissions, study of atmospheric cycles, etc. LPDMs are driven by numerical weather prediction (NWP) data from either research models, e.g. the weather research and forecasting (WRF) model or the mesoscale non-hydrostatic (Meso-NH) model, or operational forecasting models, e.g. AROME[8]. The release of a tracer in the atmosphere is represented by a number of air parcels moving in the ambient flow along mean wind fields, and undergoing subgrid scale processes such as turbu-

---

[8]applications de la recherche à l'opérationnel à méso-echelle

lence, deep convection, etc. Each air parcel carries a certain amount of mass which can be lost during transport due to i) radioactive decay, ii) deposition processes, or iii) chemical losses (e.g. oxidation by OH). In contrast to Eulerian models[9], LPDMs track the location of a gas in a moving frame of reference that follows the center of mass of the air parcel under investigation. As a result, narrow plumes are well represented in this type of models. A disadvantage of this formalism however is the sensitivity to both temporal and spatial interpolations to the local 4-D position of air masses that may not realistically represent reality (Stohl et al., 1995). This can be mediated by using average rather than instantaneous meteorological fields from the NWP model (Brioude et al., 2012). Plume dispersion in LPDMs is handled by averaging kernels, spreading the mass of an air parcel over a certain volume, and particle splitting algorithms. Examples of LPDMs are the stochastic time-inverted transport model (STILT), and the FLEXible PARTicle dispersion model (FLEXPART), described by Lin et al. (2003) and Pisso et al. (2019) respectively.

Turbulence in LPDMs

Turbulence manifests itself as instantaneous chaotic temporal fluctuations on an average taken over a longer period of time. Let us consider the instantaneous velocity in a 1-D system at time t, at location z to be $w(t, z)$. We can deconstruct this velocity in its average value taken over a longer period of time, $\bar{w}(t, z)$, and its instantaneous deviation of this average, $w'(t, z)$:

$$w(t, z) = \bar{w}(t, z) + w'(t, z). \tag{2.12}$$

As the average wind component, $\bar{w}(t, z)$, is obtained by linear interpolation of the wind fields obtained from the Eulerian model driving the LPDM, we will focus on the fluctuating contribution, $w'(t, z)$, i.e. the turbulent component of the velocity vector. We use a Markovian process to describe

---

[9]Eulerian models represent the atmosphere as a stack of volumes which exchange mass among each other. The disadvantage of these models lies in the instant well-mixed tracer over the new volume when mass is exchanged in the grid. This formalism is less suited for transport modeling but is effective to model chemical interactions in the atmosphere as each volume acts as chemical reactor in which gasses interact.

its increment at time t, dw_t:

$$dw_t = a(t, z, w_t)dt + b(t, z, w_t)dW, \qquad (2.13)$$

where dW is the incremental component of a Wiener process with mean zero and variance dt. This stochastic differential equation needs to be solved taking into account physical constraints and making assumptions (e.g., Thomson, 1987). If we neglect the density variation in the atmosphere and assume the probability distribution of $w'(t, z)$ to be Gaussian[10], the resulting Langevin equation is:

$$dw_t = -\frac{w_t}{\tau}dt + \sqrt{\frac{2\sigma^2}{\tau}}dW, \qquad (2.14)$$

where σ is the standard deviation of the Gaussian probability distribution on the turbulent velocity and τ is the Lagrangian timescale(Thomson, 1987). Corrective terms to this Lagrangian equation have been introduced by Stohl and Thomson (1999) and McNider et al. (1988) to correct for non-homogeneous atmospheric density and turbulence

$$dw_t = -\frac{w_t}{\tau}dt + \frac{\sigma^2}{\rho}\frac{\partial \rho}{\partial z}dt + \frac{\partial \sigma^2}{\partial z}dt + \sqrt{\frac{2\sigma^2}{\tau}}dW, \qquad (2.15)$$

where ρ is the atmospheric density. Both the density and drift corrections (respectively the third and fourth term) have been taken into account for simulating transport using the FLEXPART model (Stohl et al., 2005). The STILT model however uses the Thomson reflection–transmission formalism (Thomson et al., 1997) with a density correction taken into account and thus does not require the corrective terms.

Receptor-oriented modelling

Using the LPDM in backward mode is particularly interesting when the number of sources is larger than the number of receptors. Instead of tracing transport of pollution, as is done in forward modelling, the backward model determines which sources have an influence on the air-masses observed at the receptor site. Some of the differences in scientific use of backward vs forward modelling is illustrated in Table 2.1. Instead of concentrations of tracers, the backward model provides users with residence times (RTs), i.e.

---

[10]This is in principle only valid for neutral and stable boundary layer conditions.
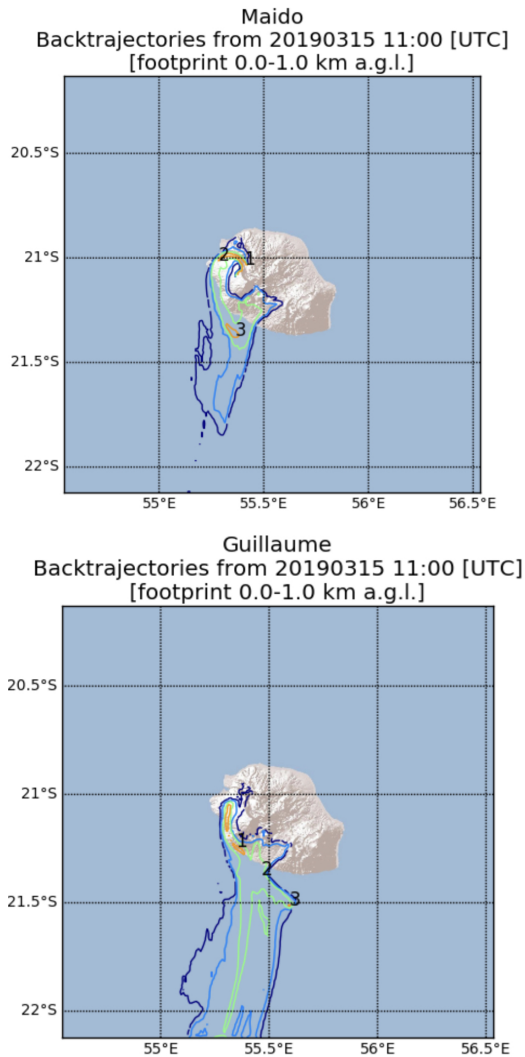
Figure 2.6: FLEXPART-AROME footprint maps generated for the BIO-MAIDO campaign at two different receptor sites (Maïdo and Guillaume). The color scale is qualitative and indicates the impact of emissions on a measurement on the site. Dark blue (red) regions have the lowest (highest) impact on measurements at the receptor site. Emissions of a point source of a lower impact level should be 10 times stronger than a point source in a higher impact region to have the same effect on measurements at the receptor site. The number X (1, 2, or 3) correspond to the location of the center of mass on the footprint map X hours before the air-parcels were initialised in the model.

Forward	Backward
Where does the air go?	Where does the air come from?
What is the downwind impact of air coming from a location of interest (source)?	What are the upwind influences on the location of interest (receptor)?
Whereto are tracers transported?	What are the source regions of tracers?
How much is the concentration of a passive tracer at downwind locations affected by a unit emission of the source?	How strong is the sensitivity of the receptor to a particular upwind source region?

Table 2.1: Questions addressed by using LPDMs in backward or forward modes. From (Lin, 2013).

the accumulated time the particles are located in a certain grid cell. The RT is proportional to the impact of the emission rate at a certain point on the concentration at the receptor site. The theory of backward modelling is explained in detail by Seibert and Frank (2004). We will be using back-trajectories to analyse data and evaluate emission rates in Chapter 3 where you can find the main mathematical principles of the method.

As a simple example, footprints obtained from back-trajectories generated using FLEXPART-AROME in the framework of the BIO-MAÏDO campaign (March-April 2019) are shown in Figure 2.6. The footprints, i.e. the source-receptor relationship (SRR) in a layer located near the surface, indicate the impact of surface emissions on the concentrations measured at the receptor site. The numbers on the figure are located on the center of mass of the first three hours before they were initialised at the receptor site.

2.3.3 Chemical transport models

Offline chemical transport models (CTMs) are important tools in atmospheric sciences which are used to understand chemical processes, study observations, and make projections of air quality. They can be operated from local to global scales and incorporate emissions, transport, chemical
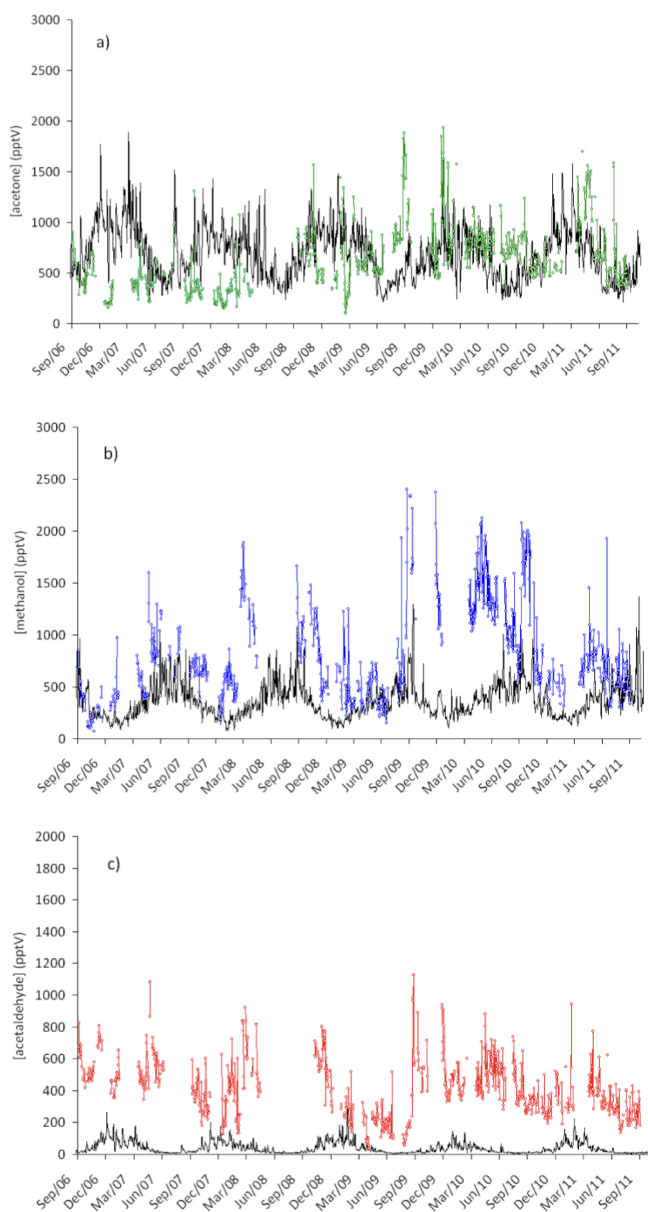
Figure 2.7: Multi-annual comparison between daily observations at the Cape Verde atmospheric observatory (color) and the CAM-chem model (black) of CH_3COCH_3 (top), CH_3OH (middle), and CH_3CHO (bottom) from a study in 2012 (Read et al., 2012).

and physical processes in the atmosphere, and deposition in order to describe the atmospheric composition. CTMs are built using the latest knowledge and constrained using both remote sensing and in situ data sets. Due to a paucity in data from the SH and tropics, CTMs are poorly constrained in these regions resulting in larger divergences between model predictions and data.

As an example, we demonstrate how models have been shown to misrepresent concentrations of ubiquitous OVOCs in specific regions of Earth's atmosphere. Multi-annual observations at the Cape Verde atmospheric observatory of methanol (CH_3OH), acetaldehyde (CH_3CHO), and acetone (CH_3COCH_3) showed large inconsistencies between model and observations in remote tropical Atlantic air masses (Figure 2.7). Concentrations of CH_3CHO were originally underestimated by a factor of 10–40 (Read et al., 2012). However, the introduction of a two-way ocean–atmosphere parametrisation based on seawater measurements made in the Atlantic Ocean reduced the discrepancy to a factor of 3 (Read et al., 2012). The annual average concentrations of CH_3COCH_3 only differ by 21% from the originally modelled concentrations but bad seasonal differences resulted in an underestimation in autumn (factor of 2) and overestimation in winter (Read et al., 2012). Including the two-way interaction between ocean and atmosphere further increased the discrepancy observed in autumn (Read et al., 2012). Concentrations of CH_3OH were originally underestimated by a factor of 2–4, but the inclusion of the two-way ocean–atmosphere interactions resulted in satisfactory agreement between model and measurements (Read et al., 2012). Millet et al. (2010) showed a ubiquitous underestimation of acetaldehyde concentrations in the free troposphere (factor 2–30 depending on location and altitude) and found that the modelled vertical gradient is too steep compared to observations. Production of CH_3CHO in the remote troposphere by photolysis of organic aerosols strongly reduced the discrepancy but was insufficient to explain the high concentrations in the remote FT (Wang et al., 2019). A recent study showed that the CAM-chem model overestimates CH_3COCH_3 in the upper troposphere over the SH and argues that this is unlikely due to photo-chemistry or transport but rather originates from the poor representation of ocean–atmosphere exchanges (Wang et al., 2020).

Bibliography

Brioude, J., Angevine, W. M., McKeen, S. A., and Hsie, E.-Y.: Numerical Uncertainty at Mesoscale in a Lagrangian Model in Complex Terrain, Geoscientific Model Development, 5, 1127–1136, https://doi.org/10.5194/gmd-5-1127-2012, 2012.

Danielsen, E. F.: Trajectories: Isobaric, Isentropic and Actual, Journal of Atmospheric Sciences, 18, 479 – 486, https://doi.org/10.1175/1520-0469(1961)018<0479:TIIAA>2.0.CO;2, 1961.

Haagenson, P. L., Kuo, Y.-H., Syumanich, M., and Seaman, N. L.: Tracer Verification of Trajectory Models, Journal of Applied Meteorology and Climatology, 26, 410 – 426, https://doi.org/10.1175/1520-0450(1987)026<0410:TVOTM>2.0.CO;2, 1987.

Héron, D., Evan, S., Brioude, J., Rosenlof, K., Posny, F., Metzger, J.-M., and Cammas, J.-P.: Impact of Convection on the Upper-Tropospheric Composition (Water Vapor and Ozone) over a Subtropical Site (Réunion Island; 21.1° S, 55.5° E) in the Indian Ocean, Atmospheric Chemistry and Physics, 20, 8611–8626, https://doi.org/10.5194/acp-20-8611-2020, 2020.

Jiang, J., Khan, A. U., Shi, B., Tang, S., and Khan, J.: Application of Positive Matrix Factorization to Identify Potential Sources of Water Quality Deterioration of Huaihe River, China, Applied Water Science, 9, 63, https://doi.org/10.1007/s13201-019-0938-4, 2019.

Khaykin, S., Legras, B., Bucci, S., Sellitto, P., Isaksen, L., Tencé, F., Bekki, S., Bourassa, A., Rieger, L., Zawada, D., Jumelet, J., and Godin-Beekmann, S.: The 2019/20 Australian Wildfires Generated a Persistent Smoke-Charged Vortex Rising up to 35 Km Altitude, Communications Earth & Environment, 1, 22, https://doi.org/10.1038/s43247-020-00022-5, 2020.

Lin, J. C.: Lagrangian Modeling of the Atmosphre: An Introduction, in: Geophysical Monograph Series, edited by Lin, J., Brunner, D., Gerbig, C., Stohl, A., Luhar, A., and Webley, P., pp. 1–11, American Geophysical Union, Washington, D. C., https://doi.org/10.1029/2012GM001376, 2013.

Lin, J. C., Gerbig, C., Wofsy, S. C., Andrews, A. E., Daube, B. C., Davis, K. J., and Grainger, C. A.: A Near-Field Tool for Simulating the Upstream Influence of Atmospheric Observations: The Stochastic Time-Inverted Lagrangian Transport (STILT) Model, Journal of Geophysical Research: Atmospheres, 108, https://doi.org/10.1029/2002JD003161, 2003.

McNider, R. T., Moran, M. D., and Pielke, R. A.: Influence of Diurnal and Inertial Boundary-Layer Oscillations on Long-Range Dispersion, Atmospheric Environment (1967), 22, 2445–2462, https://doi.org/10.1016/0004-6981(88)90476-3, 1988.

Millet, D. B., Guenther, A., Siegel, D. A., Nelson, N. B., Singh, H. B., de Gouw, J. A., Warneke, C., Williams, J., Eerdekens, G., Sinha, V., Karl, T., Flocke, F., Apel, E., Riemer, D. D., Palmer, P. I., and Barkley, M.: Global Atmospheric Budget of Acetaldehyde: 3-D Model Analysis and Constraints from in-Situ and Satellite Observations, Atmospheric Chemistry and Physics, 10, 3405–3425, https://doi.org/10.5194/acp-10-3405-2010, 2010.

Petit, J.-E., Favez, O., Sciare, J., Canonaco, F., Croteau, P., Močnik, G., Jayne, J., Worsnop, D., and Leoz-Garziandia, E.: Submicron Aerosol Source Apportionment of Wintertime Pollution in Paris, France by Double Positive Matrix Factorization (PMF<Sup>2</Sup>) Using an Aerosol Chemical Speciation Monitor (ACSM) and a Multi-Wavelength Aethalometer, Atmospheric Chemistry and Physics, 14, 13 773–13 787, https://doi.org/10.5194/acp-14-13773-2014, 2014.

Pisso, I., Sollum, E., Grythe, H., Kristiansen, N. I., Cassiani, M., Eckhardt, S., Arnold, D., Morton, D., Thompson, R. L., Groot Zwaaftink, C. D., Evangeliou, N., Sodemann, H., Haimberger, L., Henne, S., Brunner, D., Burkhart, J. F., Fouilloux, A., Brioude, J., Philipp, A., Seibert, P., and Stohl, A.: The Lagrangian Particle Dispersion Model FLEXPART Version 10.4, Geoscientific Model Development, 12, 4955–4997, https://doi.org/10.5194/gmd-12-4955-2019, 2019.

Read, K. A., Carpenter, L. J., Arnold, S. R., Beale, R., Nightingale, P. D., Hopkins, J. R., Lewis, A. C., Lee, J. D., Mendes, L., and Pickering, S. J.: Multiannual Observations of Acetone, Methanol, and Acetaldehyde in Remote Tropical Atlantic Air: Implications for Atmospheric OVOC Budgets and Oxidative Capacity, Environmental Science & Technology, 46, 11 028–11 039, https://doi.org/10.1021/es302082p, 2012.

Rocco, M., Colomb, A., Baray, J.-L., Amelynck, C., Verreyken, B., Borbon, A., Pichon, J.-M., Bouvier, L., Schoon, N., Gros, V., Sarda-Esteve, R., Tulet, P., Metzger, J.-M., Duflot, V., Guadagno, C., Peris, G., and Brioude, J.: Analysis of Volatile Organic Compounds during the OCTAVE Campaign: Sources and Distributions of Formaldehyde on Reunion Island, Atmosphere, 11, 140, https://doi.org/10.3390/atmos11020140, 2020.

Scire, J. S., Strimaitis, D. G., Yamartino, R. J., et al.: A user's guide for the CALPUFF dispersion model, Earth Tech, Inc, 521, 1–521, 2000.

Seibert, P. and Frank, A.: Source-Receptor Matrix Calculation with a Lagrangian Particle Dispersion Model in Backward Mode, Atmospheric Chemistry and Physics, 4, 51–63, https://doi.org/10.5194/acp-4-51-2004, 2004.

Seinfeld, J. H. and Pandis, S. N.: Atmospheric Chemistry and Physics: From Air Pollution to Climate Change, John Wiley & Sons, Hoboken, New Jersey, third edition edn., 2016.

Stohl, A. and Thomson, D. J.: A Density Correction for Lagrangian Particle Dispersion Models, Boundary-Layer Meteorology, 90, 155–167, https://doi.org/10.1023/A:1001741110696, 1999.

Stohl, A. and Wotawa, G.: A Method for Computing Single Trajectories Representing Boundary Layer Transport, Atmospheric Environment, 29, 3235–3238, https://doi.org/10.1016/1352-2310(95)00259-2, 1995.

Stohl, A., Wotawa, G., Seibert, P., and Kromp-Kolb, H.: Interpolation Errors in Wind Fields as a Function of Spatial and Temporal Resolution and Their Impact on Different Types of Kinematic Trajectories, Journal of Applied Meteorology, 34, 2149–2165, https://doi.org/10.1175/1520-0450(1995)034<2149:IEIWFA>2.0.CO;2, 1995.

Stohl, A., Forster, C., Frank, A., Seibert, P., and Wotawa, G.: Technical Note: The Lagrangian Particle Dispersion Model FLEXPART Version 6.2, Atmospheric Chemistry and Physics, 5, 2461–2474, https://doi.org/10.5194/acp-5-2461-2005, 2005.

Thomson, D. J.: Criteria for the Selection of Stochastic Models of Particle Trajectories in Turbulent Flows, Journal of Fluid Mechanics, 180, 529–556, https://doi.org/10.1017/S0022112087001940, 1987.

Thomson, D. J., Physick, W. L., and Maryon, R. H.: Treatment of Interfaces in Random Walk Dispersion Models, Journal of Applied Meteorology, 36, 1284–1295, https://doi.org/10.1175/1520-0450(1997)036<1284: TOIIRW>2.0.CO;2, 1997.

Vernier, J.-P., Thomason, L. W., Pommereau, J.-P., Bourassa, A., Pelon, J., Garnier, A., Hauchecorne, A., Blanot, L., Trepte, C., Degenstein, D., and Vargas, F.: Major Influence of Tropical Volcanic Eruptions on the Stratospheric Aerosol Layer during the Last Decade: VOLCANIC INFLUENCE AERO STRATO, Geophysical Research Letters, 38, n/a–n/a, https://doi.org/10.1029/2011GL047563, 2011.

Wallace, J. M. and Hobbs, P. V.: Atmospheric Science: An Introductory Survey, no. v. 92 in International Geophysics Series, Elsevier Academic Press, Amsterdam ; Boston, 2nd ed edn., 2006.

Wang, S., Hornbrook, R. S., Hills, A., Emmons, L. K., Tilmes, S., Lamarque, J.-F., Jimenez, J. L., Campuzano-Jost, P., Nault, B. A., Crounse, J. D., Wennberg, P. O., Kim, M., Allen, H., Ryerson, T. B., Thompson, C. R., Peischl, J., Moore, F., Nance, D., Hall, B., Elkins, J., Tanner, D., Huey, L. G., Hall, S. R., Ullmann, K., Orlando, J. J., Tyndall, G. S., Flocke, F. M., Ray, E., Hanisco, T. F., Wolfe, G. M., St. Clair, J., Commane, R., Daube, B., Barletta, B., Blake, D. R., Weinzierl, B., Dollner, M., Conley, A., Vitt, F., Wofsy, S. C., Riemer, D. D., and Apel, E. C.: Atmospheric Acetaldehyde: Importance of Air-Sea Exchange and a Missing Source in the Remote Troposphere, Geophysical Research Letters, 46, 5601–5613, https://doi.org/10.1029/2019GL082034, 2019.

Wang, S., Apel, E. C., Schwantes, R. H., Bates, K. H., Jacob, D. J., Fischer, E. V., Hornbrook, R. S., Hills, A. J., Emmons, L. K., Pan, L. L., Honomichl, S., Tilmes, S., Lamarque, J.-F., Yang, M., Marandino, C. A., Saltzman, E. S., Bruyn, W., Kameyama, S., Tanimoto, H., Omori, Y., Hall, S. R., Ullmann, K., Ryerson, T. B., Thompson, C. R., Peischl, J., Daube, B. C., Commane, R., McKain, K., Sweeney, C., Thames, A. B., Miller, D. O., Brune, W. H., Diskin, G. S., DiGangi, J. P., and Wofsy, S. C.: Global Atmospheric Budget of Acetone: Air-Sea Exchange and the Contribution to Hydroxyl Radicals, Journal of Geophysical Research: Atmospheres, 125, https://doi.org/10.1029/2020JD032553, 2020.

Whiteman, C. D.: Mountain Meteorology: Fundamentals and Applications, Oxford University Press, https://doi.org/10.1093/oso/9780195132717. 001.0001, 2000.

Chapter 3

Measuring in situ VOC concentrations in the atmosphere

Because of their vital role in tropospheric chemistry, VOC measurements are of interest in all atmospheric chemistry field campaigns aiming at an improved understanding of the atmospheric gas phase and aerosol composition, along with other reactive trace gases such as nitrogen oxides and ozone. Except in highly polluted areas, mixing ratios of VOCs in the atmosphere are generally very low (ppb or less) and therefore very sensitive techniques are required for their measurement. In atmospheric sciences only two in situ techniques are widely used to measure VOCs: sampling on adsorptive media followed by thermal desorption and gas chromatographic (GC) detection, and chemical ionization mass spectrometry techniques, of which proton-transfer-reaction mass-spectrometry (PTR-MS) is the most widely applied one.

3.1 Gas chromatography

GC is the most widely used VOC analysis technique in atmospheric chemistry and is usually preceded by dynamic VOC sampling on an adsorbent medium (e.g. TENAX for sampling of biogenic VOCs). The sampling time (20-30 minutes) determines the time resolution of the measurement. Sampling is generally followed by off-line thermal desorption and subsequent chromatographic separation after which mass spectrometric detec-
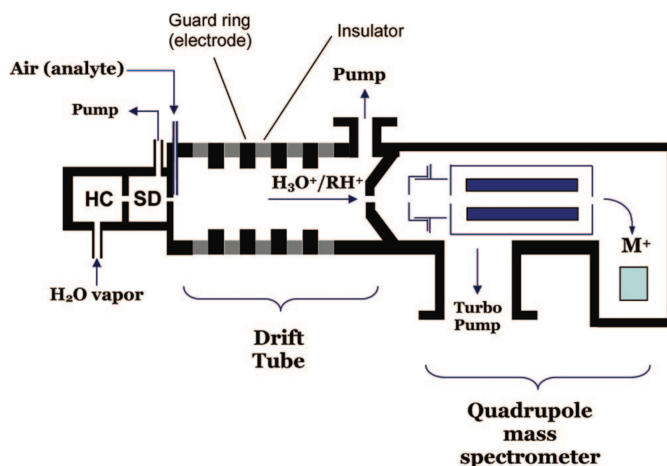
Figure 3.1: A schematic overview of a PTR-MS instrument with a quadrupole based mass spectrometer with an ion source (left), drift tube and a quadrupole mass spectrometer. HC: hollow cathode discharge ion source. SD: source drift region. Figure from (Blake et al., 2009).

tion (GC-MS) or flame ionization detection (GC-FID) is performed. Prior to gas chromatographic separation, the desorbed sample containing the analytes of interest[1] is injected in a flow of carrier gas (mobile phase), usually nitrogen or helium, and transported through a long capillary column. In the column, the analytes interact differently with the column walls (stationary phase), resulting in different retention times of the different analytes. Species with short retention times will exit the column first while species with long retention times will only exit the column after a longer period of time. This technique is considered as the 'gold standard' in VOC speciation. However, it is labor intensive and requires some preprocessing of the sample before it can be analysed, allowing for potential artefacts.

3.2 PTR-MS

Proton Transfer Reaction Mass Spectrometry was developed over 2 decades ago (Lindinger et al., 1998) and has since become a widespread analytical technique in atmospheric sciences (de Gouw and Warneke, 2007; Blake

---

[1]The analyte is the substance to be analysed.

et al., 2009; Yuan et al., 2017) and other scientific domains (e.g. food and breath analysis). Its main advantage is the possibility to measure atmospheric composition online at a high frequency (response time of only a few hundred ms) and with high sensitivity. The technique is not labor-intensive which makes it very suitable for long-term remote operation. The drawback of the PTR-MS technique, however, is that it does not allow selective detection of isomeric[2] species and that quadrupole-based instruments don't allow selective detection/identification of isobaric[3] species because of limited mass resolution. In what follows we will briefly discuss the different components of a PTR-MS VOC analyser and the method used to quantify VOC concentrations by PTR-MS. Subsequently, we will describe the specific PTR-MS set-up that was deployed at the Maïdo observatory at Réunion Island to acquire the long dataset that has been analysed in the framework of this thesis.

3.2.1 Working principle of PTR-MS

PTR-MS instruments consist of an ion source, a reactor and a mass spectrometer (see Figure 3.1). Hydronium ions (H_3O^+) are the most frequently used reactant ions in PTR-MS. They are very suitable for ambient air analysis as they don't react with the major air constituents (N_2, O_2, Ar) and they undergo fast exothermic proton transfer reactions with many atmospheric trace gases. They are produced by adding pure water vapor to a hollow cathode (HC) discharge. Electron impact ionization of water in the ion source results in the formation of mainly H_2O^+, H_2^+, O^+ and H^+ ions, which react further with H_2O to H_3O^+ in the intermediate source drift region (SD). The H_3O^+ ions are subsequently injected in a drift tube reactor through which a continuous ambient air flow is pumped. Both the sampling line and the drift tube reactor of the PTR-MS are kept at a sufficiently high temperature to prevent losses of condensable or sticky compounds. While being transported downstream the drift tube by a homogeneous electric field, the reactant H_3O^+ ions react with atmospheric trace gases R having a proton affinity larger than that of H_2O. The resulting nascent excited

---

[2]Isomeric compounds have the same atomic composition but a different chemical structure, e.g. *o*-xylene, *m*-xylene, *p*-xylene, and ethyl-benzene (C_8H_{10}).

[3]isobaric compounds have the same nominal mass but a different chemical composition, e.g. isoprene (C_5H_8) and furan (C_4H_4O), both have a nominal molar mass of 68 g. However, the exact molar masses of C_5H_8 and C_4H_4O are 68.117 g, and 68.074 g, respectively.

protonated molecules are either stabilized by collision with a third body or undergo fragmentation. Both reactant and product ions can undergo clustering reactions with H_2O, hereby complicating the ion chemistry, but excessive clustering is prevented by collision-induced cluster dissociation which strongly depends on the E/N ratio in the drift field reactor[4]. However, it is important that E/N is not excessively large in order to keep product ion fragmentation to a minimum. Typical values of E/N vary between 100 and 145 Townsend (Td, $10^{-21}Vm^2$). At the end of the drift tube, reactant and product ions are sampled into the mass spectrometer, where they are filtered or separated according to their mass-to-charge ratio (m/z) and finally detected. Whereas early instruments were all equipped with a quadrupole mass filter for ion selection, more recent instruments are equipped with a time-of-flight mass analyser, providing simultaneous acquisition of whole mass spectra, a better transmission for higher m/z ions, and a higher mass resolution.

3.2.2 VOC quantification by PTR-MS

By solving the rate equation governing the loss of reactant H_3O^+ ions due to bimolecular proton transfer reactions with trace reactants R, one can easily prove that, at normal PTR-MS operating conditions, the concentration [R] of a trace gas in the drift tube reactor is given by:

$$[R] = \frac{1}{k\tau} \frac{[HR^+]}{[H_3O^+]} \tag{3.1}$$

Where τ is the ion residence time in the reactor (in s), k is the proton transfer rate coefficient (in molecules cm^{-3} s^{-1}) and $\frac{[HR^+]}{[H_3O^+]}$ is the ratio of product to reactant ion concentrations at the end of the drift tube. The latter corresponds to the ratios of the intensities of the respective ions in the mass spectra, after correction for mass-dependent transmission of the mass spectrometer. The mixing ratio of the compound in ambient air is finally obtained by dividing [R] by the air number density in the drift tube reactor. VOC mixing ratios derived in this way can be prone to large uncertainties, mainly because of the large uncertainties on the rate coefficients. More accurate quantification can be obtained by calibrating the

---

[4]The strength of the electric field in the drift tube E serves to supply energy to ion-molecule collisions. However, as the number of collisions depend on the number density N of the gas, the important quantity to prevent excessive clustering in the drift tube is called the reduced electric field E/N.

instrument by means of a certified dilute gas mixture containing accurately known amounts of the VOCs to be quantified.

3.2.3   PTR-MS set-up at Maïdo

The long term series of VOC concentrations in ambient air at the Maïdo observatory at La Réunion was obtained with a high-sensitivity quadrupole-based PTR-MS VOC analyser (hs-PTR-Quad-MS, Ionicon Analytic GmbH, Austria). The instrument was operated at a drift tube pressure and temperature of 2.2 hPa and 333 K, respectively. The E/N value was 136 Td, resulting in low contributions of $H_3O^+ \cdot H_2O$ reactant ions. Impurities of NO^+ and O_2^+ ions in the reactant ion spectrum were also very low. Mass separation occurs by a quadrupole filter, implying that mass spectra are acquired by scanning over the mass range, which results in a very short duty cycle. In order to increase the duty cycle and to increase the time resolution and precision of the measured compounds, the PTR-MS was operated in MID (Multiple Ion Detection) mode in which the instrument continuously cycled through a series of 19 m/z ratios, which are listed in Table 3.1. The VOC related ion m/z values in this table correspond to the most abundant ion signals that were present in full mass spectra that were acquired occasionally during the campaign. Those ion masses can all be related to compounds which have been detected in ambient air by PTR-MS instruments in different ecosystems worldwide. Since the reactant hydronium ion has a very high count rate, its count rate was inferred by multiplying the one of the $H_3{}^{18}O^+$ isotope at nominal m/z 21 by its isotopic ratio (~ 500). The signal at m/z 32 ($O_2{}^+$) was used for subtraction of its isotope at m/z 33 ($^{17}O^{16}O^+$) from the signal at m/z 33 which is associated to protonated methanol. Because of the high intensities of the ion signals at m/z 21, 32 and 37, the corresponding dwell times[5] were limited to 2, 0.1 and 0.1 s, respectively. Dwell times for the VOC-related ion signals at the other 16 m/z ratios were 10 s. The instrument is characterized by a high sensitivity, but has only unit mass resolution, which does not allow to distinguish isobaric species. Based on PTR-MS studies carried out in several environments (e.g., de Gouw and Warneke, 2007; Yuan et al., 2017), major interferences from isobaric compounds are not expected for the VOC species listed in Table 3.1. An exception is formaldehyde (HCHO, at m/z 31) for which po-

---

[5]The dwell time corresponds to the amount of time during which the instrument is collecting ions at a specific m/z ratio (corresponding to specific voltage settings).

Figure 3.2: Top left: sampling point on top of the roof of the Maïdo observatory together with the filter box after which the sampling line is thermally insulated and heated by a few degrees above ambient temperatures. Top right: heated sampling line from the filter box towards the window of the observatory. Bottom: sampling line entering the laboratory through a custom board replacing the window and connecting to the manifold which controls the air flow towards the hs-PTR-Quad-MS. Photos by C. Amelynck.
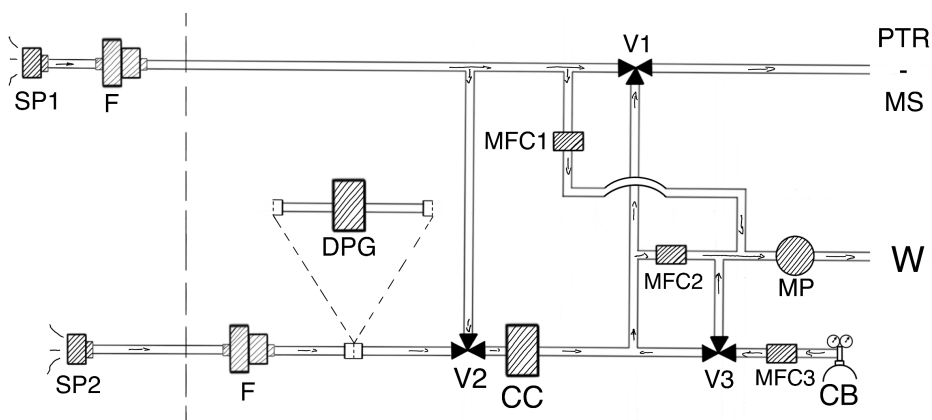
Figure 3.3: Schematic representation of the manifold setup. The dashed line represents the custom connection, replacing the window, between the outside (left) and the laboratory (right) through which the sampling lines are fed. SP1 denotes the main sampling line. SP2 represents the back-up sampling point. F represent filters. MFC and V are mass flow controllers and valves which can be controlled remotely. CC represents the catalytic converter. CB is the calibration bottle. MP is a membrane pump. W denotes waste that is pumped back to the outside. PTR-MS represents the hs-PTR-Quad-MS instrument.

Table 3.1: A list of mass-to-charge ratios (m/z) observed in multiple ion detection mode by the hs-PTR-Quad-MS with the associated chemical compounds, dwell times (DT, in seconds), the proton affinity (PA) (PA, in kJ mol^{-1}), and atmospheric lifetime with respect to the OH-sink (τ_{OH}) per compound (N/A: not applicable). Dwell times are shown for 1 cycle. PA values from (Hunter and Lias, 1998), consulted from (Linstrom, 1997). Atmospheric lifetimes are calculated assuming [OH] = 2 10^6 molecules cm^{-3} and 20°C.

m/z	Compound	DT	PA	τ_{OH}
21	$H_3{}^{18}O^+$	2	N/A	N/A
31	formaldehyde (HCHO)	10	712.9	16 h
32	O_2^+	0.1	N/A	N/A
33	methanol (CH_3OH)	10	754.3	6.5 days
37	$H_3O^+.H_2O$	0.1	N/A	N/A
42	acetonitrile (CH_3CN)	10		
45	acetaldehyde (CH_3CHO)	10	768.5	9 days
47	formic acid (HCOOH)	10	742.0	13 days
59	acetone (CH_3COCH_3)	10	812	60 days
61	acetic acid (CH_3COOH)	10	783.7	7 days
63	dimethyl sulphide (DMS)	10		5 h
69	isoprene (C_5H_8)	10	826.4	1.4 h
71	methyl vinyl ketone (MVK)	10	834.7	7 h
	+ methacrolein (MACR)		808.7	5 h
	+ hydroxy hydroperoxides from isoprene (ISOPOOH)			
73	methyl ethyl ketone (MEK)	10		5 days
79	benzene (C_6H_6)	10	750.4	5 days
81	sum of monoterpenes ($C_{10}H_{16}$)	10		2.6 h[†]
93	toluene (C_7H_8)	10	784.0	1 day
107	C_8-aromatics (C_8H_{10})	10		6–18 h[*]
137	$C_{10}H_{16}$	10		

[*]Longest lifetimes of C_8-aromatics are due to ethyl benzene, lifetime of different xylenes are 6–12 h.

[†]Lifetime for monoterpenes is given by the lifetime for α-pinene.

Rate coefficients obtained from the Master Chemical Mechanism MCMv3 (`http://mcm.leeds.ac.uk/MCM/`, last access: 14 February 2021).

tential interferences by methylhydroperoxide, methanol and ethanol have been reported in the literature (Inomata et al., 2008). Despite careful and regular calibration of the PTR-MS versus relative humidity, no satisfactory agreement was found between the PTR-MS HCHO measurements and those obtained with an Aerolaser instrument during two short intercomparisons. PTR-MS HCHO results were therefore not further analysed in this thesis.

Figure 3.2 shows the experimental setup from the sampling point up to the hs-PTR-Quad-MS instrument. Ambient air was sampled using a PFA (perfluoralkoxy) Teflon sampling tube (Dyneon 6502T, Fluorotechniek Deutschland, Germany) 2.86 m above the roof of the observatory (8.20 m above ground level) and filtered 2.46 m downstream of the sampling point using a PTFE (polytetrafluoroethylene) membrane filter (Zefluor, Pall laboratory, MI, USA) with a pore size of 2 μm, held in a PFA filter holder. Once the ambient air was filtered, the sampling line was thermally insulated and heated 5–10 °C above ambient temperature to avoid condensation. The length of the 3/8 inch outer diameter PFA sampling line is 10.35 m and the air residence time in the sampling line is 2.5 s. Before characterising ambient air with the hs-PTR-Quad-MS instrument, the air flow passed through an experimental setup, referred to as the manifold (Figure 3.3). The estimated air residence time in this part of the instrumental setup is estimated to be 650 ms. The manifold was controlled using a LabVIEW[6] program which allowed automated and remote manipulation of the setup by connecting to the on-site computer via either the TeamViewer software or a Virtual Network Computing (VNC) protocol. The manifold was set up in such a way that it allowed remote monitoring and calibration of the instrument. In nominal conditions, V1 was set to sample air from the main sampling line (SP1) directly. Every 4 hours, zero measurements were performed automatically for 30 minutes by activating V1 and sampling ambient air from SP1 that was scrubbed by the catalytic converter (CC). Every ∼3 days, calibrations of the instrument were done remotely by controlling the valves V1 and V3, and the mass flow from the calibration bottle (MFC3).

Regular on-site manipulations were limited to:

- changing the filter every two weeks,
- performing intensive calibrations by incorporating a dew point generator (LI-COR LI610, NE, USA) between the manifold and the backup sampling line (SP2) every two months,

---

[6]Laboratory Virtual Instrument Engineering Workbench

- refill the water reservoir used as a source to generate H_3O^+ ions in the instrument every $\sim$ 5 months, and

- maintenance periods replacing the H_3O^+ source (3 times) and the ion detector (twice).

Additional on-site manipulations were due to cyclonic activity in the region. During the passage of a cyclone close to the observatory, the instrumentation needed to be secured and the connection through the window was temporarily broken in order to lower the blinds of the laboratory. This only occurred twice in 2018, during the passage of cyclones Berguitta (15 January – 23 January) and Dumazile (2 March – 8 March).

The instrument setup and calibration is discussed further in Chapters 6 and 7. Extra information about data processing, calibration, and the status of the hs-PTR-Quad-MS over the 2-year campaign is given in Appendix B.

Bibliography

Blake, R. S., Monks, P. S., and Ellis, A. M.: Proton-Transfer Reaction Mass Spectrometry, Chemical Reviews, 109, 861–896, https://doi.org/10.1021/cr800364q, 2009.

de Gouw, J. and Warneke, C.: Measurements of Volatile Organic Compounds in the Earth's Atmosphere Using Proton-transfer-reaction Mass Spectrometry, Mass Spectrometry Reviews, 26, 223–257, https://doi.org/10.1002/mas.20119, 2007.

Hunter, E. P. L. and Lias, S. G.: Evaluated Gas Phase Basicities and Proton Affinities of Molecules: An Update, Journal of Physical and Chemical Reference Data, 27, 413–656, https://doi.org/10.1063/1.556018, 1998.

Inomata, S., Tanimoto, H., Kameyama, S., Tsunogai, U., Irie, H., Kanaya, Y., and Wang, Z.: Technical Note: Determination of Formaldehyde Mixing Ratios in Air with PTR-MS: Laboratory Experiments and Field Measurements, Atmospheric Chemistry and Physics, 8, 273–284, https://doi.org/10.5194/acp-8-273-2008, 2008.

Lindinger, W., Hansel, A., and Jordan, A.: On-Line Monitoring of Volatile Organic Compounds at Pptv Levels by Means of Proton-Transfer-Reaction Mass Spectrometry (PTR-MS) Medical Applications,

Food Control and Environmental Research, International Journal of Mass Spectrometry and Ion Processes, 173, 191–241, https://doi.org/10.1016/S0168-1176(97)00281-4, 1998.

Linstrom, P.: NIST Chemistry WebBook, NIST Standard Reference Database 69, https://doi.org/10.18434/T4D303, 1997.

Yuan, B., Koss, A. R., Warneke, C., Coggon, M., Sekimoto, K., and de Gouw, J. A.: Proton-Transfer-Reaction Mass Spectrometry: Applications in Atmospheric Sciences, Chemical Reviews, 117, 13 187–13 229, https://doi.org/10.1021/acs.chemrev.7b00325, 2017.

Chapter 4

Motivation and objectives

4.1 Motivation

In the previous chapters, we have seen that, although they are only present in trace amounts in the atmosphere, VOCs have a significant impact on the atmospheric composition. The biosphere constitutes the largest source of VOCs in the atmosphere. Biogenically emitted VOCs (BVOCs) play a major role in forested regions. However, due to their generally short atmospheric lifetimes, they play only a minor role in the remote marine atmosphere. In this type of regions, OVOC species contribute more strongly to the oxidative capacity of the atmosphere as they constitute the largest sink of OH relative to all other VOCs (Travis et al., 2020). Model underestimations of OH-reactivity have been suggested to be related to a missing source of short-lived VOC and OVOC emitted by the ocean in remote regions (Thames et al., 2020). Large model discrepancies in OVOC global budgets, especially in remote tropical regions (Read et al., 2012), and the free troposphere (Millet et al., 2010; Wang et al., 2020), are cause for large uncertainties related to the lifetime of methane and consequentially, climate (Zhao et al., 2019). A paucity of OVOC measurements in these remote tropical regions contributes to the large uncertainties related to their global budgets.

In order to address these issues, the Belgian-French project, funded by the Belgian Science Policy Office (BELSPO) through the 'Belgian Research Action through Interdisciplinary Network' program (BRAIN-Be), OCTAVE

(oxygenated compounds in the tropical atmosphere: variability and exchanges) was set up. The OCTAVE-project aims to improve the appraisal of global budgets for key OVOCs and their role in tropical regions by using an integrated approach combining in situ measurements, satellite retrievals, and global modelling. The key objectives of OCTAVE are found at the project website (`octave.aeronomie.be`; last accessed 5 Feb 2021). A first goal of the OCTAVE project was the generation of a 2-year data set of in situ OVOC measurements by mass-spectrometry (PTR-MS) and remote sensing infrared spectrometry (FTIR) at the high-altitude Maïdo observatory located on La Réunion, a remote tropical island located in the south-west Indian Ocean. This data was to be supplemented by performing additional measurements of OVOC concentrations between the observatory and the coastline during an intensive measurement campaign. OCTAVE also aims to identify and quantify OVOC sources contributing to the measurements at La Réunion with the help of multivariate statistical analysis, back-trajectory calculations, and 3-D modelling. Furthermore, the project targets the application of an innovative methodology to generate improved global distributions of column abundances of methanol and other VOCs using multi-annual remote sensing data from the IASI sensor on the MetOp satellite. Finally, an updated model evaluation of the budget of OVOCs based on data from satellite measurements and a wide collection of aircraft, ship-borne, and ground-based measurements, including those at La Réunion, was to be performed in the framework of OCTAVE.

This thesis was performed in the framework of the OCTAVE-project and focuses specifically on:

- the generation of the 2-year in-situ VOC data set at the Maïdo observatory using the PTR-MS technique,

- developing a mesoscale Lagrangian transport model that can be used to analyse a long term data set and is capable of representing transport features induced by the island's complex terrain, and

- the analysis of the in situ VOC concentrations combining the PTR-MS data set and the mesoscale Lagrangian transport model.

4.1.1   La Réunion

La Réunion is a remote tropical island located in the south-west Indian Ocean with a complex orographic profile (Figure 4.1). Due to its remote-
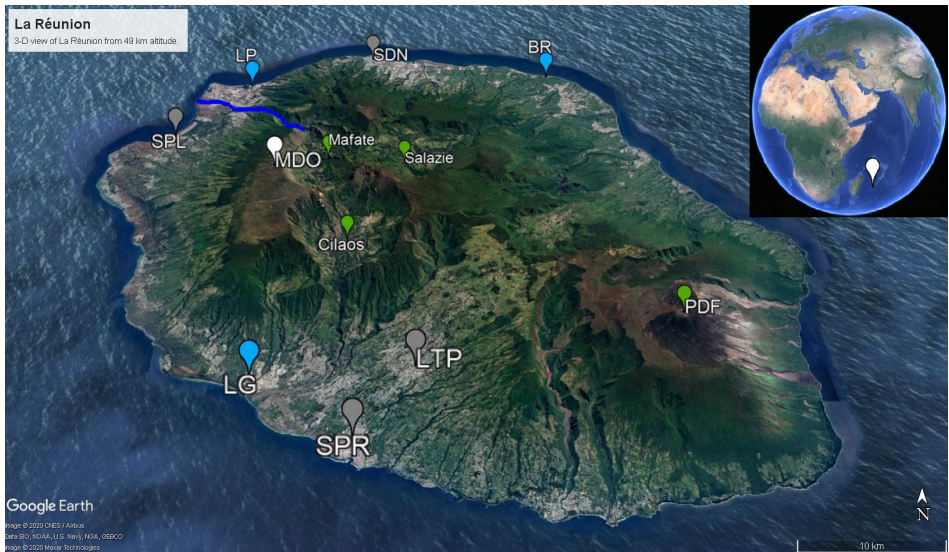
Figure 4.1: La Réunion, viewed from 49 km height. The Maïdo observatory (MDO) is indicated in white. Cities with population over 50,000 habitants — i.e. Saint-Denis (SDN), Saint-Paul (SPL), Le Tampon (LTP), and Saint-Pierre (SPR) — are shown in gray. The largest industrial sites — Le Port (LP), Bois-Rouge (BR), and Le Gol (LG) — are indicated in blue. Geological landmarks — Calderas Mafate, Salazie, and Ciloas as well as the shield volcano Piton de la Fournaise (PDF) — in green. The river Rivière des Galets between Mafate and Le Port is indicated as a dark blue line. This figure is used in Chapter 7. Image generated with Google Earth Pro, data SOI, NOAA, U.S. Navy, GA, GEBCO. ©2020 CNES/Airbus, ©2020 Maxar Technologies.
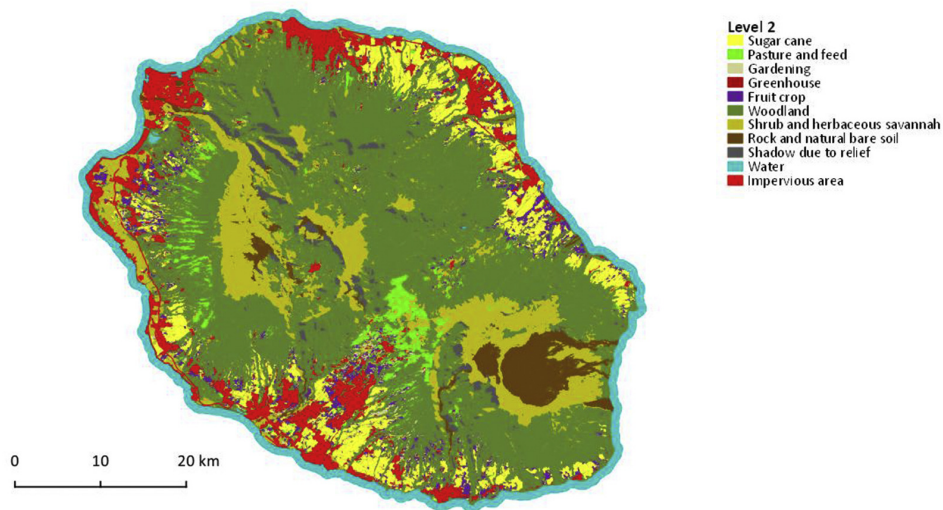
Figure 4.2: Landcover map of La Réunion from 2017. Image from (Dupuy et al., 2020).

ness, La Réunion is ideally located to study sources and sinks of VOCs in the remote tropical atmosphere.

The island is home to the Piton de la Fournaise volcano, a shield volcano which is among the most active effusive volcanoes in the world. The island's relatively small surface ($2,500$ km^2) in combination with its composite geological structure (three calderas: cirque de Cilaos, cirque de Mafate, and cirque de Salazie; high peaks: Piton des Neiges with 3,071 m altitude, and Piton de la Fournaise at 2,600 m altitude), makes for complex mesoscale airmass transport and weather phenomena. The general easterly flow near the surface, owing to global general circulation patterns, incident on the island is split around the island resulting in faster winds along the coasts parallel to the synoptic scale flow and calmer winds on the lee side of La Réunion (northwestern side). On this part of the island, mesoscale transport consists of a coupling between the sea/land-breeze and the upslope/downslope transport during the day/at night respectively. Rainfall occurs predominantly along the eastern slopes of the island through orographically forced clouds while the western part is mostly dry.

Outside of the southwestern part of the island — where occasional lava-flows from the volcano can reach the shore — coastal regions are largely

urbanised. Sugar-cane is the most popular crop cultivated at La Réunion. A land cover map of the island in 2017, constructed using high-resolution satellite images is shown in Figure 4.2 (Dupuy et al., 2020). Here we see that shrubs and herbaceous savanna occur mostly in the western part of the island and at high altitudes.

The Maïdo observatory is located near the summit of the Maïdo slope on the northwestern part of the island. Due to its location, transport towards Maïdo is largely determined by the thermally driven mesoscale transport features. During daytime, it is located in air masses originating in the marine boundary layer, flowing towards the island along the sea-breeze and conducted along the hot surface towards the observatory. During this process, the clean marine air masses are enriched with tracers from anthropogenic and biogenic sources located on the island. At night however, the cold surface cools the air, contracting the atmosphere and causing subsidence of air masses originating in the free troposphere towards the observatory. Air mass transport on La Réunion has been described by numereous other studies (e.g., Baray et al., 2013; Tulet et al., 2017; Guilpart et al., 2017; Foucart et al., 2018; Duflot et al., 2019; Rocco et al., 2020). Dispersion of pollutants over the island from different emission hotspots has been studied in more detail by Lesouëf et al. (2011) before construction of the Maïdo observatory. The mesoscale transport of marine boundary layer air masses towards the observatory and the systematic formation of orographically forced clouds along the Maïdo mountain slope provide a unique natural laboratory to study interactions between VOCs from various sources, cloud droplets, and SOA. Preliminary results for the FARCE campaign (Forests gAses aeRosols Clouds Exploratory, March–April 2015) were presented by Duflot et al. (2019). In the period March–April 2018, a second PTR-MS instrument was deployed near the coast and in a forest site on the island, results of which were published by Rocco et al. (2020). Most recently, during March–April 2019, two additional PTR-MS instruments were deployed along the Maïdo mountain slope in the framework of the BIO-MAÏDO campaign to study VOC–cloud–aerosol interactions.

4.2 Scientific questions and roadmap

The overall objective of this thesis is to improve the understanding of the (O)VOC composition and its variability in the remote tropical marine atmo-

sphere, more particularly at the high-altitude Maïdo observatory located on La Réunion. This work presented here focuses around the scientific questions found below.

1. What are the major source categories contributing to the (O)VOC composition at the Maïdo observatory and how do concentrations and source contributions vary at different time scales?

2. In how far is the atmosphere at the Maïdo observatory, and by extension the pristine marine boundary layer above the south-west Indian Ocean influenced by remote VOC sources.

3. To what extent is the (O)VOC composition at the Maïdo observatory influenced by mesoscale atmospheric transport?

4. How can we adapt a current transport tool to represent mesoscale atmospheric dynamics in orographically complex regions such as La Réunion?

The roadmap of the thesis is described in the paragraphs below. Note that the order of the roadmap does not correspond to the order in which the scientific questions are posed but rather the actual workflow of the project from start to finish.

As the atmospheric composition at a specific location is strongly influenced by transport, I started by developing a tool capable of simulating mesoscale transport features induced by the complex terrain of the island. To correctly describe this, a Lagrangian particle dispersion model (LPDM) needs to be driven by meteorological data obtained from the mesoscale AROME (applications de la recherche à l'opérationnel à méso-echelle) model which is the operational numerical weather prediction (NWP) model used by Météo France in the region. The AROME forecast model provides the resolution needed (2.5×2.5 km^2 horizontal resolution) to simulate the mesoscale transport features on La Réunion taking into account the complex orographic profile. As the PBL top variation is an important factor for transport towards the Maïdo observatory, turbulence in the LPDM needs to be well described and should correspond with the NWP. For this, I started by implementing a novel turbulent scheme in the new limited domain version of the FLEXible PARTicle dispersion model (FLEXPART), FLEXPART-AROME (Chapter 5, published work by Verreyken et al. (2019)).

Using remote sensing measurements, it has been established in the past that the period from August to November corresponds with a large impact of biomass burning (BB) plumes passing over the observatory (Vigouroux et al., 2012; Duflot et al., 2010). I investigated the impact of pyrogenic emissions originating from African and Madagascan burning events on the air quality at Maïdo and the marine boundary layer over the south-west Indian Ocean by making use of in situ VOC measurements from the hs-PTR-Quad-MS instrument, and the Lagrangian transport model FLEXPART (Chapter 6, published work by Verreyken et al. (2020)).

Lastly, I analysed the complete 2-year VOC data set by a combination of i) discussing the diel, seasonal, and inter-annual variability making use of tracers unequivocally linked to specific sources, ii) performing a multi-variate statistical analysis using a positive matrix factorisation (PMF) algorithm, and iii) calculating 24-hour back-trajectories for every hour from October 2017 to November 2019 with the FLEXPART-AROME model. This is done in order to attribute VOCs to their sources and identify emission hotspots on the island (Chapter 7, peer review of a preprint, Verreyken et al. (2021), is currently underway).

Bibliography

Baray, J.-L., Courcoux, Y., Keckhut, P., Portafaix, T., Tulet, P., Cammas, J.-P., Hauchecorne, A., Godin Beekmann, S., Mazière, M. D., Hermans, C., Desmet, F., Sellegri, K., Colomb, A., Ramonet, M., Sciare, J., Vuillemin, C., Hoareau, C., Dionisi, D., Duflot, V., Vérèmes, H., Porteneuve, J., Gabarrot, F., Gaudo, T., Metzger, J.-M., Payen, G., Leclair de Bellevue, J., Barthe, C., Posny, F., Ricaud, P., Abchiche, A., and Delmas, R.: Maïdo Observatory: A New High-Altitude Station Facility at Reunion Island (21° S, 55° E) for Long-Term Atmospheric Remote Sensing and in Situ Measurements, Atmospheric Measurement Techniques, 6, 2865–2877, https://doi.org/10.5194/amt-6-2865-2013, 2013.

Duflot, V., Dils, B., Baray, J. L., Mazière, M. D., Attié, J. L., Vanhaelewyn, G., Senten, C., Vigouroux, C., Clain, G., and Delmas, R.: Analysis of the Origin of the Distribution of CO in the Subtropical Southern Indian Ocean in 2007, Journal of Geophysical Research: Atmospheres, 115, https://doi.org/10.1029/2010JD013994, 2010.

Duflot, V., Tulet, P., Flores, O., Barthe, C., Colomb, A., Deguillaume, L., Vaïtilingom, M., Perring, A., Huffman, A., Hernandez, M. T., Sellegri, K., Robinson, E., O'Connor, D. J., Gomez, O. M., Burnet, F., Bourrianne, T., Strasberg, D., Rocco, M., Bertram, A. K., Chazette, P., Totems, J., Fournel, J., Stamenoff, P., Metzger, J.-M., Chabasset, M., Rousseau, C., Bourrianne, E., Sancelme, M., Delort, A.-M., Wegener, R. E., Chou, C., and Elizondo, P.: Preliminary Results from the FARCE 2015 Campaign: Multidisciplinary Study of the Forest–Gas–Aerosol–Cloud System on the Tropical Island of La Réunion, Atmospheric Chemistry and Physics, 19, 10 591–10 618, https://doi.org/10.5194/acp-19-10591-2019, 2019.

Dupuy, S., Gaetano, R., and Le Mézo, L.: Mapping Land Cover on Reunion Island in 2017 Using Satellite Imagery and Geospatial Ground Data, Data in Brief, 28, 104 934, https://doi.org/10.1016/j.dib.2019.104934, 2020.

Foucart, B., Sellegri, K., Tulet, P., Rose, C., Metzger, J.-M., and Picard, D.: High Occurrence of New Particle Formation Events at the Maïdo High-Altitude Observatory (2150 m), Réunion (Indian Ocean), Atmospheric Chemistry and Physics, 18, 9243–9261, https://doi.org/10.5194/acp-18-9243-2018, 2018.

Guilpart, E., Vimeux, F., Evan, S., Brioude, J., Metzger, J.-M., Barthe, C., Risi, C., and Cattani, O.: The Isotopic Composition of Near-Surface Water Vapor at the Maïdo Observatory (Reunion Island, Southwestern Indian Ocean) Documents the Controls of the Humidity of the Subtropical Troposphere, Journal of Geophysical Research: Atmospheres, 122, 9628–9650, https://doi.org/10.1002/2017JD026791, 2017.

Lesouëf, D., Gheusi, F., Delmas, R., and Escobar, J.: Numerical Simulations of Local Circulations and Pollution Transport over Reunion Island, Annales Geophysicae, 29, 53–69, https://doi.org/10.5194/angeo-29-53-2011, 2011.

Millet, D. B., Guenther, A., Siegel, D. A., Nelson, N. B., Singh, H. B., de Gouw, J. A., Warneke, C., Williams, J., Eerdekens, G., Sinha, V., Karl, T., Flocke, F., Apel, E., Riemer, D. D., Palmer, P. I., and Barkley, M.: Global Atmospheric Budget of Acetaldehyde: 3-D Model Analysis and Constraints from in-Situ and Satellite Observations, Atmospheric Chemistry and Physics, 10, 3405–3425, https://doi.org/10.5194/acp-10-3405-2010, 2010.

Read, K. A., Carpenter, L. J., Arnold, S. R., Beale, R., Nightingale, P. D., Hopkins, J. R., Lewis, A. C., Lee, J. D., Mendes, L., and Pickering, S. J.: Multiannual Observations of Acetone, Methanol, and Acetaldehyde in Remote Tropical Atlantic Air: Implications for Atmospheric OVOC Budgets and Oxidative Capacity, Environmental Science & Technology, 46, 11 028–11 039, https://doi.org/10.1021/es302082p, 2012.

Rocco, M., Colomb, A., Baray, J.-L., Amelynck, C., Verreyken, B., Borbon, A., Pichon, J.-M., Bouvier, L., Schoon, N., Gros, V., Sarda-Esteve, R., Tulet, P., Metzger, J.-M., Duflot, V., Guadagno, C., Peris, G., and Brioude, J.: Analysis of Volatile Organic Compounds during the OCTAVE Campaign: Sources and Distributions of Formaldehyde on Reunion Island, Atmosphere, 11, 140, https://doi.org/10.3390/atmos11020140, 2020.

Thames, A. B., Brune, W. H., Miller, D. O., Allen, H. M., Apel, E. C., Blake, D. R., Bui, T. P., Commane, R., Crounse, J. D., Daube, B. C., Diskin, G. S., DiGangi, J. P., Elkins, J. W., Hall, S. R., Hanisco, T. F., Hannun, R. A., Hintsa, E., Hornbrook, R. S., Kim, M. J., McKain, K., Moore, F. L., Nicely, J. M., Peischl, J., Ryerson, T. B., St. Clair, J. M., Sweeney, C., Teng, A., Thompson, C. R., Ullmann, K., Wennberg, P. O., and Wolfe, G. M.: Missing OH Reactivity in the Global Marine Boundary Layer, Atmospheric Chemistry and Physics, 20, 4013–4029, https://doi.org/10.5194/acp-20-4013-2020, 2020.

Travis, K. R., Heald, C. L., Allen, H. M., Apel, E. C., Arnold, S. R., Blake, D. R., Brune, W. H., Chen, X., Commane, R., Crounse, J. D., Daube, B. C., Diskin, G. S., Elkins, J. W., Evans, M. J., Hall, S. R., Hintsa, E. J., Hornbrook, R. S., Kasibhatla, P. S., Kim, M. J., Luo, G., McKain, K., Millet, D. B., Moore, F. L., Peischl, J., Ryerson, T. B., Sherwen, T., Thames, A. B., Ullmann, K., Wang, X., Wennberg, P. O., Wolfe, G. M., and Yu, F.: Constraining Remote Oxidation Capacity with ATom Observations, Atmospheric Chemistry and Physics, 20, 7753–7781, https://doi.org/10.5194/acp-20-7753-2020, 2020.

Tulet, P., Muro, A. D., Colomb, A., Denjean, C., Duflot, V., Arellano, S., Foucart, B., Brioude, J., Sellegri, K., Peltier, A., Aiuppa, A., Barthe, C., Bhugwant, C., Bielli, S., Boissier, P., Boudoire, G., Bourrianne, T., Brunet, C., Burnet, F., Cammas, J.-P., Gabarrot, F., Galle, B., Giudice, G., Guadagno, C., Jeamblu, F., Kowalski, P., Leclair de Bellevue, J., Marquestaut, N., Mékies, D., Metzger, J.-M., Pianezze, J., Portafaix, T.,

Sciare, J., Tournigand, A., and Villeneuve, N.: First Results of the Piton de La Fournaise STRAP 2015 Experiment: Multidisciplinary Tracking of a Volcanic Gas and Aerosol Plume, Atmospheric Chemistry and Physics, 17, 5355–5378, https://doi.org/10.5194/acp-17-5355-2017, 2017.

Verreyken, B., Brioude, J., and Evan, S.: Development of Turbulent Scheme in the FLEXPART-AROME v1.2.1 Lagrangian Particle Dispersion Model, Geoscientific Model Development, 12, 4245–4259, https://doi.org/10.5194/gmd-12-4245-2019, 2019.

Verreyken, B., Amelynck, C., Brioude, J., Müller, J.-F., Schoon, N., Kumps, N., Colomb, A., Metzger, J.-M., Lee, C. F., Koenig, T. K., Volkamer, R., and Stavrakou, T.: Characterisation of African Biomass Burning Plumes and Impacts on the Atmospheric Composition over the South-West Indian Ocean, Atmospheric Chemistry and Physics, 20, 14 821–14 845, https://doi.org/10.5194/acp-20-14821-2020, 2020.

Verreyken, B., Amelynck, C., Schoon, N., Müller, J.-F., Brioude, J., Kumps, N., Hermans, C., Metzger, J.-M., and Stavrakou, T.: Measurement report: Source apportionment of volatile organic compounds at the remote high-altitude Maïdo observatory, Atmospheric Chemistry and Physics Discussions, 2021, 1–37, https://doi.org/10.5194/acp-2021-124, 2021.

Vigouroux, C., Stavrakou, T., Whaley, C., Dils, B., Duflot, V., Hermans, C., Kumps, N., Metzger, J.-M., Scolas, F., Vanhaelewyn, G., Müller, J.-F., Jones, D. B. A., Li, Q., and Mazière, M. D.: FTIR Time-Series of Biomass Burning Products (HCN, C_2H_6, C_2H_2, CH_3OH, and HCOOH) at Reunion Island (21° S, 55° E) and Comparisons with Model Data, Atmospheric Chemistry and Physics, 12, 10 367–10 385, https://doi.org/10.5194/acp-12-10367-2012, 2012.

Wang, S., Apel, E. C., Schwantes, R. H., Bates, K. H., Jacob, D. J., Fischer, E. V., Hornbrook, R. S., Hills, A. J., Emmons, L. K., Pan, L. L., Honomichl, S., Tilmes, S., Lamarque, J.-F., Yang, M., Marandino, C. A., Saltzman, E. S., Bruyn, W., Kameyama, S., Tanimoto, H., Omori, Y., Hall, S. R., Ullmann, K., Ryerson, T. B., Thompson, C. R., Peischl, J., Daube, B. C., Commane, R., McKain, K., Sweeney, C., Thames, A. B., Miller, D. O., Brune, W. H., Diskin, G. S., DiGangi, J. P., and Wofsy, S. C.: Global Atmospheric Budget of Acetone: Air-Sea Exchange and the Contribution to Hydroxyl Radicals, Journal of Geophysical Research: Atmospheres, 125, https://doi.org/10.1029/2020JD032553, 2020.

Zhao, Y., Saunois, M., Bousquet, P., Lin, X., Berchet, A., Hegglin, M. I., Canadell, J. G., Jackson, R. B., Hauglustaine, D. A., Szopa, S., Stavert, A. R., Abraham, N. L., Archibald, A. T., Bekki, S., Deushi, M., Jöckel, P., Josse, B., Kinnison, D., Kirner, O., Marécal, V., O'Connor, F. M., Plummer, D. A., Revell, L. E., Rozanov, E., Stenke, A., Strode, S., Tilmes, S., Dlugokencky, E. J., and Zheng, B.: Inter-Model Comparison of Global Hydroxyl Radical (OH) Distributions and Their Impact on Atmospheric Methane over the 2000–2016 Period, Atmospheric Chemistry and Physics, 19, 13 701–13 723, https://doi.org/10.5194/acp-19-13701-2019, 2019.

PART II

Research

Chapter 5

FLEXPART-AROME

5.1 Objectives and methodology

From the clear diel profile of VOC sources recorded at the Maïdo observatory (see Rocco et al. (2020), and Chapter 7), it is clear that mesoscale transport has a large influence on the atmospheric composition recorded at the Maïdo observatory. Transport towards the Maïdo observatory has been studied in the past using the mesoscale non-hydrostatic (Meso-NH, Lac et al. (2018)) research model (e.g., Lesouëf et al., 2011; Duflot et al., 2019). This model can be used not only to study dynamical features in the atmosphere, but can also include online full chemistry. Using the Meso-NH model to analyse a two-year data set generated at the Maïdo observatory however was not feasible due to the long computation times, especially to simulate full chemistry. Moreover, a high-resolution inventory to reproduce biogenic emissions may be available, but the resolution of anthropogenic emission hotspots on the island is not yet sufficient to accurately simulate the interactions between both.

In order to study the impact of mesoscale emissions and transport on the air composition recorded at the Maïdo observatory, the limited domain model version of FLEXPART, FLEXPART-AROME was developed. The AROME[1] model is used by Météo France as the operational mesoscale numerical weather prediction (NWP) model in the region. As such, data is made available 4 times every day to drive the offline FLEXPART-AROME

---

[1]applications de la recherche à l'opérationnel à méso-echelle (AROME)

model. With its 2.5 x 2.5 km^2 horizontal resolution, AROME was deemed sufficient to simulate mesoscale transport towards the observatory for a two-year data set. However, as the Maïdo observatory is located near the top of the PBL, it was noted that consistent representation of turbulence between the online NWP and the offline Lagrangian particle dispersion model (LPDM) was critical to correctly reproduce transport towards the observatory. As such, we revisited previous efforts to drive turbulence in a limited domain version of FLEXPART, FLEXPART-WRF, directly by 3-D turbulent kinetic energy (TKE) fields obtained from the NWP model. Originally, these efforts resulted in numerical accumulation at the top of the PBL (Brioude et al., 2013), violating the well-mixedness criterion, one of the basic principles of LPDMs (Thomson, 1987). The idea was to constrain transport over discrete TKE interfaces in FLEXPART-AROME using the approach proposed by Thomson et al. (1997), already used in the stochastic time-inverted transport model (STILT) (Lin et al., 2003). Although the implementation of this formalism reduced the accumulation strongly, residual accumulation in regions with short turbulent mixing lengths was still observed. This problem was resolved by the implementation of an adaptive turbulent time step. A paper discussing the development of FLEXPART-AROME was published in Geoscientific Model Development (Verreyken et al., 2019).

The FLEXPART-AROME model has been used since its development to support analysis of, among others, the VOC data set generated with the hs-PTR-Quad-MS instrument at the Maïdo observatory (Chapter 6 and 7). Additionally, it has also been used to generate back-trajectories up to 36 hours in advance to support the BIO-MAIDO campaign taking place at the island by setting up an automated system that retrieved meteorological fields from AROME, processed this data to be read by the FLEXPART-AROME model, tunneled the data to a local server where simulations were performed and the maps shown in Figure 2.6 were generated, after which they were made available online[2]. This system was setup by myself and consisted of a combination of bash and python scripts that were executed by cron jobs[3] on two Unix-based operating systems.

---

[2]Made available online through the website: `https://geosur.univ-reunion.fr/public_html/cgi-bin/web/display_biomaido_v2.py`

[3]Cron is a time-base job scheduler software utility tool.

Bibliography

Brioude, J., Arnold, D., Stohl, A., Cassiani, M., Morton, D., Seibert, P., Angevine, W., Evan, S., Dingwell, A., Fast, J. D., Easter, R. C., Pisso, I., Burkhart, J., and Wotawa, G.: The Lagrangian Particle Dispersion Model FLEXPART-WRF Version 3.1, Geoscientific Model Development, 6, 1889–1904, https://doi.org/10.5194/gmd-6-1889-2013, 2013.

Duflot, V., Tulet, P., Flores, O., Barthe, C., Colomb, A., Deguillaume, L., Vaïtilingom, M., Perring, A., Huffman, A., Hernandez, M. T., Sellegri, K., Robinson, E., O'Connor, D. J., Gomez, O. M., Burnet, F., Bourrianne, T., Strasberg, D., Rocco, M., Bertram, A. K., Chazette, P., Totems, J., Fournel, J., Stamenoff, P., Metzger, J.-M., Chabasset, M., Rousseau, C., Bourrianne, E., Sancelme, M., Delort, A.-M., Wegener, R. E., Chou, C., and Elizondo, P.: Preliminary Results from the FARCE 2015 Campaign: Multidisciplinary Study of the Forest–Gas–Aerosol–Cloud System on the Tropical Island of La Réunion, Atmospheric Chemistry and Physics, 19, 10 591–10 618, https://doi.org/10.5194/acp-19-10591-2019, 2019.

Lac, C., Chaboureau, J.-P., Masson, V., Pinty, J.-P., Tulet, P., Escobar, J., Leriche, M., Barthe, C., Aouizerats, B., Augros, C., Aumond, P., Auguste, F., Bechtold, P., Berthet, S., Bielli, S., Bosseur, F., Caumont, O., Cohard, J.-M., Colin, J., Couvreux, F., Cuxart, J., Delautier, G., Dauhut, T., Ducrocq, V., Filippi, J.-B., Gazen, D., Geoffroy, O., Gheusi, F., Honnert, R., Lafore, J.-P., Lebeaupin Brossier, C., Libois, Q., Lunet, T., Mari, C., Maric, T., Mascart, P., Mogé, M., Molinié, G., Nuissier, O., Pantillon, F., Peyrillé, P., Pergaud, J., Perraud, E., Pianezze, J., Redelsperger, J.-L., Ricard, D., Richard, E., Riette, S., Rodier, Q., Schoetter, R., Seyfried, L., Stein, J., Suhre, K., Taufour, M., Thouron, O., Turner, S., Verrelle, A., Vié, B., Visentin, F., Vionnet, V., and Wautelet, P.: Overview of the Meso-NH Model Version 5.4 and Its Applications, Geoscientific Model Development, 11, 1929–1969, https://doi.org/10.5194/gmd-11-1929-2018, 2018.

Lesouëf, D., Gheusi, F., Delmas, R., and Escobar, J.: Numerical Simulations of Local Circulations and Pollution Transport over Reunion Island, Annales Geophysicae, 29, 53–69, https://doi.org/10.5194/angeo-29-53-2011, 2011.

Lin, J. C., Gerbig, C., Wofsy, S. C., Andrews, A. E., Daube, B. C., Davis, K. J., and Grainger, C. A.: A Near-Field Tool for Simulating the Upstream Influence of Atmospheric Observations: The Stochastic Time-Inverted Lagrangian Transport (STILT) Model, Journal of Geophysical Research: Atmospheres, 108, https://doi.org/10.1029/2002JD003161, 2003.

Rocco, M., Colomb, A., Baray, J.-L., Amelynck, C., Verreyken, B., Borbon, A., Pichon, J.-M., Bouvier, L., Schoon, N., Gros, V., Sarda-Esteve, R., Tulet, P., Metzger, J.-M., Duflot, V., Guadagno, C., Peris, G., and Brioude, J.: Analysis of Volatile Organic Compounds during the OCTAVE Campaign: Sources and Distributions of Formaldehyde on Reunion Island, Atmosphere, 11, 140, https://doi.org/10.3390/atmos11020140, 2020.

Thomson, D. J.: Criteria for the Selection of Stochastic Models of Particle Trajectories in Turbulent Flows, Journal of Fluid Mechanics, 180, 529–556, https://doi.org/10.1017/S0022112087001940, 1987.

Thomson, D. J., Physick, W. L., and Maryon, R. H.: Treatment of Interfaces in Random Walk Dispersion Models, Journal of Applied Meteorology, 36, 1284–1295, https://doi.org/10.1175/1520-0450(1997)036<1284:TOIIRW>2.0.CO;2, 1997.

Verreyken, B., Brioude, J., and Evan, S.: Development of Turbulent Scheme in the FLEXPART-AROME v1.2.1 Lagrangian Particle Dispersion Model, Geoscientific Model Development, 12, 4245–4259, https://doi.org/10.5194/gmd-12-4245-2019, 2019.

Geoscientific Model Development

Development of turbulent scheme in the FLEXPART-AROME v1.2.1 Lagrangian particle dispersion model

Bert Verreyken[1,2,3], **Jérome Brioude**[1], **and Stéphanie Evan**[1]

[1]Laboratoire de l'Atmosphère et des Cyclones, UMR 8105 CNRS, University of Réunion Island, Réunion, France
[2]Belgian Institute for Space Aeronomy, Ringlaan 3, 1180 Brussels, Belgium
[3]Department of Chemistry, Ghent University, Krijgslaan 281-S3, 9000 Ghent, Belgium

Correspondence: Bert Verreyken (bert.verreyken@aeronomie.be)

Abstract. The FLEXible PARTicle dispersion model FLEX-PART, first released in 1998, is a Lagrangian particle dispersion model developed to simulate atmospheric transport over large and mesoscale distances. Due to FLEXPART's success and its open source nature, different limited area model versions of FLEXPART were released making it possible to run FLEXPART simulations by ingesting WRF (Weather Research Forecasting model), COSMO (Consortium for Small-scale Modeling) or MM5 (mesoscale community model maintained by Penn State university) meteorological fields on top of the ECMWF (European Centre for Medium-Range Weather Forecasts) and GFS (Global Forecast System) meteorological fields. Here, we present a new FLEXPART limited area model that is compatible with the AROME mesoscale meteorological forecast model (the Applications of Research to Operations at Mesoscale model).[1] FLEXPART-AROME was originally developed to study mesoscale transport around La Réunion, a small volcanic island in the southwest Indian Ocean with a complex orographic structure, which is not well represented in current global operational models. We present new turbulent modes in FLEXPART-AROME. They differ from each other by dimensionality, mixing length parameterization, turbulent transport constraint interpretation and time step configuration. A novel time step was introduced in FLEXPART-AROME. Performances of new turbulent modes are compared to the ones in FLEXPART-WRF by testing the conservation of well-mixedness by turbulence, the dispersion of a point release at the surface and the marine boundary layer evolution around Réunion. The novel time step configuration proved necessary to conserve the well-mixedness in the new turbulent modes. An adaptive vertical turbulence time step was implemented, allowing the model to adapt on a finer timescale when significant changes in the local turbulent state of the atmosphere occur.

1 Introduction

Atmospheric transport models are divided into Eulerian and Lagrangian transport models. Eulerian models represent the atmosphere in a grid with mass being exchanged between grid cells. They are especially useful to model chemical interactions in the atmosphere. However, Eulerian models have difficulties maintaining the shape of narrow plumes due to numerical diffusion in their advection scheme. A number of techniques can be applied to dampen these diffusions, but they generally come with great computational costs (Alam and Lin, 2008). The Lagrangian models on the other hand describe the evolution of air masses in pregenerated 3-D meteorological fields obtained from a numerical weather prediction (NWP) model, allowing precise and fast modeling of atmospheric tracers released from point sources. Uncertainties in Lagrangian models originate from linear temporal and spatial interpolation from the 3-D meteorological fields of the NWP model (Stohl et al., 1995). Lagrangian particle dispersion models (LPDMs) such as the FLEXible PARTicle (FLEXPART) particle dispersion model represent an air mass by a large amount of infinitesimally small air parcels, also called particles. Each individual particle is advected along

---

[1]Applications de la Recherche à l'Opérationnel à Méso-Echelle.

the resolved wind fields with a turbulent diffusion superimposed (Zannetti, 1990).

LPDMs are used in a variety of atmospheric studies such as source apportionment of chemical compounds (Gentner et al., 2014; Warneke et al., 2010), studying atmospheric water vapor transport (Bertò et al., 2004; D'Aulerio et al., 2005; James et al., 2008), characterizing deep stratospheric intrusions (Brioude et al., 2007; Akritidis et al., 2012), as well as hazard preparedness exercises (Stohl, 2013). Regional inverse modeling studies are also an increasingly important field of applications of LPDMs (Lin et al., 2003; Manning et al., 2003; Stohl et al., 2009; Brioude et al., 2011).

Pisso et al. (2019) describe the FLEXPART offline transport model, including the available limited area model versions. The limited area versions of FLEXPART (FLEXPART-WRF (Brioude et al., 2013), FLEXPART-COSMO (Henne et al., 2016), FLEXPART-MM5) allow particle transport in higher-resolved grids to better represent mesoscale phenomena.

The AROME (Applications de la Recherche à l'Opérationnel à Méso-Echelle) mesoscale forecast model has been the operation weather forecasting model at Météo France since 2008. It is designed for fine-scale modeling with grid sizes ranging from 0.5 to 2.5 km. AROME is developed by combining efforts of the French Meso-NH research model community and the ALADIN consortium.[2] Since 2015, mainland France is covered by a 1.3 km horizontally resolved grid in a Lambert conformal projection, which results not only in a more realistic representation of topologically induced physical phenomena but also allows for a fine-scale variation in surface types impacting for instance the sensible heat flux at the surface (MétéoFrance, 2018). FLEXPART-AROME was developed by the LACy laboratory to model particle transport around La Réunion, a French overseas territory which is covered by an AROME grid in the southwest Indian Ocean (SWIO) with 2.5 km × 2.5 km resolution in a Lambert conformal projection. With its 90 vertical hybrid sigma levels it reaches an atmospheric altitude of about 24 km above sea level. A provisional version of FLEXPART-AROME was successfully used in the 2015 STRAP campaign to forecast transport of a volcanic plume on the island (Tulet et al., 2017).

FLEXPART-AROME is based on the FLEXPART-WRF v3.1.3 code which is able to use the Lambert conformal projections in the horizontal coordinate. The hybrid sigma levels are projected on Cartesian terrain-following vertical levels used by FLEXPART. To simulate turbulence induced by the complex orographic structure of the volcanic island of La Réunion and by shallow convection, we built on the turbulent modes implemented in FLEXPART-WRF by ingesting

the 3-D turbulent kinetic energy (TKE) field from the NWP in FLEXPART in order to harmonize turbulent motions between both.

2 Turbulent inconsistency between NWP and LPDM

Incoherent turbulent representations may introduce unrealistic tracer transport features. For instance, if the planetary boundary layer (PBL) height is overestimated in the transport model, tracers will be advected along stronger free-tropospheric (FT) winds with a different direction. If the reverse is true and the PBL height is underestimated, a passive tracer released at the surface will be well-mixed over a smaller vertical range, overestimating tracer concentrations in the boundary layer.

The FLEXPART Lagrangian particle dispersion model uses the turbulent parameterization proposed by Hanna (1982) and computes the PBL top along the method of Vogelezang and Holtslag (1996). In the large-scale global grids, deep convection is a relevant sub-grid-scale process. To describe this, Forster et al. (2007) adapted the convective parameterization by Emanuel and Živković Rothman (1999) in FLEXPART. Deep convection is assumed to be resolved in the mesoscale grids from AROME. The scheme was switched off by setting the LCONVECTION input parameter, inherited from FLEXPART-WRF, to zero. FLEXPART-WRF introduced two new turbulent modes using the 3-D TKE fields from the NWP model. They were, however, reported to violate the well-mixedness condition, described by Thomson (1987), which states that turbulence cannot change an initially well-mixed atmospheric tracer. To resolve this in the newly implemented turbulent modes in FLEXPART-AROME, we applied the method proposed by Thomson et al. (1997), successfully used in the Stochastic Time-Inverted Lagrangian Transport (STILT) model (Lin et al., 2003), to constrain particle transport at discrete interfaces in the model.

In contrast to the Hanna turbulence in FLEXPART, AROME TKE fields include shallow convective transport, allowing novel turbulent modes in FLEXPART-AROME to mix boundary layer air with free-tropospheric air masses.

Figure 1 illustrates the difference between the TKE fields from AROME and the calculated boundary layer top from FLEXPART.[3] We note that there is a large difference in turbulent motions in FLEXPART-WRF modes, where turbulence is only treated within the PBL, and the turbulent kinetic energy fields retrieved from AROME. The inclusion of shallow convection and convective clouds in the TKE fields will allow particles at the surface to mix to higher altitudes in the atmosphere.

---

[2]The ALADIN consortium contains the Algerian, Austrian, Belgian, Bulgarian, Croatian, Czech, French, Hungarian, Moroccan, Polish, Portuguese, Romanian, Slovakian, Slovenian, Tunisian and Turkish weather services.

[3]Sub-grid-scale orography variations and enveloping PBL height considerations, which can be taken into account in FLEXPART, are not taken into account since they do not make sense at the current mesoscale resolutions.
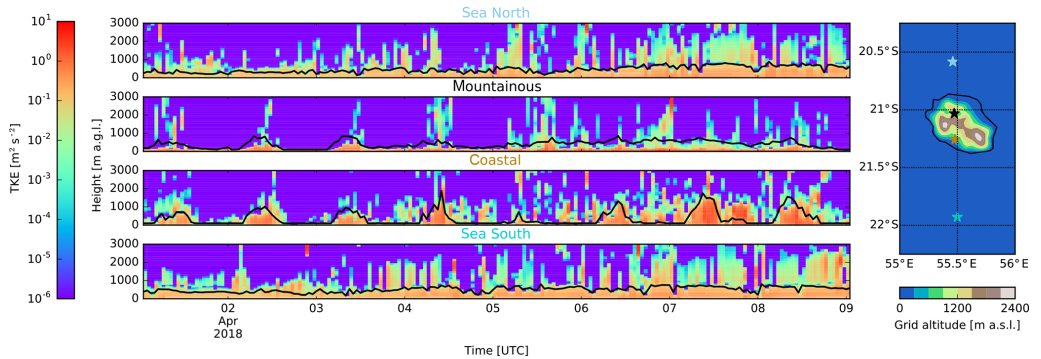
Figure 1. Temporal evolution of TKE fields retrieved from AROME in four different types of area around Réunion overlaid with a black curve showing the PBL top as calculated in FLEXPART. The vertical evolution plots on the left correspond from top to bottom with the locations indicated on the map from north to south, respectively. Height of the vertical profiles is expressed in meters above ground level; over the mountainous and coastal areas this corresponds to an added 1.2 and 0.4 km above sea level, respectively.

3   Turbulent scheme development

Turbulence in FLEXPART and FLEXPART-AROME is assumed Gaussian and parameterized using a Markov process to solve the Langevin equation. For an implementation with a discrete time step, dt, this results in

$$\left(\frac{w}{\sigma_w}\right)_{k+1} = r_w \left(\frac{w}{\sigma_w}\right)_k + \sqrt{1+r_w^2}\zeta + \frac{\partial \sigma_w}{\partial z}\tau_{L_w}(1-r_w) + \frac{\sigma_w}{\rho}\frac{\partial \rho}{\partial z}\tau_{L_w}(1-r_w),$$
(1)

where w is the vertical wind component of the turbulent motion, L_w the turbulent mixing length, τ_{L_w} the Lagrangian timescale for the vertical autocorrelation, σ_w the vertical turbulent velocity distribution width, ρ the air density, z the altitude, $r_w = \exp\left(-dt/\tau_{L_w}\right)$ the autocorrelation of the vertical wind, and ζ a normally distributed random number with mean zero and unit standard deviation. The subscript k and $k+1$ refers to subsequent times separated by dt. The first two terms on the right-hand side represent the native autocorrelated turbulent velocity behavior. The third and fourth terms represent drift and density corrections, respectively (Stohl et al., 2005).

To determine τ_{L_w} and σ_w, FLEXPART-WRF has four modes defined by the TURB_OPTION input parameter introduced by Brioude et al. (2013):

– TURB_OPTION = 0: turbulent velocities are set to zero.

– TURB_OPTION = 1: turbulence is computed using the standard FLEXPART configuration using the parameterization proposed by Hanna (1982).

– TURB_OPTION = 2: a hybrid configuration combining TKE fields from WRF and the FLEXPART parameterization. Surface-layer scaling and local stability with the Hanna scheme determine the 3-D partitioning of the turbulent kinetic energy.

– TURB_OPTION = 3: turbulent motions are characterized directly by the TKE field from WRF and 3-D partitioning is based on balancing production and dissipation of turbulent energy.

Brioude et al. (2013) reported spurious accumulation when using modes where TKE fields from the WRF are taken to characterize the turbulence.

In the FLEXPART-AROME code, the drift correction is set to zero and replaced by the numerical method discussed in Sect. 3.2. Turbulent modes are extended by 24 configurations. We separated the new options according to the characteristics of each mode; these characteristics will be discussed in greater detail below. The user has a choice in the time loop configuration, the computation of local TKE and parameterizations for mixing length. Turbulent motions can be restricted to the vertical axis (1-D), as is the case in the AROME configuration over the SWIO, or partitioned in 3-D using the diagnostic equations from Cuxart et al. (2000), implemented in the Meso-NH (Lac et al., 2018) mesoscale model. The 3-D modes are not explicitly evaluated here but rather are implemented to anticipate future AROME developments and the use of the model in combination with Meso-NH simulations resolved on the fine-scale.

The different novel turbulent modes together with their input parameters are summarized in Table A1 (Appendix A).

3.1 Particle time loop

FLEXPART discriminates between the particles below and those above the PBL top. Above the PBL, particles are advanced in one user-defined model synchronization (LSYNC) time step. In the PBL, particle positions are updated along a leap frog method between turbulent transport and resolved wind fields. The Δt time step, used by the leap frog method, is determined by the atmospheric stability and the user-defined input parameter CTL. Vertical turbulent transport is handled in a second IFINE time loop with a time step $dt = \frac{\Delta t}{\text{IFINE}}$, where IFINE is a third user-defined input parameter.

A major difference between the FLEXPART-AROME model and other FLEXPART versions is the treatment of turbulence at the PBL top. By direct use of TKE field from the NWP model, we do not characterize the PBL height explicitly. All particles are put through the time loops. In low turbulent regions, σ_w is small, which naturally results in longer time steps:

$$\tau_w = \frac{L_w}{\sigma_w}, \Delta t = \frac{\tau_w}{\text{CTL}}, \tag{2}$$

where L_w is the turbulent mixing length.

Traditionally, dt is fixed over a Δt period. However, in the new turbulent modes from FLEXPART-AROME, TKE can change abruptly, resulting in significant differences between adjacent dt time steps that are not represented. To resolve this, an adaptive vertical turbulence time step (AVTTS) was implemented. The local time step is computed as

$$dt' = \frac{\tau_w}{\text{CTL} \times \text{IFINE}}. \tag{3}$$

After IFINE displacements, the local dt' steps are accumulated in $\Delta t = \sum_{i=1}^{\text{IFINE}} dt'_i$, which is then used as the time step to displace the particle along the resolved winds.

This new time loop configuration is significantly different to the traditional fixed vertical turbulence time step (FVTTS) configuration. As will be shown in Sect. 4.1, the FVTTS is not compatible with new turbulent modes and users of FLEXPART-AROME should always use the AVTTS configuration.

3.2 Thomson's approach

Thomson et al. (1997) discussed the transport of particles through discrete interfaces in a random walk dispersion model. To conserve a well-mixed profile in a turbulent system with discrete TKE steps, particle transport is constrained between different TKE regions. By imposing a net zero mass flux at TKE interfaces in a well-mixed system and assuming maximal mixing, particles attempting to cross an interface have a probability α of reflection. This probability is proportional to the ratio of Gaussian turbulent velocity distribution widths. Lin et al. (2003) introduced a correction to this probability due to density variations. In FLEXPART-AROME, this

correction was not implemented as it is taken into account when solving the Langevin equation (Stohl and Thomson, 1999).

In FLEXPART-AROME, two possible interpretations of Thomson's approach have been implemented. The first considers each displacement to be a small discontinuity while the second arises from the grid definition of the FLEXPART-AROME model. In the small-discontinuity approximation (SDA), turbulent kinetic energy is interpolated in time and space for both the initial and the final position of a time step dt. The particle is supposed to cross an imaginary interface located at the middle of its trajectory. The probability of crossing is given by $\alpha = \frac{\sigma_f}{\sigma_i}$, where σ_i and σ_f represent the widths of the turbulent velocity distributions at the initial and final position, respectively. Alternatively, one can regard the FLEXPART grid as a stack of homogeneous turbulent cells. The cell boundaries are discrete TKE interfaces and particles attempting to cross into a neighboring cell are reflected with a probability α. In this mode (Step TKE), particles moving a distance dz are checked to see if they cross the cell boundary. If so, the time step is split up into the time it takes for the particle to get to the boundary (dt_1) and the remaining time ($dt_2 = dt - dt_1$). When a particle crosses the boundary, the turbulent velocity is recalculated at the boundary to be consistent with the new local turbulence. The difference between both interpretations is visualized in Fig. 2.

Both options have their merit. The SDA is recommended when users are interested in a more detailed vertical profile for the FLEXPART-AROME output. Once the SDA mode is selected, users should pay attention to the IFINE and CTL parameters. If their values are low,[4] the small-discontinuity hypothesis no longer stands. When users want to speed up their model run and are not interested in detailed vertical distributions near the surface, we suggest the use of the Step TKE option.

3.3 Turbulent mixing length

There are currently three parameterizations for the turbulent mixing length available in FLEXPART-AROME. The first is based on the grid size (DELTA). It is commonly used as the characteristic length scale of sub-grid eddies and is justified when the grid size falls into the inertial subrange of the turbulent flow and is recommended when the NWP model has high resolution and a nearly isotropic grid (Cuxart et al., 2000). The second parameterization is the Bougeaul–Lacarrère mixing length (BL89), a nonlocal turbulent mixing length parameterization proposed by Bougeault and Lacarrère (1989)

---

[4]In our experience, we found that values of IFINE and CTL of 5 were advisable from the different tests. Simulations with CTL values of 2 showed accumulation in all modes, even when combined with IFINE values of up to 10. When using the Step TKE mode modes, we suggest not going to values of IFINE and CTL below 5 and 3, respectively. Our recommendations for the SDA mode are to keep to a minimum of 5 for both parameters.
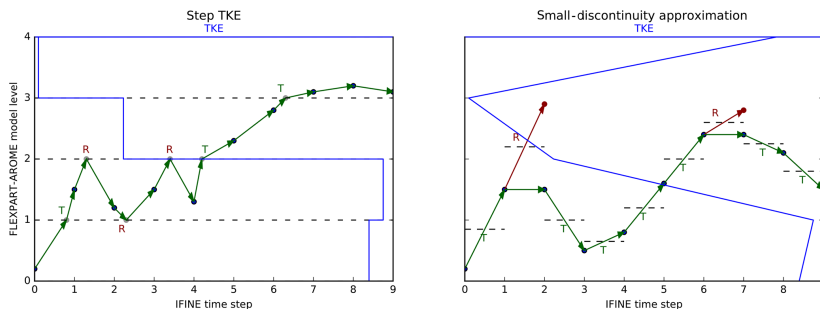
Figure 2. Illustrative difference between Step TKE and SDA configurations. Dashed lines represent TKE interfaces; in the Step TKE configuration they are fixed with homogeneous TKE regions in between; SDA interpolates TKE to the particle position and initializes an imaginary temporary TKE interface halfway along the particle trajectory at each step. Every time the particle tries to cross an interface we evaluate the probability of crossing, and the particle will be either transmitted (T) through or reflected (R) at the interface. The Step TKE configuration updates particle positions to the boundary before computing the probability of crossing (gray points); when particles are transmitted, their turbulent velocity is adapted to the new model layer. The SDA configuration uses a virtual position which becomes the new position upon transmission or which is never realized upon reflection (red points).

that balances the TKE with buoyancy effects to determine the mixing length. This parameterization is the default mixing length used in the AROME model over the SWIO domain. The last parameterization (DEARDORFF) is the analytical limit of BL89 in a stably stratified atmospheric limit, which corresponds to the results of Deardorff (1980). It is implemented to study the model behavior in numerical tests. The use of this last parameterization is discouraged for realistic atmospheric transport. The implementation of these parameterizations is discussed in Appendix B. Users of FLEXPART-AROME are encouraged to use the same mixing length parameterization as their AROME domain to get consistent results between the NWP and the LPDM.

4 Validation

Validation tests were run using LSYNC = 300, CTL = 5 and IFINE = 5 with output every 30 min during a period of 24 h. For each test 250 000 particles are initialized. The particles are not advected along resolved winds to isolate vertical turbulent motions. The horizontal domain is constrained to one AROME grid cell area over land or over the sea. The output kernel of FLEXPART, spreading a fraction of particle mass over adjacent horizontal cells, was compensated for by adding the output between adjacent cells of FLEXPART-AROME output. The grid cells over land and sea were randomly selected to perform our tests. The cell over land has coordinates 21.124° S, 55.379° E, corresponding to a forest area on Réunion. The cell over the sea is located at 22.409° S, 53.939° E, a cell 200 km southwest of the island. The vertical output grid goes up to 5 km and is resolved by 100 m thick layers. Real TKE fields were used for the test, which is why two types of area were explicitly tested. Simulations above

the sea are shown here, results over land were similar unless explicitly stated otherwise. The TKE profile and the diagnosed PBL height from FLEXPART in the cell above the sea are shown in Fig. 3

4.1 Turbulent conservation of a well-mixed passive tracer

Initially well-mixed passive tracers in position and velocity space should remain unchanged in a turbulent flow. Isolating the vertical turbulence and using the MDOMAINFILL option to initialize a well-mixed passive tracer, all turbulent modes in FLEXPART-AROME were tested. Accumulation is normalized to the initial mean mixing ratio. By using the MDOMAINFILL option, numerical fluctuations lead to background accumulations and dilutions of 3.5 % and 4.0 %, respectively. Results above the sea are shown in Fig. 4.

The Hanna parameterization shows systematic accumulation at the surface (11.0 %). Turbulent modes introduced in FLEXPART-WRF based on TKE violate the well-mixed criterion consistently. Dilution at the surface in the hybrid FLEXPART-WRF mode is 46.4 %; accumulation at the PBL top is 42.3 %. The results in the second FLEXPART-WRF mode are slightly better with a maximum dilution of 43.3 % near the surface and an accumulation of 31.5 % at the PBL top.

The AVTTS configurations perform consistently better than their FVTTS counterparts. The FVTTS result with DELTA mixing length has the largest surface accumulation of novel FLEXPART-AROME modes (surface accumulation up to 25.7 %). The AVTTS DEARDORFF mode in a Step TKE configuration has the least accumulation and dilution of all models (4.3 % and 7.4 %, respectively); however, the use
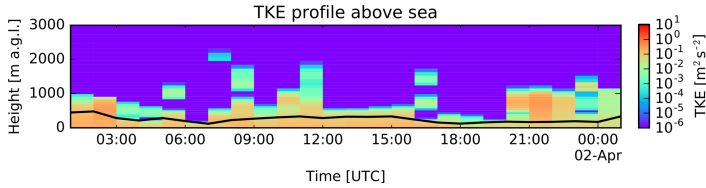
Figure 3. The real TKE profile used in the validation tests above the sea. The black curve corresponds to the PBL height computed by FLEXPART.
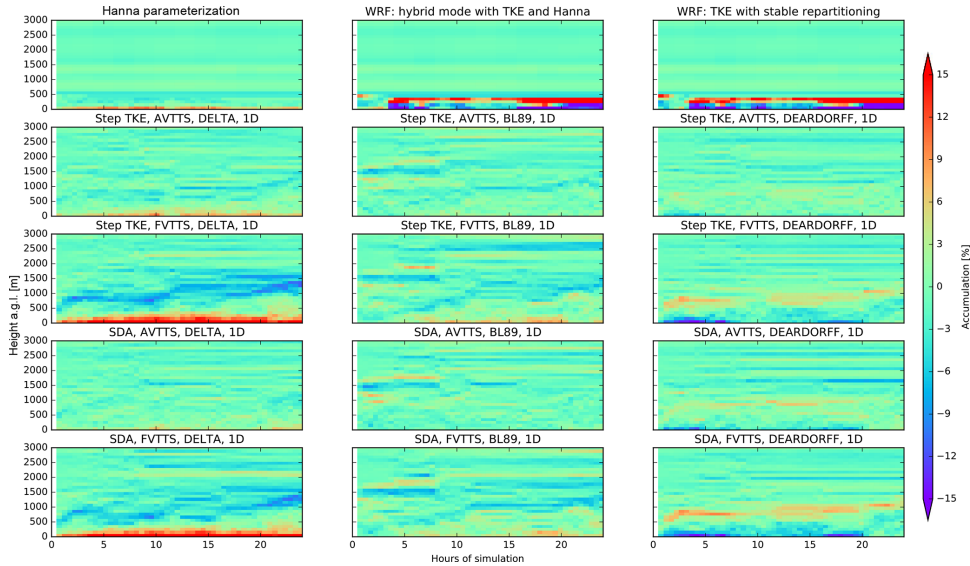
Figure 4. The vertical profile of accumulation in a well-mixed test from all the different turbulence configurations in FLEXPART-AROME is shown throughout the 24 h simulation test. These tests were run in a single column over the ocean surface.

of DEARDORFF is not recommended since it is only valid in a stably stratified atmosphere. Aside from the DEARDORFF configuration, modes combining AVTTS with BL89 best conserve the well-mixed state of the passive tracer. The Step TKE option performs slightly better than the SDA in this example (0.9 % less dilution and 2 % more accumulation). Tests over land however showed that SDA had better results (Appendix C).

The remaining accumulation is due to gradients in mixing length. The DELTA mode has smaller L_w near the surface while DEARDORFF has larger mixing lengths at the surface compared to higher altitudes. We see that mass accumulates in these small mixing length regions.

4.2 Vertical dispersion of a passive surface tracer in the planetary boundary layer

The vertical dispersion of a passive surface tracer is an important test to ensure efficient vertical turbulent mixing. The conservation of well-mixedness might be due to inefficient mixing, and so the surface tracer is a necessary supplementary test. We expect the tracer to be well-mixed throughout the turbulent regions within 3 h after the initial release.

A point release at the surface at $t = 0$, corresponding to 04:00 local time in a FLEXPART-AROME simulation with isolated vertical turbulent motions driven with transient meteorological field was performed. The dispersion of the tracer for different turbulence modes is shown in Fig. 5. The final mixing ratio profiles of are shown in Appendix D.

In the Hanna mode and the FLEXPART-WRF modes, the tracer is mixed up to 500 m above ground level within the first 3 h. This corresponds to the maximum boundary layer top within this period. It is obvious however that the tracer is not well-mixed in the FLEXPART-WRF configurations based on the turbulent kinetic energy.

Similar to the traditional configurations, the novel FLEXPART-AROME turbulent modes succeed in mixing the surface tracer well within the first 3 h. But rather than mixing up to the 500 m above ground level, where the boundary layer top is situated, the novel modes mix the tracer up to an altitude of 1000 m above ground level. This corresponds to the maximum height of the turbulent layer according to the TKE fields in the same period. There is also limited mixing between turbulent and nonturbulent regions above the shallow convective zone present in the new modes. This in contrast to the sharp PBL in FLEXPART-WRF, where all particles are reflected at the PBL top in the isolated turbulence configuration. Note that the use of dynamic TKE fields results in the shifting in time of the convective zone. Particles can be mixed higher up at certain times after which they will no longer mix down but rather remain at the same position.

Due to the inclusion of shallow convective mixing in new turbulent modes, particles are allowed to breach the PBL top, and near-surface concentrations in the traditional turbulent option are approximately 3 times larger compared to the new modes. The tracer is mixed over a larger vertical range causing a dilution not present in Hanna or FLEXPART-WRF turbulent modes. We highlight that, in this case, more than half of the total mass emitted at the surface is transported above the boundary layer by the new turbulent modes. This enables transport along the stronger free-tropospheric winds, creating further inconsistencies in dispersion between the traditional and novel turbulent methods.

5 Performance

5.1 Marine boundary layer tracer

FLEXPART-AROME was built to simulate atmospheric transport around Réunion to analyze measurements at the high-altitude Maïdo observatory (Baray et al., 2013). To study the marine boundary layer (MBL) impact on measurements taken at the observatory, we continuously release a passive tracer between 0 and 5 m above the sea with a lifetime of 24 h. Results shown are after a spin-up time of 24 h; LSYNC is set to 300; IFINE and CTL are equal to 5.

Due to the strong coupling of the sea breeze and upslope mountainous transport, the observatory is located in the MBL during the day, while at night the reverse process flushes marine tracers with free-tropospheric air as found in isotopic analysis of water vapor at the Maïdo observatory by Guilpart et al. (2017). Figure 6 shows the MBL tracer at Maïdo using (i) no turbulent motions, (ii) Hanna turbulence and (iii) the

selected new mode (TURB_OPTION = 0, 1 and 111, respectively). Differences between modes with turbulence are limited in this example. The passive tracer arrives an hour earlier and has a larger vertical distribution when arriving at the observatory in the new mode compared to the performance of Hanna turbulence.

Figure 7 shows the marine boundary layer tracer above a random grid cell at sea. In this figure we clearly see the influence of clouds on the dispersion of passive marine tracer in the vertical. Tracers are convected through strong shallow convection in turbulent clouds that are not resolved in the traditional FLEXPART configuration. Surface mixing ratios in the Hanna mode are elevated compared to those obtained with the new turbulent mode as seen in the point release test.

5.2 Computation time

We compared the total computation time between the different simulations run for this work. Simulations were run on a workstation with a single CPU INTEL CORE I7-7700, 32 Gb of DDR4 SDRAM with a GNU compiler. The machine was dedicated to the FLEXPART-AROME simulations to minimize the impact of parallel processes on the computation times. A complete overview of run times in reference to the Hanna parameterization is shown in Table 1.

Traditionally particles above the PBL are not considered to be turbulent and get advected in one single LSYNC time step. In the new turbulent modes, particles above the PBL top are treated in the same way as those below it. This can imply vertical turbulent loops for particles above the PBL if the LSYNC input parameter is large. In the well-mixed tests we use the MDOMAINFILL option and initialize a large amount of particles above the PBL. Due to this the relevant novel modes (excluding DEARDORFF) have a mean run time of 4.8 times that of Hanna. We exclude DEARDORFF in this comparison since (i) its mixing length has no lower limit except for the implicit limit imposed by limiting the minimum time step and (ii) its use is discouraged since the mixing length is only valid in very specific cases. The DEARDORFF modes have a run time of 7.5 times the Hanna run time in testing the well-mixedness.

When running the point release the relevant new modes are 15 % slower than the original mode. In the marine boundary layer, the turbulent mode combining the SDA, AVTTS and BL89 options in a 1-D configuration ran 37 % longer than the Hanna parameterization. We also remark that no turbulent parameterization leads to longer run times in these two tests. This is due to the straightforward implementation of turbulent velocities being set to zero. Time steps in displacing the particle are conserved, and since the vertical turbulent dispersion is not represented, particles remain in regions with a very low time step.
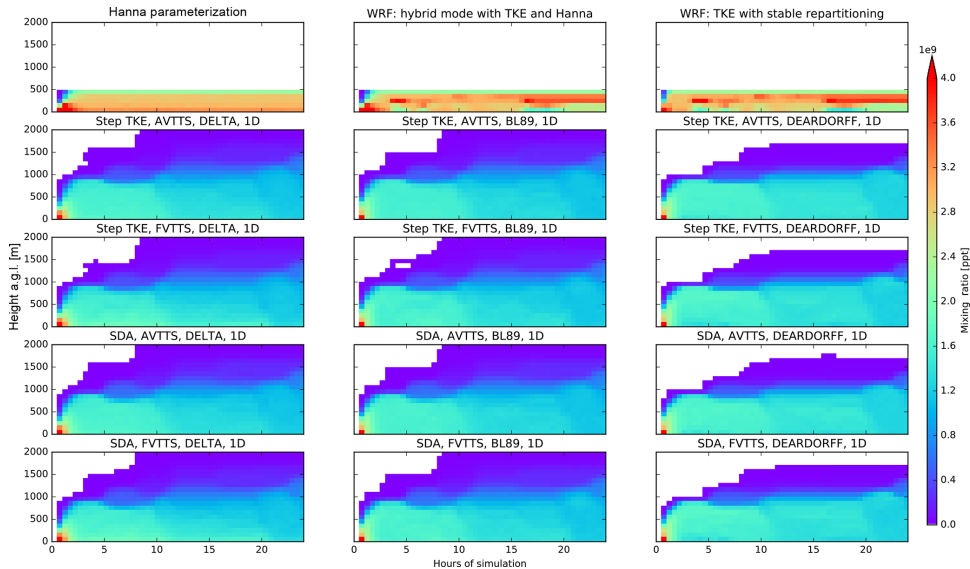
Figure 5. Vertical dispersion of point release at the surface are shown by the time evolution of the vertical mixing ratio profiles throughout the 24 h simulation test for the different turbulent modes in FLEXPART-AROME. These tests were performed in a single column over the ocean surface.
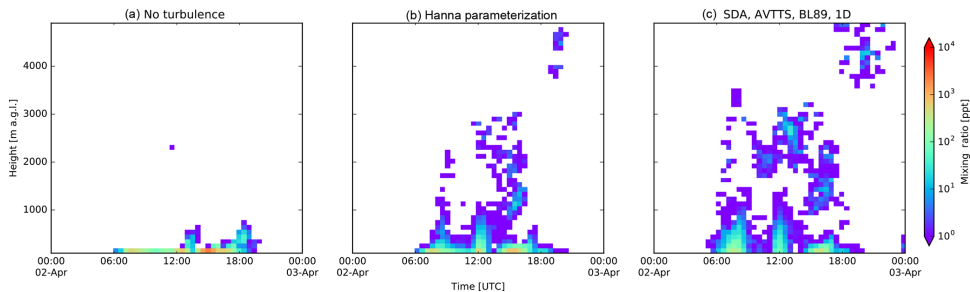
Figure 6. Marine boundary layer tracer profile evolution at the Maïdo observatory. Panel (**a**): a simulation without turbulent motions taken into account. Panel (**b**) shows the traditional FLEXPART turbulent mode. Panel (**c**) shows the results with the new turbulent mode.

6   Conclusions

We developed the new FLEXPART-AROME limited domain model version of FLEXPART based on FLEXPART-WRF v3.1.3. This configuration was build to model transport around Réunion in the Indian Ocean, a small volcanic island which has a complex orographic structure, but it can be used with any AROME domain. To simulate turbulence consistently with the operational meteorological model in the region, we implemented new turbulent modes that ingest 3-D TKE fields from the NWP. Due to shallow convection

being taken into account in determining the TKE fields in AROME, FLEXPART-AROME is able to represent sub-grid-scale shallow convective features. There are three important developments that users should consider when selecting the turbulent option that best suits their needs.

– To better represent the local turbulent state of a particle, an adaptive time step was implemented. This configuration is referred to as the adaptive vertical turbulence time step approach and performs consistently better in

Figure 7. Marine boundary layer tracer profile evolution above the sea. Panel (**a**): a simulation without turbulent motions taken into account. Panel (**b**) shows the traditional FLEXPART turbulent mode. Panel (**c**) shows the results with the new turbulent mode.

Table 1. Computation time ratios relative to the original Hanna parameterization computation time.

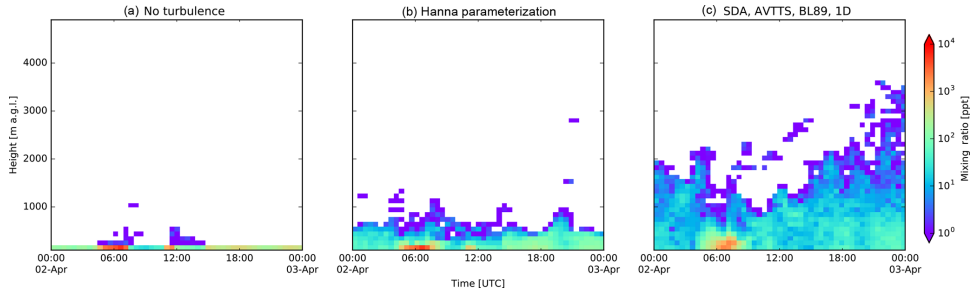| Turbulent configuration			TURB_OPTION	Well-mixed test	Point release test	Marine boundary layer run
No turbulent motion			0	0.96	2.30	1.89
Hanna parameterization			1	1.00	1.00	1.00
WRF: hybrid mode with TKE and Hanna			2	0.94	1.18	x
WRF: TKE with stable repartitioning			3	1.12	1.32	x
Step TKE	AVTTS	DELTA	10	4.95	1.06	x
		BL89	11	4.89	1.06	x
		DEARDORFF	12	6.81	1.06	x
	FVTTS	DELTA	20	4.95	1.04	x
		BL89	21	4.99	1.05	x
		DEARDORFF	22	6.44	1.02	x
SDA	AVTTS	DELTA	110	4.95	1.19	x
		BL89	111	5.21	1.32	1.37
		DEARDORFF	112	9.05	1.24	x
	FVTTS	DELTA	120	5.20	1.17	x
		BL89	121	5.58	1.31	x
		DEARDORFF	122	8.57	1.16	x

conserving the well-mixed state of the atmosphere compared to the traditional configuration.

- Turbulent drift in the model is numerically constrained by using the formalism introduced by Thomson et al. (1997). It consists in reflecting or transmitting particles at discrete turbulent interfaces to conserve the well-mixed state of an initially well-mixed atmosphere. Two possible interpretations of this formalism have been implemented. One approximates turbulence in the FLEXPART-AROME grid by considering every grid-cell to have uniform turbulence with transport being constrained at the boundaries of the model grid and is referred to as the Step TKE option. The other uses the small-discontinuity approximation where the turbulent

profile is vertically interpolated and transport is constrained at each displacement. The latter is referred to as the SDA option. If users are interested in vertical output grids with high resolution, as in the AROME grid, we advise to use the SDA option. If not, users can select the Step TKE option with lower values of the IFINE and CTL input parameters to speed up the model.

- Three different mixing length parameterizations are implemented: DELTA, BL89 and DEARDORFF. The use of the last parameterization is discouraged due to it only being valid in stably stratified atmospheres. Users are encouraged to adapt the choice of mixing length parameterization to be in accordance with the NWP.

New turbulent modes have a computation time that is about 5 times larger compared to the Hanna parameterization when a large fraction of the particles is above the PBL. However, the simulation of tracers predominantly present in the PBL using a new mode in the AROME SWIO domain only takes 15 % longer than the original configuration.

FLEXPART-AROME will be used to study the arrival of marine boundary layer tracers at Maïdo observatory on Réunion and the vertical distribution of marine aerosols above the ocean in comparison with measurements. Ingestion of meteorological fields coming from the Meso-NH mesoscale research model will also be introduced in the future to simulate transport at higher resolutions around La Réunion to help study air mass transport on a case study basis.

Code availability. The FLEXPART-AROME code is openly accessible on https://www.flexpart.eu/ (last access: 1 October 2019).

Data availability. Data used for the different tests are available upon request.

Appendix A: Different turbulent modes and their respective input parameters

Table A1 shows the different novel turbulent modes implemented in the FLEXPART-AROME code.

Table A1. Different turbulent options introduced in FLEXPART-AROME and their configuration.

TURB_OPTION		AVTTS		FVTTS	
		1-D	3-D	1-D	3-D
Step TKE	DELTA	10	15	20	25
	BL89	11	16	21	26
	DEARDORFF	12	17	22	27
SDA	DELTA	110	115	120	125
	BL89	111	116	121	126
	DEARDORFF	112	117	122	127

Appendix B: Implementation of the turbulent mixing length parameterizations

The importance of turbulent mixing length in the new modes is the closing of the turbulent parameterization. Without this value, we have no information on how far particles can mix and so we would have no information on the turbulent timescale.

There are three different implementations of turbulent mixing length L_w. The 1-D DELTA L_w is computed as follows:

$$L_w(\text{DELTA, 1-D}) = \min(0.4 * h(k), \Delta z(k)), \tag{B1}$$

where $h(k)$ and $\Delta z(k)$ represent the height and the thickness of the kth model layer, respectively. When simulations are run in the 3-D mode we use the following formula:

$$L_w(\text{DELTA, 3-D}) = \min\left(0.4 * h(k), \sqrt[3]{\Delta x \Delta y \Delta z(k)}\right), \tag{B2}$$

where Δx and Δy represent the horizontal resolutions. The DEARDORFF parameterization is computed by

$$L_w(\text{DEARDORFF}) = \begin{cases} \sqrt{\frac{2\text{TKE}\theta_{v,\text{ref}}}{g\,\partial\theta_v/\partial z}}, & \text{if } \partial\theta_v/\partial z > 0, \\ \Delta z(k), & \text{otherwise.} \end{cases} \tag{B3}$$

Here, TKE is the local turbulent kinetic energy, $\theta_{v,\text{ref}}$ is the virtual potential temperature of the reference state, $\partial\theta_v/\partial z$ is the vertical gradient of the virtual potential temperature and g is earth's gravitational acceleration constant. In FLEXPART-AROME, however, the virtual potential temperature is approximated by the potential temperature, neglecting the humidity effect on the air masses.

The BL89 parameterization computes the distance that an air parcel can travel upward and downwards by using the local turbulent kinetic energy and combines both to compute the turbulent mixing length:

$$\text{TKE} = \int_z^{z+l_{\text{up}}} \frac{g}{\theta_{v,\text{ref}}}(\theta(z') - \theta(z))\text{d}z', \tag{B4}$$

$$\text{TKE} = \int_{z-l_{\text{down}}}^{z} \frac{g}{\theta_{v,\text{ref}}}(\theta(z) - \theta(z'))\text{d}z', \tag{B5}$$

$$L_w(\text{BL89}) = \left(\frac{l_{\text{up}}^{-2/3} + l_{\text{down}}^{-2/3}}{2}\right)^{-3/2}. \tag{B6}$$

These equations are solved on the discrete model layers. As a consequence, the minimal mixing length equals Δz. Similar as in the DEARDORFF parameterization, the virtual potential temperatures are approximated by the potential temperatures. The 1-D and 3-D parameterizations do not differ for both the DEARDORFF and the BL89 parameterizations.

It is important here to note that the DEARDORFF parameterization is the only parameterization that does not have a lower limit based on the grid definition. It only falls back on the minima of the other implementations when its value becomes negative. The lower limit is rather a computational remnant which stems from the minimal time step. In Eq. (3) the dt' has a fixed minimum which means that the turbulent timescale is numerically forced to a specific value. When computing τ_w in Eq. (2), the σ_w value is fixed by the input, which means that when its value is forced by the algorithm, we artificially adapt the turbulent mixing length.

Appendix C: Conservations of well-mixedness over land

Shown in Fig. C1 is the conservation of well-mixedness over land in the morning when the PBL is growing. We see that the DELTA modes all have some accumulation near the surface, the AVTTS SDA mode having the least accumulation, similar to the stable PBL over the sea. A surface accumulation over land in Hanna in the bottom layer of maximum 14.5 %. Comparing the best-performing relevant TURB_OPTION parameters 11 and 111, we see that the accumulation in the Step TKE mode near the surface is 2.0 % larger with the accumulation occurring at the surface from 10 h simulations onward.
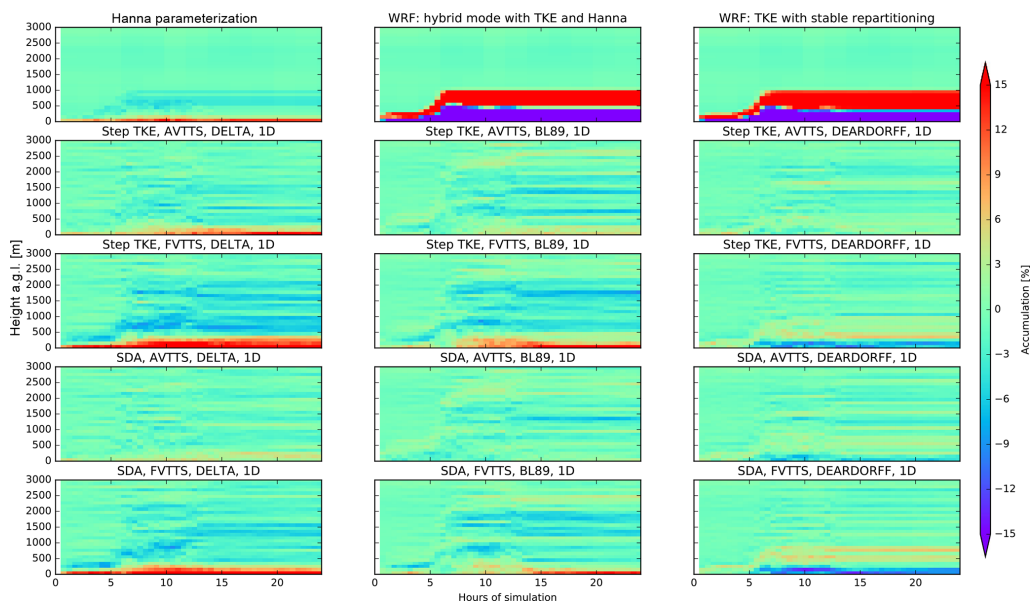
Figure C1. Accumulation in well-mixed test in all different turbulence configurations in FLEXPART-AROME. These tests were run in a column over the ocean surface.

Appendix D: Final vertical distribution in the passive tracer surface release

After the 24 h simulation of a passive tracer released at the surface, final mixing ratio profiles for all tested turbulent modes are shown in Fig. D1. Due to the shallow PBL in the traditional modes the mixing ratios of the FLEXPART-WRF configurations are a factor 2 to 3 larger. The new turbulent modes are all well-mixed near the surface. Due to the shifting convective zone near the top, there is no sharp difference between PBL and FT.
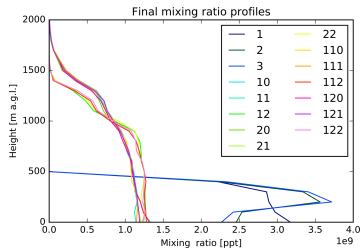
Figure D1. Final mixing ratio profiles in the surface tracers test released over the sea. The legend shows the numerical value of the TURB_OPTION parameter input.

We can clearly see two different kinds of mixing between the DEARDORFF parameterizations on the one hand and the DELTA and BL89 modes on the other hand. While DEAR-DORFF is based on an analytical formula with no real lower limit except the one implicitly imposed by the minimal time step, vertical mixing above the more turbulent layer is slower. This results in a mixing ratio profiles which do not reach as high as the other modes whose lower limit on turbulent mixing length is based on the grid definition.

References

Akritidis, D., Zanis, P., Pytharoulis, I., Mavrakis, A., and Karacostas, T.: A deep stratospheric intrusion event down to the Earth's surface of the megacity of Athens, Meteorol. Atmos. Phys., 109, 9–18, https://doi.org/10.1007/s00703-010-0096-6, 2012.

Alam, J. M. and Lin, J. C.: Toward a Fully Lagrangian Atmospheric Modeling System, Mon. Weather Rev., 136, 4653–4667, https://doi.org/10.1175/2008MWR2515.1, 2008.

Baray, J.-L., Courcoux, Y., Keckhut, P., Portafaix, T., Tulet, P., Cammas, J.-P., Hauchecorne, A., Godin Beekmann, S., De Mazière, M., Hermans, C., Desmet, F., Sellegri, K., Colomb, A., Ramonet, M., Sciare, J., Vuillemin, C., Hoareau, C., Dionisi, D., Duflot, V., Vérèmes, H., Porteneuve, J., Gabarrot, F., Gaudo, T., Metzger, J.-M., Payen, G., Leclair de Bellevue, J., Barthe, C., Posny, F., Ricaud, P., Abchiche, A., and Delmas, R.: Maïdo observatory: a new high-altitude station facility at Reunion Island (21° S, 55° E) for long-term atmospheric remote sensing and in situ measurements, Atmos. Meas. Tech., 6, 2865–2877, https://doi.org/10.5194/amt-6-2865-2013, 2013.

Bertò, A., Buzzi, A., and Zardi, D.: Back-tracking water vapour contributing to a precipitation event over Trentino: a case study, Meteorol. Z., 13, 189–200, https://doi.org/10.1127/0941-2948/2004/0013-0189, 2004.

Bougeault, P. and Lacarrère, P.: Parameterization of Orography-Induced Turbulence in a Mesobeta–Scale Model, Mon. Weather Rev., 117, 1872–1890, https://doi.org/10.1175/1520-0493(1989)117<1872:POOITI>2.0.CO;2, 1989.

Brioude, J., Cooper, O. R., Trainer, M., Ryerson, T. B., Holloway, J. S., Baynard, T., Peischl, J., Warneke, C., Neuman, J. A., De Gouw, J., Stohl, A., Eckhardt, S., Frost, G. J., McKeen, S. A., Hsie, E.-Y., Fehsenfeld, F. C., and Nédélec, P.: Mixing between a stratospheric intrusion and a biomass burning plume, Atmos. Chem. Phys., 7, 4229–4235, https://doi.org/10.5194/acp-7-4229-2007, 2007.

Brioude, J., Kim, S.-W., Angevine, W. M., Frost, G. J., Lee, S.-H., McKeen, S. A., Trainer, M., Fehsenfeld, F. C., Holloway, J. S., Ryerson, T. B., Williams, E. J., Petron, G., and Fast, J. D.: Top-down estimate of anthropogenic emission inventories and their interannual variability in Houston using a mesoscale inverse modeling technique, J. Geophys. Res.-Atmos., 116, D20305, https://doi.org/10.1029/2011JD016215, 2011.

Brioude, J., Arnold, D., Stohl, A., Cassiani, M., Morton, D., Seibert, P., Angevine, W., Evan, S., Dingwell, A., Fast, J. D., Easter, R. C., Pisso, I., Burkhart, J., and Wotawa, G.: The Lagrangian particle dispersion model FLEXPART-WRF version 3.1, Geosci. Model Dev., 6, 1889–1904, https://doi.org/10.5194/gmd-6-1889-2013, 2013.

Cuxart, J., Bougeault, P., and Redelsperger, J.-L.: A turbulence scheme allowing for mesoscale and large-eddy simulations, Q. J. Roy. Meteor. Soc., 126, 1–30, https://doi.org/10.1002/qj.49712656202, 2000.

D'Aulerio, P., Fierli, F., Congeduti, F., and Redaelli, G.: Analysis of water vapor LIDAR measurements during the MAP campaign: evidence of sub-structures of stratospheric intrusions, Atmos. Chem. Phys., 5, 1301–1310, https://doi.org/10.5194/acp-5-1301-2005, 2005.

Deardorff, J. W.: Stratocumulus-capped mixed layers derived from a three-dimensional model, Bound.-Lay. Meteorol., 18, 495–527, https://doi.org/10.1007/BF00119502, 1980.

Emanuel, K. A. and Živković Rothman, M.: Development and Evaluation of a Convection Scheme for Use in Climate Models, J. Atmos. Sci., 56, 1766–1782, https://doi.org/10.1175/1520-0469(1999)056<1766:DAEOAC>2.0.CO;2, 1999.

Forster, C., Stohl, A., and Seibert, P.: Parameterization of Convective Transport in a Lagrangian Particle Dispersion Model and Its Evaluation, J. Appl. Meteorol. Climatol., 46, 403–422, https://doi.org/10.1175/JAM2470.1, 2007.

Gentner, D. R., Ford, T. B., Guha, A., Boulanger, K., Brioude, J., Angevine, W. M., de Gouw, J. A., Warneke, C., Gilman, J. B., Ryerson, T. B., Peischl, J., Meinardi, S., Blake, D. R., Atlas, E., Lonneman, W. A., Kleindienst, T. E., Beaver, M. R., Clair, J. M. St., Wennberg, P. O., VandenBoer, T. C., Markovic, M. Z., Murphy, J. G., Harley, R. A., and Goldstein, A. H.: Emissions of organic carbon and methane from petroleum and dairy operations in California's San Joaquin Valley, Atmos. Chem. Phys., 14, 4955–4978, https://doi.org/10.5194/acp-14-4955-2014, 2014.

Guilpart, E., Vimeux, F., Evan, S., Brioude, J., Metzger, J.-M., Barthe, C., Risi, C., and Cattani, O.: The isotopic composition of near-surface water vapor at the Maïdo Observatory (Reunion Island, Southwestern Indian Ocean) documents the controls of the humidity of the subtropical troposphere: Water vapor isotopes in Reunion Island, J. Geophys. Res.-Atmos., 122, 9628–9650, https://doi.org/10.1002/2017JD026791, 2017.

Hanna, S. R.: Applications in Air Pollution Modeling, 275–310, Springer Netherlands, Dordrecht, https://doi.org/10.1007/978-94-010-9112-1_7, 1982.

Henne, S., Brunner, D., Oney, B., Leuenberger, M., Eugster, W., Bamberger, I., Meinhardt, F., Steinbacher, M., and Emmenegger, L.: Validation of the Swiss methane emission inventory by atmospheric observations and inverse modelling, Atmos. Chem. Phys., 16, 3683–3710, https://doi.org/10.5194/acp-16-3683-2016, 2016.

James, R., Bonazzola, M., Legras, B., Surbled, K., and Fueglistaler, S.: Water vapor transport and dehydration above convective outflow during Asian monsoon, Geophys. Res. Lett., 35, L20810, https://doi.org/10.1029/2008GL035441, 2008.

Lac, C., Chaboureau, J.-P., Masson, V., Pinty, J.-P., Tulet, P., Escobar, J., Leriche, M., Barthe, C., Aouizerats, B., Augros, C., Aumond, P., Auguste, F., Bechtold, P., Berthet, S., Bielli, S., Bosseur, F., Caumont, O., Cohard, J.-M., Colin, J., Couvreux, F., Cuxart, J., Delautier, G., Dauhut, T., Ducrocq, V., Filippi, J.-B., Gazen, D., Geoffroy, O., Gheusi, F., Honnert, R., Lafore, J.-P., Lebeaupin Brossier, C., Libois, Q., Lunet, T., Mari, C., Maric, T., Mascart, P., Mogé, M., Molinié, G., Nuissier, O., Pantillon, F., Peyrillé, P., Pergaud, J., Perraud, E., Pianezze, J., Redelsperger, J.-L., Ricard, D., Richard, E., Riette, S., Rodier, Q., Schoetter, R., Seyfried, L., Stein, J., Suhre, K., Taufour, M., Thouron, O., Turner, S., Verrelle, A., Vié, B., Visentin, F., Vionnet, V., and Wautelet, P.: Overview of the Meso-NH model version 5.4 and its applications, Geosci. Model Dev., 11, 1929–1969, https://doi.org/10.5194/gmd-11-1929-2018, 2018.

Lin, J. C., Gerbig, C., Wofsy, S. C., Andrews, A. E., Daube, B. C., Davis, K. J., and Grainger, C. A.: A near-field tool for simulating the upstream influence of atmospheric observations: The Stochastic Time-Inverted Lagrangian Transport (STILT) model, J. Geophys. Res.-Atmos., 108, https://doi.org/10.1029/2002JD003161, 4492, 2003.

Manning, A. J., Ryall, D. B., Derwent, R. G., Simmonds, P. G., and O'Doherty, S.: Estimating European emissions of ozone-depleting and greenhouse gases using observations and a modeling back-attribution technique, J. Geophys. Res.-Atmos., 108, 4405, https://doi.org/10.1029/2002JD002312, 2003.

MétéoFrance: le modele a maille fine AROME, available at: http://www.meteofrance.fr/prevoir-le-temps/la-prevision-du-temps/le-modele-a-maille-fine-arome, last access: 1 December 2018.

Pisso, I., Sollum, E., Grythe, H., Kristiansen, N., Cassiani, M., Eckhardt, S., Arnold, D., Morton, D., Thompson, R. L., Groot Zwaaftink, C. D., Evangeliou, N., Sodemann, H., Haimberger, L., Henne, S., Brunner, D., Burkhart, J. F., Fouilloux, A., Brioude, J., Philipp, A., Seibert, P., and Stohl, A.: The Lagrangian particle dispersion model FLEXPART version 10.3, Geosci. Model Dev. Discuss., https://doi.org/10.5194/gmd-2018-333, in review, 2019.

Stohl, A.: Operational Emergency Preparedness Modeling-Overview, Chap. 22, 266–269, American Geophysical Union (AGU), https://doi.org/10.1029/2012GM001444, 2013.

Stohl, A. and Thomson, D. J.: A Density Correction for Lagrangian Particle Dispersion Models, Bound.-Lay. Meteorol., 90, 155–167, https://doi.org/10.1023/A:1001741110696, 1999.

Stohl, A., Wotawa, G., Seibert, P., and Kromp-Kolb, H.: Interpolation Errors in Wind Fields as a Function of Spatial and Temporal Resolution and Their Impact on Different Types of Kinematic Trajectories, J. Appl. Meteorol., 34, 2149–2165, https://doi.org/10.1175/1520-0450(1995)034<2149:IEIWFA>2.0.CO;2, 1995.

Stohl, A., Forster, C., Frank, A., Seibert, P., and Wotawa, G.: Technical note: The Lagrangian particle dispersion model FLEXPART version 6.2, Atmos. Chem. Phys., 5, 2461–2474, https://doi.org/10.5194/acp-5-2461-2005, 2005.

Stohl, A., Seibert, P., Arduini, J., Eckhardt, S., Fraser, P., Greally, B. R., Lunder, C., Maione, M., Mühle, J., O'Doherty, S., Prinn, R. G., Reimann, S., Saito, T., Schmidbauer, N., Simmonds, P. G., Vollmer, M. K., Weiss, R. F., and Yokouchi, Y.: An analytical inversion method for determining regional and global emissions of greenhouse gases: Sensitivity studies and application to halocarbons, Atmos. Chem. Phys., 9, 1597–1620, https://doi.org/10.5194/acp-9-1597-2009, 2009.

Thomson, D. J.: Criteria for the selection of stochastic models of particle trajectories in turbulent flows, J. Fluid Mechan., 180, 529–556, https://doi.org/10.1017/S0022112087001940, 1987.

Thomson, D. J., Physick, W. L., and Maryon, R. H.: Treatment of Interfaces in Random Walk Dispersion Models, J. Appl. Meteorol., 36, 1284–1295, https://doi.org/10.1175/1520-0450(1997)036<1284:TOIIRW>2.0.CO;2, 1997.

Tulet, P., Di Muro, A., Colomb, A., Denjean, C., Duflot, V., Arellano, S., Foucart, B., Brioude, J., Sellegri, K., Peltier, A., Aiuppa, A., Barthe, C., Bhugwant, C., Bielli, S., Boissier, P., Boudoire, G., Bourrianne, T., Brunet, C., Burnet, F., Cammas, J.-P., Gabarrot, F., Galle, B., Giudice, G., Guadagno, C., Jeamblu, F., Kowalski, P., Leclair de Bellevue, J., Marquestaut, N., Mékies, D., Metzger, J.-M., Pianezze, J., Portafaix, T., Sciare, J., Tournigand, A., and Villeneuve, N.: First results of the Piton de la Fournaise STRAP 2015 experiment: multidisciplinary tracking of a volcanic gas and aerosol plume, Atmos. Chem. Phys., 17, 5355–5378, https://doi.org/10.5194/acp-17-5355-2017, 2017.

Vogelezang, D. H. P. and Holtslag, A. A. M.: Evaluation and model impacts of alternative boundary-layer height formulations, Bound.-Lay. Meteorol., 81, 245–269, https://doi.org/10.1007/BF02430331, 1996.

Warneke, C., de Gouw, J. A., Del Negro, L., Brioude, J., McKeen, S., Stark, H., Kuster, W. C., Goldan, P. D., Trainer, M., Fehsenfeld, F. C., Wiedinmyer, C., Guenther, A. B., Hansel, A., Wisthaler, A., Atlas, E., Holloway, J. S., Ryerson, T. B., Peischl, J., Huey, L. G., and Hanks, A. T. C.: Biogenic emission measurement and inventories determination of biogenic emissions in the eastern United States and Texas and comparison with biogenic emission inventories, J. Geophys. Res.-Atmos., 115, D00F18, https://doi.org/10.1029/2009JD012445, 2010.

Zannetti, P.: Lagrangian Dispersion Models, 185–222, Springer US, Boston, MA, https://doi.org/10.1007/978-1-4757-4465-1_8, 1990.

Chapter 6

Biomass burning signals at the Maïdo observatory

6.1 Objectives and methodology

Synoptic scale transport towards the Maïdo observatory is clearest from biomass burning (BB) plumes reaching the observatory between August and November every year. We selected six different BB plume intrusions at the observatory to study in greater detail[1]. The objective of this work was to estimate the impact of African and Madagascan burning sources on the atmospheric composition recorded at Maïdo and on the marine boundary layer over the south-west Indian Ocean in general.

The hs-PTR-Quad-MS data set constituted the core data set for this publication but was supplemented by in situ measurements of CO and O_3, and remote sensing data of NO_2. Using FLEXPART-AROME, we found that the plumes were predominantly located in the free troposphere. The chemical makeup of the BB plumes was characterised by using enhancement ratios (EnRs). We also compared the impact of BB plumes on the atmospheric composition simulated with the near-real-time (NRT) atmo-

---

[1] All selected plumes were events in August 2018 and August 2019. The restriction to case studies in August is due to the low background contributions to the biomass burning signals, which would otherwise complicate the data analysis. The selection of the first events of the biomass burning season allows the use of seasonal median diel profiles to characterise the background.

spheric composition model of the Copernicus atmosphere monitoring service (CAMS). As we will see, the CO concentrations were well reproduced by the CAMS-NRT model which validated the CO emissions from the global fire assimilation system (GFAS) inventory and confirmed the limited impact of mesoscale transport on the atmospheric composition at the location of Maïdo during the BB intrusions. This allowed us to use the GFAS CO emissions to simulate the transport of excess CO from pyrogenic emissions using FLEXPART. These simulations were used to i) estimate the average plume age during the different BB intrusions at the observatory, and ii) estimate the impact of BB on the atmospheric composition of the marine boundary layer over the south-west Indian Ocean. The latter was done by combining the FLEXPART simulation of excess CO with the EnRs relative to CO of VOCs using the hs-PTR-Quad-MS data. A paper presenting the performed work was published in the journal Atmospheric Chemistry and Physics in 2020 (Verreyken et al., 2020).

Bibliography

Verreyken, B., Amelynck, C., Brioude, J., Müller, J.-F., Schoon, N., Kumps, N., Colomb, A., Metzger, J.-M., Lee, C. F., Koenig, T. K., Volkamer, R., and Stavrakou, T.: Characterisation of African Biomass Burning Plumes and Impacts on the Atmospheric Composition over the South-West Indian Ocean, Atmospheric Chemistry and Physics, 20, 14 821–14 845, https://doi.org/10.5194/acp-20-14821-2020, 2020.

Atmospheric
Chemistry
and Physics

Characterisation of African biomass burning plumes and impacts on the atmospheric composition over the south-west Indian Ocean

Bert Verreyken[1,2,3], **Crist Amelynck**[1,2], **Jérôme Brioude**[3], **Jean-François Müller**[1], **Niels Schoon**[1], **Nicolas Kumps**[1], **Aurélie Colomb**[4], **Jean-Marc Metzger**[5], **Christopher F. Lee**[6,7], **Theodore K. Koenig**[6,7], **Rainer Volkamer**[6,7], **and Trissevgeni Stavrakou**[1]

[1]Royal Belgian Institute for Space Aeronomy, 1180 Brussels, Belgium
[2]Department of Chemistry, Ghent University, 9000 Ghent, Belgium
[3]Laboratoire de l'Atmosphère et des Cyclones, UMR 8105, CNRS, Université de La Réunion, 97744 Saint-Denis, France
[4]Laboratoire de Météorologie Physique, UMR6016, CNRS, Université Clermont Auvergne, 63178 Aubière, France
[5]Observatoire des Science de l'Univers de La Réunion, UMS3365, 97744 Saint-Denis, France
[6]Cooperative Institute for Research in Environmental Sciences (CIRES), University of Colorado, Boulder, CO, USA
[7]Department of Chemistry, University of Colorado, Boulder, CO, USA

Correspondence: Bert Verreyken (bert.verreyken@aeronomie.be)

Abstract. We present an investigation of biomass burning (BB) plumes originating from Africa and Madagascar based on measurements of a suite of volatile organic compounds (VOCs), carbon monoxide (CO), ozone (O_3) and nitrogen dioxide (NO_2) obtained during the dry season of 2018 and 2019 at the high-altitude Maïdo observatory ($21.1°$ S, $55.4°$ E, 2160 m a.s.l.), located on the remote island of La Réunion in the south-west Indian Ocean (SWIO). Biomass burning plume episodes were identified from increased acetonitrile (CH_3CN) mixing ratios. Enhancement ratios (EnRs) – relative to CO – were calculated from in situ measurements for CH_3CN, acetone (CH_3COCH_3), formic acid (HCOOH), acetic acid (CH_3COOH), benzene (C_6H_6), methanol (CH_3OH) and O_3. We compared the EnRs to emission ratios (ERs) – relative to CO – reported in the literature in order to estimate loss or production of these compounds during transport. For CH_3CN and CH_3COOH, the calculated EnRs are similar to the ERs. For C_6H_6 and CH_3OH, the EnR is lower than the ER, indicating a net sink of these compounds which was found to be in line with the expected atmospheric lifetime. For CH_3COCH_3 and HCOOH, the calculated EnRs are larger than the ERs. The discrepancy reaches an order of magnitude for HCOOH (18–34 pptv ppbv^{-1} compared to 1.8–4.5 pptv ppbv^{-1}). This points to significant secondary production of HCOOH during transport. The Copernicus Atmospheric Monitoring Service (CAMS) global model simulations reproduce the temporal variation of CO mixing ratios well at the observatory but underestimate O_3 and NO_2 mixing ratios in the plumes by on average 16 ppbv and 60 pptv respectively. This discrepancy between modelled and measured O_3 mixing ratios was attributed to (i) large uncertainties in VOC and NO_x ($NO + NO_2$) emissions due to BB in CAMS and (ii) misrepresentation of NO_x recycling in the model during transport. Finally, transport of pyrogenically emitted CO is calculated with FLEXPART in order to (i) determine the mean plume age during the intrusions at the observatory and (ii) estimate the impact of BB on the pristine marine boundary layer (MBL). By multiplying the excess CO in the MBL with inferred EnRs at the observatory, we calculated the expected impact of BB on CH_3CN, CH_3COCH_3, CH_3OH and C_6H_6 concentrations in the MBL. These excesses constitute increases of $\sim 20\%$–150% compared to background measurements in the SWIO MBL reported in the literature.

1 Introduction

Non-methane volatile organic compounds (NMVOCs) are key tropospheric constituents. Many of them are highly reactive with the major atmospheric oxidants, especially with the OH radical, and therefore they strongly affect the oxidation capacity of the troposphere (Atkinson, 2000). By being a strong sink for OH, they also exert control on the lifetime of methane (Zhao et al., 2019) and thus on climate. Moreover, OH-initiated NMVOC oxidation modulates tropospheric O_3 concentrations and is the major source of this secondary pollutant in high-NO_x ($NO + NO_2$) environments (Monks et al., 2015). Less volatile NMVOC oxidation products contribute to the formation and growth of secondary organic aerosol, which deteriorates air quality and affects radiative forcing, and hence climate, both in a direct (by interacting with solar radiation) and indirect way (by acting as cloud condensation nuclei) (IPCC, 2013).

Whereas atmospheric oxidation of precursor VOC species is the dominant source of many oxygenated VOCs (OVOCs), primary anthropogenic emissions and (bidirectional) exchange with the biosphere and the ocean and biomass and biofuel burning also contribute to the atmospheric OVOC burden (Mellouki et al., 2015). Photochemical degradation and dry and wet deposition are the major sink processes. Global OVOC budgets are still prone to large uncertainties due to an incomplete understanding of direct emissions, photochemical production and loss processes, ocean–atmosphere exchange (Millet et al., 2010; Fischer et al., 2012; Read et al., 2012; Wang et al., 2019), and a paucity of (O)VOC data, especially in remote marine areas where the oxidative capacity of the atmosphere is mainly controlled by OVOCs in comparison to all other NMVOCs (Lewis et al., 2005; Carpenter and Nightingale, 2015; Travis et al., 2020).

The south-west Indian Ocean (SWIO) is one of the few pristine regions on Earth. It is largely decoupled from emissions originating from large bodies of land and is well suited to characterise remote marine air composition and ocean emissions (Colomb et al., 2009; Mallet et al., 2018). Located in the SWIO is the French overseas department La Réunion, a small volcanic island, home to the high-altitude Maïdo atmospheric observatory (21.1° S, 55.4° E, 2160 m a.s.l.) (Baray et al., 2013), hereafter referred to as RUN. From October 2017 to November 2019, a high-sensitivity quadrupole-based proton transfer reaction mass spectrometry VOC analyser (hs-PTR-MS) was deployed at RUN in the framework of the OCTAVE (Oxygenated Compounds in the Tropical Atmosphere: Variability and Exchanges) project (http://octave. aeronomie.be, last access: 25 October 2020). In combination with other ground-based and satellite data, the resulting near-continuous high-time-resolution 2-year dataset will serve to better constrain VOC emissions in the remote tropical marine atmosphere and to identify missing sources. Part of this dataset has already been used in a source apportionment study of formaldehyde (HCHO) (Rocco et al., 2020).

The present paper contributes to the disentanglement of the different sources contributing to the (O)VOC composition at RUN by focusing on the role of biomass burning (BB). It is established from ground-based remote-sensing Fourier transform infrared (FTIR) observations that BB impacts the atmosphere over La Réunion. The BB events affecting the region occur most frequently in southern Africa and Madagascar, but impacts from burning in South America and Malaysia have also been identified (Duflot et al., 2010; Vigouroux et al., 2012). Seasonality of in situ CO concentrations at RUN indicates that BB plumes also impact the atmospheric composition at the surface (Zhou et al., 2018). This was confirmed by the hs-PTR-MS dataset generated at RUN for the OCTAVE project (Fig. A1). Biomass burning represents the second largest global source of NMVOC emissions (Yokelson et al., 2008; Akagi et al., 2011). Pyrogenic emissions are reasonably well constrained by numerous laboratory studies (e.g. Holzinger et al., 1999; Christian et al., 2003; Yokelson et al., 2008) and observations of BB plumes in the atmosphere (e.g. Lefer et al., 1994; Yokelson et al., 1999, 2003; Jost et al., 2003; de Gouw et al., 2006; Vigouroux et al., 2012; Akagi et al., 2014). Emission factors for numerous compounds have been compiled recently by Andreae (2019). The investigation of compositional changes during BB plume transport may provide valuable clues for identifying missing sources of reactive trace species (e.g. Jost et al., 2003; de Gouw et al., 2006; Chaliyakunnel et al., 2016). This is of particular interest for the carboxylic acids, as current models underestimate their observed abundances, possibly in part due to a misrepresentation of the contribution of biomass burning (Paulot et al., 2011; Chaliyakunnel et al., 2016).

In this work, we focused on the first BB plume intrusions from the fire season in 2018 and 2019. Enhancement ratios (EnRs) – relative to excess CO – of excess acetonitrile (CH_3CN), formic acid (HCOOH), acetone (CH_3COCH_3), acetic acid (CH_3COOH), benzene (C_6H_6), methanol (CH_3OH) and O_3 were calculated from in situ measurements at RUN for the first time. Other VOCs could also be present in the BB plumes but either were not the focus of this study or local emissions from the island interfered too much with the signal to reliably quantify the EnRs (e.g. methyl ethyl ketone, MEK). In addition, observations of BB plumes at RUN were used to evaluate the global near-real-time (NRT) CO, O_3 and NO_2 modelled concentrations at RUN from the Copernicus Atmospheric Monitoring Service (CAMS). Finally, we propose a way to use in situ VOC measurements at RUN to estimate the impact of BB plumes on the pristine marine boundary layer (MBL) over the SWIO. This is done for CH_3CN, CH_3COCH_3, C_6H_6 and CH_3OH.

In Sect. 2 the instruments, methods and models used in this study are presented. The results are shown in Sect. 3 and discussed in Sect. 4.

2 Observations and methods

2.1 Observations

2.1.1 In situ air mass characterisation

RUN houses routine instruments characterising in situ air constituents in the context of global networks such as GAW (Global Atmospheric Watch), ICOS (Integrated Carbon Observation System) and ACTRIS (European Research Infrastructure for the observation of Aerosol, Clouds and Trace Gases). A summary of routine measurements from the observatory used in this study is shown in Table 1. A detailed description of these and other operational routine instruments at the observatory can be found in Duflot et al. (2019), Baray et al. (2013) and Zhou et al. (2018).

In the frame of the OCTAVE project, a hs-PTR-MS instrument (Ionicon Analytik GmbH, Austria) was deployed at RUN from October 2017 to November 2019. This resulted in a near-continuous high-time-resolution 2-year dataset of volatile organic compounds (VOCs). The instrument was run in the multiple ion detection mode using H_3O^+ precursor ions with a total cycle time of ~ 2.7 min. Regular calibrations of the hs-PTR-MS were performed by diluting a gravimetrically prepared VOC/N_2 mixture (Apel-Riemer Environmental Inc., Miami, FL, USA; stated accuracy of 5 % for all VOCs) with zero-VOC air obtained by sending ambient air through a catalytic converter (Parker, type HPZA-3500, Haverhill, MA, USA). This resulted in VOC concentrations in the lower range of parts per billion by volume (ppbv). Calibrations as a function of relative humidity were performed bimonthly by controlling the humidity of the zero air with a dew point generator (LI-COR LI610, Lincoln, Nebraska, USA). The calibration factor (CF) for acetic acid (CH_3COOH) was estimated from the experimentally determined CF for CH_3COCH_3. This is done by considering the calculated collision rate constants of H_3O^+ with CH_3COOH and CH_3COCH_3 (Su, 1994), the contributions of the protonated molecules to the respective product ion distributions (Schwarz et al., 2009; Inomata and Tanimoto, 2010), and by assuming the same hs-PTR-MS transmission efficiency for ions with a mass difference of 2 Da. Similarly, the CF of HCOOH was determined from the measured one of acetaldehyde. The humidity dependence of formic and acetic acid CFs obtained at similar hs-PTR-MS operating conditions has been reported in the literature (Baasandorj et al., 2015) and has been taken into account for quantification. By considering the uncertainties in the different parameters involved in the carboxylic acid quantification in the present study, the total uncertainty in their mixing ratio is estimated to be 50 %. Measurements were averaged over 1 h to lower the limit of detection (LoD) and the random fluctuations of the measurements. A list of masses, and their associated compound(s), recorded by the hs-PTR-MS together with the LoD, dwell

time and whether the compounds are directly calibrated is shown in Table 2.

2.1.2 Ground-based remote sensing

The University of Colorado Multi-AXis Differential Optical Absorption Spectroscopy (CU MAX-DOAS) instrument consists of a scanning (horizon–zenith–horizon) telescope coupled to two ultraviolet–visible grating spectrometers (Coburn et al., 2011). Scattered-light solar spectra are collected along lines of sight at different elevation angles above the horizon (Hönninger et al., 2004) and analysed using DOAS least-square fitting (Platt and Stutz, 2008) to retrieve trace gas slant column densities (SCDs) by the QDOAS software package (Danckaert et al., 2017). For this analysis, NO_2 (Vandaele et al., 1998) and O_2–O_2 (Thalman and Volkamer, 2013) were retrieved in a fitting window from 425 to 490 nm, using the further fit settings as described in Kreher et al. (2020). Near-surface volume mixing ratios of NO_2 were retrieved from limb (0° elevation angle) spectra following Dix et al. (2016). This approach takes advantage of the fact that the limb-viewing geometry is highly sensitive to absorbers near instrument altitude. O_2–O_2 is used to parameterise aerosol extinction near instrument altitude, avoiding the need for complex aerosol profile information (Sinreich et al., 2013; Dix et al., 2016). The NO_2 profile shape was constructed using a typical tropical background with BB enhancements collocated to excess CO from FLEXPART (see Sect. 2.3.2). Variations on the retrieval settings and profile assumptions indicate that ~ 10 pptv NO_2 can be quantified with an uncertainty of 5 pptv using this approach. Further tests using NO_2 and O_4 at shorter wavelengths (Kreher et al., 2020) determined that the retrieved NO_2 volume mixing ratios generally agree within the reported uncertainty, despite the different spectral ranges' average NO_2 over different horizontal spatial scales. This indicates that the NO_2 mixing ratio is representative of the regional lower troposphere predicted by the CAMS model.

2.2 Enhancement ratios

The impact of BB events on an atmospheric species X is often quantified by an emission factor (EF_X) or an enhancement ratio relative to a compound Y ($EnR_{X/Y}$). The first is defined as the mass of compound X that is released by burning 1 kg of dry fuel, whereas the second is defined as the excess mixing ratio – due to BB – of compound X (ΔX), with respect to that of a reference species Y (ΔY). If the EnR is measured close to the source and/or if both X and Y were minimally affected by physico-chemical interactions, it is also referred to as the emission ratio of compound X normalised to Y ($ER_{X/Y}$). The ER can be computed from the EF by taking the molecular weights (MWs) of both species into

Table 1. In situ routine observations at RUN and their respective limits of detection (LoDs) and statistical uncertainties (σ) (Zhou et al., 2018; Duflot et al., 2019).

Compound	Instrument	Technique	LoD (ppbv)	σ (ppbv)
CO	Picarro G2401	Cavity ring down spectroscopy	1	1.5
O_3	Thermo Scientific model 49i	UV photometric analyser	0.05	1

Table 2. A list of mass-to-charge ratios (m/z) observed in multiple ion detection mode by the hs-PTR-MS at RUN with the associated chemical compounds, dwell times and information about the instrument calibration limit of detection (LoD) per compound (Y: yes, N: no, n/a: not applicable). Dwell time is shown for one cycle. The LoD is computed for the hourly averages used here. The corresponding accumulated dwell times are about 22 times the stated dwell times of an individual cycle.

m/z	Compound	Dwell time (s)	Calibrated	LoD (pptv)
21	$H_3^{18}O^+$	2	n/a	n/a
31	formaldehyde (HCHO)	10	Y	100
32	O_2^+	0.1	n/a	n/a
33	methanol (CH_3OH)	10	Y	40
37	$H_3O^+ \cdot H_2O$	0.1	n/a	n/a
42	acetonitrile (CH_3CN)	10	Y	1
45	acetaldehyde (CH_3CHO)	10	Y	18
47	formic acid (HCOOH)	10	N	50
59	acetone (CH_3COCH_3)	10	Y	4
61	acetic acid (CH_3COOH)	10	N	7
63	dimethyl sulfide (DMS)	10	Y	6
69	isoprene (C_5H_8)	10	Y	5
71	methyl vinyl ketone (MVK)/methacrolein (MACR)/	10	Y	2
	hydroxy hydroperoxides from isoprene (ISOPOOH)			
73	methyl ethyl ketone (MEK)	10	Y	3
79	benzene (C_6H_6)	10	Y	2
81	sum of monoterpenes[a] ($C_{10}H_{16}$)	10	Y	5
93	toluene (C_7H_8)	10	Y	7
107	xylenes[a] (C_8H_{10})	10	Y	7
137	sum of monoterpenes[a] ($C_{10}H_{16}$)	10	Y	8

[a] o-Xylene and limonene were used for calibration.

account:

$$\mathrm{ER}_{X/Y} = \frac{\mathrm{EF}_X}{\mathrm{EF}_Y} \frac{\mathrm{MW}_Y}{\mathrm{MW}_X}. \tag{1}$$

A list of EFs with the associated fuel type has been compiled most recently by Andreae (2019). When comparing the EnR values derived from our observations to ERs from the literature, production and loss of plume constituents during transport should be taken into consideration. Enhancement and emissions ratios are often used with CO as the reference species Y. Hereafter, enhancement ratios are always considered with respect to CO unless specifically stated otherwise.

Excess mixing ratios are determined above the background – unaffected by BB – diel profiles which were approximated by the seasonal median diel profiles (Appendix A2). During the day, mesoscale transport at La Réunion results in the observatory being located in the planetary boundary layer (PBL). The chemical composition of the PBL is determined by marine, biogenic and anthropogenic sources and sinks interacting in physico-chemical atmospheric processes. At night, air masses arriving at RUN originate primarily from the free troposphere (FT). This mesoscale transport results in a natural diel variation of compound mixing ratios which needs to be taken into account when calculating EnR.

2.3 Modelling

Below we discuss the model simulations used in this study. Each model is used with a specific goal in mind. First, we evaluate the CAMS NRT atmospheric composition service using in situ measurements. It is important that CAMS correctly reproduces CO concentrations at RUN as pyrogenic emissions used in this service will be used to calculate transport of excess CO (ΔCO) over the SWIO with the Lagrangian FLEXible PARTicle dispersion model, FLEXPART (Stohl et al., 1998, 2005; Stohl and Thomson, 1999; Pisso et al., 2019). We use FLEXPART to calculate the mean plume ages during the BB episodes at RUN but also to calcu-

late the impact of pyrogenic emissions on the pristine MBL over the SWIO. Finally FLEXPART-AROME (Verreyken et al., 2019) is used to simulate mesoscale transport in complex terrain towards the observatory. This last simulation is performed in an effort to quantify the PBL–FT mixing during BB intrusions and identify the main transport mode of the plumes.

2.3.1 CAMS NRT

The CAMS NRT service was developed based on a series of Monitoring Atmospheric Composition and Climate (MACC) research projects. It provides daily forecasts of reactive trace gases, greenhouse gases and aerosol concentrations. The data are generated by the Integrated Forecast System (IFS) at the European Centre for Medium-Range Weather Forecasts (ECMWF). The chemical mechanism used is an extended version of the Carbon Bond 2005 lumped chemistry scheme (Flemming et al., 2015). BB emissions implemented in the NRT service rely on the Global Fire Assimilation System v1.2 (GFAS v1.2) inventory. The GFAS assimilates fire radiative power observations from the NASA MODIS satellites to quantify BB emissions (Di Giuseppe et al., 2018; Rémy et al., 2017; Kaiser et al., 2012). On 9 July 2019, the model was updated to use the CAMS emission inventories, CAMS_GLOB_ANT v2.1 and CAMS_GLOB_BIO v1.1 (Granier et al., 2019), instead of the previous MACCity (Lamarque et al., 2010) and the MEGAN_MACC (Sindelarova et al., 2014) inventories. BB plume injection heights were also introduced in this update. A full description and validation of the update was reported by Basart et al. (2019).

We used modelled mass mixing ratios at the location of RUN calculated on different pressure levels (1000, 950, 925, 900, 850, 800, 700 and 600 mbar levels) every 3 h (00:00, 03:00, 06:00, 09:00, 12:00, 15:00, 18:00, 21:00 UT) from the midnight forecast at $0.5° \times 0.5°$ resolution (available at: https://apps.ecmwf.int/datasets/data/cams-nrealtime/levtype=pl/, last access: 9 January 2020). The CO, O_3 and NO_2 mass mixing ratios are transformed to volume mixing ratios and compared to the in situ measurements.

2.3.2 FLEXPART

FLEXPART, driven by ECMWF IFS meteorology at $0.5° \times 0.5°$ horizontal resolution, was used to calculate the transport of ΔCO due to BB during 15 June–31 August 2018 and 17 June–22 August 2019. The CO emissions are provided by the GFAS v1.2 inventory. Three-hourly mean mixing ratios of CO were generated on vertical layers of 500 m depth between 0 and 3500 m a.g.l. The output was given on a $0.5° \times 0.5°$ grid. Due to the low horizontal resolution, the orographic profile of La Réunion is not well resolved. For example, the ground level of RUN is only 284 m a.s.l. in the model, much below the true altitude of 2160 m a.s.l.

Age classes (ACs) are used to estimate the mean plume age (T) for the different intrusions. The CO plumes are categorised by age with 2 d resolution ($T_{AC} = 1 \pm 1$, 3 ± 1, …, 23 ± 1 d). BB plume excesses are traced for 24 d, after which the plume is assumed to be diluted to negligible background levels. The mean BB plume age is obtained from the FLEXPART output by

$$T = \frac{\sum_{j=0}^{11} \Delta CO_j \times T_j}{\sum_{j=0}^{11} \Delta CO_j}, \qquad (2)$$

where ΔCO_j is the mean mixing ratio calculated by FLEXPART with $AC = j$.

To estimate the impact of BB on the MBL for compound X, we use

$$\Delta X_{estimate} = \Delta CO \times EnR_X, \qquad (3)$$

where ΔCO is calculated by FLEXPART and EnR_X is inferred from data. In this approach, the role of an ocean sink is neglected.

2.3.3 FLEXPART-AROME

FLEXPART-AROME 24 h back-trajectory simulations are used to estimate the respective contribution of the PBL and the free troposphere to the in situ measurements at RUN. Lesouëf et al. (2011) characterised the PBL impact on the Maïdo mountain region by using a passive boundary layer tracer initialised in an approximation of the minimal boundary layer. This PBL proxy is defined as 500 m a.g.l., capped at 1000 m a.s.l. Here, the inverse approach is used by calculating the fraction of time air parcels have spent in the PBL proxy during the 24 h back-trajectory simulation. This fraction measures the potential impact of surface emissions on the in situ measurements. We will split this fraction up according to surface type (land/ocean) and call the separate components the mixing fraction (MF). Given the lack of a high-resolution anthropogenic emission inventory over La Réunion, we are not able to use the model to quantify mixing ratios unperturbed by BB plumes and instead use the median diel profile as stated in Sect. 2.2.

3 Results

3.1 Data analysis

Six episodes of enhanced CH_3CN, which is a typical BB compound, were identified in August 2018 and August 2019 (Fig. 1). The correlation (r) between the excess mixing ratio of the monitored trace gases and ΔCH_3CN, during the identified intrusions, is shown in Table 3. As dimethyl sulfide (DMS) is only marginally present in pyrogenic emissions

Table 3. Pearson correlation coefficients (r) between the excess of chemical compound X (ΔX) and the excess of the typical BB marker CH_3CN during the BB episodes.

X	r	X	r
CO	0.98	DMS	0.60
HCOOH	0.89	HCHO	0.55
CH_3COCH_3	0.88	MEK	0.39
CH_3COOH	0.87	CH_3CHO	0.12
O_3	0.83	C_5H_8	−0.08
C_6H_6	0.81	MVK/MACR/ISOPOOH	−0.22
CH_3OH	0.71		

(0.0022–0.05 g emitted per kilogram of dry matter burned from tropical forest and agricultural residue burning respectively, Andreae, 2019) and has a short atmospheric lifetime (less than 1 d, Blake et al., 1999), the correlation between ΔDMS and ΔCH_3CN is not expected to be directly related to the BB emissions. For this reason, compounds that correlated less well with ΔCH_3CN than ΔDMS were not considered as plume constituents. Plume constituents in this analysis are thus limited to CH_3CN, HCOOH, CH_3COCH_3, CH_3COOH, O_3, C_6H_6 and CH_3OH.

Mean background (i.e. outside BB episodes) concentrations of plume constituents in austral winter together with the mean excesses during the different BB intrusions (in percentage) are shown in Table 4. Correlation with CH_3CN is especially strong for compounds showing large excesses compared to the diel background pattern (illustrated in Appendix A2). We note that trace species such as HCHO, MEK and acetaldehyde (CH_3CHO) show elevated concentrations during the night in BB episodes, which suggests that they are related to BB. However, as the diel patterns for these compounds are subject to strong variability, excesses are poorly characterised during the day and not analysed further here.

For each of the intrusions, the EnR is computed for CH_3CN, CH_3OH, CH_3COCH_3, C_6H_6, HCOOH, CH_3COOH and O_3. Figure 1 shows the scatter plots correlating the excess of the trace species monitored by the hs-PTR-MS instrument and ΔCO. The calculated EnRs are found in Table 5.

3.2 Comparison with model

3.2.1 FLEXPART-AROME

Figure 2 shows the fraction of time spent in the PBL-proxy from Lesouëf et al. (2011) over sea (blue) and land (brown), during the 24 h back-trajectory calculations with FLEXPART-AROME, together with the relative humidity (RH) at the observatory. Biomass burning intrusions have lower than average RH values. The humidity peaks during the BB episodes are coincident with peak impacts of the MBL. It is also shown that the impact of mesoscale PBL

emissions on the VOC concentrations is lower during the BB intrusions in August 2018 than in August 2019.

3.2.2 CAMS near-real-time model simulations

The modelled mixing ratios at RUN calculated by the CAMS NRT service are compared to data recorded at the observatory for CO, O_3 and NO_2 (Fig. 3). The model bias for CO, during the BB intrusions, is lowest on the 800 mbar pressure level (bias of 9.7 ppbv), which is closest to the mean pressure measured at the observatory during the same period (792.8 mbar). Note that CAMS reflects the CO mixing ratios well at Maïdo both during and outside (5.1 ppbv bias) BB episodes. As CO is a chemically stable compound in the atmosphere, the agreement between model and measurements indicates that synoptic-scale transport and mesoscale mixing with the BB plumes at the location of RUN is sufficiently reproduced by the CAMS NRT model.

The O_3 model bias is 16 ppbv during the BB episodes with a maximum bias of 39 ppbv (67 % above the calculated value). Outside the BB episodes, the CAMS O_3 concentrations show only a small bias (0.8 ppbv), within the uncertainty of measurements. This good agreement outside of the BB events suggests that mesoscale O_3 sources and sinks either have a limited impact or are correctly calculated by the model at the location of RUN.

The NO_2 bias reaches 60 pptv during BB episodes, while it is only 9 pptv (within 10 pptv DOAS accuracy error) in other periods. Note that the NO_2 measurements are from the ground-based remote sensing CU MAX-DOAS instrument and reflect the NO_2 mixing ratio in the lower free troposphere. The large discrepancy in modelled and measured NO_2 on 3 August 2019 may be due to a weak BB plume passing near RUN (Appendix B).

3.2.3 FLEXPART forward simulation

A comparison between ΔCO obtained from measurements and the calculated ΔCO from transport of the GFAS v1.2 emission inventory, simulated by FLEXPART, is shown in Fig. 4. Due the misrepresentation of the orographic profile of La Réunion, ground level at the location of the observatory is only 284 m a.s.l. in the model. The real altitude of RUN (2160 m a.s.l.) is situated near the boundary between layers 1500–2000 and 2000–2500 m a.g.l. in the FLEXPART output. In reality, mesoscale transport, not resolved in FLEXPART, mixes the different vertical layers, and data recorded at Maïdo correspond to a mixture between different output levels. In what follows, we consider RUN to be located in the layer between 2000 and 2500 m a.g.l.

The model overestimates ΔCO mixing ratios at RUN by 37 and 17 ppbv on average during the BB episodes in 2018 and 2019 respectively. Peak differences between modelled and observed mixing ratios are 340 ppbv during the BB episodes in 2018 and 162 ppbv during those in 2019. The
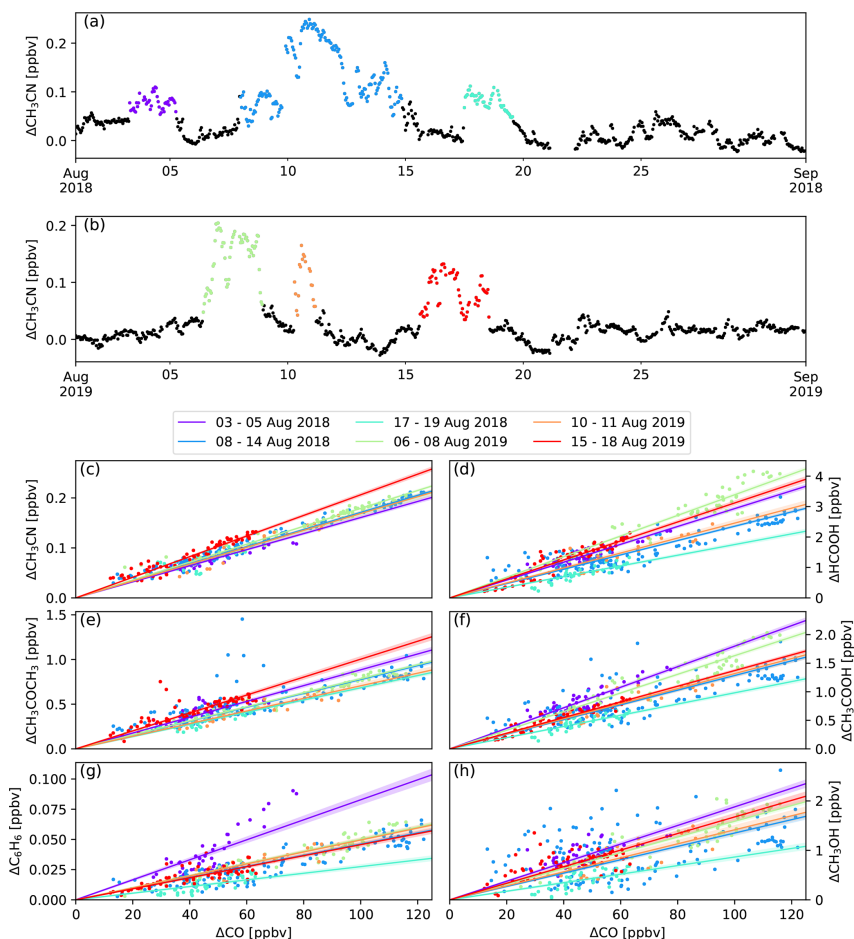
Figure 1. Panels (a) and (b) show the six BB intrusions identified using ΔCH_3CN (purple: 3–5 August 2018, blue: 8–14 August 2018, cyan: 17–19 August 2018, green: 6–8 August 2019, orange: 10–11 August 2019, red: 15–18 August 2019). The bottom six panels show the EnR fits for CH_3CN (c), $HCOOH$ (d), CH_3COOH (e), CH_3COCH_3 (f), C_6H_6 (g) and CH_3OH (h). EnRs are normalised to the excess mixing ratio of CO for the six intrusions in the colours used in panels (a) and (b). Uncertainty in the linear regression is shown as a coloured band around the curves.

model bias outside BB episodes, decreases to 3 ppbv for both 2018 and 2019.

As the timing of BB intrusions is well represented in the model, as can be visually confirmed from Fig. 4, calculated mean plume ages during the different episodes are expected to be accurate. The calculated plume ages are, in chronological order of arrival at RUN, 7.5, 10.6 and 11.3 d in 2018 and 7.4, 9.3 and 13.7 d in 2019.

4 Discussion

4.1 Transport and dominant sink

The relative humidity during the BB intrusions was generally low (see Fig. 2). Peak RH values correspond to a large impact of the MBL and often lower ΔCH_3CN concentration (e.g. 7 and 17 August 2019, Fig. 2). From this, we expect the plume to be primarily located in the free troposphere, which is drier than the PBL. This is consistent with results

Table 4. Mean background mixing ratio during the daytime (10:00–16:00 LT, reflecting planetary boundary layer air composition) and nighttime (22:00–04:00 LT, measuring free tropospheric air masses), μ_{PBL} (ppbv) and μ_{FT} (ppbv) respectively, and mean excesses (%) during the August 2018 and August 2019 BB intrusions. The reported background values are mean mixing ratios recorded during austral winter (June, July, August), excluding BB incidents.

	μ_{PBL} (ppbv)	μ_{FT} (ppbv)	3–5 Aug 2018	8–14 Aug 2018	17–19 Aug 2018	6–8 Aug 2019	10–11 Aug 2019	15–18 Aug 2019
CH_3CN	0.091 (0.035)	0.092 (0.042)	96 %	164 %	99 %	182 %	128 %	103 %
CO	67 (15)	61 (17)	81 %	129 %	78 %	140 %	110 %	68 %
HCOOH	0.87 (0.62)	0.40 (0.62)	466 %	630 %	285 %	942 %	515 %	379 %
CH_3COCH_3	0.40 (0.17)	0.30 (0.19)	153 %	221 %	118 %	227 %	157 %	147 %
CH_3COOH	0.40 (0.30)	0.17 (0.31)	709 %	893 %	398 %	1155 %	754 %	450 %
C_6H_6	0.025 (0.014)	0.012 (0.012)	303 %	314 %	123 %	360 %	274 %	156 %
CH_3OH	1.2 (0.42)	0.63 (0.36)	131 %	163 %	63 %	188 %	132 %	101 %

Table 5. Calculated EnRs (pptv ppbv^{-1}) – relative to CO – for the identified BB intrusions. Between parentheses are the standard deviations of the EnR (pptv ppbv^{-1}) obtained from the linear fit.

	3–5 Aug 2018	8–14 Aug 2018	17–19 Aug 2018	6–8 Aug 2019	10–11 Aug 2019	15–18 Aug 2019
CH_3CN	1.61 (0.02)	1.71 (0.01)	1.69 (0.04)	1.79 (0.01)	1.69 (0.04)	2.06 (0.03)
HCOOH	29.3 (0.5)	23.5 (0.3)	17.5 (0.5)	33.8 (0.5)	24.6 (0.9)	31.2 (0.6)
CH_3COCH_3	8.85 (0.22)	7.76 (0.13)	6.84 (0.14)	7.85 (0.08)	7.06 (0.26)	10.0 (0.3)
CH_3COOH	18.0 (0.3)	12.9 (0.2)	9.8 (0.3)	16.3 (0.2)	13.2 (0.5)	13.7 (0.2)
O_3	640 (19)	438 (9)	635 (27)	461 (9)	410 (20)	422 (16)
C_6H_6	0.83 (0.04)	0.46 (0.01)	0.27 (0.01)	0.50 (0.01)	0.50 (0.02)	0.46 (0.02)
CH_3OH	18.8 (0.6)	13.5 (0.4)	8.7 (0.5)	15.9 (0.3)	14.2 (0.8)	16.8 (0.7)

from FLEXPART (Fig. 4), where ΔCO is especially significant in layers above 1500 m a.g.l. The same is also found from the CAMS NRT model where elevated CO mixing ratios are calculated between the 850 and 700 mbar pressure levels ($\sim$ 1500–3000 m a.s.l.). As the BB plume is primarily located in the FT during austral winter (the dry season) we expect that wet deposition is negligible for all compounds.

4.2 Plume characterisation

The emission ratios – computed based on emission factors from Andreae (2019) – of CH_3CN, HCOOH, CH_3COOH, CH_3COCH_3, C_6H_6 and CH_3OH are shown in Table 6. Possible fuel types for BB plumes arriving at RUN are savanna and grassland, tropical forest, or agricultural residue. Enhancement ratios are compared to the emission ratios to check for consistency with accepted knowledge regarding sources and sinks during transport.

4.2.1 Acetonitrile, acetone, methanol and benzene

During the synoptic-scale transport in the free troposphere, the photochemical sink is expected to be dominant over wet scavenging. As the lifetime with regards to this sink is larger than the maximum plume age (13.7 d) for both CH_3CN (τ_{CH_3CN} = 1.4 years, de Gouw et al., 2003) and CH_3COCH_3 ($\tau_{CH_3COCH_3}$ = 36–39 d, Arnold et al., 2005; Fischer et al., 2012), the EnRs are expected to correspond well with the ERs from the literature. This is the case for CH_3CN (Table 6).

In contrast, the EnR of acetone ($\sim$ 8 pptv ppbv^{-1}) is at least a factor of $\sim$ 2 larger than the ER from the literature (Table 6), a likely indication of secondary CH_3COCH_3 formation in the BB plume. Acetone production has been recorded in BB plumes over the eastern Mediterranean (Holzinger et al., 2005) and over Namibia (Jost et al., 2003). In contrast, aged BB plumes over eastern Canada and Alaska did not show evidence of acetone production (de Gouw et al., 2006). Known pyrogenic CH_3COCH_3 precursors are propane, i-butane and i-butene (Singh et al., 1994). Using the EFs from Andreae (2019), we find $ER_{propane}$ = 1.2–3.2 pptv ppbv^{-1}, $ER_{i\text{-butane}}$ = 0.05–0.1 pptv ppbv^{-1} and $ER_{i\text{-butene}}$ = 0.30–0.52 pptv ppbv^{-1}. Taking these known precursors of secondary CH_3COCH_3 into account, as well as acetone formation yields at high NO_x estimated based on the Master Chemical Mechanism MCMv3 (http://mcm.leeds.ac.uk/MCM/, last access: 4 June 2020) (Saunders et al., 2003), the secondary production of acetone can be estimated. It is found to enhance the acetone EnR by 1.16–2.80 pptv ppbv^{-1}, therefore explaining the major part of the discrepancy. This is at odds with results from Jost et al. (2003) where fast CH_3COCH_3 production is observed and propane could not be considered as a precursor since this conversion is a slow process.

Both methanol and benzene have shorter expected lifetimes compared to the age of the BB plume arriving at RUN: τ_{CH_3OH} = 7 d (Jacob et al., 2005), $\tau_{C_6H_6}$ = 9 d (Monod et al., 2001). This is consistent with the reduced EnRs inferred from
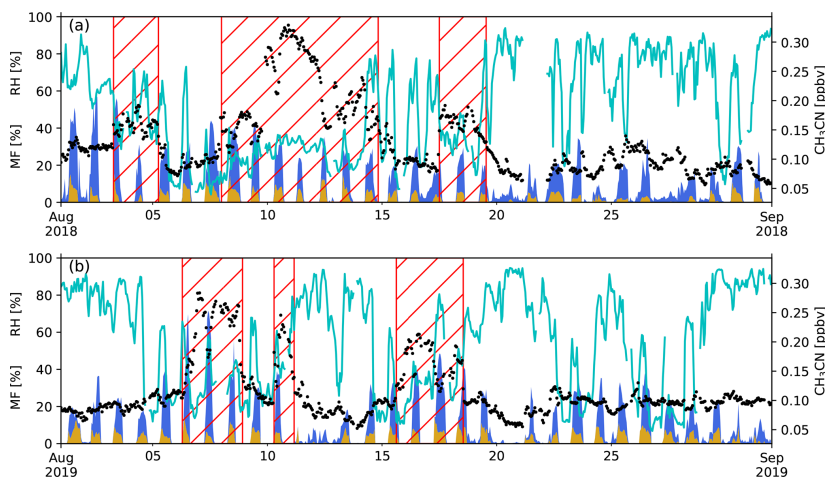
Figure 2. Measured relative humidity (RH, cyan curve), CH_3CN mixing ratio (ppbv) (black points) and modelled mesoscale MF (fraction of time air parcels are situated over a certain source in the PBL proxy from Lesouëf et al., 2011) (%) from 24 h back-trajectories using FLEXPART-AROME in August 2018 **(a)** and August 2019 **(b)**. Blue denotes the marine boundary layer MF, brown represents the island surface PBL MF. The hatched red area represents the different BB intrusions.

Table 6. ER (pptv ppbv^{-1}) – relative to CO – for the three most probable fuel types (savanna and grassland, tropical forest, and agricultural residue) of the BB plume sampled at RUN. Between parentheses is the uncertainty obtained by combining the standard deviations of the EFs recorded by Andreae (2019).

	CH_3CN	HCOOH	CH_3COOH	CH_3COCH_3	C_6H_6	CH_3OH
Savanna and grassland	1.68 (1.62)	1.85 (1.59)	15.6 (10.3)	3.28 (2.24)	1.72 (0.87)	17.1 (21.1)
Tropical forest	3.21 (3.10)	2.87 (2.47)	14.8 (9.76)	2.92 (-)	1.31 (0.664)	23.5 (29.1)
Agricultural residue	2.24 (2.17)	4.48 (3.86)	37.4 (24.7)	4.5 (3.07)	1.27 (0.646)	38.0 (46.9)
Vigouroux et al. (2012)[a]		4.6 (0.3)				11.6 (0.6)
de Gouw et al. (2006)[b]	1.18 (0.14)–3.24 (0.09)		0.9 (0.3)–12.9 (0.5)	2.6 (0.3)–22.8 (1.0)	0.8 (0.2)–1.41 (0.04)	2 (2)–21 (2)
Lefer et al. (1994)[c]		8.2–62	6–34			
This work[d]		1.76 (0.146)	26.7 (5.44)	14.0 (2.61)	8.06 (1.09)	0.50 (0.16)	14.6 (3.18)

[a] EnRs derived from FTIR measurements at RUN. [b] EnR ranges from 11 forest fire plumes sampled during NEAQS-ITCT 2k4. [c] EnR ranges from 10 subarctic forest fire plumes sampled during ABLE 3B. [d] This work, mean EnR and the standard deviation.

data at RUN compared to the reported average emission ratios from the literature (Table 6).

4.2.2 Carboxylic acids

Due to the relatively short global average atmospheric lifetime of HCOOH (τ_{HCOOH} = 2–4 d, Stavrakou et al., 2012) and CH_3COOH ($\tau_{CH_3COOH} \approx$ 2 d, Khan et al., 2018), EnRs in aged BB plumes should not be compared to emissions ratios from the literature (Paulot et al., 2011). However, as wet- and dry deposition are dominant sinks for both CH_3COOH and HCOOH, their effective lifetime during transport in the FT is expected to be much longer ($\tau_{HCOOH} \approx$ 25 d from photochemical oxidation, Millet et al., 2015).

The much higher HCOOH enhancement ratio estimated from RUN data (20–30 pptv ppbv^{-1}) compared to reported emission ratios (2–4 pptv ppbv^{-1}) points to significant secondary production during transport to RUN. Similar to secondary production of CH_3COCH_3, we identified HCOOH precursor species from the literature and cross-referenced these with pyrogenic EFs (Andreae, 2019). A potential precursor to HCOOH strongly emitted by agricultural residue burning is glycolaldehyde (ER = 19 ± 12 pptv ppbv^{-1}, Andreae, 2019). The yield of HCOOH from glycolaldehyde oxidation has been measured to be 18 % at 296 K and 52 % at 233 K (Butkovskaya et al., 2006). This may account for part of the HCOOH production during transport. However, recent studies indicate that this production is effective only in high
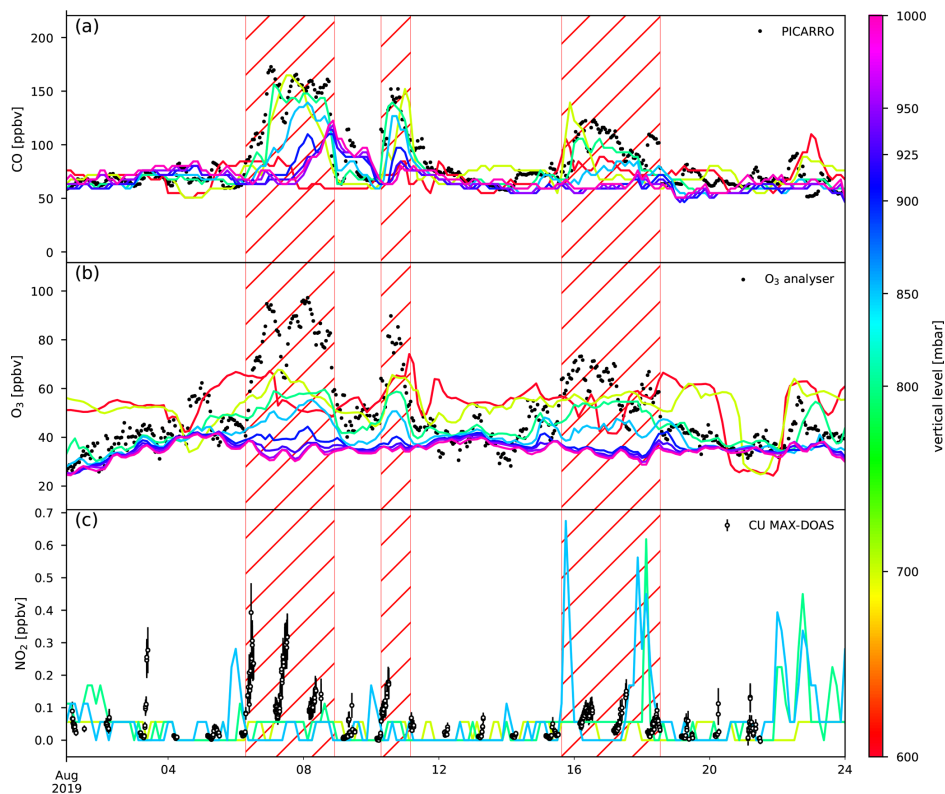
Figure 3. Comparison between measured (black dots) and calculated mixing ratios (coloured lines) of CO **(a)**, O_3 **(b)** and NO_2 **(c)** from CAMS. The coloured lines indicate the lowest eight pressure levels in the model (1000, 950, 925, 900, 850, 800, 700 and 600 mbar). The hatched red area represents the different BB intrusions.

NO_x conditions that are not realistic in a natural environment (Orlando et al., 2012; Orlando and Tyndall, 2020). Production of HCOOH from glycolaldehyde is thus most likely only a minor source. No other known precursors of HCOOH were identified in pyrogenic emissions to account for the high production during transport to RUN suggesting a missing source in current knowledge.

Secondary production of HCOOH was also found in BB plumes over Canada (Lefer et al., 1994) but was not observed in previous ground-based FTIR studies at La Réunion (Vigouroux et al., 2012). Enhancement ratios of HCOOH calculated from the Tropospheric Emission Spectrometer instrument aboard the NASA's Aura spacecraft over Africa ranged from 26 to 28 pptv ppbv^{-1} (Chaliyakunnel et al., 2016), consistent with our results. This secondary HCOOH production in BB plumes could account for part of the discrepancy in the global HCOOH budget between models and

observations (Chaliyakunnel et al., 2016). As these EnRs are inferred from data over biomass burning hotspots in Africa, HCOOH is probably formed primarily close to the source and conserved during synoptic-scale transport towards RUN.

For CH_3COOH the enhancement ratio (EnR$_{CH_3COOH} \approx$ 14 pptv ppbv^{-1}) is of the same order of magnitude as the emission ratios from the literature (Table 6). Therefore, in contrast with the case of HCOOH, no significant secondary production of acetic acid in BB plumes is identified.

4.2.3 Ozone and NO_2

It is generally accepted that O_3 is produced in BB plumes during transport (Taupin et al., 2002; Jaffe and Wigder, 2012; Parrington et al., 2013; Arnold et al., 2015; Brocchi et al., 2018). The EnRs obtained in this study (410–640 pptv ppbv^{-1}) are in agreement with the range of EnRs
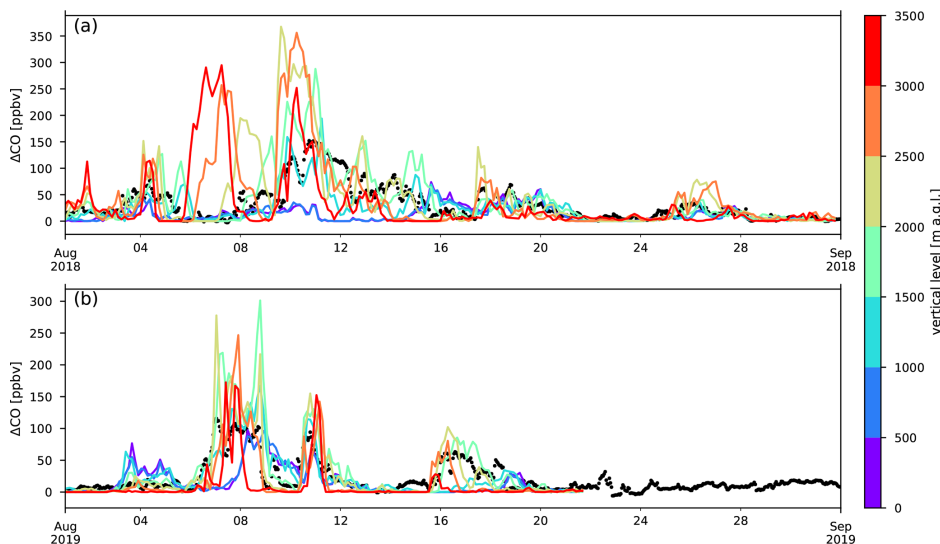
Figure 4. Comparison between measured excess CO (black) at RUN to that modelled on different vertical levels of the FLEXPART model during August 2018 **(a)** and August 2019 **(b)**. FLEXPART output levels are defined in metres above ground level (m a.g.l.).

obtained in tropical BB plumes older than 5 d, compiled by Jaffe and Wigder (2012), 410–750 pptv ppbv^{-1}.

Figure 3 shows that the CAMS model reproduces correctly the O_3 concentrations at RUN outside the BB episodes but underestimates O_3 during these episodes. The large underestimation of O_3 during these episodes indicates a misrepresentation of the BB emissions at the source and/or missing O_3 production during transport in the chemically complex plumes.

The O_3 production in the troposphere is highly dependent on the ratio between VOCs and NO_x. The CAMS NRT service is known to overestimate NO_2 over southern Africa in austral winter–spring (Flemming et al., 2015; Basart et al., 2020). However, this overestimation was reduced since the upgrade in 2017 (Basart et al., 2020). Total BB VOC emissions in the IFS of ECMWF was ~ 40 Tg in the year 2008 (Flemming et al., 2015). This is too low in comparison with the top-down estimate by Stavrakou et al. (2015) where the global pyrogenic VOC emissions are estimated to be 67–75 Tg yr^{-1}.

Ozone production in BB plumes tends to be NO_x-limited (Jaffe and Wigder, 2012). The measured NO_2 mixing ratio during BB episodes is significantly higher than those calculated by CAMS (Fig. 3). The largest and smallest difference between model and measurements for both NO_2 and O_3 were recorded during the first and last BB intrusion in 2019 respectively. This mismatch for NO_2 may be caused by an underestimation of NO_x emissions by fires or by a misrepre-

sentation of NO_x recycling (e.g. through peroxyacetyl nitrate or PAN). BB plumes reaching RUN are located at relatively low altitudes where warmer temperatures make thermal decomposition of PAN a likely source of NO_x. This could be a decisive factor in harmonising modelled and recorded O_3 mixing ratios as an increase in VOC emissions related to BB is unlikely to lead to O_3 production in the absence of NO_x.

Uncertainties in VOC and NO_x emissions by BB and misrepresentations of NO_x recycling during transport are both likely contributors to the misrepresentation of O_3 mixing ratios at the location of RUN.

4.3 Plume dispersion over the SWIO

Transport of BB plumes recorded by the hs-PTR-MS at RUN takes place primarily in the lower FT. This implies that dispersion of the plume into the MBL is possible through turbulent mixing in shallow cumulus clouds and development of the MBL. Figure 5 shows ΔCO due to pyrogenic emissions from plumes between 4 and 16 d old (corresponding to the extremes of plume ages observed at Maïdo) as calculated with FLEXPART on the model output layer 0–500 m a.g.l. By using Eq. (3), estimates of ΔCH_3CN, ΔCH_3COCH_3, ΔCH_3OH and ΔC_6H_6 in the pristine marine boundary layer environment were made (Fig. 5). To illustrate the importance of these BB plumes on the MBL composition, these expected excesses are compared with background VOC measurements performed in the SWIO during the MANCHOT campaign
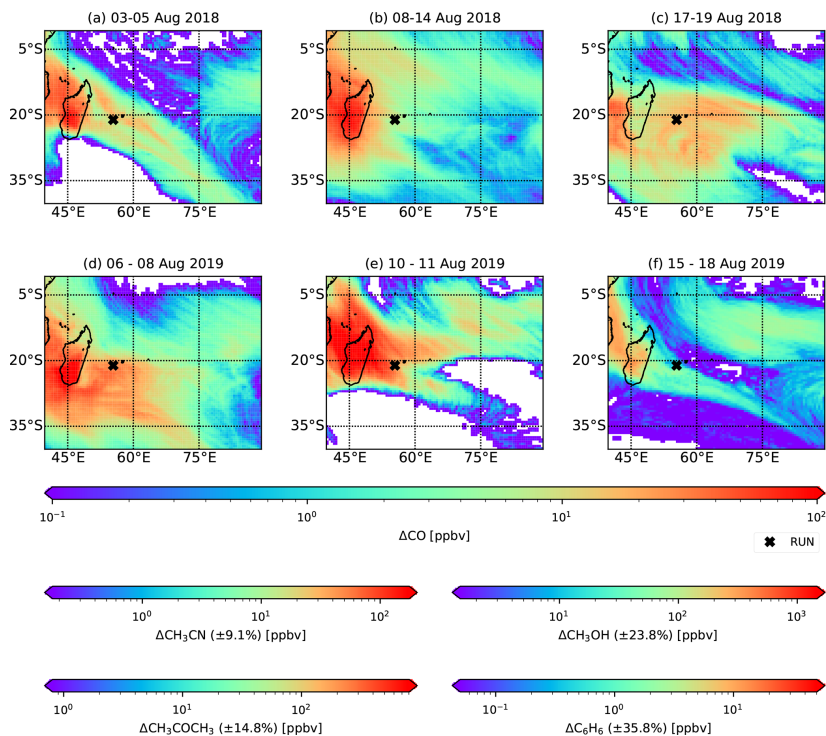
Figure 5. Excess CO over the south-west Indian Ocean between 0 and 500 m a.g.l. from BB emissions as simulated by FLEXPART. Additional colour scales quantify the projected CH_3CN, CH_3COCH_3, C_6H_6 and CH_3OH excesses.

that took place in December 2004 (Colomb et al., 2009). Shipborne measurements of VOC concentrations were performed south of La Réunion to characterise the impact of oceanic fronts on MBL composition (Colomb et al., 2009). We use background measurements north (zone I, 24.2–30.2° S) and south (zone III, 45.9–49.2° S) of the different oceanic fronts that were under consideration (Colomb et al., 2009). Due to the higher concentrations of anthropogenic tracers in zone I of the campaign, it was suggested that there may have been an impact of African outflow on these backgrounds (Colomb et al., 2009). Note that MANCHOT took place in December 2004, which is typically the end of the BB season over the SWIO. Due to the long lifetime of CH_3CN and to a lesser extent CH_3COCH_3, part of these concentrations in zone I may be originating from accumulation of BB plumes in the troposphere.

The low variability in EnRs, between different BB intrusions at RUN, for both CH_3CN and CH_3COCH_3 allows for characterisation of mixing ratios in the marine boundary layer with small relative uncertainties (8.3 % and 13.5 % re-

spectively). The local impact of ΔCH_3CN in the SWIO MBL during the August BB episodes ($\sim$ 50 pptv) constitutes an increase of $\sim$ 60 %–150 % over the SWIO as measured during the MANCHOT campaign (zone I: 80 ± 20 pptv, zone III: 20 ± 10 pptv). Acetone excesses are based on the assumption that acetone production in the BB plume is similar in the free troposphere and in the marine boundary layer. The excesses over the SWIO can reach up to 300 pptv, $\sim$ 30 %–75 % above the backgrounds recorded during MANCHOT.

The relatively short lifetimes of CH_3OH and C_6H_6 result in a larger variability of the enhancement ratios between different BB intrusions. This is reflected in the larger relative uncertainty in the calculated excesses over the SWIO (21.7 % and 32.6 % for CH_3OH and C_6H_6 respectively). Calculated ΔCH_3OH over the SWIO is $\sim$ 0.5 ppbv, corresponding to an increase of 25 % (zone I) to at least 100 % (zone III) compared to the values recorded during MANCHOT (Colomb et al., 2009). The expected ΔC_6H_6 over the SWIO is 30 pptv. This is only a minor increase compared to zone I of the MANCHOT campaign (160 ± 40 pptv) but constitutes a sig-

nificant increase (150 %) in zone III, further south over the SWIO.

Due to the short lifetime of carboxylic acids in the humid marine boundary layer, the method used above to estimate the BB impact on the SWIO is not valid for HCOOH and CH_3COOH.

5 Conclusions

We have shown that BB plumes were recorded with the hs-PTR-MS instrument deployed at the high-altitude Maïdo observatory located in the south-west Indian Ocean. Six different episodes of biomass burning plumes have been identified and studied in August 2018 and August 2019. Enhancement ratios relative to CO have been calculated for CH_3CN (1.61–2.06 pptv ppbv^{-1}), HCOOH (17.5–33.8 pptv ppbv^{-1}), CH_3COCH_3 (6.84–10.0 pptv ppbv^{-1}), CH_3COOH (9.8–18.0 pptv ppbv^{-1}), C_6H_6 (0.27–0.83 pptv ppbv^{-1}), CH_3OH (8.7–18.8 pptv ppbv^{-1}) and O_3 (410–640 pptv ppbv^{-1}). Comparison between these EnRs and the ERs calculated from the literature showed production of CH_3COCH_3 and HCOOH. Secondary production of CH_3COCH_3 was accounted for by pyrogenic emission of precursor species propane and to a lesser extent i-butane and i-butene. Production was especially significant for HCOOH with EnRs about 10 times larger than the ERs. This HCOOH production can not be accounted for by known precursor species.

The CAMS NRT atmospheric composition service was shown to reproduce the CO concentrations well at RUN both during and outside BB episodes. In contrast, O_3 concentrations were only correctly reproduced outside the BB episodes. The large underestimation of O_3 concentrations during the BB episodes were linked to (i) large uncertainties in VOC and NO_x emissions and (ii) misrepresentation of NO_x recycling during transport of the BB plume in the CAMS NRT service. FLEXPART-AROME mesoscale back-trajectory simulations showed that biomass burning plumes were diluted at the observatory when the impact of PBL air increased. This implies that the BB plume recorded at the observatory is primarily transported through the FT. Large-scale transport of ΔCO originating from pyrogenic emissions, simulated with FLEXPART, supported this by showing larger ΔCO concentrations at higher altitudes. Finally, the horizontal distribution of ΔCO in the SWIO MBL – calculated with FLEXPART – is multiplied with the EnR values inferred from data at the Maïdo observatory. This provided estimates for the impact of BB on air mass composition in the MBL over the SWIO. We compared the calculated estimates with background VOC measurements in the region reported in the literature. Expected excesses for CH_3CN, CH_3COCH_3, C_6H_6 and CH_3OH represent an increase in background concentrations by 60 %–150 %, 30 %–75 %, 15 %–150 % and 25 %–> 100 %, respectively. In the future, synchronous VOC measurements at RUN and marine campaigns should be conducted in order to (i) better quantify the ocean–atmosphere interaction in regions with locally enhanced atmospheric concentrations of these species from BB and (ii) identify the different ageing mechanisms during transport in the MBL compared to transport in the FT. This would be especially valuable for CH_3COCH_3 and CH_3OH, for which the role of the ocean on the total atmospheric budget remains uncertain.

Appendix A: In situ measurement data visualisation

A1   Seasonal biomass burning profile

Hourly averages of CO and CH_3CN are shown in Fig. A1. Both CO and CH_3CN have large peak values from August to November. This corresponds to the biomass burning season as determined from ground-based remote-sensing data studies performed at La Réunion (Duflot et al., 2010; Vigouroux et al., 2012). The analysis presented in this study focuses on the first biomass burning intrusions measured for each season. The motivation for this choice is that the variability in diel profiles between different days is less pronounced during this period and backgrounds do not suffer from accumulated BB tracers for compounds with long atmospheric lifetimes.

A2   Austral winter variation of in situ measurements at RUN

The temporal evolution of biomass burning plume constituents during austral winter 2018 and austral winter 2019 are shown together with the diel distribution of hourly averaged mixing ratio from Figs. A2 to A10. The median diel profile is used as an estimate of background variation above which the biomass burning excesses are determined. This works especially well for compounds with relatively small variability between different days compared to the excesses due to biomass burning (e.g. CO, CH_3CN, HCOOH, CH_3COCH_3 and CH_3COOH) but may introduce errors for other compounds (e.g. C_6H_6, CH_3OH and O_3). When this difference becomes negligible, the analysis no longer works and these compounds are not considered (e.g. HCHO and CH_3CHO).
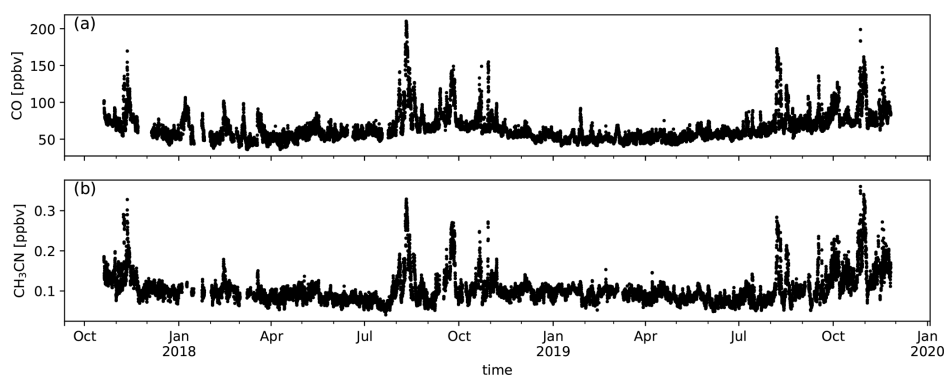
Figure A1. Measured CO (**a**) and CH_3CN (**b**) mixing ratios (ppbv) during the deployment of the hs-PTR-MS for the OCTAVE project.

Figure A2. Measured CO mixing ratios (ppbv) during austral winter 2018 **(a)** and austral winter 2019 **(b)** together with the diel distribution of hourly averages **(c)**. Biomass burning plumes under investigation are highlighted in colours.

Figure A3. Measured CH_3CN mixing ratios (ppbv) during austral winter 2018 **(a)** and austral winter 2019 **(b)** together with the diel distribution of hourly averages **(c)**. Biomass burning plumes under investigation are highlighted in colours.

Figure A4. Measured HCOOH mixing ratios (ppbv) during austral winter 2018 **(a)** and austral winter 2019 **(b)** together with the diel distribution of hourly averages **(c)**. Biomass burning plumes under investigation are highlighted in colours.
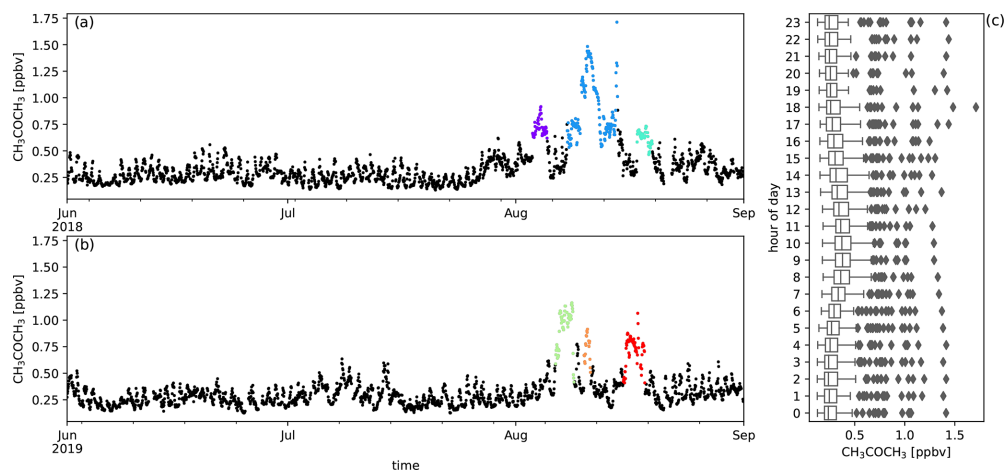
Figure A5. Measured CH_3COCH_3 mixing ratios (ppbv) during austral winter 2018 **(a)** and austral winter 2019 **(b)** together with the diel distribution of hourly averages **(c)**. Biomass burning plumes under investigation are highlighted in colours.
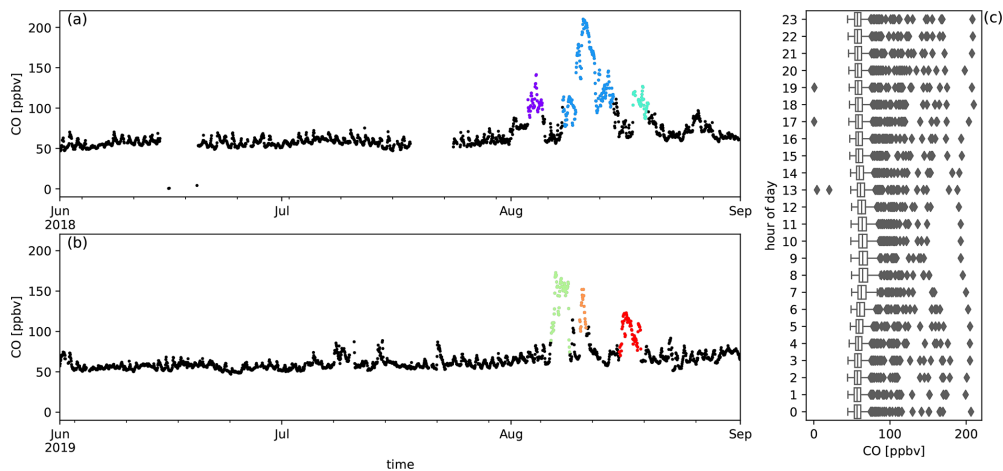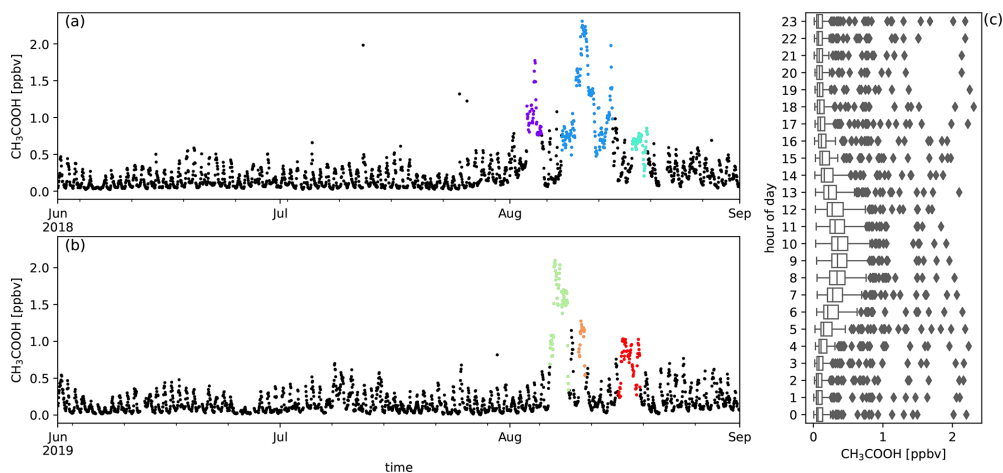
Figure A6. Measured CH$_3$COOH mixing ratios (ppbv) during austral winter 2018 **(a)** and austral winter 2019 **(b)** together with the diel distribution of hourly averages **(c)**. Biomass burning plumes under investigation are highlighted in colours.
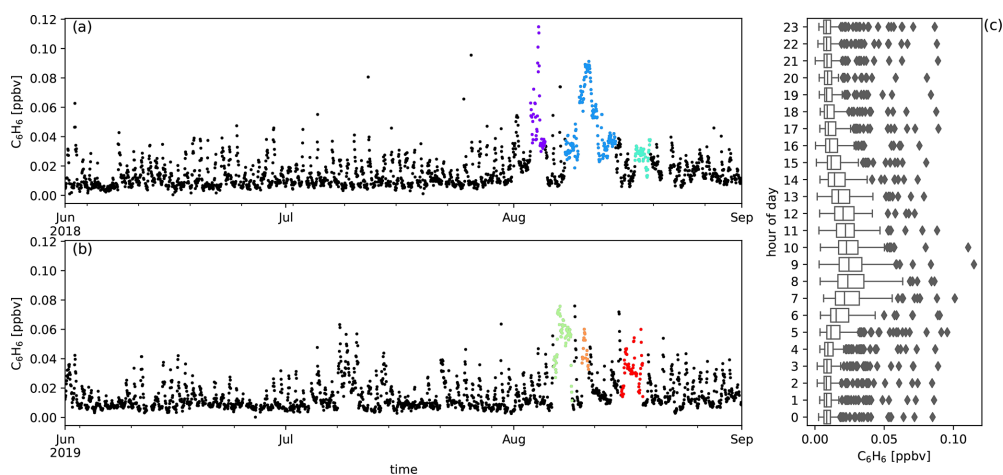
Figure A7. Measured C$_6$H$_6$ mixing ratios (ppbv) during austral winter 2018 **(a)** and austral winter 2019 **(b)** together with the diel distribution of hourly averages **(c)**. Biomass burning plumes under investigation are highlighted in colours.
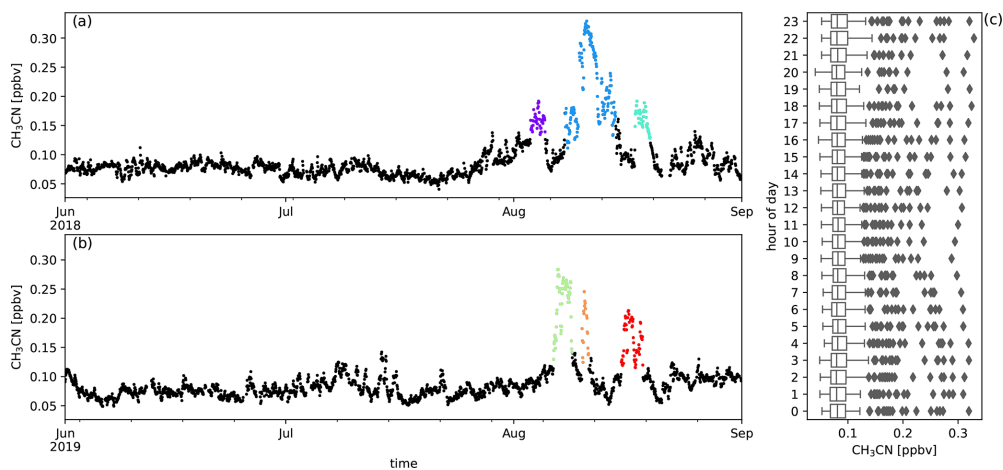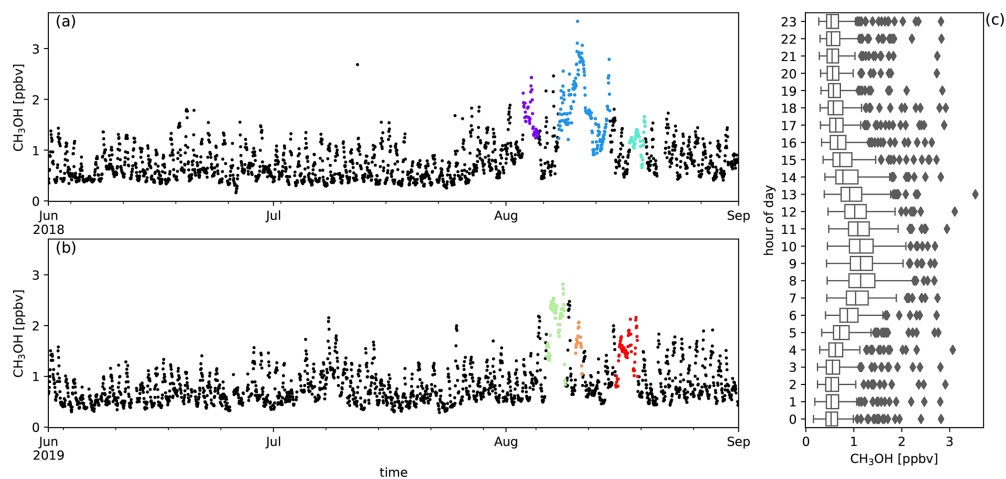
Figure A8. Measured CH$_3$OH mixing ratios (ppbv) during austral winter 2018 **(a)** and austral winter 2019 **(b)** together with the diel distribution of hourly averages **(c)**. Biomass burning plumes under investigation are highlighted in colours.
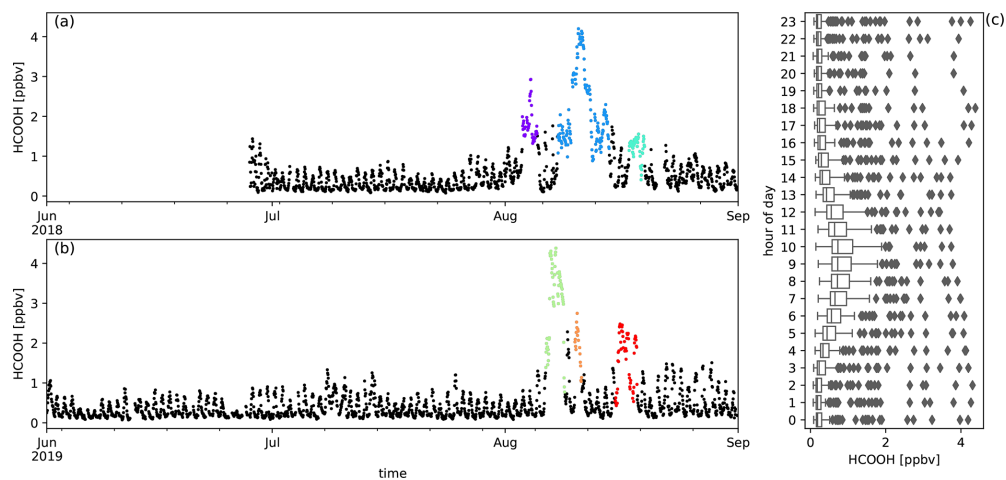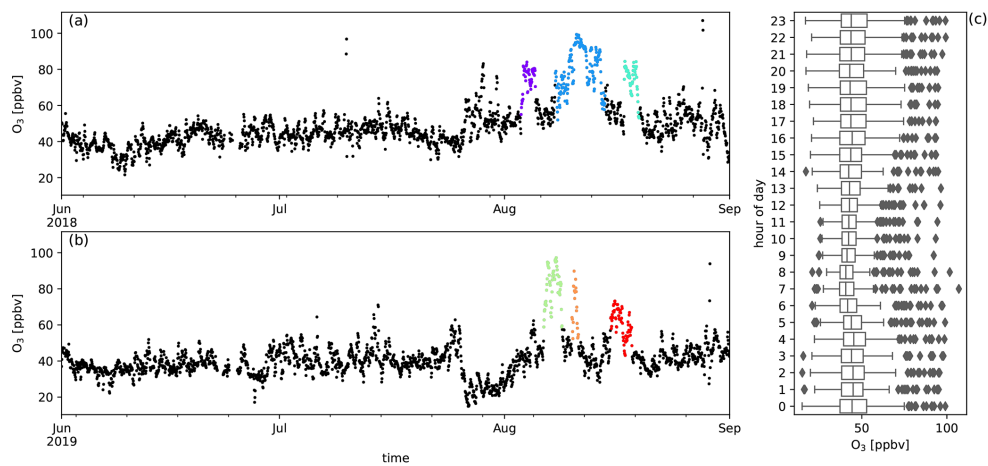

Figure A9. Measured O$_3$ mixing ratios (ppbv) during austral winter 2018 **(a)** and austral winter 2019 **(b)** together with the diel distribution of hourly averages **(c)**. Biomass burning plumes under investigation are highlighted in colours.
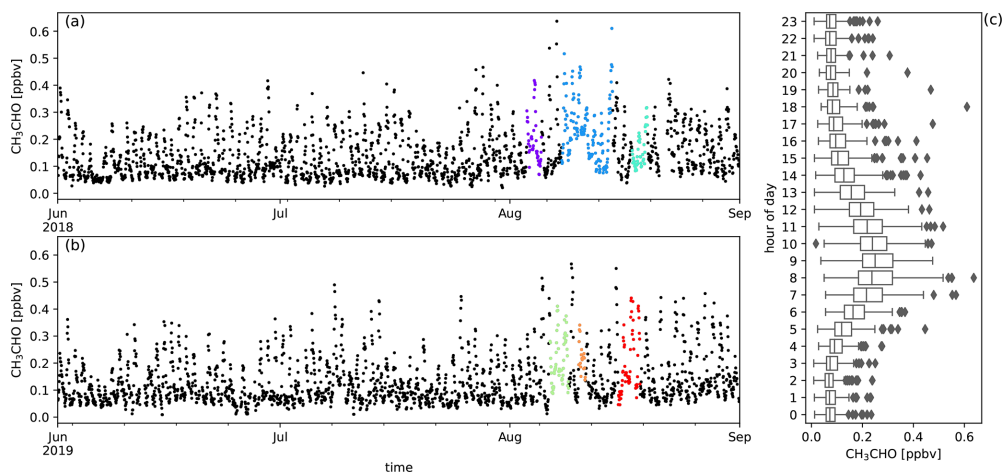
Figure A10. Measured CH$_3$CHO mixing ratios (ppbv) during austral winter 2018 **(a)** and austral winter 2019 **(b)** together with the diel distribution of hourly averages **(c)**. Biomass burning plumes under investigation are highlighted in colours.
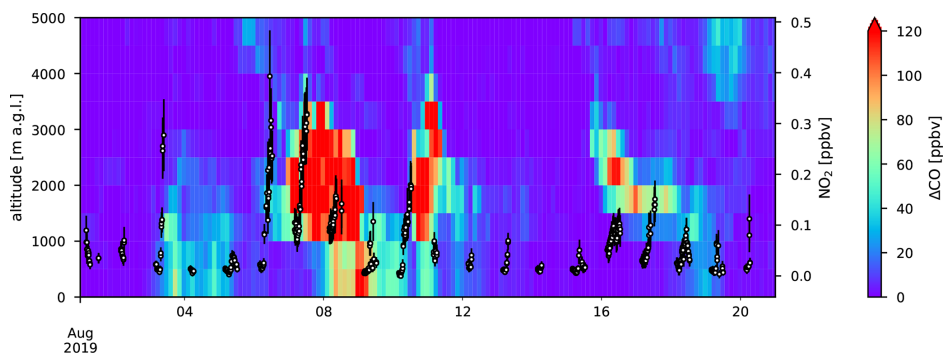

**Figure A11.** NO$_2$ (ppbv) from CU MAX-DOAS in comparison with ΔCO (ppbv) from FLEXPART simulations. Altitude (m a.g.l.) corresponds with vertical layers in the FLEXPART output at the location of RUN. The ground level of RUN in the model is 284 m a.s.l.

Appendix B: NO_2 coincidence with FLEXPART simulations

NO_2 volume mixing ratios from the CU MAX-DOAS instrument are generally lower than 100 pptv outside of the BB episodes. A notable exception to this is 3 August 2019 when it reaches ~ 280 pptv. This coincides with slightly elevated ΔCO signals simulated by FLEXPART at RUN (Fig. A11). At the visible wavelengths, the horizontal spatial scale probed is about 40 km and the overlap with the PBL is only a few kilometres. As a results, measurements from the CU MAX-DOAS instrument are expected to compare well to the FLEXPART and CAMS models, which have a low spatial resolution. Note that when the NO_2 mixing ratio from the CU MAX-DOAS instrument is above 100 pptv, FLEXPART ΔCO is generally enhanced between 1000 and 1500 m a.g.l.

As the plume on 3 August is not clearly observed in the in situ measurements we assume that it is not well mixed with boundary layer air at RUN and do not investigate it further here.

References

Akagi, S. K., Yokelson, R. J., Wiedinmyer, C., Alvarado, M. J., Reid, J. S., Karl, T., Crounse, J. D., and Wennberg, P. O.: Emission factors for open and domestic biomass burning for use in atmospheric models, Atmos. Chem. Phys., 11, 4039–4072, https://doi.org/10.5194/acp-11-4039-2011, 2011.

Akagi, S. K., Burling, I. R., Mendoza, A., Johnson, T. J., Cameron, M., Griffith, D. W. T., Paton-Walsh, C., Weise, D. R., Reardon, J., and Yokelson, R. J.: Field measurements of trace gases emitted by prescribed fires in southeastern US pine forests using an open-pa th FTIR system, Atmos. Chem. Phys., 14, 199–215, https://doi.org/10.5194/acp-14-199-2014, 2014.

Amelynck, C., Schoon, N., and Verreyken, B.: Supplement to "Characterisation of African biomass burning plumes and impacts on the atmospheric composition over the South-West Indian Ocean" by Bert Verreyken et al., Atmospheric Chemistry and Physics, in review (2020) [Data set], Royal Belgian Institute for Space Aeronomy, https://doi.org/10.18758/71021059, 2020.

Andreae, M. O.: Emission of trace gases and aerosols from biomass burning – an updated assessment, Atmos. Chem. Phys., 19, 8523–8546, https://doi.org/10.5194/acp-19-8523-2019, 2019.

Arnold, S. R., Chipperfield, M. P., and Blitz, M. A.: A three-dimensional model study of the effect of new temperature-dependent quantum yields for acetone photolysis, J. Geophys. Res.-Atmos., 110, D22305, https://doi.org/10.1029/2005JD005998, 2005.

Arnold, S. R., Emmons, L. K., Monks, S. A., Law, K. S., Ridley, D. A., Turquety, S., Tilmes, S., Thomas, J. L., Bouarar, I., Flemming, J., Huijnen, V., Mao, J., Duncan, B. N., Steenrod, S., Yoshida, Y., Langner, J., and Long, Y.: Biomass burning influence on high-latitude tropospheric ozone and reactive nitrogen in summer 2008: a multi-model analysis based on POLMIP simulations, Atmos. Chem. Phys., 15, 6047–6068, https://doi.org/10.5194/acp-15-6047-2015, 2015.

Atkinson, R.: Atmospheric chemistry of VOCs and NO_x, Atmos. Environ., 34, 2063–2101, https://doi.org/10.1016/S1352-2310(99)00460-4, 2000.

Baasandorj, M., Millet, D. B., Hu, L., Mitroo, D., and Williams, B. J.: Measuring acetic and formic acid by proton-transfer-reaction mass spectrometry: sensitivity, humidity dependence, and quantifying interferences, Atmos. Meas. Tech., 8, 1303–1321, https://doi.org/10.5194/amt-8-1303-2015, 2015.

Baray, J.-L., Courcoux, Y., Keckhut, P., Portafaix, T., Tulet, P., Cammas, J.-P., Hauchecorne, A., Godin Beekmann, S., De Mazière, M., Hermans, C., Desmet, F., Sellegri, K., Colomb, A., Ramonet, M., Sciare, J., Vuillemin, C., Hoareau, C., Dionisi, D., Duflot, V., Vérèmes, H., Porteneuve, J., Gabarrot, F., Gaudo, T., Metzger, J.-M., Payen, G., Leclair de Bellevue, J., Barthe, C., Posny, F., Ricaud, P., Abchiche, A., and Delmas, R.: Maïdo observatory: a new high-altitude station facility at Reunion Island (21° S, 55° E) for long-term atmospheric remote sensing and in situ measurements, Atmos. Meas. Tech., 6, 2865–2877, https://doi.org/10.5194/amt-6-2865-2013, 2013.

Basart, S., Benedictow, A., Bennouna, Y., Blechschmidt, A.-M., Chabrillat, S., Christophe, Y., Cuevas, E., Eskes, H. J., Hanse, K. M., Jorba, O., Kapsomenakis, J., Langerock, B., Pay, T., Richter, A., Sudarchikova, N., Schulz, M., Wagner, A., and Zerefos, C.: Upgrade verification note for the CAMS real-time global atmospheric composition service Evaluation of the e-suite for the CAMS upgrade of July 2019, report, The Copernicus Atmosphere Monitoring Service (CAMS), https://doi.org/10.24380/fcwq-yp50, 2019.

Basart, S., Benedictow, A., Bennouna, Y., Blechschmidt, A.-M., Chabrillat, S., Cuevas, E., El-Yazidi, A., Flentje, H., Hansen, K. M., Im, U., Kapsomenakis, J., Langerock, B., Richter, A., Sudarchikova, N., Thouret, V., Warneke, T., and Zerefos, C.: Validation report of the CAMS near-real-time global atmospheric composition service. Period September–November 2019, report, The Copernicus Atmosphere Monitoring Service (CAMS), https://doi.org/10.24380/xzkk-bz05, 2020.

Blake, N. J., Blake, D. R., Wingenter, O. W., Sive, B. C., Kang, C. H., Thornton, D. C., Bandy, A. R., Atlas, E., Flocke, F., Harris, J. M., and Rowland, F. S.: Aircraft measurements of the

latitudinal, vertical, and seasonal variations of NMHCs, methyl nitrate, methyl halides, and DMS during the First Aerosol Characterization Experiment (ACE 1), J. Geophys. Res.-Atmos., 104, 21803–21817, https://doi.org/10.1029/1999JD900238, 1999.

Brocchi, V., Krysztofiak, G., Catoire, V., Guth, J., Marécal, V., Zbinden, R., El Amraoui, L., Dulac, F., and Ricaud, P.: Intercontinental transport of biomass burning pollutants over the Mediterranean Basin during the summer 2014 ChArMEx-GLAM airborne campaign, Atmos. Chem. Phys., 18, 6887–6906, https://doi.org/10.5194/acp-18-6887-2018, 2018.

Butkovskaya, N. I., Pouvesle, N., Kukui, A., and Le Bras, G.: Mechanism of the OH-Initiated Oxidation of Glycolaldehyde over the Temperature Range 233–296 K, J. Phys. Chem. A, 110, 13492–13499, https://doi.org/10.1021/jp064993k, 2006.

Carpenter, L. J. and Nightingale, P. D.: Chemistry and Release of Gases from the Surface Ocean, Chem. Rev., 115, 4015–4034, https://doi.org/10.1021/cr5007123, 2015.

Chaliyakunnel, S., Millet, D., Wells, K., Cady-Pereira, K., and Shephard, M.: A Large Underestimate of Formic Acid from Tropical Fires: Constraints from Space-Borne Measurements, Environ. Sci. Technol., 50, 5631–5640, https://doi.org/10.1021/acs.est.5b06385, 2016.

Christian, T. J., Kleiss, B., Yokelson, R. J., Holzinger, R., Crutzen, P. J., Hao, W. M., Saharjo, B. H., and Ward, D. E.: Comprehensive laboratory measurements of biomass-burning emissions: 1. Emissions from Indonesian, African, and other fuels, J. Geophys. Res.-Atmos., 108, 4719, https://doi.org/10.1029/2003JD003704, 2003.

Coburn, S., Dix, B., Sinreich, R., and Volkamer, R.: The CU ground MAX-DOAS instrument: characterization of RMS noise limitations and first measurements near Pensacola, FL of BrO, IO, and CHOCHO, Atmos. Meas. Tech., 4, 2421–2439, https://doi.org/10.5194/amt-4-2421-2011, 2011.

Colomb, A., Gros, V., Alvain, S., Sarda-Esteve, R., Bonsang, B., Moulin, C., Klüpfel, T., and J., W.: Variation of atmospheric volatile organic compounds over the Southern Indian Ocean (30–49° S), Environ. Chem., 6, 80–82, https://doi.org/10.1071/EN08072, 2009.

Danckaert, T., Fayt, C., Van Roozendael, M., De Smedt, I., Letocart, V., Merlaud, A., and Pinardi, G.: QDOAS software user manual, v3.2, available at: http://uv-vis.aeronomie.be/software/QDOAS (last access: 10 June 2019), 2017.

de Gouw, J. A., Warneke, C., Parrish, D. D., Holloway, J. S., Trainer, M., and Fehsenfeld, F. C.: Emission sources and ocean uptake of acetonitrile (CH₃CN) in the atmosphere, J. Geophys. Res.-Atmos., 108, 4329, https://doi.org/10.1029/2002JD002897, 2003.

de Gouw, J. A., Warneke, C., Stohl, A., Wollny, A. G., Brock, C. A., Cooper, O. R., Holloway, J. S., Trainer, M., Fehsenfeld, F. C., Atlas, E. L., Donnelly, S. G., Stroud, V., and Lueb, A.: Volatile organic compounds composition of merged and aged forest fire plumes from Alaska and western Canada, J. Geophys. Res.-Atmos., 111, D10303, https://doi.org/10.1029/2005JD006175, 2006.

Di Giuseppe, F., Rémy, S., Pappenberger, F., and Wetterhall, F.: Using the Fire Weather Index (FWI) to improve the estimation of fire emissions from fire radiative power (FRP) observations, Atmos. Chem. Phys., 18, 5359–5370, https://doi.org/10.5194/acp-18-5359-2018, 2018.

Dix, B., Koenig, T. K., and Volkamer, R.: Parameterization retrieval of trace gas volume mixing ratios from Airborne MAX-DOAS, Atmos. Meas. Tech., 9, 5655–5675, https://doi.org/10.5194/amt-9-5655-2016, 2016.

Duflot, V., Dils, B., Baray, J. L., De Mazière, M., Attié, J. L., Vanhaelewyn, G., Senten, C., Vigouroux, C., Clain, G., and Delmas, R.: Analysis of the origin of the distribution of CO in the subtropical southern Indian Ocean in 2007, J. Geophys. Res.-Atmos., 115, D22106, https://doi.org/10.1029/2010JD013994, 2010.

Duflot, V., Tulet, P., Flores, O., Barthe, C., Colomb, A., Deguillaume, L., Vaïtilingom, M., Perring, A., Huffman, A., Hernandez, M. T., Sellegri, K., Robinson, E., O'Connor, D. J., Gomez, O. M., Burnet, F., Bourrianne, T., Strasberg, D., Rocco, M., Bertram, A. K., Chazette, P., Totems, J., Fournel, J., Stamenoff, P., Metzger, J.-M., Chabasset, M., Rousseau, C., Bourrianne, E., Sancelme, M., Delort, A.-M., Wegener, R. E., Chou, C., and Elizondo, P.: Preliminary results from the FARCE 2015 campaign: multidisciplinary study of the forest–gas–aerosol–cloud system on the tropical island of La Réunion, Atmos. Chem. Phys., 19, 10591–10618, https://doi.org/10.5194/acp-19-10591-2019, 2019.

Fischer, E. V., Jacob, D. J., Millet, D. B., Yantosca, R. M., and Mao, J.: The role of the ocean in the global atmospheric budget of acetone, Geophys. Res. Lett., 39, L01807, https://doi.org/10.1029/2011GL050086, 2012.

Flemming, J., Huijnen, V., Arteta, J., Bechtold, P., Beljaars, A., Blechschmidt, A.-M., Diamantakis, M., Engelen, R. J., Gaudel, A., Inness, A., Jones, L., Josse, B., Katragkou, E., Marecal, V., Peuch, V.-H., Richter, A., Schultz, M. G., Stein, O., and Tsikerdekis, A.: Tropospheric chemistry in the Integrated Forecasting System of ECMWF, Geosci. Model Dev., 8, 975–1003, https://doi.org/10.5194/gmd-8-975-2015, 2015.

Granier, C., Darras, S., van der Gon, H. D., Doubalova, J., Elguindi, N., Galle, B., Gauss, M., Guevara, M., Jalkanen, J.-P., Kuenen, J., Liousse, C., Quack, B., Simpson, D., and Sindelarova, K.: The Copernicus Atmosphere Monitoring Service global and regional emissions (April 2019 version), report, The Copernicus Atmosphere Monitoring Service (CAMS), https://doi.org/10.24380/d0bn-kx16, 2019.

Holzinger, R., Warneke, C., Hansel, A., Jordan, A., Lindinger, W., Scharffe, D. H., Schade, G., and Crutzen, P. J.: Biomass burning as a source of formaldehyde, acetaldehyde, methanol, acetone, acetonitrile, and hydrogen cyanide, Geophys. Res. Lett., 26, 1161–1164, https://doi.org/10.1029/1999GL900156, 1999.

Holzinger, R., Williams, J., Salisbury, G., Klüpfel, T., de Reus, M., Traub, M., Crutzen, P. J., and Lelieveld, J.: Oxygenated compounds in aged biomass burning plumes over the Eastern Mediterranean: evidence for strong secondary production of methanol and acetone, Atmos. Chem. Phys., 5, 39–46, https://doi.org/10.5194/acp-5-39-2005, 2005.

Hönninger, G., von Friedeburg, C., and Platt, U.: Multi axis differential optical absorption spectroscopy (MAX-DOAS), Atmos. Chem. Phys., 4, 231–254, https://doi.org/10.5194/acp-4-231-2004, 2004.

Inomata, S. and Tanimoto, H.: A Quantitative Examination of the Detection Sensitivities of Proton-Transfer Reaction Mass Spectrometry for Gaseous 2-Propanol and Acetic Acid, B. Chem. Soc. Jpn., 83, 900–904, https://doi.org/10.1246/bcsj.20100043, 2010.

IPCC: Climate Change 2013: The Physical Science Basis, Contribution of Working Group I to the Fifth Assessment Report of the Intergovernmental Panel on Climate Change, Cambridge University Press, Cambridge, UK and New York, NY, USA, 2013.

Jacob, D. J., Field, B. D., Li, Q., Blake, D. R., de Gouw, J., Warneke, C., Hansel, A., Wisthaler, A., Singh, H. B., and Guenther, A.: Global budget of methanol: Constraints from atmospheric observations, J. Geophys. Res.-Atmos., 110, D08303, https://doi.org/10.1029/2004JD005172, 2005.

Jaffe, D. A. and Wigder, N. L.: Ozone production from wildfires: A critical review, Atmos. Environ., 51, 1–10, https://doi.org/10.1016/j.atmosenv.2011.11.063, 2012.

Jost, C., Trentmann, J., Sprung, D., Andreae, M. O., and Dewey, K.: Deposition of acetonitrile to the Atlantic Ocean off Namibia and Angola and its implications for the atmospheric budget of acetonitrile, Geophys. Res. Lett., 30, 1837–1841, https://doi.org/10.1029/2003GL017347, 2003.

Kaiser, J. W., Heil, A., Andreae, M. O., Benedetti, A., Chubarova, N., Jones, L., Morcrette, J.-J., Razinger, M., Schultz, M. G., Suttie, M., and van der Werf, G. R.: Biomass burning emissions estimated with a global fire assimilation system based on observed fire radiative power, Biogeosciences, 9, 527–554, https://doi.org/10.5194/bg-9-527-2012, 2012.

Khan, M. A. H., Lyons, K., Chhantyal-Pun, R., McGillen, M. R., Caravan, R. L., Taatjes, C. A., Orr-Ewing, A. J., Percival, C. J., and Shallcross, D. E.: Investigating the Tropospheric Chemistry of Acetic Acid Using the Global 3-D Chemistry Transport Model, STOCHEM-CRI, J. Geophys. Res.-Atmos., 123, 6267–6281, https://doi.org/10.1029/2018JD028529, 2018.

Kreher, K., Van Roozendael, M., Hendrick, F., Apituley, A., Dimitropoulou, E., Frieß, U., Richter, A., Wagner, T., Lampel, J., Abuhassan, N., Ang, L., Anguas, M., Bais, A., Benavent, N., Bösch, T., Bognar, K., Borovski, A., Bruchkouski, I., Cede, A., Chan, K. L., Donner, S., Drosoglou, T., Fayt, C., Finkenzeller, H., Garcia-Nieto, D., Gielen, C., Gómez-Martín, L., Hao, N., Henzing, B., Herman, J. R., Hermans, C., Hoque, S., Irie, H., Jin, J., Johnston, P., Khayyam Butt, J., Khokhar, F., Koenig, T. K., Kuhn, J., Kumar, V., Liu, C., Ma, J., Merlaud, A., Mishra, A. K., Müller, M., Navarro-Comas, M., Ostendorf, M., Pazmino, A., Peters, E., Pinardi, G., Pinharanda, M., Piters, A., Platt, U., Postylyakov, O., Prados-Roman, C., Puentedura, O., Querel, R., Saiz-Lopez, A., Schönhardt, A., Schreier, S. F., Seyler, A., Sinha, V., Spinei, E., Strong, K., Tack, F., Tian, X., Tiefengraber, M., Tirpitz, J.-L., van Gent, J., Volkamer, R., Vrekoussis, M., Wang, S., Wang, Z., Wenig, M., Wittrock, F., Xie, P. H., Xu, J., Yela, M., Zhang, C., and Zhao, X.: Intercomparison of NO_2, O_4, O_3 and HCHO slant column measurements by MAX-DOAS and zenith-sky UV–visible spectrometers during CINDI-2, Atmos. Meas. Tech., 13, 2169–2208, https://doi.org/10.5194/amt-13-2169-2020, 2020.

Lamarque, J.-F., Bond, T. C., Eyring, V., Granier, C., Heil, A., Klimont, Z., Lee, D., Liousse, C., Mieville, A., Owen, B., Schultz, M. G., Shindell, D., Smith, S. J., Stehfest, E., Van Aardenne, J., Cooper, O. R., Kainuma, M., Mahowald, N., McConnell, J. R., Naik, V., Riahi, K., and van Vuuren, D. P.: Historical (1850–2000) gridded anthropogenic and biomass burning emissions of reactive gases and aerosols: methodology and application, Atmos. Chem. Phys., 10, 7017–7039, https://doi.org/10.5194/acp-10-7017-2010, 2010.

Lefer, B. L., Talbot, R. W., Harriss, R. H., Bradshaw, J. D., Sandholm, S. T., Olson, J. O., Sachse, G. W., Collins, J., Shipham, M. A., Blake, D. R., Klemm, K. I., Klemm, O., Gorzelska, K., and Barrick, J.: Enhancement of acidic gases in biomass burning impacted air masses over Canada, J. Geophys. Res.-Atmos., 99, 1721–1737, https://doi.org/10.1029/93JD02091, 1994.

Lesouëf, D., Gheusi, F., Delmas, R., and Escobar, J.: Numerical simulations of local circulations and pollution transport over Reunion Island, Ann. Geophys., 29, 53–69, https://doi.org/10.5194/angeo-29-53-2011, 2011.

Lewis, A. C., Hopkins, J. R., Carpenter, L. J., Stanton, J., Read, K. A., and Pilling, M. J.: Sources and sinks of acetone, methanol, and acetaldehyde in North Atlantic marine air, Atmos. Chem. Phys., 5, 1963–1974, https://doi.org/10.5194/acp-5-1963-2005, 2005.

Mallet, P.-E., Pujol, O., Brioude, J., Evan, S., and Jensen, A.: Marine aerosol distribution and variability over the pristine Southern Indian Ocean, Atmos. Environ., 182, 17–30, https://doi.org/10.1016/j.atmosenv.2018.03.016, 2018.

Mellouki, A., Wallington, T. J., and Chen, J.: Atmospheric Chemistry of Oxygenated Volatile Organic Compounds: Impacts on Air Quality and Climate, Chem. Rev., 115, 3984–4014, https://doi.org/10.1021/cr500549n, 2015.

Millet, D. B., Guenther, A., Siegel, D. A., Nelson, N. B., Singh, H. B., de Gouw, J. A., Warneke, C., Williams, J., Eerdekens, G., Sinha, V., Karl, T., Flocke, F., Apel, E., Riemer, D. D., Palmer, P. I., and Barkley, M.: Global atmospheric budget of acetaldehyde: 3-D model analysis and constraints from in-situ and satellite observations, Atmos. Chem. Phys., 10, 3405–3425, https://doi.org/10.5194/acp-10-3405-2010, 2010.

Millet, D. B., Baasandorj, M., Farmer, D. K., Thornton, J. A., Baumann, K., Brophy, P., Chaliyakunnel, S., de Gouw, J. A., Graus, M., Hu, L., Koss, A., Lee, B. H., Lopez-Hilfiker, F. D., Neuman, J. A., Paulot, F., Peischl, J., Pollack, I. B., Ryerson, T. B., Warneke, C., Williams, B. J., and Xu, J.: A large and ubiquitous source of atmospheric formic acid, Atmos. Chem. Phys., 15, 6283–6304, https://doi.org/10.5194/acp-15-6283-2015, 2015.

Monks, P. S., Archibald, A. T., Colette, A., Cooper, O., Coyle, M., Derwent, R., Fowler, D., Granier, C., Law, K. S., Mills, G. E., Stevenson, D. S., Tarasova, O., Thouret, V., von Schneidemesser, E., Sommariva, R., Wild, O., and Williams, M. L.: Tropospheric ozone and its precursors from the urban to the global scale from air quality to short-lived climate forcer, Atmos. Chem. Phys., 15, 8889–8973, https://doi.org/10.5194/acp-15-8889-2015, 2015.

Monod, A., Sive, B. C., Avino, P., Chen, T., Blake, D. R., and Rowland, F. S.: Monoaromatic compounds in ambient air of various cities: a focus on correlations between the xylenes and ethylbenzene, Atmos. Environ., 35, 135–149, https://doi.org/10.1016/S1352-2310(00)00274-0, 2001.

Orlando, J. J. and Tyndall, G. S.: The atmospheric oxidation of hydroxyacetone: Chemistry of activated and stabilized $CH_3C(O)CH(OH)OO\cdot$ radicals between 252 and 298 K, Int. J. Chem. Kinet., 52, 236–250, https://doi.org/10.1002/kin.21346, 2020.

Orlando, J. J., Tyndall, G. S., and Taraborrelli, D.: Atmospheric Oxidation of Two Isoprene By-Products, Hydroxyacetone and Gly-

colaldehyde, in: AGU Fall Meeting Abstracts, 3–7 December 2012, San-Francisco, California, USA, vol. 2012, A33L–0315, 2012.

Parrington, M., Palmer, P. I., Lewis, A. C., Lee, J. D., Rickard, A. R., Di Carlo, P., Taylor, J. W., Hopkins, J. R., Punjabi, S., Oram, D. E., Forster, G., Aruffo, E., Moller, S. J., Bauguitte, S. J.-B., Allan, J. D., Coe, H., and Leigh, R. J.: Ozone photochemistry in boreal biomass burning plumes, Atmos. Chem. Phys., 13, 7321–7341, https://doi.org/10.5194/acp-13-7321-2013, 2013.

Paulot, F., Wunch, D., Crounse, J. D., Toon, G. C., Millet, D. B., DeCarlo, P. F., Vigouroux, C., Deutscher, N. M., González Abad, G., Notholt, J., Warneke, T., Hannigan, J. W., Warneke, C., de Gouw, J. A., Dunlea, E. J., De Mazière, M., Griffith, D. W. T., Bernath, P., Jimenez, J. L., and Wennberg, P. O.: Importance of secondary sources in the atmospheric budgets of formic and acetic acids, Atmos. Chem. Phys., 11, 1989–2013, https://doi.org/10.5194/acp-11-1989-2011, 2011.

Pisso, I., Sollum, E., Grythe, H., Kristiansen, N. I., Cassiani, M., Eckhardt, S., Arnold, D., Morton, D., Thompson, R. L., Groot Zwaaftink, C. D., Evangeliou, N., Sodemann, H., Haimberger, L., Henne, S., Brunner, D., Burkhart, J. F., Fouilloux, A., Brioude, J., Philipp, A., Seibert, P., and Stohl, A.: The Lagrangian particle dispersion model FLEX-PART version 10.4, Geosci. Model Dev., 12, 4955–4997, https://doi.org/10.5194/gmd-12-4955-2019, 2019.

Platt, U. and Stutz, J.: Differential optical absorption spectroscopy – principles and applications, Springer, Heidelberg, Germany, 2008.

Read, K. A., Carpenter, L. J., Arnold, S. R., Beale, R., Nightingale, P. D., Hopkins, J. R., Lewis, A. C., Lee, J. D., Mendes, L., and Pickering, S. J.: Multiannual observations of acetone, methanol, and acetaldehyde in remote tropical atlantic air: implications for atmospheric OVOC budgets and oxidative capacity, Environ. Sci. Technol., 46, 11028–11039, https://doi.org/10.1021/es302082p, 2012.

Rémy, S., Veira, A., Paugam, R., Sofiev, M., Kaiser, J. W., Marenco, F., Burton, S. P., Benedetti, A., Engelen, R. J., Ferrare, R., and Hair, J. W.: Two global data sets of daily fire emission injection heights since 2003, Atmos. Chem. Phys., 17, 2921–2942, https://doi.org/10.5194/acp-17-2921-2017, 2017.

Rocco, M., Colomb, A., Baray, J.-L., Amelynck, C., Verreyken, B., Borbon, A., Pichon, J.-M., Bouvier, L., Schoon, N., Gros, V., Sarda-Esteve, R., Tulet, P., Metzger, J.-M., Duflot, V., Guadagno, C., Peris, G., and Brioude, J.: Analysis of Volatile Organic Compounds during the OCTAVE Campaign: Sources and Distributions of Formaldehyde on Reunion Island, Atmosphere, 11, 110, https://doi.org/10.3390/atmos11020140, 2020.

Saunders, S. M., Jenkin, M. E., Derwent, R. G., and Pilling, M. J.: Protocol for the development of the Master Chemical Mechanism, MCM v3 (Part A): tropospheric degradation of non-aromatic volatile organic compounds, Atmos. Chem. Phys., 3, 161–180, https://doi.org/10.5194/acp-3-161-2003, 2003.

Schwarz, K., Filipiak, W., and Amann, A.: Determining concentration patterns of volatile compounds in exhaled breath by PTR-MS, J. Breath Res., 3, 027002, https://doi.org/10.1088/1752-7155/3/2/027002, 2009.

Sindelarova, K., Granier, C., Bouarar, I., Guenther, A., Tilmes, S., Stavrakou, T., Müller, J.-F., Kuhn, U., Stefani, P., and Knorr, W.: Global data set of biogenic VOC emissions calculated by the MEGAN model over the last 30 years, Atmos. Chem. Phys., 14, 9317–9341, https://doi.org/10.5194/acp-14-9317-2014, 2014.

Singh, H. B., O'Hara, D., Herlth, D., Sachse, W., Blake, D. R., Bradshaw, J. D., Kanakidou, M., and Crutzen, P. J.: Acetone in the atmosphere: Distribution, sources, and sinks, J. Geophys. Res.-Atmos., 99, 1805–1819, https://doi.org/10.1029/93JD00764, 1994.

Sinreich, R., Merten, A., Molina, L., and Volkamer, R.: Parameterizing radiative transfer to convert MAX-DOAS dSCDs into near-surface box-averaged mixing ratios, Atmos. Meas. Tech., 6, 1521–1532, https://doi.org/10.5194/amt-6-1521-2013, 2013.

Stavrakou, T., Müller, J.-F., Peeters, J., Razavi, A., Clarisse, L., Clerbaux, C., Coheur, P.-F., Hurtmans, D., Mazière, M. D., Vigouroux, C., Deutscher, N. M., Griffith, D. W. T., Jones, N., and Paton-Walsh, C.: Satellite evidence for a large source of formic acid from boreal and tropical forests, Nat. Geosci., 5, 26–30, https://doi.org/10.1038/ngeo1354, 2012.

Stavrakou, T., Müller, J.-F., Bauwens, M., De Smedt, I., Van Roozendael, M., De Mazière, M., Vigouroux, C., Hendrick, F., George, M., Clerbaux, C., Coheur, P.-F., and Guenther, A.: How consistent are top-down hydrocarbon emissions based on formaldehyde observations from GOME-2 and OMI?, Atmos. Chem. Phys., 15, 11861–11884, https://doi.org/10.5194/acp-15-11861-2015, 2015.

Stohl, A. and Thomson, D. J.: A Density Correction for Lagrangian Particle Dispersion Models, Bound.-Lay. Meteorol., 90, 155–167, https://doi.org/10.1023/A:1001741110696, 1999.

Stohl, A., Hittenberger, M., and Wotawa, G.: Validation of the Lagrangian particle dispersion model FLEXPART against large-scale tracer experiment data, Atmos. Environ., 32, 4245–4264, https://doi.org/10.1016/S1352-2310(98)00184-8, 1998.

Stohl, A., Forster, C., Frank, A., Seibert, P., and Wotawa, G.: Technical note: The Lagrangian particle dispersion model FLEXPART version 6.2, Atmos. Chem. Phys., 5, 2461–2474, https://doi.org/10.5194/acp-5-2461-2005, 2005.

Su, T.: Parametrization of kinetic energy dependences of ion–polar molecule collision rate constants by trajectory calculations, J. Chem. Phys., 100, 4703–4703, https://doi.org/10.1063/1.466255, 1994.

Taupin, F. G., Beekmann, M., Brémaud, P. J., and Randriambelo, T.: Ozone generation over the Indian Ocean during the South African biomass-burning period: case study of October 1992, Ann. Geophys., 20, 547–557, https://doi.org/10.5194/angeo-20-547-2002, 2002.

Thalman, R. and Volkamer, R.: Temperature dependent absorption cross-sections of O_2–O_2 collision pairs between 340 and 630 nm and at atmospherically relevant pressure, Phys. Chem. Chem. Phys., 15, 15371–15381, https://doi.org/10.1039/C3CP50968K, 2013.

Travis, K. R., Heald, C. L., Allen, H. M., Apel, E. C., Arnold, S. R., Blake, D. R., Brune, W. H., Chen, X., Commane, R., Crounse, J. D., Daube, B. C., Diskin, G. S., Elkins, J. W., Evans, M. J., Hall, S. R., Hintsa, E. J., Hornbrook, R. S., Kasibhatla, P. S., Kim, M. J., Luo, G., McKain, K., Millet, D. B., Moore, F. L., Peischl, J., Ryerson, T. B., Sherwen, T., Thames, A. B., Ullmann, K., Wang, X., Wennberg, P. O., Wolfe, G. M., and Yu, F.: Constraining remote oxidation capacity with ATom observations, Atmos. Chem. Phys., 20, 7753–7781, https://doi.org/10.5194/acp-20-7753-2020, 2020.

Vandaele, A., Hermans, C., Simon, P., Carleer, M., Colin, R., Fally, S., Mérienne, M., Jenouvrier, A., and Coquart, B.: Measurements of the NO_2 absorption cross-section from $42\,000\,cm^{-1}$ to $10\,000\,cm^{-1}$ (238–1000 nm) at 220 K and 294 K, J. Quant. Spectrosc. Ra., 59, 171–184, https://doi.org/10.1016/S0022-4073(97)00168-4, 1998.

Verreyken, B., Brioude, J., and Evan, S.: Development of turbulent scheme in the FLEXPART-AROME v1.2.1 Lagrangian particle dispersion model, Geosci. Model Dev., 12, 4245–4259, https://doi.org/10.5194/gmd-12-4245-2019, 2019.

Vigouroux, C., Stavrakou, T., Whaley, C., Dils, B., Duflot, V., Hermans, C., Kumps, N., Metzger, J.-M., Scolas, F., Vanhaelewyn, G., Müller, J.-F., Jones, D. B. A., Li, Q., and De Mazière, M.: FTIR time-series of biomass burning products (HCN, C_2H_6, C_2H_2, CH_3OH, and HCOOH) at Reunion Island (21° S, 55° E) and comparisons with model data, Atmos. Chem. Phys., 12, 10367–10385, https://doi.org/10.5194/acp-12-10367-2012, 2012.

Wang, S., Hornbrook, R. S., Hills, A., Emmons, L. K., Tilmes, S., Lamarque, J.-F., Jimenez, J. L., Campuzano-Jost, P., Nault, B. A., Crounse, J. D., Wennberg, P. O., Kim, M., Allen, H., Ryerson, T. B., Thompson, C. R., Peischl, J., Moore, F., Nance, D., Hall, B., Elkins, J., Tanner, D., Huey, L. G., Hall, S. R., Ullmann, K., Orlando, J. J., Tyndall, G. S., Flocke, F. M., Ray, E., Hanisco, T. F., Wolfe, G. M., St. Clair, J., Commane, R., Daube, B., Barletta, B., Blake, D. R., Weinzierl, B., Dollner, M., Conley, A., Vitt, F., Wofsy, S. C., Riemer, D. D., and Apel, E. C.: Atmospheric Acetaldehyde: Importance of Air-Sea Exchange and a Missing Source in the Remote Troposphere, Geophys. Res. Lett., 46, 5601–5613, https://doi.org/10.1029/2019GL082034, 2019.

Yokelson, R. J., Goode, J. G., Ward, D. E., Susott, R. A., Babbitt, R. E., Wade, D. D., Bertschi, I., Griffith, D. W. T., and Hao, W. M.: Emissions of formaldehyde, acetic acid, methanol, and other trace gases from biomass fires in North Carolina measured by airborne Fourier transform infrared spectroscopy, J. Geophys. Res.-Atmos., 104, 30109–30125, https://doi.org/10.1029/1999JD900817, 1999.

Yokelson, R. J., Bertschi, I. T., Christian, T. J., Hobbs, P. V., Ward, D. E., and Hao, W. M.: Trace gas measurements in nascent, aged, and cloud-processed smoke from African savanna fires by airborne Fourier transform infrared spectroscopy (AFTIR), J. Geophys. Res.-Atmos., 108, 8478, https://doi.org/10.1029/2002JD002322, 2003.

Yokelson, R. J., Christian, T. J., Karl, T. G., and Guenther, A.: The tropical forest and fire emissions experiment: laboratory fire measurements and synthesis of campaign data, Atmos. Chem. Phys., 8, 3509–3527, https://doi.org/10.5194/acp-8-3509-2008, 2008.

Zhao, Y., Saunois, M., Bousquet, P., Lin, X., Berchet, A., Hegglin, M. I., Canadell, J. G., Jackson, R. B., Hauglustaine, D. A., Szopa, S., Stavert, A. R., Abraham, N. L., Archibald, A. T., Bekki, S., Deushi, M., Jöckel, P., Josse, B., Kinnison, D., Kirner, O., Marécal, V., O'Connor, F. M., Plummer, D. A., Revell, L. E., Rozanov, E., Stenke, A., Strode, S., Tilmes, S., Dlugokencky, E. J., and Zheng, B.: Inter-model comparison of global hydroxyl radical (OH) distributions and their impact on atmospheric methane over the 2000–2016 period, Atmos. Chem. Phys., 19, 13701–13723, https://doi.org/10.5194/acp-19-13701-2019, 2019.

Zhou, M., Langerock, B., Vigouroux, C., Sha, M. K., Ramonet, M., Delmotte, M., Mahieu, E., Bader, W., Hermans, C., Kumps, N., Metzger, J.-M., Duflot, V., Wang, Z., Palm, M., and De Mazière, M.: Atmospheric CO and CH_4 time series and seasonal variations on Reunion Island from ground-based in situ and FTIR (NDACC and TCCON) measurements, Atmos. Chem. Phys., 18, 13881–13901, https://doi.org/10.5194/acp-18-13881-2018, 2018.

Chapter 7

Mesoscale transport and source attribution

7.1 Objectives and methodology

The objective was to perform a complete identification of sources and sinks of VOCs in the remote tropical atmosphere using the two-year data set generated using the hs-PTR-Quad-MS instrument deployed at the Maïdo observatory between October 2017 and November 2019. This was done by a combination of i) describing diel, seasonal and inter-annual patterns in VOC concentrations recorded at the observatory, ii) making use of a PMF algorithm to identify different sources using a multivariate statistical approach, and iii) calculating 24-hour back-trajectories every hour using FLEXPART-AROME for the complete duration of the deployment of the hs-PTR-Quad-MS instrument at the Maïdo observatory. Here, we confirm that at night, air masses originating in the FT reach the observatory while during daytime, mesoscale sources located on the island have a major impact on the atmospheric composition at Maïdo. The paper serves as an evaluation of previous studies describing mesoscale transport processes towards the Maïdo observatory using an extensive base of measurements and the mesoscale Lagrangian transport model FLEXPART-AROME. This is in contrast with previous studies which describe the transport either qualitatively (Baray et al., 2013; Tulet et al., 2017; Foucart et al., 2018, e.g.,), based on the identification of case studies (Duflot et al., 2019, e.g.,), or

perform numerical simulations to estimate the impact of pollutant sources at the observatory without extensive testing using measurements (Lesouëf et al., 2011). The work which resembles the validation of mesoscale transport presented here closest was done by analysis of 1-year measurements of water isotopes showing that nighttime measurements originate indeed in the FT (Guilpart et al., 2017). The work presented hereafter focuses on the impact of transport on VOC concentrations, identifies the dominant mesoscale emission sources affecting air quality at the location of Maïdo, and characterises the composition of air masses originating in the FT. The manuscript has recently been accepted for peer review in the journal Atmospheric Chemistry and Physics. A preprint is published in the journal Atmospheric Chemistry and Physics Discussions (Verreyken et al., 2021).

Bibliography

Baray, J.-L., Courcoux, Y., Keckhut, P., Portafaix, T., Tulet, P., Cammas, J.-P., Hauchecorne, A., Godin Beekmann, S., Mazière, M. D., Hermans, C., Desmet, F., Sellegri, K., Colomb, A., Ramonet, M., Sciare, J., Vuillemin, C., Hoareau, C., Dionisi, D., Duflot, V., Vérèmes, H., Porteneuve, J., Gabarrot, F., Gaudo, T., Metzger, J.-M., Payen, G., Leclair de Bellevue, J., Barthe, C., Posny, F., Ricaud, P., Abchiche, A., and Delmas, R.: Maïdo Observatory: A New High-Altitude Station Facility at Reunion Island (21° S, 55° E) for Long-Term Atmospheric Remote Sensing and in Situ Measurements, Atmospheric Measurement Techniques, 6, 2865–2877, https://doi.org/10.5194/amt-6-2865-2013, 2013.

Duflot, V., Tulet, P., Flores, O., Barthe, C., Colomb, A., Deguillaume, L., Vaïtilingom, M., Perring, A., Huffman, A., Hernandez, M. T., Sellegri, K., Robinson, E., O'Connor, D. J., Gomez, O. M., Burnet, F., Bourrianne, T., Strasberg, D., Rocco, M., Bertram, A. K., Chazette, P., Totems, J., Fournel, J., Stamenoff, P., Metzger, J.-M., Chabasset, M., Rousseau, C., Bourrianne, E., Sancelme, M., Delort, A.-M., Wegener, R. E., Chou, C., and Elizondo, P.: Preliminary Results from the FARCE 2015 Campaign: Multidisciplinary Study of the Forest–Gas–Aerosol–Cloud System on the Tropical Island of La Réunion, Atmospheric Chemistry and Physics, 19, 10 591–10 618, https://doi.org/10.5194/acp-19-10591-2019, 2019.

Foucart, B., Sellegri, K., Tulet, P., Rose, C., Metzger, J.-M., and Pi-

card, D.: High Occurrence of New Particle Formation Events at the Maïdo High-Altitude Observatory (2150 m), Réunion (Indian Ocean), Atmospheric Chemistry and Physics, 18, 9243–9261, https://doi.org/10.5194/acp-18-9243-2018, 2018.

Guilpart, E., Vimeux, F., Evan, S., Brioude, J., Metzger, J.-M., Barthe, C., Risi, C., and Cattani, O.: The Isotopic Composition of Near-Surface Water Vapor at the Maïdo Observatory (Reunion Island, Southwestern Indian Ocean) Documents the Controls of the Humidity of the Subtropical Troposphere, Journal of Geophysical Research: Atmospheres, 122, 9628–9650, https://doi.org/10.1002/2017JD026791, 2017.

Lesouëf, D., Gheusi, F., Delmas, R., and Escobar, J.: Numerical Simulations of Local Circulations and Pollution Transport over Reunion Island, Annales Geophysicae, 29, 53–69, https://doi.org/10.5194/angeo-29-53-2011, 2011.

Tulet, P., Muro, A. D., Colomb, A., Denjean, C., Duflot, V., Arellano, S., Foucart, B., Brioude, J., Sellegri, K., Peltier, A., Aiuppa, A., Barthe, C., Bhugwant, C., Bielli, S., Boissier, P., Boudoire, G., Bourrianne, T., Brunet, C., Burnet, F., Cammas, J.-P., Gabarrot, F., Galle, B., Giudice, G., Guadagno, C., Jeamblu, F., Kowalski, P., Leclair de Bellevue, J., Marquestaut, N., Mékies, D., Metzger, J.-M., Pianezze, J., Portafaix, T., Sciare, J., Tournigand, A., and Villeneuve, N.: First Results of the Piton de La Fournaise STRAP 2015 Experiment: Multidisciplinary Tracking of a Volcanic Gas and Aerosol Plume, Atmospheric Chemistry and Physics, 17, 5355–5378, https://doi.org/10.5194/acp-17-5355-2017, 2017.

Verreyken, B., Amelynck, C., Schoon, N., Müller, J.-F., Brioude, J., Kumps, N., Hermans, C., Metzger, J.-M., and Stavrakou, T.: Measurement report: Source apportionment of volatile organic compounds at the remote high-altitude Maïdo observatory, Atmospheric Chemistry and Physics Discussions, 2021, 1–37, https://doi.org/10.5194/acp-2021-124, 2021.

Measurement report: Source apportionment of volatile organic compounds at the remote high-altitude Maïdo observatory

Bert Verreyken[1,2,3], Crist Amelynck[1,2], Niels Schoon[1], Jean-François Müller[1], Jérôme Brioude[3], Nicolas Kumps[1], Christian Hermans[1], Jean-Marc Metzger[4], and Trissevgeni Stavrakou[1]

[1]Royal Belgian Institute for Space Aeronomy, B-1180 Brussels
[2]Department of Chemistry, Ghent University, B-9000 Ghent, Belgium
[3]Laboratoire de l'Atmosphère et des Cyclones, UMR 8105, CNRS, Université de La Réunion, Météo France, 97744 Saint-Denis, France
[4]Observatoire des Sciences de l'Univers de La Réunion, UMS3365, CNRS, Université de La Réunion, Météo-France, Saint-Denis, La Réunion, France

Correspondence: Bert Verreyken (bert.verreyken@aeronomie.be)

Abstract. We present a source apportionment study of a near-continuous 2-year dataset of volatile organic compounds (VOCs), recorded between October 2017 and November 2019 with a quadrupole-based high-sensitivity proton-transfer-reaction mass-spectrometry (hs-PTR-MS) instrument deployed at the Maïdo observatory (21.1°S, 55.4°E, 2,160 m altitude). The observatory is located on La Réunion island in the south-west Indian Ocean. We discuss seasonal and diel profiles of six key VOC species unequivocally linked to specific sources — acetonitrile (CH_3CN), isoprene (C_5H_8), isoprene oxidation products (Iox), benzene (C_6H_6), C_8-aromatics (C_8H_{10}), and dimethyl sulfide (DMS). The data are analyzed using the positive matrix factorization (PMF) method and back-trajectory calculations based on the Lagrangian mesoscale transport model FLEXPART-AROME to identify the impact of different sources on air masses recorded at the observatory. As opposed to the biomass burning tracer CH_3CN, which does not exhibit a consistent diel variability, we identify pronounced diel profiles with a daytime maximum for the biogenic (C_5H_8 and Iox) and anthropogenic (C_6H_6, C_8H_{10}) tracers. The marine tracer DMS generally displays a daytime maximum except for the austral winter when the difference between daytime and nighttime mixing ratios vanishes. Four factors were identified by the PMF: background/biomass burning, anthropogenic, primary biogenic and secondary biogenic. Despite human activity being concentrated in few coastal areas, the PMF results indicate that the anthropogenic source factor is the dominant contributor to the VOC load (38%), followed by the background/biomass burning source factor originating in the free troposphere (33%), and by the primary (15%) and secondary biogenic sources (14%). FLEXPART-AROME simulations showed that the observatory was most sensitive to anthropogenic emissions west of Maïdo while the strongest biogenic contributions coincided with airmasses passing over the north-eastern part of La Réunion. At night, the observatory is often located in the free troposphere while during the day, the measurements are influenced by mesoscale sources. Interquartile ranges of nighttime 30-minute average concentrations of methanol (CH_3OH), CH_3CN, acetaldehyde (CH_3CHO), formic acid (HCOOH), acetone (CH_3COCH_3), acetic acid (CH_3COOH) and methyl ethyl ketone (MEK), representative for the atmospheric composition of the free troposphere, were found to be 525–887 pptv, 79–110 pptv, 61–101 pptv, 172–335 pptv, 259–379 pptv, 64–164 and 11–21 pptv, respectively.

1 Introduction

25 Non-methane volatile organic compounds (NMVOCs) are key players in atmospheric chemistry. Their reaction with the main atmospheric oxidants modulates the oxidative capacity of the atmosphere (Zhao et al., 2019) and, in combination with NO_x, results in the production of tropospheric ozone (O_3) and secondary organic aerosol (SOA), both air pollutants affecting human health (Jerrett et al., 2009) and short-term climate forcers. Whereas increases in tropospheric O_3 contribute to global warming, SOA affects radiative forcing both through direct interaction with radiation and indirectly by acting as cloud condensation

30 nuclei (CCN), resulting in an overall cooling effect (IPCC, 2013). Besides pure hydrocarbon compounds, which are emitted in huge amounts at the global scale and mainly by terrestrial vegetation, an important NMVOC class is composed of oxygenated compounds (OVOCs). These OVOCs can be directly emitted to the atmosphere by multiple sources, including the biosphere (vegetation and soils), biomass burning, anthropogenic activities and the ocean. Secondary production by oxidation of primary emitted NMVOCs, however, is a very important and often badly quantified source for many OVOCs as well. Moreover, recent

35 research has pointed to the importance of bidirectional exchange of OVOCs with oceans (Yang et al., 2014) and terrestrial vegetation (Farmer and Riches, 2020), a process which is not well described in atmospheric models and which complicates OVOC budget calculations. In the absence of high concentrations of highly reactive non-methane hydrocarbons, OVOCs are expected to account for most of the OH reactivity in the remote tropical marine atmosphere (Travis et al., 2020). However, due to scarcity of observational constraints, OVOC sources and sinks are prone to large uncertainties in these regions (Millet

40 et al., 2010; Read et al., 2012; Travis et al., 2020). The OCTAVE project (https://octave.aeronomie.be, last access: 11 December 2020) aims at reducing those uncertainties through in situ measurements, satellite retrievals of global OVOC concentrations and tropospheric modelling. In the framework of this project, a quadrupole-based high-sensitivity proton-transfer-reaction mass-spectrometry VOC analyzer (hs-PTR-MS) was deployed for two years at the remote high-altitude Maïdo observatory (21.1°S, 55.4°E, 2,160 m altitude) at Réunion Island, a remote tropical French volcanic island in the south-west Indian Ocean. The

45 instrument continuously measured marine boundary layer air enriched with compounds originating from urbanized areas and ecosystems native to the island during the day. At night, the observatory is frequently located in or near the free troposphere. Part of this hs-PTR-MS dataset (April 2018), in combination with Aerolaser formaldehyde measurements, has already been used for formaldehyde source apportionment on the Island using positive matrix factorization (PMF) (Rocco et al., 2020). Another study focused on the detection of African biomass burning plumes during August 2018 and 2019 and their impact on

50 the (O)VOC composition at the Maïdo observatory (Verreyken et al., 2020).

The present study makes use of the complete dataset and aims at a better characterization of mesoscale (O)VOC sources by studying their seasonal, diel and inter-annual variability using PMF and back-trajectory calculations. Previous studies have described the mesoscale transport features over La Réunion and the impact on measurement campaigns taking place on the island (Lesouëf et al., 2011; Baray et al., 2013; Tulet et al., 2017; Guilpart et al., 2017; Foucart et al., 2018; Duflot et al.,

55 2019). The recent development of FLEXPART-AROME (Verreyken et al., 2019) — a Lagrangian transport model driven by

2

Year	Start	End	Duration	Type	Comments
2017	27 December	9 January	13 days	Tropical cyclone, Ava	Technical issues with the hs-PTR-MS instrument.
2018	9 January	20 January	11 days	Intense tropical cyclone, Berguitta	Maïdo closed
	1 March	6 March	5 days	Intense tropical cyclone, Dumazile	Maïdo closed
	13 March	20 March	7 days	Sever tropical storm, Eli-akim	
	3 April	4 April	17 hours	Volcanic eruption	
	20 April	25 April	5 days	Tropical cyclone, Fakir	
	27 April	25 May	27 days	Volcanic eruption	Accompanied by occasional vegetation fires
	13 July	13 July	13 hours	Volcanic eruption	
	17 November	25 November	8 days	Social unrest due to the 'yellow vests' protests	Last 5 days had a partial curfew
2019	18 February	10 March	21 days	Volcanic eruption	
	10 June	13 June	54 hours	Volcanic eruption	
	29 July	30 July	24 hours	Volcanic eruption	
	11 August	15 August	4 days	Volcanic eruption	
	25 October	27 October	2 days	Volcanic Eruption	

Table 1. Special events with potential impact on VOC concentrations during the two-year deployment of the hs-PTR-MS. During some of these events the hs-PTR-MR was shut down due to security measures at the Maïdo observatory. Information from (Fournaise Info, 2018; Le Monde, 2018; Météo France, 2020).

meteorological data obtained from the operational mesoscale numerical weather prediction models used in the region by Météo France — provides the opportunity to study mesoscale transport and its impact on the near-continuous 2-year (O)VOC dataset recorded at the observatory. We start by describing the measurement site, the instruments, and the source attribution tools used in Section 2. We present the diel, seasonal and inter-annual variability of key tracers linked to known sources in Section 3.1. This variability is discussed in light of sources identified by the PMF algorithm (Section 3.2) and back-trajectories calculated with FLEXPART-AROME (Section 3.3).
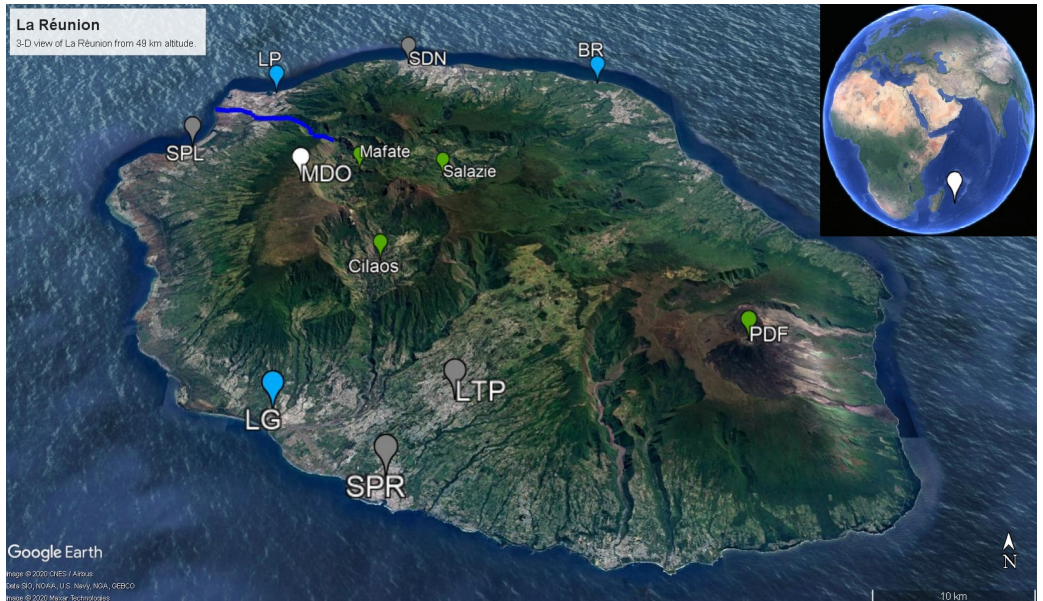
Figure 1. La Réunion, viewed from 49 km height. The Maïdo observatory (MDO) is indicated in white. Cities with population over 50,000 habitants — i.e. Saint-Denis (SDN), Saint-Paul (SPL), Le Tampon (LTP), and Saint-Pierre (SPR) — are shown in gray. The largest industrial sites — Le Port (LP), Bois-Rouge (BR), and Le Gol (LG) — are indicated in blue. Geological landmarks — Calderas Mafate, Salazie, and Ciloas as well as the shield volcano Piton de la Fournaise (PDF) — in green. The river Rivière des Galets between Mafate and Le Port is indicated as a dark blue line. Image generated with Google Earth Pro, data SOI, NOAA, U.S. Navy, GA, GEBCO. ©2020 CNES/Airbus, ©2020 Maxar Technologies.

2 Materials and methods

2.1 Description of measurement site

La Réunion — a small tropical island located in the south-west Indian Ocean, shown in Figure 1 — is home to the high-altitude Maïdo observatory (21.1°S, 55.4°E, 2,160 m altitude) (Baray et al., 2013). Despite urbanization of the coastal areas, the island still houses about 10,000 ha of native ecosystems (Duflot et al., 2019). The Maïdo observatory is located in a National Park and surrounded by mountain shrublands and heathlands (Duflot et al., 2019). The largest city is the capital, Saint-Denis. Other large cities (population over 50,000) are Saint-Paul, Saint-Pierre, and Le Tampon. Industrial emission hotspots at La Réunion are located near the power plants in Le Port (diesel power plant), Le Gol (biomass power plant), and Bois-Rouge (biomass power plant). The island is home to the very active Piton de La Fournaise volcano (Tulet et al., 2017). La Réunion is isolated

4

from large landmasses and provides an ideal location to study complex processes and interactions in the remote atmosphere of anthropogenic, biogenic and volcanic emissions as illustrated by studies of e.g. volcanic plume emissions and ageing (Tulet et al., 2017), new particle formation (Foucart et al., 2018), and forest-gas-aerosol-cloud system interaction (Duflot et al., 2019). A recently published land-cover map of La Réunion (Dupuy et al., 2020) shows that a large fraction of the coastal zone is used to cultivate sugar cane, which is by far the dominant agricultural crop, and fruit. While the eastern part of the island is mainly covered by woodlands. The western region is typically drier throughout the year and houses relatively more shrub and herbaceous savanna near the coast (Dupuy et al., 2020). Orographically-induced precipitation along the western mountain slope allows woodlands to be dominant at mid-level altitudes (Dupuy et al., 2020). There are two distinct seasons on the island, the warm and wet season (December to March) and the cold dry season (May to November) (Foucart et al., 2018). From October to May, the region is sensitive to tropical cyclone activity. Synoptic scale air-mass transport in the region is dominated by east-south-easterly trade winds near the surface and westerlies in the free troposphere (FT) (Baldy et al., 1996; Lesouëf et al., 2011; Baray et al., 2013). These trade winds weaken from December to March but intensify from April to November (Baldy et al., 1996). The complex orographic profile of La Réunion (highest point over 3,000 m altitude) introduces a major obstacle in the stable wind flow pattern. Trade winds are split around the island with winds accelerating along the coastlines parallel to the synoptic flow (Lesouëf et al., 2011). The northwestern area (lee side) of the island is sheltered from trade winds by the mountainous profile. Counter-flowing vortices in the wake of the island can trap polluted air masses (Lesouëf et al., 2011). Transport in the northwestern sector of the island is dominated by the coupling of sea (land)-breeze with upslope (downslope) transport during the day (night). During the day, the Maïdo observatory — located West of the Maïdo mountain peak — resides in the planetary boundary layer (PBL) while at night it is frequently in or near the FT (Lesouëf et al., 2011; Baray et al., 2013; Guilpart et al., 2017; Duflot et al., 2019). During the day, a horizontal wind shear front located at the confluence of the mesoscale-driven upslope transport and overflowing trade winds determines air mass origins at the observatory (Duflot et al., 2019). When the front is west of the observatory, surface emissions have less impact on the composition of air masses as they originate mostly from 2,000 m altitude (Duflot et al., 2019). During the OCTAVE measurement period, several events occurred which could have affected in situ air mass composition and VOC mixing ratio diel profiles (tropical storms and cyclones, volcanic eruptions). These are summarized in Table 1 but are not studied in detail as their effects are outside the scope of the current work.

2.2 Instrumentation and sampling setup

2.2.1 hs-PTR-MS

In October 2017, a high-sensitivity quadrupole-based proton-transfer-reaction mass-spectrometry instrument (hs-PTR-MS, Ionicon Analytik GmbH, Austria) was deployed at the Maïdo observatory. It was run in multiple ion detection mode to generate a near-continuous dataset of (mostly) oxygenated volatile organic compounds from 19 October, 2017 to 26 November, 2019. The instrument was operated in H_3O^+ reactant ion mode at a drift tube pressure and temperature of 2.2 hPa and 333 K, respectively, and at a drift field of 600 V, which resulted in an E/N value (the ratio of the electric field to the number density in the drift

tube) of 136 Td. VOC-related product ion signals were sequentially recorded at mass-to-charge ratios (m/z) 31 (formaldehyde, HCHO), 33 (methanol, CH_3OH), 42 (acetonitrile, CH_3CN), 45 (acetaldehyde, CH_3CHO), 47 (formic acid, HCOOH), 59 (acetone, CH_3COCH_3), 61 (acetic acid, CH_3COOH), 63 (dimethylsulfide, DMS), 69 (isoprene, C_5H_8), 71 (methyl vinyl ketone, MVK; methacrolein, MACR; and possible contributions from isoprene hydroxy hydroperoxides (Rivera-Rios et al., 2014), ISOPOOH), 73 (methyl ethyl ketone, MEK), 79 (benzene, C_6H_6), 81 (sum of monoterpenes, $C_{10}H_{16}$), 93 (toluene, C_7H_8), 107 (C_8-aromatics, C_8H_{10}) and 137 ($C_{10}H_{16}$), each with a 10 s dwell time. In addition, ions at m/z 21 ($H_3^{18}O^+$), 32 (O_2^+) and 37 ($H_3O^+ \cdot H_2O$) were monitored with dwell times of 2s, 100 ms and 100 ms, respectively. A complete measurement cycle lasted 2.7 min. Ion signals at m/z 31, 81 and 93 were not considered in the present analysis because of potential contributions from interfering compounds or background values which were considerably larger than the minimum values in ambient air, thus resulting in negative concentrations. It is well documented that hs-PTR-MS measurements of MVK+MACR (m/z = 71) include contributions from ISOPOOH through the formation of MVK or MACR from ISOPOOH in the instrument (Liu et al., 2013; Rivera-Rios et al., 2014; Bernhammer et al., 2017). As ISOPOOH is the major first-generation oxidation product of C_5H_8 in low nitrogen oxides ($NO_x = NO + NO_2$) environments (Wennberg et al., 2018), we expect that the MVK+MACR signal could suffer from interference from ISOPOOH. Therefore, we will refer to ion signal at m/z 71 as isoprene oxidation products or Iox. Air was sampled 2.86 m above the roof of the observatory (8.20 m above ground) and pumped towards the instrument through a 10.35 m long 3/8 inch (outer diameter) perfluoralkoxy (PFA) Teflon sampling tube (Dyneon 6502T, Fluortechniek-Deutschland, Germany) at a flow rate of 8 L min^{-1}. The sampling line was heated (5–10 degrees above ambient temperature) and thermally insulated to prevent condensation. The sampled air was filtered for particles 2.48 m downstream the sampling point by a polytetrafluoroethylene (PTFE) membrane filter (Zefluor, Pall laboratory, MI, USA) with a pore size of 2 μm. Part of the sampled air was sent through a catalytic converter (type HPZA-3500, Parker Hannifin Corp., OH, USA) for zero-VOC measurements, which took place every four hours and lasted 30 minutes of which only the last minutes were taken into account. Calibration of the hs-PTR-MS for the target VOCs was performed every 3-4 days by dynamically diluting a VOC/N_2 calibration mixture (Apel-Riemer Environmental Inc., FL, USA; stated accuracy of 5% (2σ) on the VOC mixing ratios) in zero air. In April 2018 and March 2019, the instrument was also calibrated with a commercial gas calibration unit (GCU, Ionicon Analytik GmbH, Austria) from LSCE (Laboratoire des Sciences du Climat et de l'Environment). Calibration factors for the (O)VOCs of interest obtained with the two calibration systems were found to be in excellent agreement. Calibration factors for compounds that were not present in the calibration mixture — i.e. HCOOH and CH_3COOH — were determined indirectly as mentioned in (Verreyken et al., 2020). The humidity dependence of the calibration factors was determined approximately every 2 months by controlling the humidity of the zero air with a dew point generator (LI-COR LI-610, NE, USA). The ion signal at m/z 37 was used as a proxy for air humidity. Of all compounds present in the calibration mixture, only the calibration factors for formaldehyde, isoprene, Iox and MEK showed a non-negligible humidity dependence. The humidity dependence of calibration factors for carboxylic acids – not present in the calibration mixture – was retrieved from (Baasandorj et al., 2015).

2.2.2 Additional measurements

The Maïdo observatory has recently been officially registered as an ICOS (Integrated Carbon Observation System, https://www.icos-cp.eu/, last access: 7 January 2021) atmospheric measurement site and a GAW (Global Atmosphere Watch, https://public.wmo.int/en/programmes/global-atmosphere-watch-programme, last access 7 January 2021) station. In this capacity, the observatory continuously houses a suite of both in-situ and remote sensing instruments. A list of all regular measurements can be found online (https://osur.univ-reunion.fr/observations/osu-r-stations/opar/, last access: 11 December 2020). In this study we will focus on carbon monoxide (CO) mixing ratios taken by a PICARRO G2401 instrument (PICARRO Inc., CA, USA). We will use the CO data to better characterize the presence of biomass burning (BB) plumes at Maïdo. Auxiliary data (wind direction, ambient temperature and solar radiation) were recorded by a meteorological station.

2.3 Source attribution tools

2.3.1 Positive matrix factorization

Air composition was studied using the positive matrix factorization (PMF) multivariate receptor model software released by the United States Environmental Protection Agency (EPA), EPA PMF 5.0 (Norris et al., 2014). PMF is a popular tool in atmospheric source attribution studies (e.g., Rocco et al., 2020; Pernov et al., 2020). The mathematical principle behind the PMF algorithm is based on the decomposition of measurements (x_{ij}) in a linear combination of factor profiles (f_{kj}) and factor contributions (g_{ik}), and a residual (ϵ_{ij}):

$$x_{ij} = \sum_{k=1}^{p} g_{ik} \times f_{kj} + \epsilon_{ij}. \tag{1}$$

The indices i, j and k denote the measurement time, the measured compound and the selected factor respectively. The total number of factors (p) represents the number of sources affecting the dataset and is a hyperparameter, i.e. a parameter set by the analyser to optimize the solution, for the algorithm. The only mathematical constraint to solve this equation is that all factor contributions and profiles must be positive. As a result, atmospheric sinks are not taken explicitly into account when deconstructing the dataset. The equation is solved by minimizing the objective function Q:

$$Q = \sum_{i=1}^{n} \sum_{j=1}^{m} \left[\frac{\epsilon_{ij}}{u_{ij}} \right]^2, \tag{2}$$

where n is the total number of measurements, m is the number of species and u_{ij} is the uncertainty of a measurement. In total, there are three different calculations of the objective function. The first takes into account all the residuals (Q_{true}), the second excludes a number of data points that are identified by the software as outliers (Q_{robust}), and the last version of the objective function is equal to the difference between the number of data values that are characterized as 'strong' (see Section 3.2) and the number of parameters fitted by the model ($Q_{expected}$). The $Q_{expected}$ corresponds roughly to the number of degrees of

freedom for the algorithm. The number of factors is set by scanning the parameter space and looking for a shift in both the $Q_{true}/Q_{expected}$ ratio — also called Q_{scaled} — and the maximum root mean square (RMS) of residuals for the different compounds as well as ensuring physical interpretability of the resulting factor profiles and contributions.

2.3.2 Back-trajectory modeling

The FLEXPART-AROME model, a limited domain version of the Lagrangian transport model FLEXPART (Stohl et al., 2005; Pisso et al., 2019), was developed to simulate mesoscale transport over the complex orographic profile of La Réunion (Verreyken et al., 2019). The model is driven by meteorological data generated by AROME, the operational mesoscale numerical weather prediction (NWP) model with a 2.5 km horizontal resolution used in the region by Météo-France. FLEXPART-AROME was initially developed from FLEXPART-WRF (Brioude et al., 2013) to forecast the dispersion of a volcanic plume for the STRAP campaign in 2015 (Tulet et al., 2017). In order to ensure harmonized turbulent transport in the NWP and the offline transport model, turbulence in FLEXPART-AROME was adapted to be driven by the 3D turbulent kinetic energy fields obtained from AROME (Verreyken et al., 2019). The FLEXPART-AROME model has been used to study impact of mesoscale transport on BB plumes from distant sources (Verreyken et al., 2020). The model is driven by combining AROME forecasts generated daily at 00:00, 06:00, 12:00 and 18:00 UT. From 3 November 2017 until 26 November 2019, 20,000 air parcels are initialized every hour between 0 and 20 m above ground level (a.g.l.) at 21.081 °S, 55.383 °E. The model is run in backward mode (Seibert and Frank, 2004). Air parcels are traced 24 hours backward in time and are separated in two age classes (ACs) of 12 hours. Air parcels' residence times (RTs, expressed in seconds) are computed in a grid with 0.025° (about 2.5 km) horizontal resolution between 19.5°S – 22.5°S and 53.0°E – 58.0°E with 15 vertical layers of 50 m thickness below 500 m a.g.l, 500 m thickness up to 2,000 m a.g.l and 2 additional layers above (10 km and 24 km height). Output is generated at time l and contains the RTs, i.e. the accumulated time all particles were present in grid cell m between times l and $l-1$. The RT is proportional to the impact of the emission rate of a source located in grid cell m at time l on the measurement related to the release of air parcels at the location of the observatory (receptor) in the model. This proportionality is quantified by the source-receptor relationship (SRR, also called emission sensitivity) of area m (source) at time l and is calculated by:

$$SRR_{lm} = \frac{RT_{lm}}{h}, \tag{3}$$

where h is the height of the surface layer at time l. In practice, this h cannot be higher than the PBL but may not be too shallow in order to be numerically robust (Seibert and Frank, 2004). Concentrations at the receptor site of a passive tracer X (not produced or lost during transport) can be calculated by:

$$C_X = \sum_l \sum_m E_{X,lm} \times SRR_{lm}, \tag{4}$$

where $E_{X,lm}$ is the emission rate (expressed in g m^{-2} s^{-1}) of tracer X related to area m at time l. As the (O)VOC compounds recorded with the hs-PTR-MS instrument are generally reactive compounds, the SRR from back-trajectory calculations are compared to the more robust PMF source factor contribution temporal variations. In this work, we will use the mesoscale boundary layer movement towards Maïdo using a minimal static PBL proxy used by (Lesouëf et al., 2011). They represented

the PBL using a 500 m a.g.l. layer capped at 1,000 m above sea level (a.s.l.) In order to resolve this capping, the higher vertical resolution below 500 m a.g.l. in the FLEXPART-AROME output is needed. By using the minimal PBL proxy we simulate the arrival of pollutants emitted into the boundary layer further away from the observatory. In order to quantify the impact of local emissions, a second PBL proxy which is not capped at 1000 m a.s.l. is used. Two approximations are applied here when using the SRR. Firstly, we accumulate the RTs over the complete period air parcels are transported over the specific source area for each release. By doing this, we do not consider a time dependence of emissions rates at the source. Since the largest temporal variation in emission rates manifests itself between day and night, coincident with the shift from PBL to FT air masses arriving at the observatory, we do not expect this approximation to significantly affect the results. Secondly, we separate the grid cells into three categorical variables (mountain, urban and marine) to identify the chemical signature of emissions at the source. The emission sensitivity to marine emissions is determined by air parcels located in the PBL proxy over the ocean. As urban areas are located near the coasts, generally with surface elevations below 500 m a.s.l., air parcels located in the PBL proxy over this region are categorized as sensitive to urban emissions. The remaining area is categorized as mountainous, with usually strong biogenic emissions during the day. Using the minimal PBL proxy by (Lesouëf et al., 2011), the emission sensitivity in the mountainous area is restricted to a small band of surface elevation between 500 and 950 m a.s.l. By changing to the constant 500 m a.g.l. layer as a PBL proxy, we will only change the SRR of mountainous areas. We will discuss both the capped — PBL proxy by (Lesouëf et al., 2011) — and uncapped — constant 500 m a.g.l. — mountain categories. In the following, discussion of the mountain category refers to the uncapped PBL proxy unless specified otherwise. By using the categorical variables we neglect possible hotspots of anthropogenic sources related to industry or large cities. The relatively coarse resolution of AROME (2.5 x 2.5 km^2) does not permit to resolve local transport features induced by the strong orographic profile of La Réunion for individual measurements. As such, we will be using the model output to discuss median diel profiles and combine releases in the model to identify the impact of mesoscale transport on measurements at the Maïdo observatory.

3   Results and discussion

Due to the high altitude of the Maïdo observatory, it is primarily located in the free troposphere during the night. During the day, the pristine marine boundary layer air over the ocean is thermally driven towards the observatory by the sea breeze coupled to upslope transport on the western side of the Island. This mesoscale transport is in competition with overflowing trade winds coming from the east. During the day, marine air masses pass over both anthropogenic and biogenic sources affecting the atmospheric composition. The dataset is split into nighttime — 22:00 until 05:00 LT — and daytime — 10:00 until 17:00 LT. As seen in Table 2, (O)VOC concentrations are generally higher during the day, except CH$_3$CN and DMS which present similar mixing ratios between nighttime and daytime. We will first describe and discuss the diel, seasonal and inter-annual variability of tracers recorded with the hs-PTR-MS instrument (Section 3.1). Next, the PMF algorithm is used to attribute the atmospheric (O)VOC burden to specific sources (Section 3.2) which are identified by comparing temporal variations of the PMF source factor contributions to diel and inter-annual variability of the tracers reported in Section 3.1. Finally, the results obtained in Section 3.1 and Section 3.2 are compared to back-trajectory calculations performed with FLEXPART-AROME (Section 3.3)

9

Table 2. Interquartile range of 30-minute average (O)VOC mixing ratios (MR) recorded at the remote high-altitude Maïdo observatory during nighttime (22:00 – 05:00 LT, FT) and daytime (10:00 – 17:00 LT, remote PBL). The last column indicates the median 30-minute average mixing ratio during nighttime with the standard deviation between parentheses. If the limit is below the limit of detection (LoD), we put < LoD.

Compound	Daytime MR [pptv]	Nighttime MR [pptv]	Nighttime median MR (σ) [pptv]
CH_3OH	990–1,531	525–887	724 (228)
CH_3CN	84–109	79–110	94 (39)
CH_3CHO	179–311	61–101	78 (41)
HCOOH	557–1,045	172–335	225 (474)
CH_3COCH_3	355–526	259–379	304 (152)
CH_3COOH	248–511	64–164	99 (226)
DMS	11–20	7–16	11 (7)
C_5H_8	80–223	< 9	< 9
Iox	48–136	< 3–8	4 (11)
MEK	35–69	11–21	15 (10)
C_6H_6	12–25	4–11	6 (9)
C_8H_{10}	< 10–21	< 10	< 10
$C_{10}H_{16}$	< 16–24	< 16	<16

to further validate the PMF results and assess the impact of mesoscale transport on the atmospheric composition recorded at
230   Maïdo.

3.1   Diel, seasonal and inter-annual variability

Discussion on annual and diel variability is limited to a subset of VOCs — CH_3CN, C_5H_8, Iox, C_6H_6, C_8H_{10}, and DMS — of which the patterns can be unequivocally attributed to different sources – pyrogenic, primary biogenic, secondary biogenic, anthropogenic and marine respectively. To support this discussion we use Figures 2-7 where the daily average concentrations,
235   seasonal median diel profiles and wind-separated (easterly versus westerly winds) median diel profiles for the different species under consideration and several meteorological parameters are shown.

3.1.1   Acetonitrile

Biomass burning is the main source of CH_3CN in the atmosphere (de Gouw, 2003) and is often used as an indicator for BB plumes in atmospheric studies (e.g., Verreyken et al., 2020). Its sinks are reaction with the hydroxyl radical (OH) and uptake
240   by the ocean surface. Both processes are slow, resulting in a long average atmospheric lifetime of CH_3CN, 1.4 years (de Gouw, 2003). This not only allows transport from distance sources (e.g. BB events in Africa, Madagascar but also South-America and Malaysia (Duflot et al., 2010; Verreyken et al., 2020)) but also allows the compound to be well-mixed in the atmosphere.
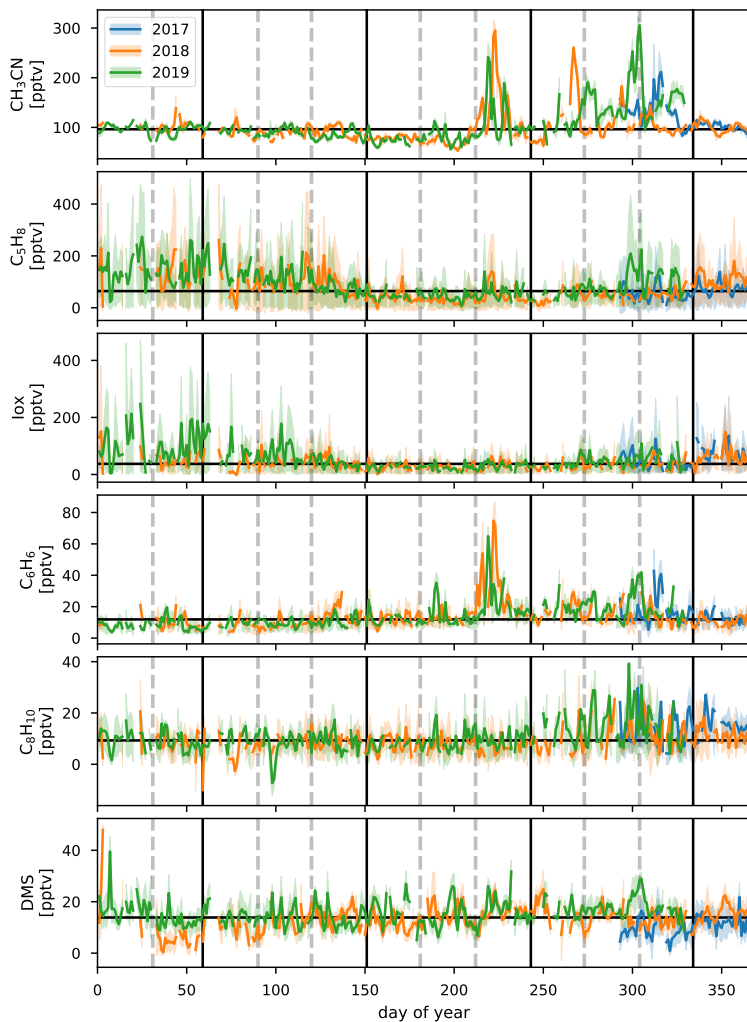
Figure 2. Daily average values of CH$_3$CN, C$_5$H$_8$, Iox, C$_6$H$_6$, C$_8$H$_{10}$, and DMS (top to bottom) for 2017, 2018, and 2019 (blue, orange and green respectively) during the deployment of the hs-PTR-MS instrument for the OCTAVE project. Shaded areas behind the curve show the diel interquartile range. Horizontal black line corresponds to the median daily average over the complete measurement period. Vertical gray dashed lines indicate the end of a month, vertical black lines separate the DJF, MAM, JJA and SON seasons.
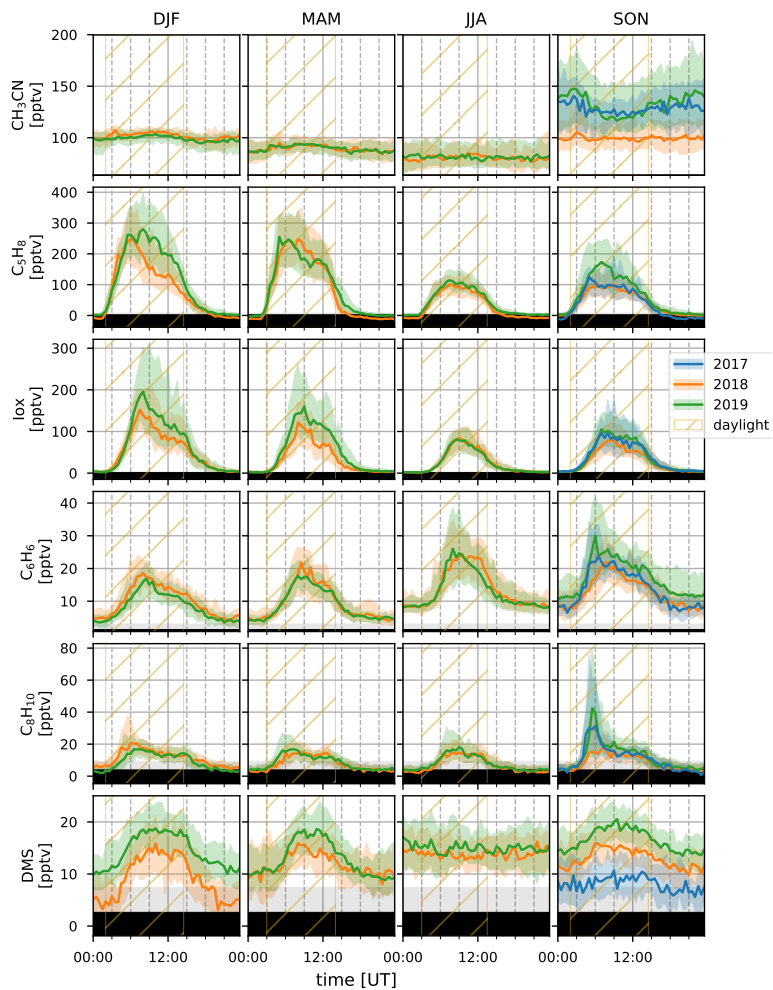
Figure 3. Median diel profiles (lines) and the interquartile distance (shaded area) for the DJF, MAM, JJA and SON seasons (columns, left to right) in 2017, 2018 and 2019 (blue, orange and green curves respectively) for CH_3CN, C_5H_8, Iox, C_6H_6, C_8H_{10}, and DMS (rows, top to bottom). The yellow hatched area illustrates daylight during the respective seasons. Gray background shows range between the median limit of detection and the minimum limit of detection of half-hour measurements. Individual half-hour measurements in the black region of the plots are not quantifiable.
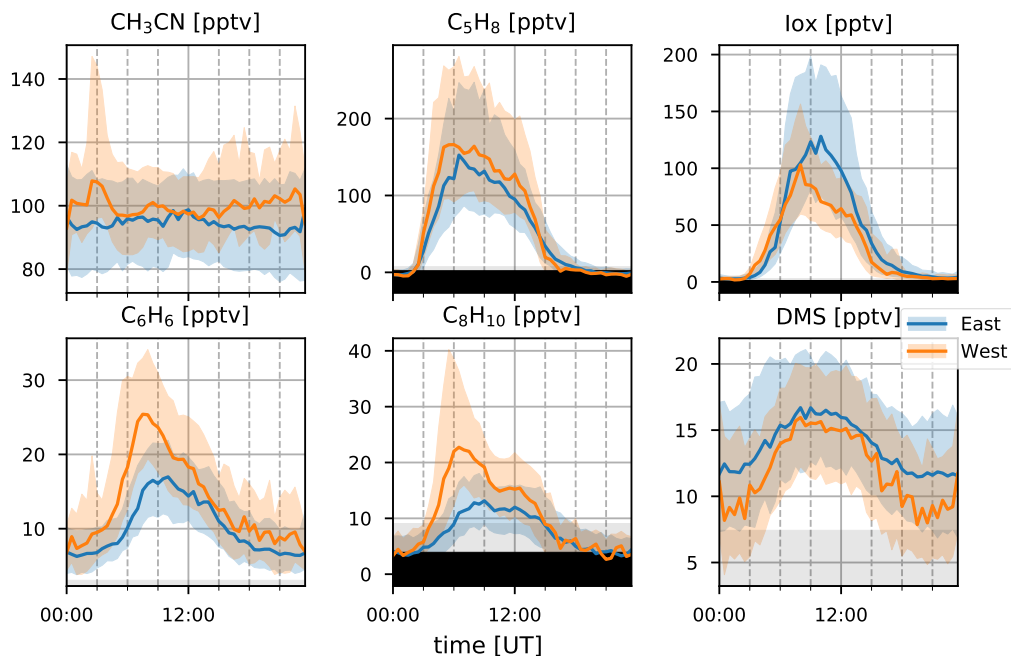
Figure 4. Median diel profiles (lines) and the interquartile distance (shaded area) for CH_3CN, C_5H_8, Iox, C_6H_6, C_8H_{10}, and DMS (top left to bottom right) separated between easterly (blue) and westerly (orange) transport recorded at the observatory. Gray background shows range between the median limit of detection and the minimum limit of detection of half-hour measurements. Individual half-hour measurements in the black region of the plots are not quantifiable.

From Figure 2 we see that high concentrations of CH_3CN occurred during August in both 2018 and 2019. This is due to direct transport of African BB plumes towards the Maïdo observatory (Verreyken et al., 2020). After these first intrusions, the daily average mixing ratio is reduced to pre-BB plume intrusions (80–100 pptv). However, from September to November these daily averages are elevated (100–150 pptv) with spurious periods of high concentrations when BB plumes reach the observatory (up to 300 pptv). This period corresponds with the BB season identified from FTIR measurements at La Réunion (Vigouroux et al., 2012). The elevated daily averages drop to a minimum from March to August (50 pptv) after which the pattern repeats itself. The seasonal diel profiles (Figure 3) show no clear pattern except for the September-October-November season (SON) of 2017 and 2019 where there is a nocturnal (nighttime maximum) signature. If we assume that CH_3CN is relatively well-mixed throughout the troposphere, this would suggest the existence of a marine sink. This was proposed from

13
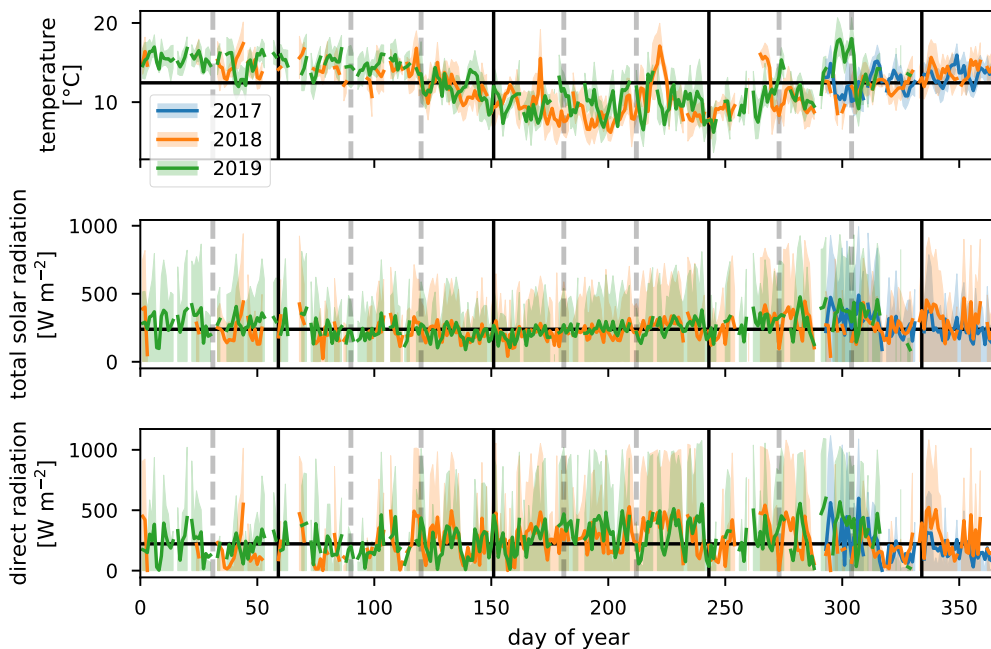
Figure 5. Daily average values of temperature, total solar radiation and direct radiation (top to bottom) for 2017, 2018, and 2019 (blue, orange and green respectively). Shaded areas behind the curve show the diel interquartile range. Horizontal black line corresponds to the median daily average over the complete measurement period. Vertical gray dashed lines indicate the end of a month, vertical black lines separate the DJF, MAM, JJA and SON seasons.

CH$_3$CN measurements at the Mauna Loa observatory in Hawaii (Karl et al., 2003). However, a study of BB plume transport of African and Madagascan pyrogenic emissions towards the Maïdo observatory found that these plumes are primarily transported through the FT (Verreyken et al., 2020). The median nocturnal pattern during the SON 2017 and 2019 seasons could likely be due to the high number of plume days recorded during these periods. After the BB season (SON), the median diel profile is flat and its mixing ratio steadily drops from December-January-February (DJF, 100 pptv) to June-July-August (JJA, 80 pptv). The wind-separated profile of CH$_3$CN does not point to a difference in sources between the East or West (Figure 4).
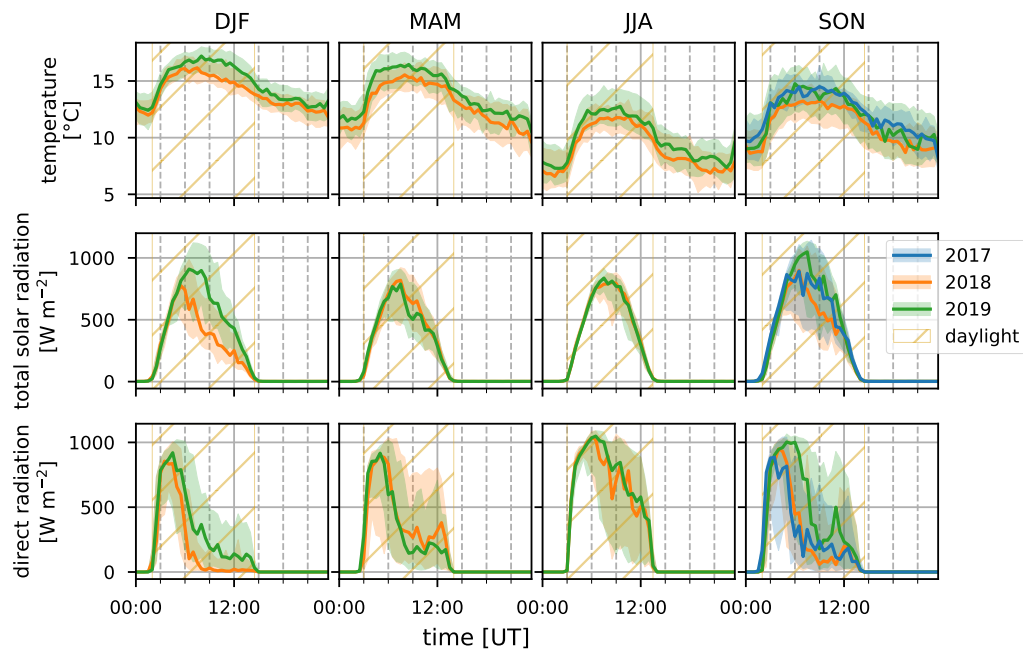
Figure 6. Median diel profiles (lines) and the interquartile distance (shaded area) for the DJF, MAM, JJA and SON seasons (columns, left to right) in 2017, 2018 and 2019 (blue, orange and green curves respectively) for temperature, total solar radiation and direct radiation (rows, top to bottom). The yellow hatched area illustrates daylight during the respective seasons.

3.1.2 Isoprene

Terrestrial biogenic emission of C_5H_8 strongly correlates to both temperature and solar radiation (Guenther et al., 1993). Due to its short atmospheric lifetime, of the order of 1 hour (assuming an OH concentration of 2×10^6 molec. cm^{-3}), C_5H_8 mixing ratios at the observatory are largely due to emissions close to the observatory. The seasonal evolution of C_5H_8 displays low values in June—September and a gradual increase in the last months of the year (Figure 2). This relates closely to the annual temperature variation as measured at the Maïdo observatory (Figure 5). A clear diurnal (daytime maximum) pattern with mixing ratios increasing directly after sunrise (Figure 3) is observed. The 2018 DJF season has lower C_5H_8 mixing ratios compared to the 2019 season. This pattern is also recorded for both the total solar radiation and the temperature during the same periods (Figure 6). The DJF 2018 and 2019 diel profiles (Figure 3) clearly illustrate the impact of the diel solar radiation and temperature profiles (Figure 6). Due to the much drier and less cloudy 2019, the DJF season profiles of the
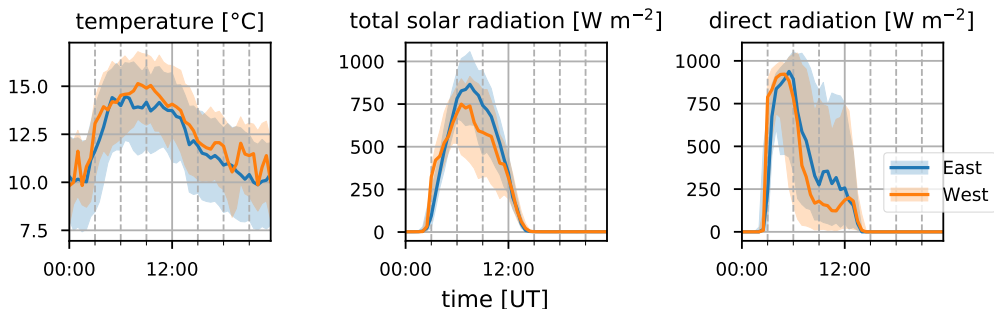
15

Figure 7. Median diel profiles (lines) and the interquartile distance (shaded area) for temperature, total solar radiation and direct radiation (left to right) separated between easterly (blue) and westerly (orange) transport recorded at the observatory.

relevant meteorological parameters and C_5H_8 mixing ratios are much more symmetrical than DJF 2018. The 2019 diurnal maximum during the SON season does not correspond with a maximum in temperature compared to other years (Figures 3 and 6) but it does relate to a maximum in measured total solar radiation. During the FARCE campaign (April 2015), it was found that mesoscale transport had a large role in the C_5H_8 mixing ratios recorded at the Maïdo observatory (Duflot et al., 2019). Easterly winds transported air masses originating mostly from 2,000 m a.s.l., thereby reducing the impact of surface emissions. Westerly winds are the result of thermally driven mesoscale transport and carry marine boundary layer (MBL) air masses over anthropogenic and biogenic sources towards the observatory. As such, westerly/easterly winds generally coincided with higher/lower C_5H_8 mixing ratios respectively. The difference in C_5H_8 concentration between the easterly and westerly flows were simulated with the non-hydrostatic mesoscale atmospheric model (Meso-NH) (Lac et al., 2018) during the FARCE campaign and were estimated to be $\sim$100 pptv (Duflot et al., 2019). When separating the C_5H_8 mixing ratios over the entire dataset of this study according to wind direction, we found that the median diurnal profile is indeed slightly more elevated when the wind is coming from the West compared to the East (Figure 4). The maximum difference in median diel profile between easterly and westerly regimes over the entire campaign is found to be 50 pptv. This takes into account the cold and dry season measurements where C_5H_8 mixing ratios are significantly lower than in April. Restricting our measurements to April 2018 and April 2019 (not shown) increases the discrepancy between wind regimes to a difference of 150 pptv with highest mixing ratios recorded from westerly transport. This is most likely related to the closer proximity of Maïdo to vegetation west of the observatory.

3.1.3 Isoprene oxidation products

As Iox generally have a longer lifetime than their precursor, their concentrations are a measure for the impact of biogenic sources further away from the observatory. The daily average variation of Iox (Figure 2) shows a similar signature as C_5H_8 with

16

high daily average mixing ratios recorded in the DJF and March-April-May (MAM, up to 250 pptv) seasons. The median diel profiles (Figure 3) show that the rise of Iox mixing ratios in the morning is delayed by about 1.5 h compared to C_5H_8, a duration similar to the expected isoprene lifetime, when assuming an OH concentration of 2×10^6 molec. cm^{-3}. Contrary to C_5H_8, Iox are elevated in the easterly wind regime (Figure 4). This contradicts results from FARCE campaign which suggested that air masses transported by easterlies originate mostly from 2000 m a.s.l. with only limited impact of surface emissions (Duflot et al., 2019) as the discrepancy in Iox is generally larger than that of C_5H_8. The stronger Iox in easterly winds compared to the westerlies could be related to either a relatively stronger sink of C_5H_8 from easterly transport — either a more distant source of C_5H_8 or elevated OH reactivity — or a larger source of C_5H_8 located to the East (either denser vegetation or larger area). Figure 7 shows that both total solar radiation and direct radiation are elevated when winds are coming from the east. This is due to reduced orographic cloud formation from the East which can enhance OH-formation through photolytic reactions and therefore accelerate the C_5H_8 sinks during easterly transport. It is however unlikely that increased production of Iox is the only possible source of the discrepancy as a similar difference in radiation is found between the MAM seasons from 2018 and 2019 (Figure 6). During MAM 2018, radiation at the observatory in the afternoon was slightly elevated compared to 2019, which could have enhanced the C_5H_8 sink and possibly Iox formation during MAM 2018 compared to 2019 (Figure 3). However, Iox signals during MAM 2019 were increased compared to 2018. From Meso-NH simulations performed in the context of the FARCE campaign, it was found that C_5H_8 concentrations in the morning (06:00 UT, 10:00 LT) are highest on the Northeastern part of the island (Duflot et al., 2019). The passage over this region of air masses arriving at the observatory from the East could explain the discrepancy between wind regimes.

3.1.4 Benzene and C_8-aromatics

The seasonal variation of C_6H_6 is linked to BB (Figure 2). The excess C_6H_6 mixing ratios due to arrival of BB plumes in August 2018 and August 2019 have been studied in previous work (Verreyken et al., 2020). For C_8H_{10}, whose sources are mostly fugitive emissions from industry, car exhaust and volatilization through solvent use, this BB variability is not visible. Not only are emission factors of C_8H_{10} at least 3 times smaller than those of C_6H_6 (Andreae, 2019), but the atmospheric lifetime of C_8H_{10} (hours) is much lower than that of C_6H_6 (weeks). C_8H_{10} is strongly enhanced during the SON seasons of 2017 and 2019. The median diel profiles of this season indicate that the SON mixing ratios of C_8H_{10} are enhanced in the morning (06:00 UT, 10:00 LT). This is most pronounced during the 2017 (maximum C_8H_{10} mixing ratio of 30 pptv) and 2019 (40 pptv) seasons. The median diel profile of C_6H_6 does show a slight elevation of mixing ratios at the same time as for C_8H_{10}, although it is less evident given the large amplitude of the regular diel profile seen in the other seasons. Comparison of the C_6H_6 and C_8H_{10} median diel profiles in westerly winds shows that the maximum in C_6H_6 occurs 1 hour after the peak in C_8H_{10} (Figure 4). The C_6H_6 median diel profile corresponds best with the diel profile of emissions related to energy production at La Réunion in the EDGAR database (Crippa et al., 2020) which has a large peak in the morning (05:00 UT, 09:00 LT) and slowly decreases towards the evening (16:00 UT, 20:00 LT) when it drops quickly. This in contrast to the median diel profile of C_8H_{10} which correspond best with the two-peak profile of emissions from both residential and road traffic sources (Crippa et al., 2020).

3.1.5 Dimethyl sulfide

DMS is predominantly produced by marine phytoplankton and emitted in the atmosphere from the ocean surface. High regional abundances of DMS are linked to the presence of phytoplankton blooms in upwelling waters (e.g, Colomb et al., 2009). It has been reported that trees may also be a net source of DMS in the atmosphere (Jardine et al., 2015; Vettikkat et al., 2020). Globally, these terrestrial emissions are negligible (370–550 Mg DMS y^{-1} (Vettikkat et al., 2020)) compared to the estimated annual marine emissions (28 Tg S y^{-1}, which corresponds to 54.5 Tg DMS y^{-1} (Lana et al., 2011)). The main atmospheric sinks of DMS are daytime oxidation by OH, accounting for 73–84% of the total sink, and nighttime oxidation by the nitrate radical NO_3 (Berglen, 2004; Kloster et al., 2006). The global average atmospheric lifetime of DMS is 1.02–1.93 days (Berglen, 2004; Kloster et al., 2006). As La Réunion is located in the Tropics, the lifetime of DMS is expected to be shorter than the global average during the day (Blake et al., 1999). The DMS mixing ratios recorded at the Maïdo observatory are much lower (7–16 pptv in the FT during the night, 11–20 pptv in the planetary boundary layer during the day, Table 2) compared to reported measurements over the ocean (e.g. 60 ± 20 pptv from ship-borne measurements south of La Réunion, 24–30.2 °S, during the MANCHOT campaign in 2004). The lower mixing ratios are likely due to the near-absence of DMS sources over land in combination with oxidation by OH during daytime, when marine air can reach the observatory. At first sight, no clear seasonal pattern is visible (Figure 2). However, the diurnal maximum in DMS diel profiles during the SON, DJF and MAM seasons is not present during JJA (Figure 3). The nighttime values vary between years for the SON and DJF seasons, for reasons still unclear. The diel profiles separated according to the wind direction (Figure 4) suggest that westerly transport during the night is accompanied by somewhat lower mixing ratios (5–15 pptv) compared to easterly transport (8–16 pptv). Caution is required, however, as only few nighttime measurements were recorded with a westerly origin.

3.2 Source identification using positive matrix factorization

The source apportionment software EPA PMF v5.0 was used to attribute the variability of VOCs to their sources. The PMF is run using CO data in combination with CH_3OH, CH_3CN, CH_3CHO, CH_3COCH_3, CH_3COOH, C_5H_8, Iox, MEK, C_6H_6, C_8H_{10} recorded with the hs-PTR-MS instrument. The 2.7-minute time resolved data from the hs-PTR-MS are accumulated over 1 h to match the temporal resolution of CO measurements and improve the signal-to-noise ratio (S/N) of the (O)VOC measurements. The mixing ratios are converted to mass concentrations [$\mu g\ m^{-3}$] for mass closure using local ambient temperature and pressure measurements. Data below the limit of detection (LoD) was set to $LoD/2$ with an associated uncertainty of $5/6 \times LoD$ in accordance with best practices (Norris et al., 2014). Measurements for which concentrations were missing for at least one of the species, were taken out of the dataset instead of replacing the missing information by an average value with high uncertainty. Data quality is quantified by using S/N. Species with low S/N ratio ($1.0 < S/N < 2.0$) were characterized as 'weak' (CH_3COOH) and corresponding uncertainties were multiplied by a factor of 3 (Norris et al., 2014). Species for which data was not available for the entire campaign (HCOOH) were excluded from the analysis. Additionally, DMS was not used in the PMF analysis, as preliminary tests indicated that including DMS would result in unexplainable factor profiles and contributions. Uncertainties are calculated using the displacement (DISP) and bootstrapping (BS) algorithms. Analysis of the complete
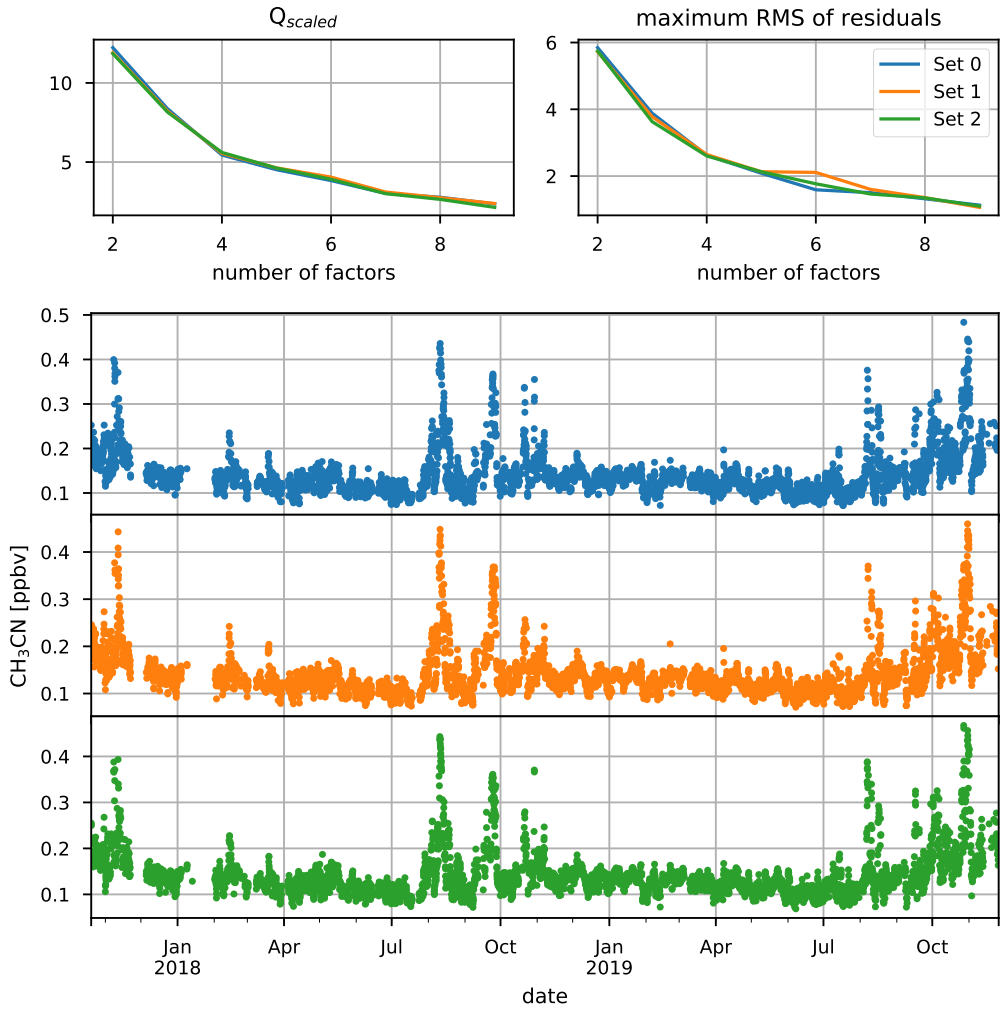
Figure 8. Dataset separation in three different subsets. The top two plots show the scaled objective function (left) and the maximal root mean square (RMS) of compound residuals (right) for a scan of the number of factor space from 2 to 9. The bottom three plots show the CH_3CN mixing ratios [ppbv] for the three different subsets which ensure near-equal occurrence of biomass burning intrusions.
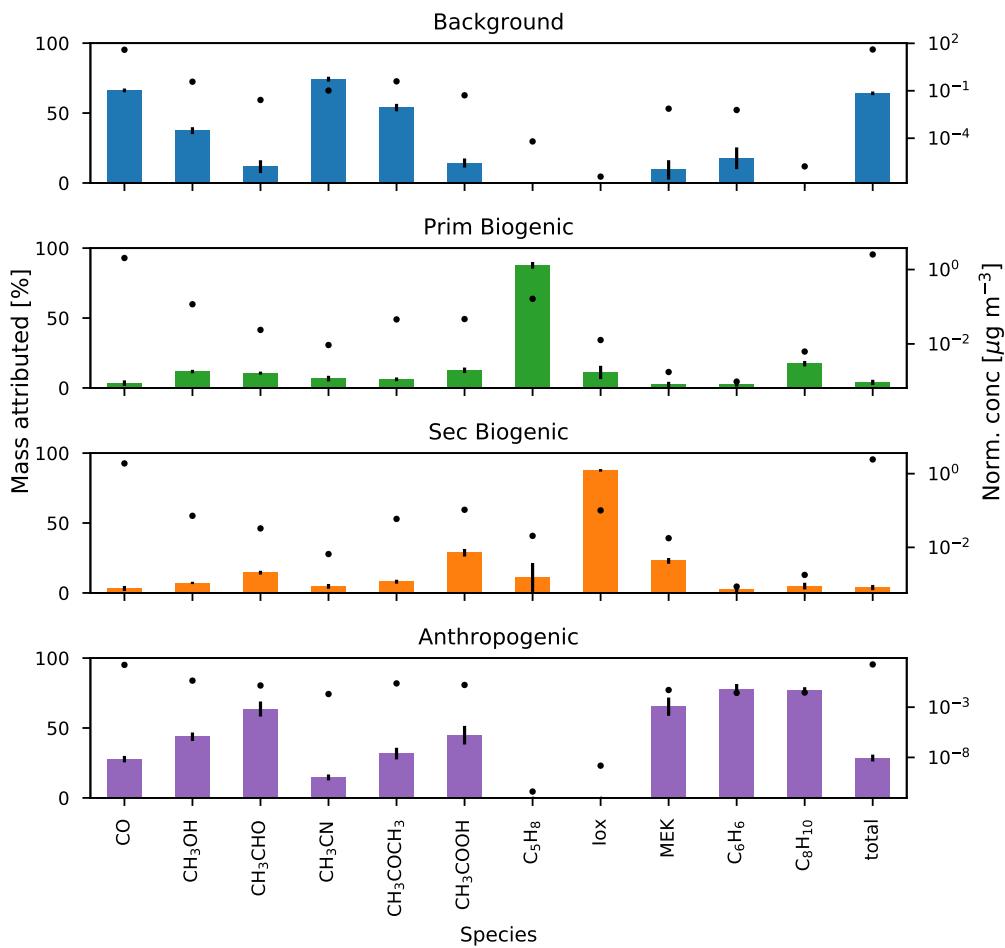
Figure 9. The median fraction of mass attributed [%] to the background, primary biogenic, secondary biogenic and anthropogenic factors calculated by the bootstrapping algorithm (bars, interquartile distance shown by error bars) and the median normalized concentration [μg m^{-3}] of the factor profiles (markers).
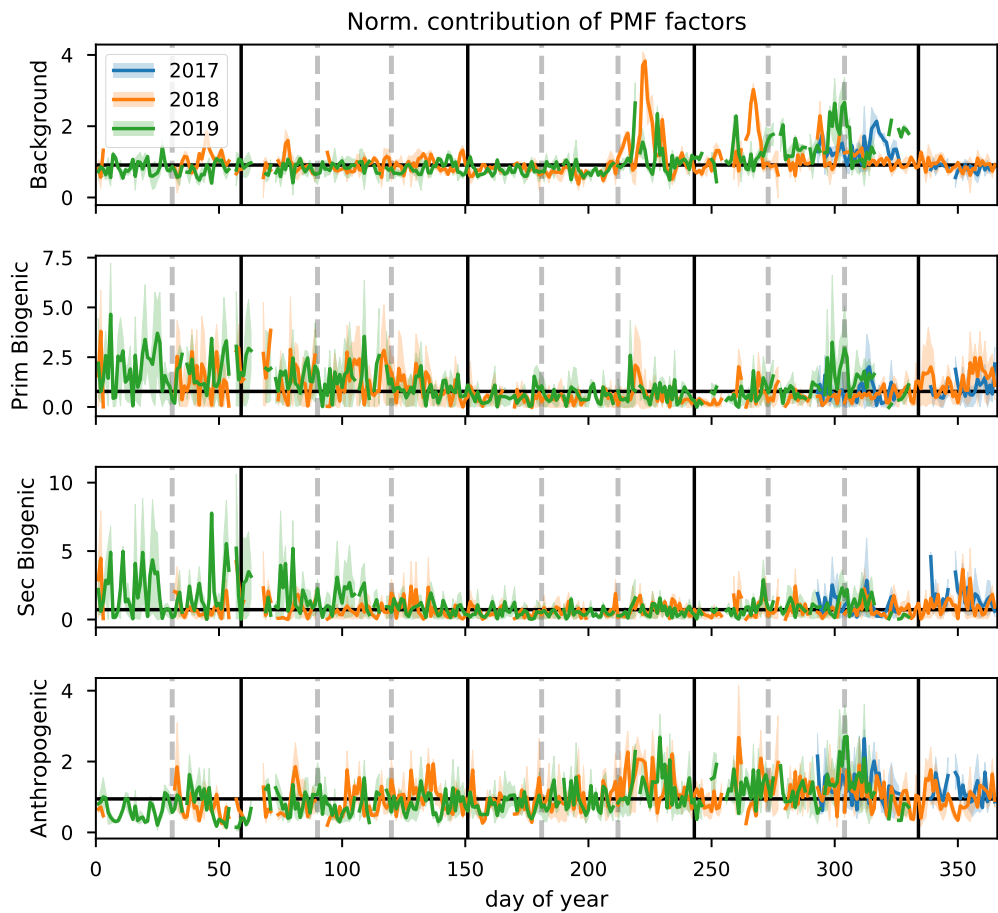
Figure 10. Daily average values of normalized contribution of the background, primary biogenic, secondary biogenic, and anthropogenic source factors (top to bottom) for 2017, 2018, and 2019 (blue, orange and green respectively). Shaded areas behind the curve show the diel interquartile range. Horizontal black line corresponds to the median daily average over the complete measurement period. Vertical gray dashed lines indicate the end of a month, vertical black lines separate the DJF, MAM, JJA and SON seasons.
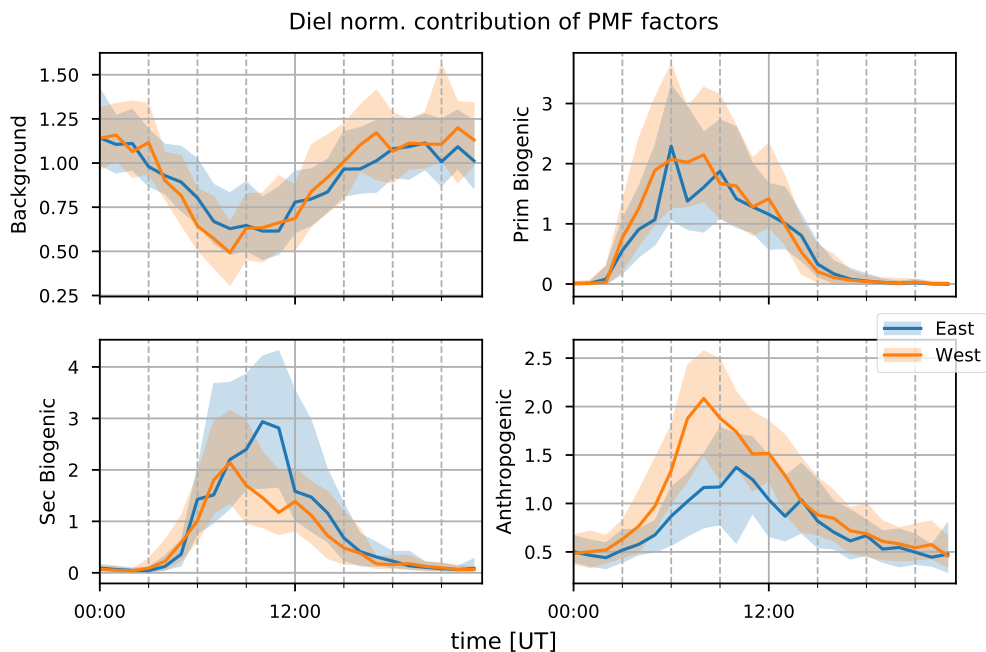
Figure 11. The median diel profile of background, primary biogenic, secondary biogenic and anthropogenic factor (top left to bottom right) normalized contributions separated along the wind directions recorded at the observatory (blue for eastern transport and orange for western transport), hourly interquartile distance is visualized by the shaded area.

355   2-year dataset by the EPA PMF 5.0 software was not possible as the dataset was too large. Instead, the dataset was randomly split up into three parts, while taking care to ensure equal contribution of BB intrusions in the three sets. This is checked using the temporal dataset of CH_3CN concentrations (Figure 8). Similar results for both the factor profiles and the contributions were obtained for all three subsets and we report here only the results for one of the subsets. After scanning the parameter space with 25 base runs for each number of factors, we selected the 4-, or 5-factor solution for further investigation based on the Q_{scaled}

360   and maximum RMS of residual curves (Figure 8). The base model was executed 100 times with a seed of 9 for both 4- and 5-factors. When using the DISP algorithm, no errors or swaps were reported using the 4- and 5-factor solutions, showing that they are free of rotational ambiguity. From the 100 BS run for the 4-factor solutions, it was found that 100% of the BS factors were mapped to the base run. This is not the case for the 5-factor solution (91%) which implies that, although still a robust solution, it is slightly more sensitive to random errors. However, the 5-factor solution had no straightforward interpretation

and was therefore discarded. A further investigation of rotational ambiguity of the 4-factor solution was performed using the F_{peak} functionality. This is used to investigate the effect of flattening (positive F_{peak} strengths) or sharpening (negative F_{peak} strengths) the factor contributions.. No decrease in the objective function was found using F_{peak} strengths of ± 0.1, ± 0.2, ± 0.5, ± 1.0, and ± 2.0, which confirms that the 4-factor solution is free from rotational ambiguity. The four factors were identified as a background (which includes BB signatures), an anthropogenic, a primary biogenic, and a secondary biogenic factor. No marine source was identified from the PMF algorithm in part due to the omission of DMS data from the analysis.

3.2.1 Background and biomass burning factor

The background and BB factor accounts for 65–68% of CO and 73–75% of CH_3CN measured at the observatory (Figure 9). This is a strong indication that the factor is indeed a combination of background and BB signals. The annual pattern of the normalized contributions (Figure 10) shows a strong influence of BB plumes reaching the observatory between August and November. No other seasonal pattern is present. The median diel profile of normalized contributions (Figure 11) shows no influence of wind direction, which implies that the source is either near the observatory or remote. As the atmospheric lifetimes of both CO and CH_3CN are long, the source is identified as remote which is again in agreement with the identification of the factor as background/BB. The nighttime maximum of the normalized factor contributions suggests that it originates in the FT. It may also indicate the presence of an ocean sink of CH_3CN, as proposed by (Karl et al., 2003) and mentioned in Section 3.1.1, which is obscured by a compensating mesoscale source of CH_3CN resulting in the recorded flat median diel profile. However, it seems unlikely that a mesoscale source would systematically compensate this atmospheric sink perfectly. We think it more likely that the PMF algorithm artificially reproduces the flat diel profile of CH_3CN (Figure 3) when it is well-mixed between the PBL and FT by attributing a small fraction of CH_3CN to other sources, inducing only small errors in the algorithm. The contribution of the background factor to the total mass of compounds included in PMF is 63–66%. This is strongly biased by the high impact of CO concentrations that account for most of the mass of species included in PMF. Taking the contribution of CO out of the equation we find that the background factor accounts for 33% of the mass of (O)VOCs recorded at the observatory. The background factor is especially relevant for CH_3OH (30–39%) and CH_3COCH_3 (51–54%).

3.2.2 Anthropogenic factor

The anthropogenic factor accounts for 25–29%, 73–85%, and 75–79% of the mass of CO, C_6H_6 and C_8H_{10}, respectively (Figure 9). This is a good indication that this factor is indeed related to anthropogenic sources. The seasonal variation (Figure 10) shows elevated normalized contributions in August-November. This may either be due to i) excess C_6H_6 present in younger BB plumes not represented in the background/BB factor (especially in August), or ii) the high C_8H_{10} mixing ratios in SON (Figure 2). The median diel pattern (Figure 11) shows a large impact from westerly transport, with a peak between 06:00 and 09:00 UT (10:00–13:00 LT), similar to C_6H_6 (Figure 4). This points to a strong influence of mesoscale transport on the contribution of an anthropogenic source to the local atmospheric composition recorded at Maïdo. The difference in diel profiles between C_8H_{10} and C_6H_6 is not resolved by the PMF. Introduction of an additional factor did not result in a second anthropogenic source (e.g. by discriminating between combustion and evaporative sources as found at La Réunion during the

23

OCTAVE intensive observation period (IOP) (Rocco et al., 2020)). The anthropogenic factor accounts for 38% of the mass of (O)VOCs — i.e. excluding CO — recorded at the observatory. Besides C_6H_6 and C_8H_{10} mentioned above, the anthropogenic source is dominant for CH_3CHO (58–68%), CH_3OH (41–47%), CH_3COOH (38–51%), and MEK (57–73%), and is the second largest source for CO and CH_3COCH_3 (28–35%) for which the background is the dominant contributor.

3.2.3 Primary biogenic factor

The primary biogenic factor accounts for 85–94% of the mass of C_5H_8 recorded at the Maïdo observatory (Figure 9). Its normalized contribution (Figure 10) is enhanced during the hot and wet months (DJF and MAM). The median diel normalized contributions separated between wind regimes are found to be similar (Figure 11). Together with the short atmospheric lifetime of C_5H_8, this implies that the primary biogenic factor is mostly determined by emissions close to the observatory. The primary biogenic factor accounts for 15% of the mass of (O)VOCs recorded at the observatory. The primary biogenic source is the dominant source for C_5H_8 and the second largest source of C_8H_{10} (15–19%) and Iox (6–13%). The first is unexpected as C_8H_{10} is not usually associated with biogenic emissions. The latter probably accounts for a fraction of C_5H_8 emitted from local sources that is rapidly oxidized. This would have a large impact especially in the morning when C_5H_8 originating from emissions further away from the observatory cannot yet reach the observatory through mesoscale transport.

3.2.4 Secondary biogenic factor

The secondary biogenic factor accounts for 87–89% of the mass of Iox (Figure 9). The seasonal variation of the normalized contributions is similar to that of the primary biogenic factor (Figure 10). The median diel normalized contribution profile however shows a significant impact of wind direction (Figure 11). Similar to the diel profile of Iox (Figure 4), the normalized factor contributions are elevated in the easterly wind regime. This shows, similar to the anthropogenic source, a significant impact of sources on the island (further away from the observatory) to the secondary biogenic factor. The secondary biogenic factor accounts for 14% of the mass of (O)VOCs recorded at the observatory. It is the second strongest contributor for C_5H_8 (0–14%), MEK (21–26%), CH_3COOH (26–33%), and CH_3CHO (13–17%).

3.3 Source identification using FLEXPART-AROME back-trajectory calculations

The FLEXPART-AROME back-trajectory calculations showed that air masses are equally sensitive to mesoscale sources located on the island during the first 12 hours of the back-trajectory calculation compared to the complete 24 hours. The SRRs for the 24 hour trajectories had only significant impact on the marine category. The average total RT of air parcels in the first AC (12 hours backward in time) was 11.6 hours. This shows that a large fraction of air masses stayed within the domain during the first 12 hours of simulation. The average total RT of air parcels during the complete 24 hour back-trajectory calculation was 17.7, illustrating that a large fraction of air parcels is transported outside the FLEXPART-AROME output domain. We will therefore limit our discussion to SRRs calculated during the first 12 hours.

24
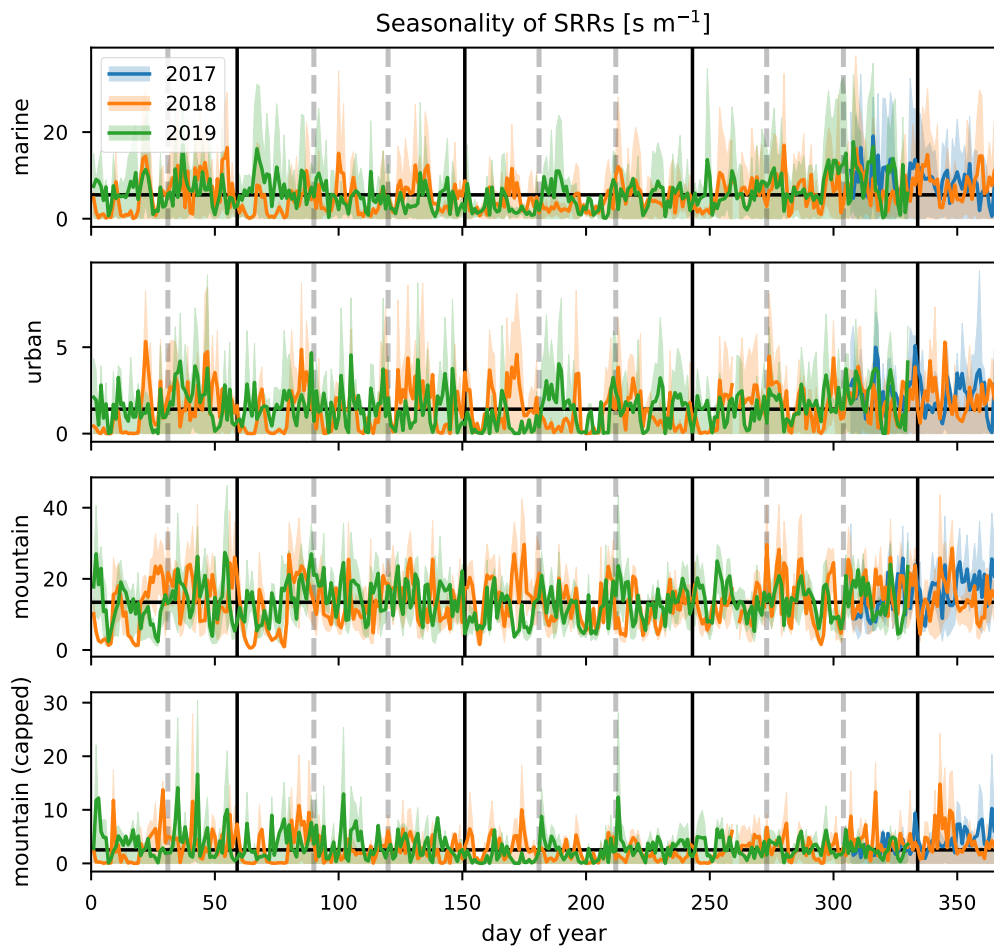
Figure 12. Daily average SRR [s m^{-1}] for marine, urban, mountain and capped mountain categories (top to bottom respectively) obtained from 12-hour FLEXPART-AROME back-trajectory calculations for the years 2017 (blue), 2018 (orange) and 2019 (green). Interquartile distance is shown as shaded area in the background.
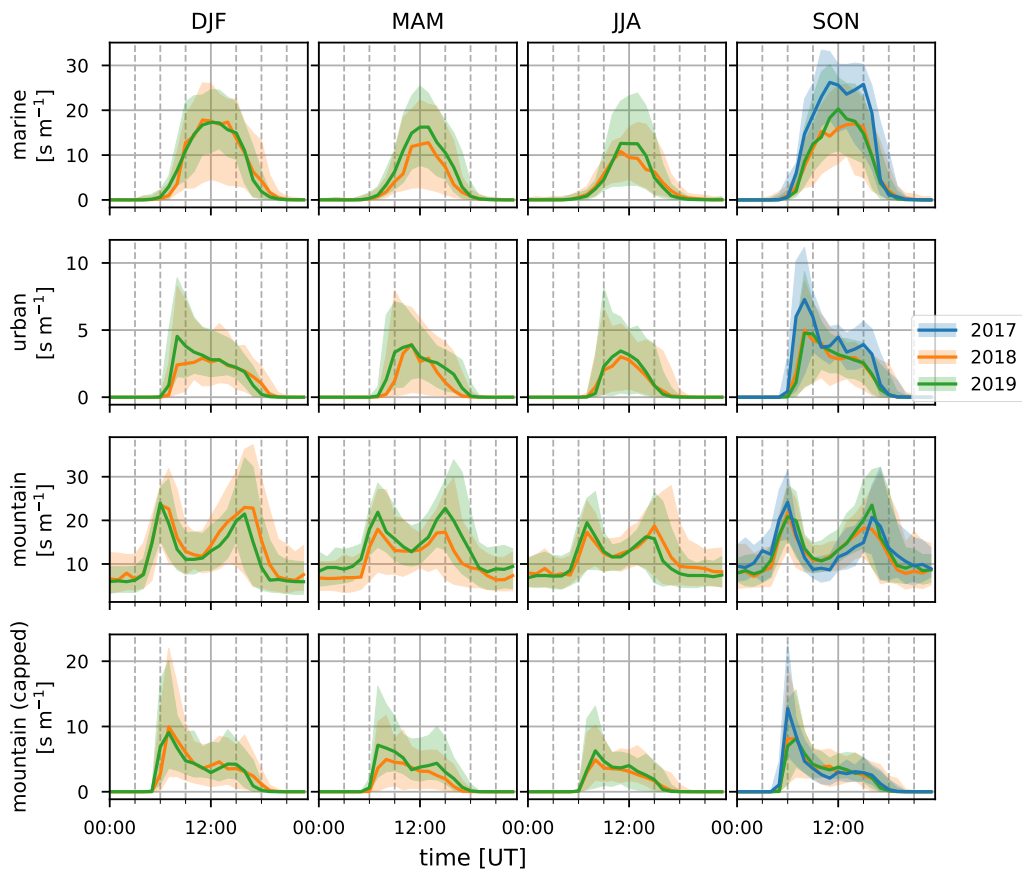
Figure 13. Median diel profile of the SRRs [s m^{-1}] calculated for the marine, urban, mountain and capped mountain categorical emission sources (columns top to bottom) with FLEXPART-AROME 12-hour back-trajectory calculations during the DJF, MAM, JJA and SON seasons (columns left to right) in 2017 (blue), 2018 (orange) and 2019 (green). The interquartile distances are shown as shaded areas.
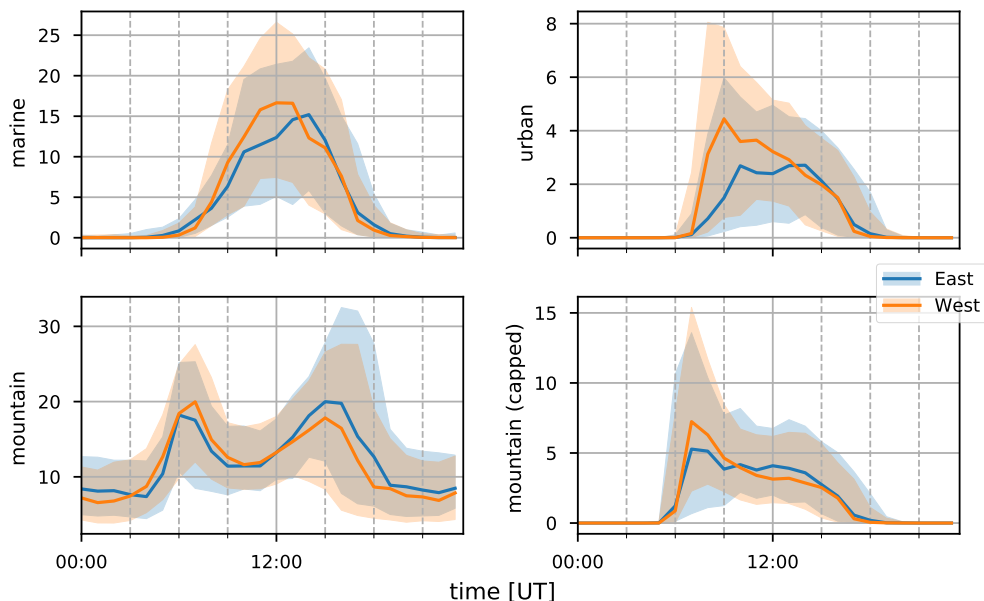
Figure 14. Wind-separated median diel profile (line) and interquartile distance (shaded area) for easterly (blue) and westerly (orange) transport for the marine (top left), urban (top right), mountain (bottom left) and capped mountain (bottom right) of categorical emission sources SRRs [s m^{-1}] as calculated using the FLEXPART-AROME 12-hour back-trajectory calculations. Wind direction separation based on measurements.

3.3.1 Diel, seasonal, and inter-annual variability

Figures 12 through 14 show the inter-annual daily averages, seasonal diel profiles and wind-separated diel profiles of the categorical SRRs. The daily average emission sensitivities for the different categories (Figure 12) do not show clear seasonal patterns for urban, and both capped and uncapped mountain emissions. The sensitivity to marine emissions is lowest during the JJA season (Figure 13). This is due to the strong trade winds during this time of year carrying air parcels outside the domain within the 12 hour period. The monthly average total RT in the first 12 hours is second lowest of all (11.1 hour). The month with lowest average RT (11.0 hour) is January due to the impact of tropical storms and cyclones (see Table 1). There are however clear seasonal differences when considering the median diel profiles shown in Figure 13. The urban SRRs profiles generally have a morning peak located at 07:00 UT (11:00 LT). This peak is less pronounced during the MAM period

and is not present during the JJA season. This may be due to the enhanced trade-winds together with a weakening of the thermally driven mesoscale transport during Austral winter resulting in overflowing easterly transport affecting the observations at the location of Maïdo more frequently. This is also what is seen in the wind-separated diel profiles (Figure 14) where the easterly regime has a low sensitivity to urban emissions before 12:00 UT (16:00 LT) compared to westerly transport. The diel profile for urban SRRs does not show the morning peak in the DJF season of 2018. The strong winds associated to tropical cyclones and storms may be the cause during this season. The wind-separated marine SRRs (Figure 14) show stronger sensitivity from westerly transport between 07:00 UT and 13:00 UT (11:00–17:00 LT). This is counter intuitive as we assume that overflowing easterly transport is organized along faster winds and thus these air parcels spend less time over the island which implies a relatively stronger impact of the ocean during the 12-hour back-trajectories. However, the amount of land to cross for these air masses is much larger. Moreover, air masses originating west of the observatory are conducted along the coast of La Réunion and may have been trapped over the ocean in the wake of the Island thus increasing the impact of marine emissions before being conducted towards the observatory through the coupled sea-breeze and upslope transport. The comparison between mountain emissions of the capped and uncapped categories manifests in two distinct features. Firstly, the median diel profile of the uncapped mountain SRR never reduces to zero at night. This implies that, according to the FLEXPART-AROME backtrajectories, the Maïdo observatory always has an impact of mesoscale PBL emissions and never measures purely free tropospheric air masses. The lack of a zero baseline is due to the location of the receptor site within the static PBL proxy for the uncapped representation in the model. The second and most striking difference is the presence of the double peak in the uncapped PBL representation compared to the single peak profile for the capped version. The first peak (present in both representations) is due to the reduced impact of the FT which is coincident with the onset of upslope transport. Afterwards the PBL is diluted as the boundary layer top rises in altitude, thus decreasing the emission sensitivity to mountain sources (both capped and uncapped). After sunset, radiative forcing becomes zero, resulting in a compression of the PBL and a decrease in upslope transport. The reduced upslope transport results in a reduction of emission sensitivities linked to the capped mountain category. The uncapped mountain category on the other hand does not depend on this mesoscale transport and thus only shows the impact of the PBL compression which increases the S-R relationship before the PBL is flushed by the FT. Note that the wind-separated diel profiles for mountain emissions are not dependent on wind direction (Figure 14). This indicates that the discrepancy in the secondary biogenic source factor contribution between easterly and westerly flows (Figure 11) is not related to transport of mountainous air masses and originates from either i) a stronger oxidative sink of primary biogenic emissions, ii) air masses loaded with more biogenic emissions (denser vegetation/larger areas) or iii) a combination of the above as discussed in Section 3.1.3. Here we can exclude the hypothesis of a larger source of biogenic emissions related to air masses passing over larger areas as this would be represented in the mountain SRRs.

3.3.2 Correspondence between FLEXPART-AROME and PMF

Table 3 shows the Pearson correlation coefficient (r) between the source-receptor relationship (SRR) of the different categories and the PMF source factor contributions. The correlations are generally low (maximum 0.45) due to the different approximations made in the categorization of SRRs and the neglected temporal variation of emission strengths, both diel and seasonal,
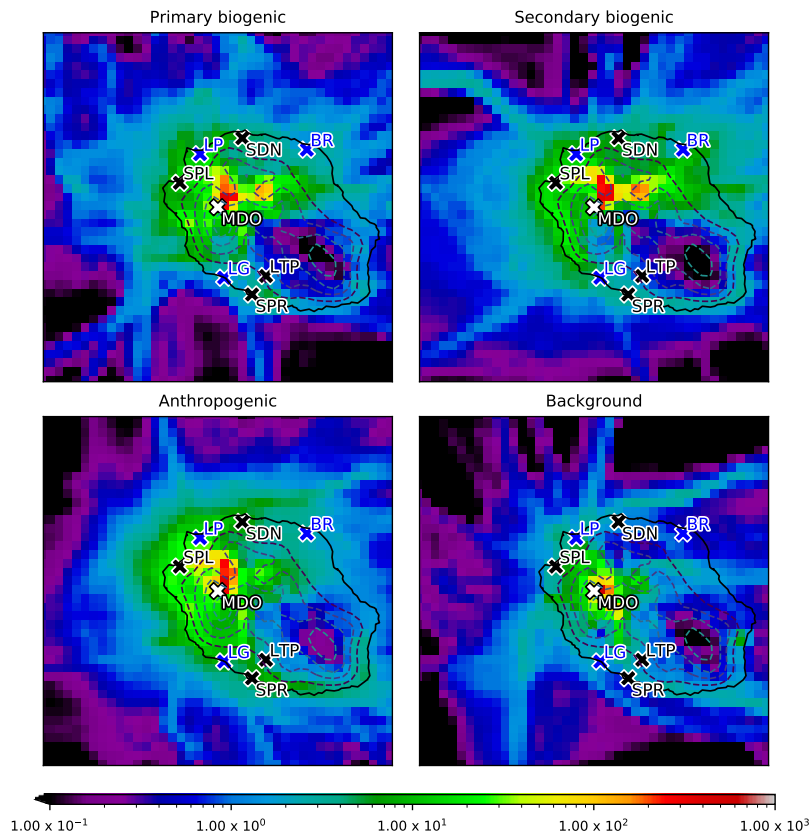
Figure 15. The spatial distribution of SRRs [s m^{-1}] over La Réunion for the top 5% source factor contributions calculated by the PMF algorithm for the primary biogenic (top left), secondary biogenic (top right), anthropogenic (bottom left) and background (bottom right) sources. The Maïdo observatory (MDO) is indicated in white. Cities with population over 50,000 habitants — i.e. Saint-Denis (SDN), Saint-Paul (SPL), Le Tampon (LTP), and Saint-Pierre (SPR) — are shown in black. The largest industrial sites — Le Port (LP), Bois-Rouge (BR), and Le Gol (LG) — are indicated in blue. Dashed lines are surface elevation contours in the FLEXPART-AROME model separated by 500 m.

Table 3. Pearson correlation coefficient (r) between categorical SRRs [m s^{-1}] and PMF normalized factor contribtuions.

r	Marine	Urban	Mountain (capped)	Mountain
Background	-0.08	-0.19	-0.25	-0.18
Anthropogenic	0.38	0.45	0.35	0.20
Primary biogenic	0.20	0.23	0.25	0.11
Secondary biogenic	0.36	0.36	0.40	0.20

at the source. The strongest correlation ($r = 0.45$) occurs between the urban SRR and the anthropogenic source contribution. This is due to the fact that the urban emissions have the most moderate seasonal profile. The low correlation is most likely due to the approximation of homogeneity of anthropogenic sources. The second highest correlation (0.40) is found between the secondary biogenic factor and the capped mountain source. It is expected that the capped mountain emission sensitivities correspond better with the biogenic (both primary and secondary) sources than the uncapped category. This is because of the dependence of biogenic emissions on solar radiation which is not represented in the SRR. After sunset, the compression of the boundary layer results in a higher emission sensitivity from the uncapped mountain category. However, this increased sensitivity is compensated by a rapid decrease in biogenic emissions after sunset resulting in low mixing ratios of C_5H_8 (Figure 3) and low primary biogenic factor contributions (Figure 11). The better correlation of the SRR between the capped mountain category and the secondary biogenic factor contributions (0.40) compared to that with the primary biogenic factor contributions (0.25) is due to the occurrence of primary biogenic emission directly after dawn near the observatory. The oxidation of C_5H_8 to Iox takes time, similar to transport of air masses from the capped PBL mountain category towards the Maïdo observatory. Figure 15 shows the spatial distribution of SRRs (i.e. not summed over the spatial index) also referred to as the field of view (Seibert and Frank, 2004) using the uncapped PBL proxy accumulated over the 5% largest source factor contributions from PMF source factors. We note that the total surface sensitivity is smallest for the background factor (4.7×10^3 s m^{-1}), other total surface sensitivities are 7.2×10^3 s m^{-1}, 8.8×10^3 s m^{-1}, 9.1×10^3 s m^{-1} for the primary biogenic, anthropogenic, and secondary biogenic sources respectively). As discussed in Section 3.2.1, the background factor contributions are a combination of air transported predominantly in the FT and BB plume signals. As the BB plumes from Africa and Madagascar are mainly transported towards the Maïdo observatory through the FT (Verreyken et al., 2020), we expect the largest 5% factor contributions to have a small SRR with mesoscale areas resolved from FLEXPART-AROME back-trajectories. From the similar median diel profiles of the wind-separated normalized factor contribution for the primary biogenic factor (Figure 11) we know that emissions are mostly located close to the observatory. However, from the C_5H_8 wind-separated profile (Figure 4), we see that there is a slight discrepancy with higher mixing ratios originating west of the observatory. This is contradicted somewhat by Figure 15 with a maximum east of the observatory. This location corresponds well with the region of highest C_5H_8 mixing ratios modeled with Meso-NH during the 2015 FARCE campaign (Duflot et al., 2019). This biogenic emission hotspot is also visible in the field of view corresponding to the strongest secondary biogenic factor contributions where a strong impact of surface emissions is seen at the same location (Figure 15). A second feature in this map is the high impact north of the observatory

which diverts to the West towards Le Port and is then transported south. This transport is organized along the canyon of the river "Rivière des Galets" between Mafate and Le Port (Figure 1). The important role of river canyons with regard to pollutant transport towards the Maïdo observatory has already been identified in the forward transport study using Meso-NH (Lesouëf et al., 2011). The field of view of the observatory related to the strongest anthropogenic factor contributions is highest west of the Maïdo observatory. The observatory is thus most sensitive to emissions from the industrial centers at Le Gol and Le Port and the second largest city Saint-Paul. Other emission hotspots of human activity did not contribute as strongly to the top 5% anthropogenic source factor contributions.

4 Conclusions

In this study, we analyzed the two-year dataset of (O)VOC concentrations obtained at Maïdo observatory between October 2017 and November 2019 in the framework of the OCTAVE project by a combination of i) diel, seasonal and inter-annual VOC concentration patterns, ii) a PMF algorithm and iii) the FLEXPART-AROME mesoscale transport model. The measurements are shown to be useful to characterize the atmospheric background composition, as evidenced by the high average impact of the background/biomass burning source factor identified using the PMF algorithm on the atmospheric (O)VOC load (33%), which is even larger during the night. During the day however, the atmosphere is loaded with anthropogenic and both primary and secondary biogenic tracers. The atmospheric loading by anthropogenic sources (38%) is dominant compared to biogenic sources (29%). This dominance is likely related to the short lifetime of C_5H_8 and its oxidation products. No marine source was identified from the PMF algorithm, in part due to the omission of DMS data from the analysis. At night, the contribution of mesoscale sources is strongly reduced and the background factor becomes dominant. This diel variability is consistent with the description of mesoscale transport in previous studies (Lesouëf et al., 2011; Baray et al., 2013; Guilpart et al., 2017; Foucart et al., 2018; Duflot et al., 2019). The observatory is located near a horizontal wind shear front between overflowing trade winds coming from the east and the coupled thermally driven sea-breeze with upslope transport during the day (Duflot et al., 2019). A previous study however found that overflowing trade winds were correlated with a reduced influence of surface emissions (Duflot et al., 2019). This is not reproduced here, as overflowing winds coming from the direction of the Maïdo mountain summit during the day were still sensitive to surface emissions. At night however, the cold island surface pulls down FT air masses towards the observatory, limiting the impact of mesoscale surface emissions on the atmospheric composition. This is consistent with known mesoscale transport features (Lesouëf et al., 2011; Baray et al., 2013; Guilpart et al., 2017; Duflot et al., 2019). The interquartile range of nighttime concentrations, characteristic for the free troposphere, of CH_3OH, CH_3CN, CH_3CHO, $HCOOH$, CH_3COCH_3, CH_3COOH and MEK were found to be 525–887 pptv, 79–110 pptv, 61–101 pptv, 172–335 pptv, 259–379 pptv, 64–164 and 11–21 pptv respectively. Combining results from FLEXPART-AROME and the PMF analysis, we identified emissions hotspots with significant impact on the atmospheric composition at the Maïdo observatory. Biogenic emission hotspots identified from both the highest contributions of primary and secondary biogenic source factors revealed a region east of the observatory, together with the "Rivière des Galets" river canyon, as important sources of biogenic tracers recorded at the observatory. The most relevant anthropogenic emission hotspots are located west of the observatory.

31

Specifically, industrial regions as Le Port and Le Gol, together with the second largest city on the island, Saint-Paul were found to have a large influence on the atmospheric composition at Maïdo. The background/biomass burning source factor from PMF was much less sensitive to surface emissions on the mesoscale compared to other sources.

Data availability. The core hs-PTR-MS dataset is made available online (Amelynck et al., 2021).

535 *Author contributions.* The analysis was conceptualized by C.A., J.B., and B.V. The formal analysis and visualisation was performed by B.V. Data acquisition, quality assurance, and processing of hs-PTR-MS data done by C.A., N.S., and B.V. The PMF analysis and FLEXPART-AROME simulations were performed by B.V. Data management of the meteorological parameters and the PICARRO instrument by C.H. and N.K. The original draft was prepared by B.V. in cooperation with C.A., J.-F.M., T.S., J.B., and N.S. All co-authors were involved in the review and editing process of the final manuscript version.

540 *Competing interests.* The authors declare to have no competing interests.

References

Amelynck, C., Schoon, N., and Verreyken, B.: Long-Term in Situ (O)VOC Measurements at the Maïdo Observatory (Reunion Island) [Data set], https://doi.org/10.18758/71021061, 2021.

Andreae, M. O.: Emission of Trace Gases and Aerosols from Biomass Burning – an Updated Assessment, Atmospheric Chemistry and Physics, 19, 8523–8546, https://doi.org/10.5194/acp-19-8523-2019, 2019.

Baasandorj, M., Millet, D. B., Hu, L., Mitroo, D., and Williams, B. J.: Measuring Acetic and Formic Acid by Proton-Transfer-Reaction Mass Spectrometry: Sensitivity, Humidity Dependence, and Quantifying Interferences, Atmospheric Measurement Techniques, 8, 1303–1321, https://doi.org/10.5194/amt-8-1303-2015, 2015.

Baldy, S., Ancellet, G., Bessafi, M., Badr, A., and Luk, D. L. S.: Field Observations of the Vertical Distribution of Tropospheric Ozone at the Island of Reunion (Southern Tropics), Journal of Geophysical Research: Atmospheres, 101, 23 835–23 849, https://doi.org/10.1029/95JD02929, 1996.

Baray, J.-L., Courcoux, Y., Keckhut, P., Portafaix, T., Tulet, P., Cammas, J.-P., Hauchecorne, A., Godin Beekmann, S., Mazière, M. D., Hermans, C., Desmet, F., Sellegri, K., Colomb, A., Ramonet, M., Sciare, J., Vuillemin, C., Hoareau, C., Dionisi, D., Duflot, V., Vérèmes, H., Porteneuve, J., Gabarrot, F., Gaudo, T., Metzger, J.-M., Payen, G., Leclair de Bellevue, J., Barthe, C., Posny, F., Ricaud, P., Abchiche, A., and Delmas, R.: Maïdo Observatory: A New High-Altitude Station Facility at Reunion Island (21° S, 55° E) for Long-Term Atmospheric Remote Sensing and in Situ Measurements, Atmospheric Measurement Techniques, 6, 2865–2877, https://doi.org/10.5194/amt-6-2865-2013, 2013.

Berglen, T. F.: A Global Model of the Coupled Sulfur/Oxidant Chemistry in the Troposphere: The Sulfur Cycle, Journal of Geophysical Research, 109, D19 310, https://doi.org/10.1029/2003JD003948, 2004.

Bernhammer, A.-K., Breitenlechner, M., Keutsch, F. N., and Hansel, A.: Technical Note: Conversion of Isoprene Hydroxy Hydroperoxides (ISOPOOHs) on Metal Environmental Simulation Chamber Walls, Atmospheric Chemistry and Physics, 17, 4053–4062, https://doi.org/10.5194/acp-17-4053-2017, 2017.

Blake, N. J., Blake, D. R., Wingenter, O. W., Sive, B. C., Kang, C. H., Thornton, D. C., Bandy, A. R., Atlas, E., Flocke, F., Harris, J. M., and Rowland, F. S.: Aircraft Measurements of the Latitudinal, Vertical, and Seasonal Variations of NMHCs, Methyl Nitrate, Methyl Halides, and DMS during the First Aerosol Characterization Experiment (ACE 1), Journal of Geophysical Research: Atmospheres, 104, 21 803–21 817, https://doi.org/10.1029/1999JD900238, 1999.

Brioude, J., Arnold, D., Stohl, A., Cassiani, M., Morton, D., Seibert, P., Angevine, W., Evan, S., Dingwell, A., Fast, J. D., Easter, R. C., Pisso, I., Burkhart, J., and Wotawa, G.: The Lagrangian Particle Dispersion Model FLEXPART-WRF Version 3.1, Geoscientific Model Development, 6, 1889–1904, https://doi.org/10.5194/gmd-6-1889-2013, 2013.

Colomb, A., Gros, V., Alvain, S., Sarda-Esteve, R., Bonsang, B., Moulin, C., Klüpfel, T., and Williams, J.: Variation of Atmospheric Volatile Organic Compounds over the Southern Indian Ocean (30–49° S), Environmental Chemistry, 6, 70–82, https://doi.org/10.1071/EN08072, 2009.

Crippa, M., Solazzo, E., Huang, G., Guizzardi, D., Koffi, E., Muntean, M., Schieberle, C., Friedrich, R., and Janssens-Maenhout, G.: High Resolution Temporal Profiles in the Emissions Database for Global Atmospheric Research, Scientific Data, 7, 121, https://doi.org/10.1038/s41597-020-0462-2, 2020.

de Gouw, J. A.: Emission Sources and Ocean Uptake of Acetonitrile (CH_3CN) in the Atmosphere, Journal of Geophysical Research, 108, 4329, https://doi.org/10.1029/2002JD002897, 2003.

Duflot, V., Dils, B., Baray, J. L., Mazière, M. D., Attié, J. L., Vanhaelewyn, G., Senten, C., Vigouroux, C., Clain, G., and Delmas, R.: Analysis of the Origin of the Distribution of CO in the Subtropical Southern Indian Ocean in 2007, Journal of Geophysical Research: Atmospheres, 115, https://doi.org/10.1029/2010JD013994, 2010.

Duflot, V., Tulet, P., Flores, O., Barthe, C., Colomb, A., Deguillaume, L., Vaïtilingom, M., Perring, A., Huffman, A., Hernandez, M. T., Sellegri, K., Robinson, E., O'Connor, D. J., Gomez, O. M., Burnet, F., Bourrianne, T., Strasberg, D., Rocco, M., Bertram, A. K., Chazette, P., Totems, J., Fournel, J., Stamenoff, P., Metzger, J.-M., Chabasset, M., Rousseau, C., Bourrianne, E., Sancelme, M., Delort, A.-M., Wegener, R. E., Chou, C., and Elizondo, P.: Preliminary Results from the FARCE 2015 Campaign: Multidisciplinary Study of the Forest–Gas–Aerosol–Cloud System on the Tropical Island of La Réunion, Atmospheric Chemistry and Physics, 19, 10 591–10 618, https://doi.org/10.5194/acp-19-10591-2019, 2019.

Dupuy, S., Gaetano, R., and Le Mézo, L.: Mapping Land Cover on Reunion Island in 2017 Using Satellite Imagery and Geospatial Ground Data, Data in Brief, 28, 104 934, https://doi.org/10.1016/j.dib.2019.104934, 2020.

Farmer, D. K. and Riches, M.: Measuring Biosphere–Atmosphere Exchange of Short-Lived Climate Forcers and Their Precursors, Accounts of Chemical Research, 53, 1427–1435, https://doi.org/10.1021/acs.accounts.0c00203, 2020.

Foucart, B., Sellegri, K., Tulet, P., Rose, C., Metzger, J.-M., and Picard, D.: High Occurrence of New Particle Formation Events at the Maïdo High-Altitude Observatory (2150 m), Réunion (Indian Ocean), Atmospheric Chemistry and Physics, 18, 9243–9261, https://doi.org/10.5194/acp-18-9243-2018, 2018.

Fournaise Info: Tableau des éruptions, https://fournaise.info/tableau_eruptions/, last access: 10 December 2020, 2018.

Guenther, A. B., Zimmerman, P. R., Harley, P. C., Monson, R. K., and Fall, R.: Isoprene and Monoterpene Emission Rate Variability: Model Evaluations and Sensitivity Analyses, Journal of Geophysical Research, 98, 12 609, https://doi.org/10.1029/93JD00527, 1993.

Guilpart, E., Vimeux, F., Evan, S., Brioude, J., Metzger, J.-M., Barthe, C., Risi, C., and Cattani, O.: The Isotopic Composition of Near-Surface Water Vapor at the Maïdo Observatory (Reunion Island, Southwestern Indian Ocean) Documents the Controls of the Humidity of the Subtropical Troposphere, Journal of Geophysical Research: Atmospheres, 122, 9628–9650, https://doi.org/10.1002/2017JD026791, 2017.

IPCC: Climate Change 2013: The Physical Science Basis. Contribution of Working Group I to the Fifth Assessment Report of the Intergovernmental Panel on Climate Change, Cambridge University Press, Cambridge, United Kingdom and New York, NY, USA, 2013.

Jardine, K., Yañez-Serrano, A. M., Williams, J., Kunert, N., Jardine, A., Taylor, T., Abrell, L., Artaxo, P., Guenther, A., Hewitt, C. N., House, E., Florentino, A. P., Manzi, A., Higuchi, N., Kesselmeier, J., Behrendt, T., Veres, P. R., Derstroff, B., Fuentes, J. D., Martin, S. T., and Andreae, M. O.: Dimethyl Sulfide in the Amazon Rain Forest: DMS in the Amazon, Global Biogeochemical Cycles, 29, 19–32, https://doi.org/10.1002/2014GB004969, 2015.

Jerrett, M., Burnett, R. T., Pope, C. A., Ito, K., Thurston, G., Krewski, D., Shi, Y., Calle, E., and Thun, M.: Long-Term Ozone Exposure and Mortality, New England Journal of Medicine, 360, 1085–1095, https://doi.org/10.1056/NEJMoa0803894, 2009.

Karl, T., Hansel, A., Märk, T., Lindinger, W., and Hoffmann, D.: Trace Gas Monitoring at the Mauna Loa Baseline Observatory Using Proton-Transfer Reaction Mass Spectrometry, International Journal of Mass Spectrometry, 223-224, 527–538, https://doi.org/10.1016/S1387-3806(02)00874-6, 2003.

Kloster, S., Feichter, J., Maier-Reimer, E., Six, K. D., Stier, P., and Wetzel, P.: DMS Cycle in the Marine Ocean-Atmosphere System – a Global Model Study, Biogeosciences, 3, 29–51, https://doi.org/10.5194/bg-3-29-2006, 2006.

Lac, C., Chaboureau, J.-P., Masson, V., Pinty, J.-P., Tulet, P., Escobar, J., Leriche, M., Barthe, C., Aouizerats, B., Augros, C., Aumond, P., Auguste, F., Bechtold, P., Berthet, S., Bielli, S., Bosseur, F., Caumont, O., Cohard, J.-M., Colin, J., Couvreux, F., Cuxart, J., Delautier,

34

620   G., Dauhut, T., Ducrocq, V., Filippi, J.-B., Gazen, D., Geoffroy, O., Gheusi, F., Honnert, R., Lafore, J.-P., Lebeaupin Brossier, C., Libois, Q., Lunet, T., Mari, C., Maric, T., Mascart, P., Mogé, M., Molinié, G., Nuissier, O., Pantillon, F., Peyrillé, P., Pergaud, J., Perraud, E., Pianezze, J., Redelsperger, J.-L., Ricard, D., Richard, E., Riette, S., Rodier, Q., Schoetter, R., Seyfried, L., Stein, J., Suhre, K., Taufour, M., Thouron, O., Turner, S., Verrelle, A., Vié, B., Visentin, F., Vionnet, V., and Wautelet, P.: Overview of the Meso-NH Model Version 5.4 and Its Applications, Geoscientific Model Development, 11, 1929–1969, https://doi.org/10.5194/gmd-11-1929-2018, 2018.

Lana, A., Bell, T. G., Simó, R., Vallina, S. M., Ballabrera-Poy, J., Kettle, A. J., Dachs, J., Bopp, L., Saltzman, E. S., Stefels, J., Johnson, J. E.,
625   and Liss, P. S.: An Updated Climatology of Surface Dimethylsulfide Concentrations and Emission Fluxes in the Global Ocean: UPDATED DMS CLIMATOLOGY, Global Biogeochemical Cycles, 25, n/a–n/a, https://doi.org/10.1029/2010GB003850, 2011.

Le Monde: Gilets jaunes: couvre-feu partiel à La Réunion, bloquée par des barrages routiers, https://www.lemonde.fr/la-reunion/article/2018/11/20/un-couvre-feu-partiel-instaure-a-la-reunion-bloquee-par-les-gilets-jaunes_5385926_1616695.html, last access: 10 December 2020, 2018.

630   Lesouëf, D., Gheusi, F., Delmas, R., and Escobar, J.: Numerical Simulations of Local Circulations and Pollution Transport over Reunion Island, Annales Geophysicae, 29, 53–69, https://doi.org/10.5194/angeo-29-53-2011, 2011.

Liu, Y. J., Herdlinger-Blatt, I., McKinney, K. A., and Martin, S. T.: Production of Methyl Vinyl Ketone and Methacrolein via the Hydroperoxyl Pathway of Isoprene Oxidation, Atmospheric Chemistry and Physics, 13, 5715–5730, https://doi.org/10.5194/acp-13-5715-2013, 2013.

635   Millet, D. B., Guenther, A., Siegel, D. A., Nelson, N. B., Singh, H. B., de Gouw, J. A., Warneke, C., Williams, J., Eerdekens, G., Sinha, V., Karl, T., Flocke, F., Apel, E., Riemer, D. D., Palmer, P. I., and Barkley, M.: Global Atmospheric Budget of Acetaldehyde: 3-D Model Analysis and Constraints from in-Situ and Satellite Observations, Atmospheric Chemistry and Physics, 10, 3405–3425, https://doi.org/10.5194/acp-10-3405-2010, 2010.

Météo France: Archive of Cyclone Seasons - Details of archived systems, http://www.meteo.fr/temps/domtom/La_Reunion/webcmrs9.0/
640   anglais/index.html, last access: 10 December 2020, 2020.

Norris, G., Duvall, R., Brown, S., and Bai, S.: EPA Postive Matrix Factorization (PMF) 5.0 Fundamentals and User Guide, 2014.

Pernov, J. B., Bossi, R., Lebourgeois, T., Nøjgaard, J. K., Holzinger, R., Hjorth, J. L., and Skov, H.: Atmospheric VOC Measurements at a High Arctic Site: Characteristics and Source Apportionment, Preprint, Gases/Field Measurements/Troposphere/Chemistry (chemical composition and reactions), https://doi.org/10.5194/acp-2020-528, 2020.

645   Pisso, I., Sollum, E., Grythe, H., Kristiansen, N. I., Cassiani, M., Eckhardt, S., Arnold, D., Morton, D., Thompson, R. L., Groot Zwaaftink, C. D., Evangeliou, N., Sodemann, H., Haimberger, L., Henne, S., Brunner, D., Burkhart, J. F., Fouilloux, A., Brioude, J., Philipp, A., Seibert, P., and Stohl, A.: The Lagrangian Particle Dispersion Model FLEXPART Version 10.4, Geoscientific Model Development, 12, 4955–4997, https://doi.org/10.5194/gmd-12-4955-2019, 2019.

Read, K. A., Carpenter, L. J., Arnold, S. R., Beale, R., Nightingale, P. D., Hopkins, J. R., Lewis, A. C., Lee, J. D., Mendes, L., and Pickering,
650   S. J.: Multiannual Observations of Acetone, Methanol, and Acetaldehyde in Remote Tropical Atlantic Air: Implications for Atmospheric OVOC Budgets and Oxidative Capacity, Environmental Science & Technology, 46, 11 028–11 039, https://doi.org/10.1021/es302082p, 2012.

Rivera-Rios, J. C., Nguyen, T. B., Crounse, J. D., Jud, W., St. Clair, J. M., Mikoviny, T., Gilman, J. B., Lerner, B. M., Kaiser, J. B., Gouw, J., Wisthaler, A., Hansel, A., Wennberg, P. O., Seinfeld, J. H., and Keutsch, F. N.: Conversion of Hydroperoxides to Carbonyls in Field
655   and Laboratory Instrumentation: Observational Bias in Diagnosing Pristine versus Anthropogenically Controlled Atmospheric Chemistry, Geophysical Research Letters, 41, 8645–8651, https://doi.org/10.1002/2014GL061919, 2014.

Rocco, M., Colomb, A., Baray, J.-L., Amelynck, C., Verreyken, B., Borbon, A., Pichon, J.-M., Bouvier, L., Schoon, N., Gros, V., Sarda-Esteve, R., Tulet, P., Metzger, J.-M., Duflot, V., Guadagno, C., Peris, G., and Brioude, J.: Analysis of Volatile Organic Compounds during the OCTAVE Campaign: Sources and Distributions of Formaldehyde on Reunion Island, Atmosphere, 11, 140, https://doi.org/10.3390/atmos11020140, 2020.

Seibert, P. and Frank, A.: Source-Receptor Matrix Calculation with a Lagrangian Particle Dispersion Model in Backward Mode, Atmospheric Chemistry and Physics, 4, 51–63, https://doi.org/10.5194/acp-4-51-2004, 2004.

Stohl, A., Forster, C., Frank, A., Seibert, P., and Wotawa, G.: Technical Note: The Lagrangian Particle Dispersion Model FLEXPART Version 6.2, Atmospheric Chemistry and Physics, 5, 2461–2474, https://doi.org/10.5194/acp-5-2461-2005, 2005.

Travis, K. R., Heald, C. L., Allen, H. M., Apel, E. C., Arnold, S. R., Blake, D. R., Brune, W. H., Chen, X., Commane, R., Crounse, J. D., Daube, B. C., Diskin, G. S., Elkins, J. W., Evans, M. J., Hall, S. R., Hintsa, E. J., Hornbrook, R. S., Kasibhatla, P. S., Kim, M. J., Luo, G., McKain, K., Millet, D. B., Moore, F. L., Peischl, J., Ryerson, T. B., Sherwen, T., Thames, A. B., Ullmann, K., Wang, X., Wennberg, P. O., Wolfe, G. M., and Yu, F.: Constraining Remote Oxidation Capacity with ATom Observations, Atmospheric Chemistry and Physics, 20, 7753–7781, https://doi.org/10.5194/acp-20-7753-2020, 2020.

Tulet, P., Muro, A. D., Colomb, A., Denjean, C., Duflot, V., Arellano, S., Foucart, B., Brioude, J., Sellegri, K., Peltier, A., Aiuppa, A., Barthe, C., Bhugwant, C., Bielli, S., Boissier, P., Boudoire, G., Bourrianne, T., Brunet, C., Burnet, F., Cammas, J.-P., Gabarrot, F., Galle, B., Giudice, G., Guadagno, C., Jeamblu, F., Kowalski, P., Leclair de Bellevue, J., Marquestaut, N., Mékies, D., Metzger, J.-M., Pianezze, J., Portafaix, T., Sciare, J., Tournigand, A., and Villeneuve, N.: First Results of the Piton de La Fournaise STRAP 2015 Experiment: Multidisciplinary Tracking of a Volcanic Gas and Aerosol Plume, Atmospheric Chemistry and Physics, 17, 5355–5378, https://doi.org/10.5194/acp-17-5355-2017, 2017.

Verreyken, B., Brioude, J., and Evan, S.: Development of Turbulent Scheme in the FLEXPART-AROME v1.2.1 Lagrangian Particle Dispersion Model, Geoscientific Model Development, 12, 4245–4259, https://doi.org/10.5194/gmd-12-4245-2019, 2019.

Verreyken, B., Amelynck, C., Brioude, J., Müller, J.-F., Schoon, N., Kumps, N., Colomb, A., Metzger, J.-M., Lee, C. F., Koenig, T. K., Volkamer, R., and Stavrakou, T.: Characterisation of African Biomass Burning Plumes and Impacts on the Atmospheric Composition over the South-West Indian Ocean, Atmospheric Chemistry and Physics, 20, 14 821–14 845, https://doi.org/10.5194/acp-20-14821-2020, 2020.

Vettikkat, L., Sinha, V., Datta, S., Kumar, A., Hakkim, H., Yadav, P., and Sinha, B.: Significant Emissions of Dimethyl Sulfide and Monoterpenes by Big-Leaf Mahogany Trees: Discovery of a Missing Dimethyl Sulfide Source to the Atmospheric Environment, Atmospheric Chemistry and Physics, 20, 375–389, https://doi.org/10.5194/acp-20-375-2020, 2020.

Vigouroux, C., Stavrakou, T., Whaley, C., Dils, B., Duflot, V., Hermans, C., Kumps, N., Metzger, J.-M., Scolas, F., Vanhaelewyn, G., Müller, J.-F., Jones, D. B. A., Li, Q., and Mazière, M. D.: FTIR Time-Series of Biomass Burning Products (HCN, C_2H_6, C_2H_2, CH_3OH, and HCOOH) at Reunion Island (21° S, 55° E) and Comparisons with Model Data, Atmospheric Chemistry and Physics, 12, 10 367–10 385, https://doi.org/10.5194/acp-12-10367-2012, 2012.

Wennberg, P. O., Bates, K. H., Crounse, J. D., Dodson, L. G., McVay, R. C., Mertens, L. A., Nguyen, T. B., Praske, E., Schwantes, R. H., Smarte, M. D., Clair, J. M. S., Teng, A. P., Zhang, X., and Seinfeld, J. H.: Gas-Phase Reactions of Isoprene and Its Major Oxidation Products, Chemical Reviews, https://doi.org/10.1021/acs.chemrev.7b00439, 2018.

Yang, M., Blomquist, B. W., and Nightingale, P. D.: Air-Sea Exchange of Methanol and Acetone during HiWinGS: Estimation of Air Phase, Water Phase Gas Transfer Velocities, Journal of Geophysical Research: Oceans, 119, 7308–7323, https://doi.org/10.1002/2014JC010227, 2014.

Zhao, Y., Saunois, M., Bousquet, P., Lin, X., Berchet, A., Hegglin, M. I., Canadell, J. G., Jackson, R. B., Hauglustaine, D. A., Szopa, S., Stavert, A. R., Abraham, N. L., Archibald, A. T., Bekki, S., Deushi, M., Jöckel, P., Josse, B., Kinnison, D., Kirner, O., Marécal, V., O'Connor, F. M., Plummer, D. A., Revell, L. E., Rozanov, E., Stenke, A., Strode, S., Tilmes, S., Dlugokencky, E. J., and Zheng, B.: Inter-Model Comparison of Global Hydroxyl Radical (OH) Distributions and Their Impact on Atmospheric Methane over the 2000–2016 Period, Atmospheric Chemistry and Physics, 19, 13 701–13 723, https://doi.org/10.5194/acp-19-13701-2019, 2019.

695

PART III

General discussions

Chapter 8

General discussion and conclusions

In the framework of the OCTAVE project, a high-sensitivity quadrupole-based proton-transfer-reaction mass-spectrometry instrument, or hs-PTR-Quad-MS, was deployed at the remote tropical Maïdo high-altitude observatory. The observatory is located on La Réunion, a french island located in the south-west Indian Ocean with a complex orographic profile. The specific objectives of the thesis were i) to develop a tool which can be used to qualify the impact of mesoscale transport on the near-continuous, 2-year data set of volatile organic compound (VOC) concentrations recorded at the observatory, ii) to disentangle local and remote (O)VOC sources affecting the atmospheric composition at La Réunion, and iii) to study the seasonality of VOC concentrations by applying a multi-variate statistical analysis and combining results with back-trajectory calculations.

We have successfully developed a new limited domain version of the FLEXible PARTicle dispersion model (FLEXPART) driven by data provided by the operational numerical weather prediction (NWP) model, AROME. We remarked that in order to correctly represent transport in the offline Lagrangian particle dispersion model (LPDM), special care needed to be taken when simulating turbulence. This is specifically important in complex terrain and more precisely, at the location of the Maïdo observatory as it is often located near the top of the planetary boundary layer (PBL). In order to assure numerical consistency in turbulence between the NWP and the LPDM, the development of FLEXPART-AROME was optimised by taking

turbulent kinetic energy (TKE) driven turbulence into account. By introducing the Thomson reflection–transmission formalism (Thomson et al., 1997) at discrete TKE interfaces in the model, accumulation near the PBL top in the model, reported in previous efforts to implement TKE-driven turbulence in FLEXPART-WRF (Brioude et al., 2013), was significantly reduced. The reduction however was not sufficient to comply with the numerical criterion of well-mixedness as stated by Thomson (1987). A novel turbulent time step was implemented and the model was found to conserve well-mixedness sufficiently for using the new TKE-driven turbulent modes. Use of the new modes was found to slow down the model by a factor of $\sim$ 5 when a large number of air-parcels were located in the free troposphere (FT). However, when the majority of air-parcels were located in the PBL, computation time was only extended by 15%. Realistically, atmospheric transport may combine parcels both in the FT and the PBL, implying that the computational cost for practical applications is expected to be somewhere in between. The delay was found acceptable for generating 24-hour back-trajectories for every hour from November 2017 to November 2019 to analyse the PTR-MS measurements in the framework of the OCTAVE project.

From remote sensing measurements, it is well known that biomass burning (BB) plumes pass over the Maïdo observatory from August to November (Duflot et al., 2010; Vigouroux et al., 2012). The FLEXPART-AROME model was used in a case study characterising six events of BB plumes recorded with the hs-PTR-Quad-MS. It was found that the selected BB plumes were primarily located in the FT. Calculating enhancement ratios (EnRs) relative to CO and comparing them to emissions ratios (ERs) from potential sources revealed a strong production of formic acid (HCOOH) during transport from the source to the Maïdo observatory. A similar HCOOH formation in BB plumes had been inferred previously from satellite data over Africa (Chaliyakunnel et al., 2016) but was not resolved in the ground-based remote sensing study of BB signals performed using data taken on La Réunion (Vigouroux et al., 2012)[1]. Currently, no production mechanism accounting for the observed HCOOH production in the BB plumes is known. An evaluation of the Copernicus atmosphere monitoring service near-real-time (CAMS-NRT) atmospheric composition model revealed

---

[1]This could be due to the data selection process employed in their study. Vigouroux et al. (2012) focused on the EnRs of all observations in the biomass burning season and filtered out outliers. These outliers were probably related to younger, dense plumes passing over the observatory.

that, although CO is well reproduced, concentrations of ozone (O_3), and NO_2 were severely underestimated. The discrepancy in O_3 concentrations were probably due to a shortage of NO_2 as it is the main source of O_3 in the troposphere. Large uncertainties to both volatile organic compound (VOC) and nitrogen oxides (NO_x=NO+NO_2) emissions from pyrogenic activity, or a misrepresentation of NO_x recycling in BB plumes are proposed as the most likely culprits for the discrepancy between the CAMS-NRT model and observations. By combining the calculated EnRs, relative to CO, at Maïdo and simulating transport of excess CO using the pyrogenic emission inventory used by the CAMS NRT model, an estimate of the impact of African and Madagascan BB sources on the marine boundary layer over the south-west Indian Ocean has been made for acetonitrile (CH_3CN), acetone (CH_3COCH_3), benzene (C_6H_6), and methanol (CH_3OH). Comparison between these estimate and historical ship-borne PTR-MS measurements in the region, from the MANCHOT campaign (Colomb et al., 2009), revealed that BB elevated the background mixing ratios by 60%–150%, 30%–75%, 15%–150% and 25%–>100%, respectively.

Finally, from previous studies, it is known that at night, the observatory is often located in, or near, the free troposphere while during daytime mesoscale transport features transport marine boundary layer air masses towards the observatory over anthropogenic and biogenic sources. This mesoscale transport feature has been simulated using the mesoscale non-hydrostatic (Meso-NH) model by Lesouëf et al. (2011) who performed forward simulation studies of major pollution sources located on the island and characterised their impact at the location of Maïdo before constructing the observatory. This transport has been described often through literature (e.g., Baray et al., 2013; Guilpart et al., 2017; Tulet et al., 2017; Foucart et al., 2018; Duflot et al., 2019; Rocco et al., 2020) but has not yet been studied using long-term data combined with mesoscale back-trajectory calculations. To further improve our understanding of sources, sinks and the impact of transport on the atmospheric composition at the location of the Maïdo observatory, the variability of VOC tracers unequivocally linked to specific sources were discussed, a positive matrix factorisation (PMF) algorithm was employed, and 24-hour back-trajectory calculations were made using FLEXPART-AROME for the period that the PTR-MS instrument was deployed at the observatory. The seasonal variability of the biogenic tracers (isoprene, C_5H_8, and isoprene oxidation products, Iox) were strongly linked to the wet and hot vs the dry and cold seasonality at La Réunion. The BB tracer (CH_3CN) also showed a clear seasonal vari-

ability with strong peaks correlated to episodes of BB plume intrusions at the observatory. The anthropogenic (C_6H_6 and C_8-aromatics, C_8H_{10}) and oceanic (dimethyl sulfide, DMS) tracers showed no clear seasonal profiles. From the median diel profiles, it was found that the anthropogenic and biogenic tracers had persistent diel profiles with a large maximum during the day. While the oceanic tracer has a similar signature most of the time, during austral winter (June–August) the median diel profile became flat. The BB tracer however did not show consistent diel variability except during the BB season (August–November) where a nighttime maximum was visible in 2017 and 2019 due to BB plumes transported predominantly in the FT. Separating the diel profile according to wind direction (west vs east) revealed a strong impact from anthropogenic sources when wind was coming from the west. When wind was coming from the east however, the diel Iox profile revealed a strong biogenic source east of the observatory. Using the PMF algorithm, 4 source factors were identified using the PTR-MS measurements, supplemented by CO concentrations. The dominant source was from antropogenic emissions accounting for 38% of the mass of VOCs recorded with the PTR-MS instrument. The second strongest contributions came from a background/biomass burning source (33%). The median diel pattern of the background/biomass burning source contributions was found to have a maximum at night which suggests this factor originates from the contribution of the FT on the measurements at Maïdo. The smallest contributions were from biogenic emissions (29% in total, 15% from primary emissions and 14% from a secondary biogenic source). The minor contributions of biogenic sources may be related to the small atmospheric lifetimes of the characteristic tracers associated with these sources (C_5H_8 and Iox). Note here that no oceanic source is resolved from the PMF algorithm. The diel and seasonal profiles of the factor contributions related to the four sources identified by the PMF algorithm were consistent with the behaviour of the tracers characteristic for their respective source. The 24-hour back-trajectories, generated for every hour during the campaign, showed that mesoscale sources on the island only affect the air mass in the 12 hours prior to observation. The strongest anthropogenic signatures were accompanied by elevated source-receptor relationships (SRRs) west of the observatory suggesting that anthropogenic emissions affecting the atmospheric composition at Maïdo mostly originate from Le Gol, Le Port, and Saint-Paul. The strongest biogenic signatures on the other hand were correlated with elevated SRRs east of the observatory and from the "Rivière des Galets" river canyon. The nighttime 30-minute average interquartile

range of VOCs measured with the PTR-MS instrument at Maïdo were 525–887 pptv, 79–110 pptv, 61–101 pptv,172–335 pptv, 259–379 pptv, 64–164 and 11–21 ppt, for CH_3OH, CH_3CN, acetaldehyde (CH_3CHO), HCOOH, CH_3COCH_3, CH_3COOH, and methyl ethyl ketone (MEK) respectively. As this pertains to nighttime measurements, these concentrations are characteristic for the atmospheric composition of the FT.

Bibliography

Baray, J.-L., Courcoux, Y., Keckhut, P., Portafaix, T., Tulet, P., Cammas, J.-P., Hauchecorne, A., Godin Beekmann, S., Mazière, M. D., Hermans, C., Desmet, F., Sellegri, K., Colomb, A., Ramonet, M., Sciare, J., Vuillemin, C., Hoareau, C., Dionisi, D., Duflot, V., Vérèmes, H., Porteneuve, J., Gabarrot, F., Gaudo, T., Metzger, J.-M., Payen, G., Leclair de Bellevue, J., Barthe, C., Posny, F., Ricaud, P., Abchiche, A., and Delmas, R.: Maïdo Observatory: A New High-Altitude Station Facility at Reunion Island (21° S, 55° E) for Long-Term Atmospheric Remote Sensing and in Situ Measurements, Atmospheric Measurement Techniques, 6, 2865–2877, https://doi.org/10.5194/amt-6-2865-2013, 2013.

Brioude, J., Arnold, D., Stohl, A., Cassiani, M., Morton, D., Seibert, P., Angevine, W., Evan, S., Dingwell, A., Fast, J. D., Easter, R. C., Pisso, I., Burkhart, J., and Wotawa, G.: The Lagrangian Particle Dispersion Model FLEXPART-WRF Version 3.1, Geoscientific Model Development, 6, 1889–1904, https://doi.org/10.5194/gmd-6-1889-2013, 2013.

Chaliyakunnel, S., Millet, D., Wells, K., Cady-Pereira, K., and Shephard, M.: A Large Underestimate of Formic Acid from Tropical Fires: Constraints from Space-Borne Measurements, Environmental Science & Technology, 50, 5631–5640, https://doi.org/10.1021/acs.est.5b06385, 2016.

Colomb, A., Gros, V., Alvain, S., Sarda-Esteve, R., Bonsang, B., Moulin, C., Klüpfel, T., and Williams, J.: Variation of Atmospheric Volatile Organic Compounds over the Southern Indian Ocean (30–49°S), Environmental Chemistry, 6, 70–82, https://doi.org/10.1071/EN08072, 2009.

Duflot, V., Dils, B., Baray, J. L., Mazière, M. D., Attié, J. L., Vanhaelewyn, G., Senten, C., Vigouroux, C., Clain, G., and Delmas, R.: Analysis of

the Origin of the Distribution of CO in the Subtropical Southern Indian Ocean in 2007, Journal of Geophysical Research: Atmospheres, 115, https://doi.org/10.1029/2010JD013994, 2010.

Duflot, V., Tulet, P., Flores, O., Barthe, C., Colomb, A., Deguillaume, L., Vaïtilingom, M., Perring, A., Huffman, A., Hernandez, M. T., Sellegri, K., Robinson, E., O'Connor, D. J., Gomez, O. M., Burnet, F., Bourrianne, T., Strasberg, D., Rocco, M., Bertram, A. K., Chazette, P., Totems, J., Fournel, J., Stamenoff, P., Metzger, J.-M., Chabasset, M., Rousseau, C., Bourrianne, E., Sancelme, M., Delort, A.-M., Wegener, R. E., Chou, C., and Elizondo, P.: Preliminary Results from the FARCE 2015 Campaign: Multidisciplinary Study of the Forest–Gas–Aerosol–Cloud System on the Tropical Island of La Réunion, Atmospheric Chemistry and Physics, 19, 10 591–10 618, https://doi.org/10.5194/acp-19-10591-2019, 2019.

Foucart, B., Sellegri, K., Tulet, P., Rose, C., Metzger, J.-M., and Picard, D.: High Occurrence of New Particle Formation Events at the Maïdo High-Altitude Observatory (2150 m), Réunion (Indian Ocean), Atmospheric Chemistry and Physics, 18, 9243–9261, https://doi.org/10.5194/acp-18-9243-2018, 2018.

Guilpart, E., Vimeux, F., Evan, S., Brioude, J., Metzger, J.-M., Barthe, C., Risi, C., and Cattani, O.: The Isotopic Composition of Near-Surface Water Vapor at the Maïdo Observatory (Reunion Island, Southwestern Indian Ocean) Documents the Controls of the Humidity of the Subtropical Troposphere, Journal of Geophysical Research: Atmospheres, 122, 9628–9650, https://doi.org/10.1002/2017JD026791, 2017.

Lesouëf, D., Gheusi, F., Delmas, R., and Escobar, J.: Numerical Simulations of Local Circulations and Pollution Transport over Reunion Island, Annales Geophysicae, 29, 53–69, https://doi.org/10.5194/angeo-29-53-2011, 2011.

Rocco, M., Colomb, A., Baray, J.-L., Amelynck, C., Verreyken, B., Borbon, A., Pichon, J.-M., Bouvier, L., Schoon, N., Gros, V., Sarda-Esteve, R., Tulet, P., Metzger, J.-M., Duflot, V., Guadagno, C., Peris, G., and Brioude, J.: Analysis of Volatile Organic Compounds during the OCTAVE Campaign: Sources and Distributions of Formaldehyde on Reunion Island, Atmosphere, 11, 140, https://doi.org/10.3390/atmos11020140, 2020.

Thomson, D. J.: Criteria for the Selection of Stochastic Models of Particle Trajectories in Turbulent Flows, Journal of Fluid Mechanics, 180, 529–556, https://doi.org/10.1017/S0022112087001940, 1987.

Thomson, D. J., Physick, W. L., and Maryon, R. H.: Treatment of Interfaces in Random Walk Dispersion Models, Journal of Applied Meteorology, 36, 1284–1295, https://doi.org/10.1175/1520-0450(1997)036<1284:TOIIRW>2.0.CO;2, 1997.

Tulet, P., Muro, A. D., Colomb, A., Denjean, C., Duflot, V., Arellano, S., Foucart, B., Brioude, J., Sellegri, K., Peltier, A., Aiuppa, A., Barthe, C., Bhugwant, C., Bielli, S., Boissier, P., Boudoire, G., Bourrianne, T., Brunet, C., Burnet, F., Cammas, J.-P., Gabarrot, F., Galle, B., Giudice, G., Guadagno, C., Jeamblu, F., Kowalski, P., Leclair de Bellevue, J., Marquestaut, N., Mékies, D., Metzger, J.-M., Pianezze, J., Portafaix, T., Sciare, J., Tournigand, A., and Villeneuve, N.: First Results of the Piton de La Fournaise STRAP 2015 Experiment: Multidisciplinary Tracking of a Volcanic Gas and Aerosol Plume, Atmospheric Chemistry and Physics, 17, 5355–5378, https://doi.org/10.5194/acp-17-5355-2017, 2017.

Vigouroux, C., Stavrakou, T., Whaley, C., Dils, B., Duflot, V., Hermans, C., Kumps, N., Metzger, J.-M., Scolas, F., Vanhaelewyn, G., Müller, J.-F., Jones, D. B. A., Li, Q., and Mazière, M. D.: FTIR Time-Series of Biomass Burning Products (HCN, C_2H_6, C_2H_2, CH_3OH, and HCOOH) at Reunion Island (21° S, 55° E) and Comparisons with Model Data, Atmospheric Chemistry and Physics, 12, 10367–10385, https://doi.org/10.5194/acp-12-10367-2012, 2012.

Chapter 9

Prospects

I have presented the development of a mesoscale Lagrangian transport model driven by the operational numerical weather prediction model, used by Météo France over the Indian Ocean, AROME. It was developed in order to analyse the 2-year data set of VOCs recorded at the Maïdo observatory. It has been used to calculate back-trajectories for the complete period the hs-PTR-Quad-MS was deployed at the observatory. These back-trajectories in turn have been used to identify the regions around the island that contribute strongest to VOC recorded at the Maïdo observatory according to the source factors identified using PMF. The source-receptor relationships calculated using the passive tracers can be applied to the longer-lived VOC directly emitted at the surface, e.g. C_6H_6, to estimate their emission located on the island. However, in order to do this, one must first estimate the impact of synoptic scale transport on their concentrations and isolate the effects of mesoscale emissions on the hs-PTR-Quad-MS data set. Alternatively, one can implement simple chemistry in the LPDM and simulate oxidation of the shorter lived compounds emitted directly from the surface, e.g. C_5H_8 or C_8H_{10}, to estimate their mesoscale emissions. For these species, one can assume that the contribution of synoptic-scale transport is negligible and one can use the mesoscale back-trajectories and the hs-PTR-Quad-MS measurements directly.

As the FLEXPART-AROME model has been prepped to handle turbulence in three dimensions, it was also adapted to be driven by meteorological data obtained from the Meso-NH research model (FLEXPART-MNH). Instead of focusing on back-trajectories calculated using FLEXPART-AROME and

the complete hs-PTR-Quad-MS data set, one can focus on identifying case studies in the data and simulate transport using FLEXPART-MNH. The main advantage of using FLEXPART-MNH is better resolution of local-scale effects, e.g. air-mass exchanges between the 3 main calderas located on La Réunion and better resolution of the location of the wind-shear front between overflowing winds and the mesoscale up-slope transport along the Maïdo mountain slope. This is especially interesting for the OCTAVE intensive observation period (March–May 2018), and the BIO-MAIDO campaign (March-April 2019), when other PTR-MS instruments were deployed at the island.

Additionally, instead of focusing on the mesoscale emission sources of VOCs, one could invest efforts in developing a way to nest meteorological data from AROME or Meso-NH with a global NWP model. This is especially interesting to simulate the impact of synoptic scale sources on the PTR-MS measurements recorded at the observatory and by extension, the island as a whole. In Chapter 6, I was forced to use simulations both from FLEX-PART, and FLEXPART-AROME in order to get a general picture of how transport processes impact the observatory. For the case-studies selected, I was lucky that mesoscale transport had a limited impact on local measurements during the intrusions. In the future, it would be advantageous to have a tool that can simultaneously model both the synoptic scale transport, and mesoscale features induced by the island.

As an alternative to using LPDMs, one can use a CTM or a mesoscale chemistry model, e.g. WRF-Chem or Meso-NH, and evaluate the discrepancies between the model and measurements which stem from either i) incomplete representation of chemical and physical interactions involving VOCs in the atmosphere, ii) poor characterisation of ocean–atmosphere interactions, or iii) insufficient representation of local sources and mesoscale transport towards the observatory. However, despite the availability of detailed information on biogenic emissions on the island available at LACy (Laboratoire de l'atmosphère et des cyclones), no such information is as of yet available for anthropogenic emissions. To provide mesoscale emissions from anthropogenic sources, an inversion driven by backtrajectories generated by FLEXPART-AROME or FLEXPART-MNH, as proposed above, might prove necessary before using a CTM to analyse the complete dataset.

Aside from furthering the analysis of the VOC data set realised in the framework of the OCTAVE-project using computations models, one can further exploit the data set to gain insight on OH-reactivity or the O_3

formation potential at the location of the Maïdo observatory. The data may be combined with those of other instruments housed at the observatory and at the island during the 2-year campaign in order to gain insight in e.g. VOC chemistry along the Maïdo mountain slope.

Lastly, additional measurements may be performed in the future to improve our understanding of (O)VOC budgets in remote regions. Comparison of synchronous (O)VOC measurements over the ocean and at the observatory during the BB season could retrieve valuable information on VOC aging mechanisms. Direct ship-borne bi-directional ocean/atmosphere flux measurements in combination with sea-water composition measurements in the south-west Indian Ocean will also be extremely valuable to characterise ocean–atmosphere exchanges in this severely undersampled region. Resolving a marine source from a source attribution study using the PMF algorithm will benefit greatly from lowering the limit of detection for DMS, a key tracer for marine emissions. The inclusion of measurements of other marine tracers, such as halogenated compounds, by deploying additional instrumentation besides a PTR-MS instrument at Maïdo may allow the resolution of an ocean source by the PMF source attribution.

Summaries

Source attribution of oxygenated volatile organic compounds in the remote tropical atmosphere

Volatile organic compounds (VOCs) are constituents of the natural atmosphere emitted by a plethora of sources. They are key ingredients for the formation of ozone (O_3) near the surface and the formation of secondary organic aerosol (SOA). As such, they impact both human health (Jerrett et al., 2009) and climate (IPCC, 2013). Due to a paucity in data from remote tropical locations and in the free troposphere (FT), chemical transport models (CTMs) are badly constrained in these regions (e.g., Millet et al., 2010; Read et al., 2012), resulting in large uncertainties in VOC sources and sinks. The oxygenated compounds in the tropical atmosphere: variability and exchanges (OCTAVE) project aims to better quantify the sources and sinks of (oxygenated) volatile organic compounds, or (O)VOCs, in the remote tropical atmosphere by an integrated approach combining in situ data, satellite retrievals and (global) CTMs. The work presented in this thesis focuses on the generation and analysis of a near-continuous data set of in situ VOC concentrations recorded with a proton-transfer-reaction mass-spectrometry (PTR-MS) VOC analyser at the high-altitude Maïdo observatory, located on La Réunion, a volcanic island in the south-west Indian Ocean.

For this, a mesoscale Lagrangian particle dispersion model (LPDM) is developed with a special focus on introducing a new, TKE-driven, turbulent mode based on the Thomson transmission–reflection formalism (Thomson et al., 1997) across discrete interfaces. It is a limited area version of the FLEXible PARTicle dispersion model (FLEXPART), FLEXPART-

AROME, and is driven by meteorological data from AROME[1]. The main advantage of using the new turbulence mode is consistency between turbulent motions in the offline LPDM and the numerical weather prediction (NWP). This is especially important for analysing data at the Maïdo observatory as it is located on the convergence between the turbulent planetary boundary layer (PBL) and the FT. A description and the numerical validation of the new turbulent mode in FLEXPART-AROME was published by Verreyken et al. (2019). It was found that the new turbulent parameterisation severely slows down the simulation of a large number of particles situated above the PBL (factor of 5). However, in case the majority of particles are constrained in the boundary layer, which is often the case for transport using mesoscale models as the focus is regional transport, the new turbulent mode came at a cost of only 15% longer computation times.

The development of FLEXPART-AROME was needed in order to analyse the near-continuous two-year VOC data-set generated with the PTR-MS instrument. The analysis of data consisted of i) a case study related to African and Madagascan biomass burning (BB) plumes arriving at the observatory (Verreyken et al., 2020), and ii) a VOC source attribution study using the complete data set (Verreyken et al., 2021).

The BB study consisted of a chemical characterisation of the plumes arriving at the Maïdo observatory, comparison of the chemical makeup to expectations from the literature, evaluation of the Copernicus atmosphere monitoring service (CAMS) near-real-time atmospheric composition model with measurements performed at the observatory, and estimating the impact of African and Madagascan BB on the marine boundary layer air composition. For this study, FLEXPART-AROME simulations were used to show that the BB plumes were primarily located in the FT and that the effect of mesoscale transport on its chemical composition was only limited. It was found that i) production of formic acid (HCOOH) during transport was unexpectedly high, ii) the CAMS model did not sufficiently represent ozone (O_3) and NO_2 concentrations during the BB episodes, and iii) African and Madagascan burning sources increase atmospheric background mixing ratios of benzene (C_6H_6), acetonitrile (CH_3CN), methanol (CH_3OH), and acetone (CH_3COCH_3) by 25 to 100 % compared to historical ship-borne measurements over the south-west Indian Ocean.

The analysis of the complete two-year data-set describes diel variability of

---

[1]Applications de la recherche à l'opérationnel à méso-echelle (AROME), the operation numerical weather prediction model used by Météo France in the region.

selected VOCs in combination with a positive matrix factorisation (PMF) analysis and 24-hour back-trajectories generated hourly from November 2017 to November 2019 using FLEXPART-AROME. We were able to identify 4 source factors from the PMF analysis, i) a background/biomass burning source, ii) an anthropogenic source, iii) a primary biogenic source, and iv) a secondary biogenic source. The background/biomass burning source was found to originate in the FT as the diel profile of its normalised contribution had a nighttime maximum. All other sources had their maximum during the day, illustrating the impact of mesoscale sources located on the island. Previously, it was shown that easterly transport towards Maïdo was coincident with overflowing tradewinds and thus low sensitivity to surface emissions (Duflot et al., 2019). This was not reproduced in this study. Easterly transport towards the Maïdo observatory was correlated with the arrival of large concentrations of secondary biogenic tracers and from back-trajectories it was found that the observatory was still sensitive to surface emissions. Biogenic emission hotspots with significant impact on the atmospheric composition at the location of the Maïdo observatory were found to be located east of the observatory and along the "Rivière des Galets" river canyon. Anthropogenic emission hotspots affecting the atmospheric composition at the observatory most strongly were found to be located west of the observatory. At night, when the background/biomass burning factor saw the largest contributions, the observatory was less sensitive to surface emissions further confirming that these air masses are mostly influenced by the FT.

Bronbepaling van zuurstofhoudende vluchtige organische stoffen in de afgelegen, tropische atmosfeer

Vluchtige organische stoffen (VOS) zijn deel van de natuurlijke atmosfeer en worden uitgestoten door een overvloed aan verschillende bronnen. Het zijn belangrijke ingrediënten voor de vorming van ozon (O_3) nabij het oppervlak en de vorming van secundaire organische aerosols (SOA). Als dusdanig hebben ze een impact op zowel de menselijke gezondheid (Jerrett et al., 2009), als op het klimaat (IPCC, 2013). Door een gebrek aan data in verafgelegen, tropische locaties en in de vrije troposfeer, presteren chemische transport modellen (CTM's) ondermaats in deze regio's (bijv., Millet et al., 2010; Read et al., 2012) met als resultaat grote onzekerheden in de bronnen en putten van VOS. Het OCTAVE project heeft als doel deze bronnen en putten van de zuurstofhoudende VOS (ZH-VOS) in afgelegen tropische regio's te bepalen aan de hand van lokale metingen van VOS in de atmosfeer, satellietdata, en globale CTM's. In dit manuscript komt de opname en analyse van een bijna-continue tweejarige dataset van VOS-concentraties aan bod. Deze dataset werd bekomen met een hs-PTR-Quad-MS instrument aan het hooggelegen Maïdo observatorium, gelegen op La Réunion, een vulkanisch eiland gelegen in de zuidwestelijke Indische Oceaan.

Hiervoor werd een Lagrangiaans luchtmassaspreidingsmodel (LLSM) ontwikkeld dat transport simuleert op mesoschaal met speciale aandacht voor de implementatie van turbulentie gedreven door turbulente kinetische energie (TKE). Deze nieuwe turbulentiemodus is gebaseerd op de reflectie–transmissiemethode voorgesteld door Thomson et al. (1997). Het nieuwe FLEXPART-AROME model is een versie van het FLEXPART model gedreven door numerieke weersvoorspellingen (NWV) gegenereerd door het AROME model. Het belangrijkste voordeel van de nieuwe modus is dat turbulentie in de LLSM consistent is met die in de NWV. Dit is essentieel voor de analyse van data opgenomen aan het Maïdo observatorium omdat het aan de rand ligt tussen de turbulente grenslaag aan het aardoppervlak en de niet-turbulente vrije troposfeer (VT). Een beschrijving van de numerieke validering van de nieuwe turbulente modus in FLEXPART-AROME werd gepubliceerd in 2019 (Verreyken et al., 2019). De nieuwe parametrisatie vertraagt het algoritme sterk wanneer er zich veel luchtmassa's in de vrije troposfeer bevinden (ongeveer een factor 5 trager). Echter, wanneer transport van luchtmassa's zich voornamelijk in de grenslaag bevinden, wat overigens meestal het geval is met dit type modellen op mesoschaal, duren

simulaties maar 15% langer.

Het model werd ontwikkeld met oog op de analyse van de twee jaar durende dataset van VOS gegenereerd aan het Maïdo observatorium. De analyse bestaat uit i) een studie van zes rookpluimen afkomstig van brandhaarden in Afrika en Madagascar (Verreyken et al., 2020) en ii) het toewijzen van VOS bronnen gebruik maakend van de volledige dataset (Verreyken et al., 2021).

De studie van Afrikaanse en Malagassische pluimen bestond uit een chemische karakterisatie van de luchtmassa's die door de brandhaarden werden beïnvloed, vergelijking van deze chemische samenstelling met de verwachtingen vanuit literatuur, evaluatie van het CAMS-NRT atmosferische compositiemodel, en het afschatten van de impact op de mariene atmosfeer. Hiervoor werd FLEXPART-AROME gebruikt om aan te tonen dat de pluimen zich voornamelijk in de vrije troposfeer bevonden en de invloed van het landschap beperkt was tijdens deze periodes. De voornaamste bevindingen van deze studie waren dat i) er een onverwacht hoge productie van mierenzuur (HCOOH) plaatsvond in de pluim, ii) het CAMS-NRT model de concentraties van O_3 en NO_x ($NO+NO_2$) in de rookpluimen onderschatte, en ii) Afrikaanse en Malagassische brandhaarden de achtergrondconcentraties van benzeen (C_6H_6), acetonitrile (CH_3CN), methanol (CH_3OH) en aceton (CH_3COCH_3) verhoogden met 25–100% vergeleken met VOS-metingen uitgevoerd in het begin van de 21ste eeuw in de regio.

Voor de analyse van de volledige dataset worden dagelijkse, seizoensafhankelijke, en jaarlijkse profielen van VOS-concentraties beschreven. Ook werd een multivariaat statisch model toegepast op de data (positieve matrix factorisatie, PMF) en werden 24-uur durende transportberekeningen met FLEXPART-AROME uitgevoerd voor elk uur dat het instrument aanwezig was in het observatorium. Vier bronnen werden geïdentificeerd aan de hand van de PMF analyse: i) een achtergrond factor waar ook de impact van rookpluimen in bevat is, ii) een antropogene bron, iii) een primaire biogene bron, en iv) een secundaire biogene bron. De achtergrondbron werd gerelateerd aan de VT aangezien de genormaliseerde bijdragen maximaal waren tijdens de nacht. Alle andere bronnen hadden hun maximum overdag, wat de impact van bronnen aanwezig op het eiland aangeeft. Eerder was aangetoond dat transport vanuit het oosten verbonden was aan overvloeiende globale winden die weinig gevoelig waren aan emissies van het landoppervlak (Duflot et al., 2019). Dit werd niet gereproduceerd hier. Transport vanuit het oosten ging gepaard met hoge impact van de secun-

daire biogene bron en uit de transportsimulaties bleek dat deze luchtmassa's wel degelijk gevoelig waren aan uitstoot op het oppervlak. Sterke biogene emissies werden geïdentificeerd ten oosten van Maïdo and langs de ravijn waarin de "Rivière des Galets" gelegen is. Antropogene emissies die het sterkst bijdragen aan vervuiling waargenomen op Maïdo bevonden zich ten westen van het observatorium. 's Nachts, wanneer de achtergrondfactor de hoogste bijdragen had, was het observatorium het minst gevoelig aan emissies van het oppervlak, wat bevestigt dat deze luchtmassa's voornamelijk onder invloed staan van de vrije troposfeer.

Attribution des sources de composés organiques volatils dans l'atmosphère tropicale isolée

Les composés organiques volatils (COVs) sont des espèces chimiques émis par une pléthore de sources naturelles et anthropiques. Ils jouent un rôle clé dans la formation de l'ozone (O_3) enbasse atmosphère, et dans la formation d'aérosols organiques secondaires. Ainsi, ils agissent à la fois sur la santé humaine (Jerrett et al., 2009) et le climat (IPCC, 2013). En raison d'un manque de données dans les régions tropicales isolées et dans la troposphère libre, les modèles de chimie-transport (Chemical Transport Model, ou CTMs en anglais) ne peuvent pas être évalués dans ces régions (e.g., Millet et al., 2010; Read et al., 2012). Il en résulte de fortes incertitudes dans les sources et les puits des COVs. Le projet OCTAVE (The oxygenated compounds in the tropical atmosphere : variability and exchanges) vise à améliorer la quantification des sources et des puits des COV oxygénés (ou COVO) dans l'atmosphère tropicale isolée, à l'aide d'une approche originale qui combine mesures in situ, données satellites et des CTM globaux. Le travail présenté dans cette thèse porte sur la production et l'analyse d'une base de données quasiment continue de 2 ans de mesures in situ de concentrations de COV. Ces mesures ont été effectuées à l'aide d'un spéctromètre de masse à proton-transfert-réaction (PTR-MS en anglais) calibré pour l'analyse des COV à l'observatoire de haute altitude du Maïdo, situé sur l'ile de la Réunion, une ile volcanique dans le bassin sud ouest de l'Océan Indien.

Pour analyser cette base de donnée, un modèle Lagrangien dispersif mésoéchelle a été développé avec une attention particulière sur l'introduction d'un nouveau schéma de turbulence, basé sur la lecture de l'énergie cinétique turbulente atmosphérique et de l'utilisation du formalisme de Thomson (Thomson et al., 1997) sur la transmission-reflection des trajectoires Lagrangiennes à travers des interfaces discrètes. Ce modèle, appelé FLEXPART-AROME, est une version à région limitée du modèle FLEXPART (FLEX-ible PARTicle dispersion model en anglais), couplé aux sorties du modèle météorologique de prévision de Météo France AROME. Le principal avantage du nouveau schéma de turbulence est d'améliorer la cohésion entre les mouvements turbulents du modèle FLEXPART et celui du modèle de prévision AROME. Ceci est particulièrement important pour l'analyse des données de l'observatoire du Maïdo car il est situé à la frontière entre la couche limite atmosphérique (CLA) et la troposphère libre.

Une description et une validation du modèle FLEXPART-AROME et du nouveau schéma turbulent a été publié par Verreyken et al. (2019). Il a été montré que la nouvelle paramétrisation ralentit grandement la simulation d'un grand nombre de trajectoires au dessus de la CLA d'un facteur 5. Cependant, dans le cas où la majorité des trajectoires est située dans la CLA, ce qui est souvent le cas des simulations du transport atmosphérique à mésoéchelle dont l'utilisation principale est le transport à proximité de la surface, le nouveau schéma de turbulence introduit une augmentation du temps de calcul de seulement 15%.

Le développement de FLEXPART-AROME était une nécessité pour pouvoir analyser à mésoéchelle la base de 2 ans de données de COV, quasi-continue, générée par le PTR-MS. L'analyse des données a consisté à i) travailler sur un cas d'étude sur des plumes de feux de biomasse d'Afrique et de Madagascar mesurées à l'observatoire du Maïdo (Verreyken et al., 2020), et ii) l'étude de l'attribution des sources de COV à l'aide de la base de données complète (Verreyken et al., 2021). L'étude sur les feux de biomasse s'est focalisée sur les propriétés chimiques des plumes arrivant à l'observatoire, une comparaison par rapport aux concentrations publiées dans la littérature, l'évaluation du modèle CAMS (Copernicus atmosphere monitoring service), modèle en temps quasi-réel de la composition chimique atmosphérique du programme européen Copernicus, et l'estimation de l'impact des feux sur la composition chimique de la couche limite marine. Le modèle FLEXPART-AROME a été utilisé pour montrer que les plumes de feux de biomasse étaient principalement situées dans la troposphère libre et que l'effet du transport mésoéchelle sur la composition chimique était limité. Il a été montré que i) la production d'acide formique (HCOOH) pendant le transport était particulièrement élevée, ii) CAMS sousestime la concentration en ozone et NO_2 pendant les épisodes de feux, et iii) les sources africaines et de Madagascar de feux de biomasse augmentent le rapport de mélange du benzene (C_6H_6), acetonitrile (CH_3CN), methanol (CH_3OH) et acétone (CH_3COCH_3) de 25 à 100% par rapport aux concentrations mesurées sur bateau dans le bassin sud ouest de l'Océan Indien.

Enfin, la base de 2 ans de données de mesures de COV a permis de mettre en évidence un cycle journalier de concentrations pour certains COV. L'interprétation de ces cycles a nécessité une analyse PMF (factorisation de matrices positives) et des rétrotrajectoires d'une durée de 24h générées toutes les heures de novembre 2017 à novembre 2019 à l'aide de FLEXPART-AROME. Nous avons pû identifier 4 facteurs sources à l'aide de l'analyse

PMF : i) source de feux de biomasse ou de concentrations de fond régionale, ii) source anthropique, iii) source biogénique primaire, iv) source biogénique secondaire. La source de feux de biomasse ou de fond a pour origine la troposphère libre, et son cycle journalier de concentration atteint un maximum la nuit. Toutes les autres sources ont un maximum en concentration en journée, confirmant l'impact du transport mésoéchelle sur les concentrations mesurées en journée à l'observatoire du Maïdo. Il avait été montré précédemment (Duflot et al., 2019) que le transport venant de l'est au niveau de l'observatoire du Maïdo coincidait avec des alizées de vents forts et une faible sensibilité des concentrations mesurées à l'observatoire du Maïdo aux émissions de surface. Ce résultat n'a pas été confirmé par notre étude. Le transport d'est était corrélé avec de fortes concentrations en traceurs biogéniques secondaires. Les rétrotrajectoires ont confirmé que l'observatoire était sous l'influence d'émissions locales malgré le régime de vent d'est. Les principales sources biogéniques influençant l'observatoire du Maïdo ont été localisées à l'est de l'observatoire et le long du canyon de la "Rivière des Galets". Les principales sources anthropiques influençant les mesures à l'observatoire du Maïdo sont situées à l'ouest de l'observatoire. La nuit, il a été montré que l'observatoire est moins sensible aux émissions locales car situé dans la troposphère libre, où la contribution des sources de feux de biomasse et des concentrations de fond régionales est maximale.

Bibliography

Duflot, V., Tulet, P., Flores, O., Barthe, C., Colomb, A., Deguillaume, L., Vaïtilingom, M., Perring, A., Huffman, A., Hernandez, M. T., Sellegri, K., Robinson, E., O'Connor, D. J., Gomez, O. M., Burnet, F., Bourrianne, T., Strasberg, D., Rocco, M., Bertram, A. K., Chazette, P., Totems, J., Fournel, J., Stamenoff, P., Metzger, J.-M., Chabasset, M., Rousseau, C., Bourrianne, E., Sancelme, M., Delort, A.-M., Wegener, R. E., Chou, C., and Elizondo, P.: Preliminary Results from the FARCE 2015 Campaign: Multidisciplinary Study of the Forest–Gas–Aerosol–Cloud System on the Tropical Island of La Réunion, Atmospheric Chemistry and Physics, 19, 10 591–10 618, https://doi.org/10.5194/acp-19-10591-2019, 2019.

IPCC: Climate Change 2013: The Physical Science Basis. Contribution of Working Group I to the Fifth Assessment Report of the Intergovernmental Panel on Climate Change, Cambridge University Press, Cambridge, United Kingdom and New York, NY, USA, 2013.

Jerrett, M., Burnett, R. T., Pope, C. A., Ito, K., Thurston, G., Krewski, D., Shi, Y., Calle, E., and Thun, M.: Long-Term Ozone Exposure and Mortality, New England Journal of Medicine, 360, 1085–1095, https://doi.org/10.1056/NEJMoa0803894, 2009.

Millet, D. B., Guenther, A., Siegel, D. A., Nelson, N. B., Singh, H. B., de Gouw, J. A., Warneke, C., Williams, J., Eerdekens, G., Sinha, V., Karl, T., Flocke, F., Apel, E., Riemer, D. D., Palmer, P. I., and Barkley, M.: Global Atmospheric Budget of Acetaldehyde: 3-D Model Analysis and Constraints from in-Situ and Satellite Observations, Atmospheric Chemistry and Physics, 10, 3405–3425, https://doi.org/10.5194/acp-10-3405-2010, 2010.

Read, K. A., Carpenter, L. J., Arnold, S. R., Beale, R., Nightingale, P. D., Hopkins, J. R., Lewis, A. C., Lee, J. D., Mendes, L., and Pickering, S. J.: Multiannual Observations of Acetone, Methanol, and Acetaldehyde in Remote Tropical Atlantic Air: Implications for Atmospheric OVOC Budgets and Oxidative Capacity, Environmental Science & Technology, 46, 11 028–11 039, https://doi.org/10.1021/es302082p, 2012.

Thomson, D. J., Physick, W. L., and Maryon, R. H.: Treatment of Interfaces in Random Walk Dispersion Models, Journal of Applied Meteorol-

ogy, 36, 1284–1295, https://doi.org/10.1175/1520-0450(1997)036<1284: TOIIRW>2.0.CO;2, 1997.

Verreyken, B., Brioude, J., and Evan, S.: Development of Turbulent Scheme in the FLEXPART-AROME v1.2.1 Lagrangian Particle Dispersion Model, Geoscientific Model Development, 12, 4245–4259, https://doi.org/10.5194/gmd-12-4245-2019, 2019.

Verreyken, B., Amelynck, C., Brioude, J., Müller, J.-F., Schoon, N., Kumps, N., Colomb, A., Metzger, J.-M., Lee, C. F., Koenig, T. K., Volkamer, R., and Stavrakou, T.: Characterisation of African Biomass Burning Plumes and Impacts on the Atmospheric Composition over the South-West Indian Ocean, Atmospheric Chemistry and Physics, 20, 14 821–14 845, https://doi.org/10.5194/acp-20-14821-2020, 2020.

Verreyken, B., Amelynck, C., Schoon, N., Müller, J.-F., Brioude, J., Kumps, N., Hermans, C., Metzger, J.-M., and Stavrakou, T.: Measurement report: Source apportionment of volatile organic compounds at the remote high-altitude Maïdo observatory, Atmospheric Chemistry and Physics Discussions, 2021, 1–37, https://doi.org/10.5194/acp-2021-124, 2021.

Scientific contributions

Contributions to key articles

I have made significant contributions to all the publications which were presented in this thesis.

The idea of developing the TKE-driven turbulence in the offline LPDM originates from J. Brioude who envisioned constraining transport across discrete TKE interfaces using the Thomson reflection–transmission formalism (Thomson et al., 1997) in FLEXPART-AROME together the different numerical tests to be performed needed as validation. This work was presented in Chapter 5 (Verreyken et al., 2019). I was responsible for implementing the formalism, evaluate the performance and write the manuscript. First tests however resulted in accumulation of particles in the PBL due to gradients in turbulent mixing lengths. The identification of the issue and the implementation of the adaptive turbulent time step were my own original contributions to the work shown. All co-authors were involved in review and editing of the final version of the paper.

The second paper which studies BB plumes was also suggested by J. Brioude who noted the large impact of African and Madagascan pyrogenic emissions on air-quality around La Réunion as a visible brown haze. He asked if this was visible in the VOC data set recorded with the hs-PTR-Quad-MS which prompted a closer analysis of this type of signals presented in Chapter 6 (Verreyken et al., 2020). The exploratory analysis and initial simulations was performed by myself. Chemical characterisation of the BB plumes and the possible implications were extensively discussed with C. Amelynck, J.-F. Müller and T. Stavrakou on matters concerning atmospheric chemistry. Processing of NO_2 data from the MAX-DOAS instrument was performed

by R. Volkamer and colleagues at CIRES which were strongly involved in the interpretation of this data. The formal analysis and simulations were performed by myself. The manuscript was written by myself and editing/reviewing of the manuscript was performed by all co-authors.

Chapter 7 (Verreyken et al., 2021) was partly envisioned at the conception of the OCTAVE project. As a deliverable of OCTAVE, it was stated that the two-year dataset will be analysed using a multivariate statistical and an inverse modelling approach. As such, diel, seasonal and inter-annual variability of VOC concentrations recorded at the Maïdo observatory are discussed and analysed using a PMF algorithm in combination with back-trajectory calculations. In collaboration with C. Amelynck, I discussed the diel, seasonal and inter-annual patterns. The PMF analysis and the back-trajectory calculations using FLEXPART-AROME were performed by me. Results from the PMF analysis were discussed with different co-authors, most frequently with C. Amelynck, T. Stavrakou, J.-F. Müller, and J. Brioude. The manuscript was written by myself. Editing and reviewing was done by all co-authors.

Contributions to hs-PTR-MS measurements

The hs-PTR-Quad-MS instrument deployed at the Maïdo observatory was operated remotely by C. Amelynck and N. Schoon, who were responsible for regular calibrations and processing of the raw data. However, as part of the mass-spectrometry team at the Royal Belgian Institute for Space Aeronomy and a local on La Réunion, I was happy to take responsibility for regular local manipulations at the observatory. This consisted of changing the filter every two weeks, performing intensive calibrations with respect to the relative humidity every two months, refill the deionised water reservoir used by the H_3O^+ ion source, and assist when intensive maintenance of the hs-PTR-Quad-MS instrument was needed every six months by either C. Amelynck or N. Schoon. Before and after the passing of a cyclone in the region when the Maïdo observatory needed to be secured, I was responsible for correctly securing the instrument and reconnecting the sampling line afterwards.

Collaborations with other campaigns

During my time at Reunion island, I took part in four field campaigns. The first was the OCTAVE intensive field campaign (March–May 2018) to which the hs-PTR-MS instrument contributed and for which I performed both mesoscale and synoptic scale backtrajectory calculations using FLEXPART-AROME and FLEXPART. The following year (2019) I contributed to the CONCIRTO (January-March), AEROMARINE (March–April), and the BIO-MAIDO (March–April) campaigns. For the CONCIRTO campaign I helped launch several weather balloons and deploy instrumentation at the Maïdo observatory. I equipped an ultra light aircraft with miniature equipment to the distribution of marine aerosols in the boundary layer over the ocean for the AEROMARINE campaign. My contribution to the BIO-MAIDO campaign was threefold. Firstly, I used the FLEXPART-AROME and FLEXPART models to generate back-trajectories for the collaboration. Mesoscale back-trajectories were made available during the campaign (up to 30 hours in advance) for collaborators to anticipate measurements for the next day. Afterwards, a reanalysis of the FLEXPART-AROME back-trajectories was performed using more up to date NWPs in order to minimise uncertainties. Second, I operated a microwave radiometer deployed at a second site along the slope of the Maïdo mountain. And lastly, the hs-PTR-MS instrument deployed at Maïdo also contributed to the BIO-MAIDO campaign. For these contributions I have been co-author on two peer-reviewed publications (Rocco et al., 2020; Martínez et al., 2020), for the OCTAVE and CONCIRTO campaigns respectively. A study by Samu et al. on aerosol composition during the OCTAVE intensive field campaign, for which I am co-author, has recently been submitted for peer review to the journal Atmospheric Chemistry and Physics. One more publication for which I am co-author is currently in preparation (Mascaut et al., in prep.) from my contributions to AERO-MARINE.

Scientific outreach

Conferences

- Stavrakou, T., et al. (2018). *Oxygenated Compounds in the Tropical Atmosphere (OCTAVE) : estimation of top-down methanol and formic acid fluxes based on IASI data* [Poster presentation at EGU2018]. 9 April.

- Verreyken, B., et al. (2018). *Coupling FLEXPART to the AROME mesoscale operational model* [Oral presentation at EGU2018]. 11 April.

- Verreyken, B., et al. (2018). *OCTAVE: First PTR-MS measurements at La Réunion Island: Influences of biomass burning and backtrajectory calculations* [Poster presentation at EGU2018]. 11 April.

- Verreyken, B., et al. (2019). *In-situ OVOC measurements in the tropical marine atmosphere for the OCTAVE project* [Poster presentation at EGU2019]. 10 April.

- Rissanen, M., et al. (2019). *Iodic acid and new particle formation observed at the high-altitude station of Maïdo (Réunion)* [Presentation at EGU2019]. 8 April.

- Surl, L., et al. (2019). *Measurement and modeling of atmospheric gaseous mercury depletion in a volcanic plume of Piton de la Fournaisa, La Réunion island,* [Poster presentation at ICMGP 2019], 9 Sep.

- Verreyken, B., et al. (2019). *Diurnal and seasonal variabilities in ground-based in situ (O)VOC measurements at the Maïdo observatory (South West Indian Ocean)* [Poster presentation at ICOS Belgium Science convention 2019], 3 October.

- Verreyken, B. et al. (2021). *Diurnal and seasonal variability in VOC composition at the remote tropical high-altitude Maïdo observatory (21.1°S, 54.4°E, 2160 m altitude) [vPICO presentation at vEGU2021], 27 Apr.]*

- Evan, S. et al. (2021). *Evidence of in situ cirrus formation in the tropical tropopause layer over the southwestern Indian Ocean)* [vPICO presentation at vEGU2021], 27 Apr.]

- Mascaut, F. et al. (2021). *Aerosol characterization in an oceanic context around Reunion island (AEROMARINE field campaign)* [vPICO presentation at vEGU2021], 27 Apr.]

Internal Meetings

- Verreyken, B. (2018). *Coupling FLEXPART to the AROME mesoscale operational model* [Oral presentation OCTAVE workshop], 1 Mar.

- Verreyken, B., et al. (2018). *FLEXPART-AROME backtrajectory tools* [oral presentation OCTAVE workshop], 4 Oct.

- Verreyken, B., et al. (2018). *Air mass transport on Réunion Island* [oral presentation OCTAVE workshop], 5 Oct.

- Verreyken, B., et al. (2019). *18 months of PTR-MS measurements at Maïdo* [Oral presentation OCTAVE annual meeting and workshop], 16 May.

- Verreyken, B., et al. (2019). *Turbulent scheme in the FLEXPART-AROME Lagrangian particle dispersion model* [Oral presentation OCTAVE annual meeting and workshop], 17 May.

- Verreyken, B., et al. (2020). *Characterisation of biomass burning plumes and their impact on the South-West Indian Ocean marine boundary layer* [Oral presentation OCTAVE annual meeting], 18 May.

Internal seminar

- Verreyken, B. et al. (2019) *Development on FLEXPART-AROME and 18 months of PTR-MS measurements@Maïdo - PhD progress during my 2 year stay at LACy* [Oral presentation], Saint-Denis, La Réunion, France, 20 Sep.

- Verreyken, B. et al. (2021) *Analysis of a near-continuous 2-year (O)VOC data set recorded with a hs-PTR-MS VOC analyser deployed*

at the Maïdo observatory [Oral presentation, organised remotely], Brussels, Belgium, 21 May.

Miscelaneous

- Guide for the visit of Ph.D. students of the university of La Réunion to the observatory.

- Volunteer at the Belgian day of sciences for the Royal Belgian Institute of Space Aeronomy in 2019.

Bibliography

Martínez, I. R., Evan, S., Wienhold, F. G., Brioude, J., Jensen, E. J., Thornberry, T. D., Héron, D., Verreyken, B., Körner, S., Vömel, H., Metzger, J.-M., and Posny, F.: Unprecedented Observations of a Nascent in Situ Cirrus in the Tropical Tropopause Layer, Geophysical Research Letters, https://doi.org/10.1029/2020GL090936, 2020.

Rocco, M., Colomb, A., Baray, J.-L., Amelynck, C., Verreyken, B., Borbon, A., Pichon, J.-M., Bouvier, L., Schoon, N., Gros, V., Sarda-Esteve, R., Tulet, P., Metzger, J.-M., Duflot, V., Guadagno, C., Peris, G., and Brioude, J.: Analysis of Volatile Organic Compounds during the OCTAVE Campaign: Sources and Distributions of Formaldehyde on Reunion Island, Atmosphere, 11, 140, https://doi.org/10.3390/atmos11020140, 2020.

Thomson, D. J., Physick, W. L., and Maryon, R. H.: Treatment of Interfaces in Random Walk Dispersion Models, Journal of Applied Meteorology, 36, 1284–1295, https://doi.org/10.1175/1520-0450(1997)036<1284:TOIIRW>2.0.CO;2, 1997.

Verreyken, B., Brioude, J., and Evan, S.: Development of Turbulent Scheme in the FLEXPART-AROME v1.2.1 Lagrangian Particle Dispersion Model, Geoscientific Model Development, 12, 4245–4259, https://doi.org/10.5194/gmd-12-4245-2019, 2019.

Verreyken, B., Amelynck, C., Brioude, J., Müller, J.-F., Schoon, N., Kumps, N., Colomb, A., Metzger, J.-M., Lee, C. F., Koenig, T. K., Volkamer, R., and Stavrakou, T.: Characterisation of African Biomass Burning

Plumes and Impacts on the Atmospheric Composition over the South-West Indian Ocean, Atmospheric Chemistry and Physics, 20, 14 821–14 845, https://doi.org/10.5194/acp-20-14821-2020, 2020.

Verreyken, B., Amelynck, C., Schoon, N., Müller, J.-F., Brioude, J., Kumps, N., Hermans, C., Metzger, J.-M., and Stavrakou, T.: Measurement report: Source apportionment of volatile organic compounds at the remote high-altitude Maïdo observatory, Atmospheric Chemistry and Physics Discussions, 2021, 1–37, https://doi.org/10.5194/acp-2021-124, 2021.

Appendices

Appendix A

Definitions of VOC

Volatile organic compounds (VOCs) are not uniquely defined. The term VOC is constrained according to the intended scope of the author. European legislature for examples defines volatile organic compounds (VOCs) as the following:

- Council Directive 1999/13/EC of 11 March 1999 on the limitation of emissions of volatile organic compounds due to the use of organic solvents in certain activities and installations:

  > volatile organic compound (VOC) shall mean any organic compound having at 293,15 K a vapour pressure of 0,01 kPa or more, or having a corresponding volatility under the particular conditions of use. For the purpose of this Directive, the fraction of creosote which exceeds this value of vapour pressure at 293,15 K shall be considered as a VOC;

- Directive 2001/81/EC of the European Parliament and of the Council of 23 October 2001 on national emission ceilings for certain atmospheric pollutants

  > "volatile organic compounds" and "VOC" mean all organic compounds arising from human activities, other than methane, which are capable of producing photochemical oxidants by reactions with nitrogen oxides in the presence of sunlight.

- Directive 2004/42/CE of the European Parliament and of the Council of 21 April 2004 on the limitation of emissions of volatile organic compounds due to the use of organic solvents in certain paints and varnishes and vehicle refinishing products and amending Directive 1999/13/EC

   > "Volatile organic compound (VOC)" means any organic compound having an initial boiling point less than or equal to 250°C measured at a standard pressure of 101,3 kPa;

- Directive 2010/75/EU of the European Parliament and of the Council of 24 November 2010 on industrial emissions (integrated pollution prevention and control)

   > 'volatile organic compound' means any organic compound as well as the fraction of creosote, having at 293,15 K a vapour pressure of 0,01 kPa or more, or having a corresponding volatility under the particular conditions of use;

Appendix B

PTR-MS data processing

B.1 Data filtering and processing

Before processing data, a detailed quality control was performed to eliminate invalid data by considering both ambient and zero measurements. In order to make this possible, a detailed digital log was kept, identifying individual measurements or periods that were manually flagged and removed from the raw data. Additionally, the ancillary meteorological measurements used in analysing the VOC concentrations were projected on the temporal resolution of the hs-PTR-Quad-MS instrument in order to combine both data sets for analysis.

A list of calibration factors is compiled using both the regular calibrations taking place every $\sim$3 days and the intensive calibrations against the humidity, performed every $\sim$2 months.

Species-dependent calibration factors (C), expressed as normalized PTR-MS product ion signal count rates (ncps) per ppb, are determined as a function of the normalised count rate of the hydrated hydronium ion at m/z 37 (I_{37}), which is used as a proxy of the humidity of the sampled air. They are given by the following relationship:

$$C = \sum_{i=1}^{n} a_i I_{37}{}^i + b. \tag{B.1}$$

The water dependence of the calibration factors was found to be especially important for formaldehyde (HCHO), isoprene (C_5H_8), isoprene oxidation products (Iox) and methyl ethyl ketone (MEK). For formalehyde, n was set to 5, all other compounds were fitted to a linear equation ($n=1$). Instantaneous calibration factors used in data processing during the campaigns are shown in Figure B.1.

The VOC mixing ratios [R] were determined from the ratio of the normalized, background subtracted VOC product ion signal and the corresponding calibration coefficient:

$$[R] = \frac{I_{R,amb} - I_{R,bg,inst}(I_{37,amb})}{C_{R,inst}(I_{37,amb})},$$ (B.2)

Backgrounds were only taken every 4 hours and were found to depend on humidity for some of the measured VOCs. As humidity can vary rapidly at the location of the Maïdo observatory, it was important to subtract a humidity-corrected background value ($I_{R,bg,instr}(I_{37,amb})$) for every single measurement in ambient air ($I_{R,amb}$) in between zero measurements. The humidity dependence of the background values was obtained by fitting a fourth degree polynomial function to all zero measurements within a four day measurement window (2 days future and 2 days past) for each compound as a function of I_{37}. In case the value of $I_{37,amb}$ was outside the range of $I_{37,bg}$ used to fit the instantaneous background, the time window was extended by 2 days (1 before and 1 after) until the value was within the humidity range used to fit the instantaneous background.

A figure in which this procedure is schematically represented is shown in Figure B.2

During the OCTAVE intensive observation period (IOP) (March–May 2018), a PTR-MS instrument from the Laboratoire des Sciences du Climat et de l'Environnement (LSCE) was deployed at La Réunion. Both instruments have been calibrated with the calibration systems foreseen by both institutes to assure correct calibration of each instrument. The calibration coefficients obtained from both systems were found to be in very good agreement (Figure B.3).
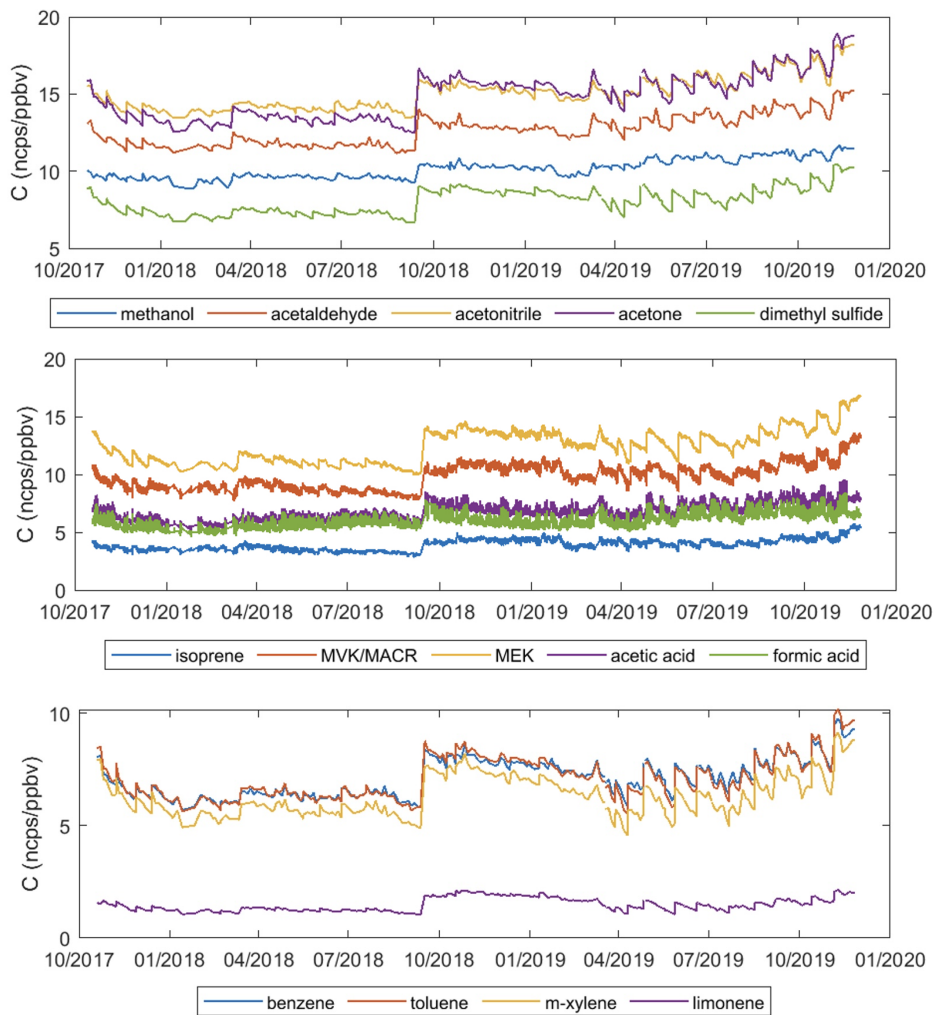
Figure B.1: Instantaneous calibration coefficients (in ncps/ppbv) for the measured compounds. The discrete increases on 13/03/2018, 12-14/09/2018 and 05-06/03/2019 are related to ion source/detector replacement. Other discrete increases in the calibration coefficients are mainly related to increases in the detector high voltage. The larger short-term variability of the calibration coefficients for isoprene, methyl vinyl ketone (MVK) + methacrolein (MACR), methyl ethyl ketone (MEK), formic and acetic acid reflects their dependence on air humidity. Figures provided by C. Amelynck.
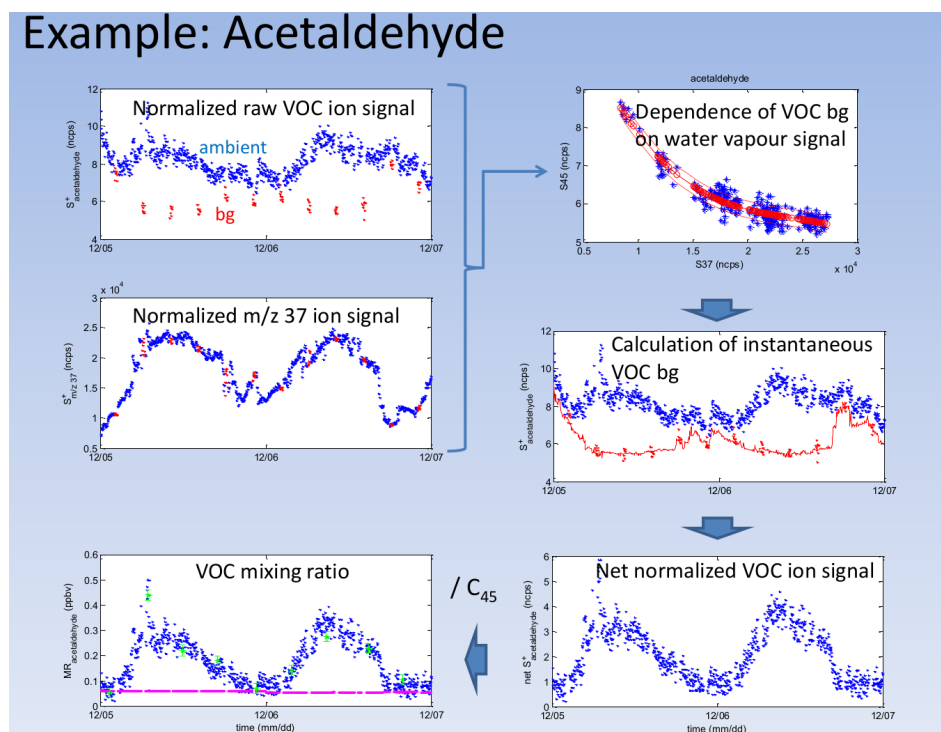
Figure B.2:   Data processing scheme of PTR-MS data taking into account the humidity dependence of the background signal and calibration factors. The example is for the processing of 2 days of data for acetaldehyde (m/z = 45), a compound for which the background was found to be strongly humidity dependent. Slide presented by C. Amelynck at the OCTAVE workshop in October 2018.
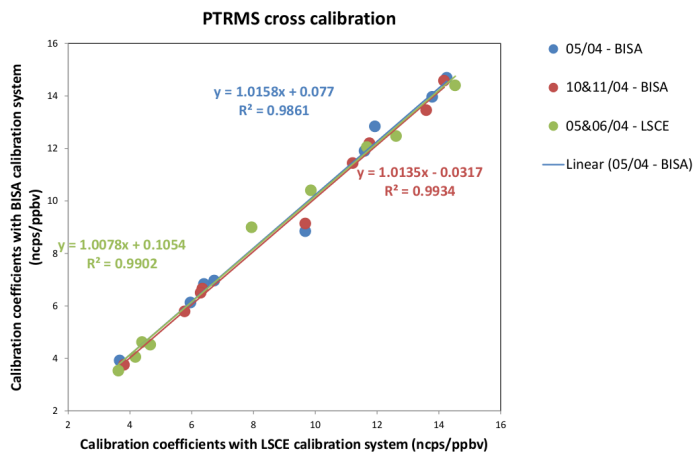
Figure B.3: Correspondence between calibration factors obtained with the custom-built BISA PTR-MS calibration system and the commercial Ionicon gas calibration unit from LSCE for both the BISA PTR-MS (05/04, 10/04 and 11/04) and the LSCE instrument (05/04 and 06/04) (data presented at the OCTAVE workshop in October 2018 by C. Amelynck.)

B.2   Operations timeline

The hs-PTR-Quad-MS instrument was deployed from October 2017 to November 2019. Large gaps in data ($>$ 7 hour data missing) only occur outside of nominal conditions, e.g. during the passing of cyclones, performing calibrations with respect to the relative humidity, regular intensive maintenance on the instrumentation, inter-calibration periods, performing scans over the complete mass range instead of running the instrument in multiple ion detection mode, or unforeseen technical disturbances. The complete timeline of PTR-MS measurements recorded at the Maïdo observatory is shown in Figure B.4. Note that a large gap in data exists for January 2018 due to the passing of cyclone Berguitta and some technical difficulties.
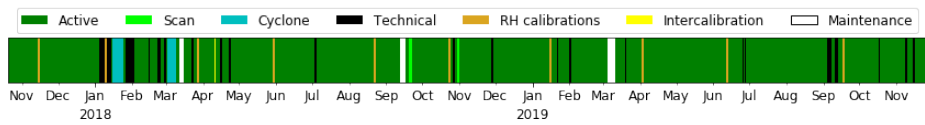
Figure B.4: Operations timeline of the hs-PTR-Quad-MS instrument deployed at the Maïdo observatory.